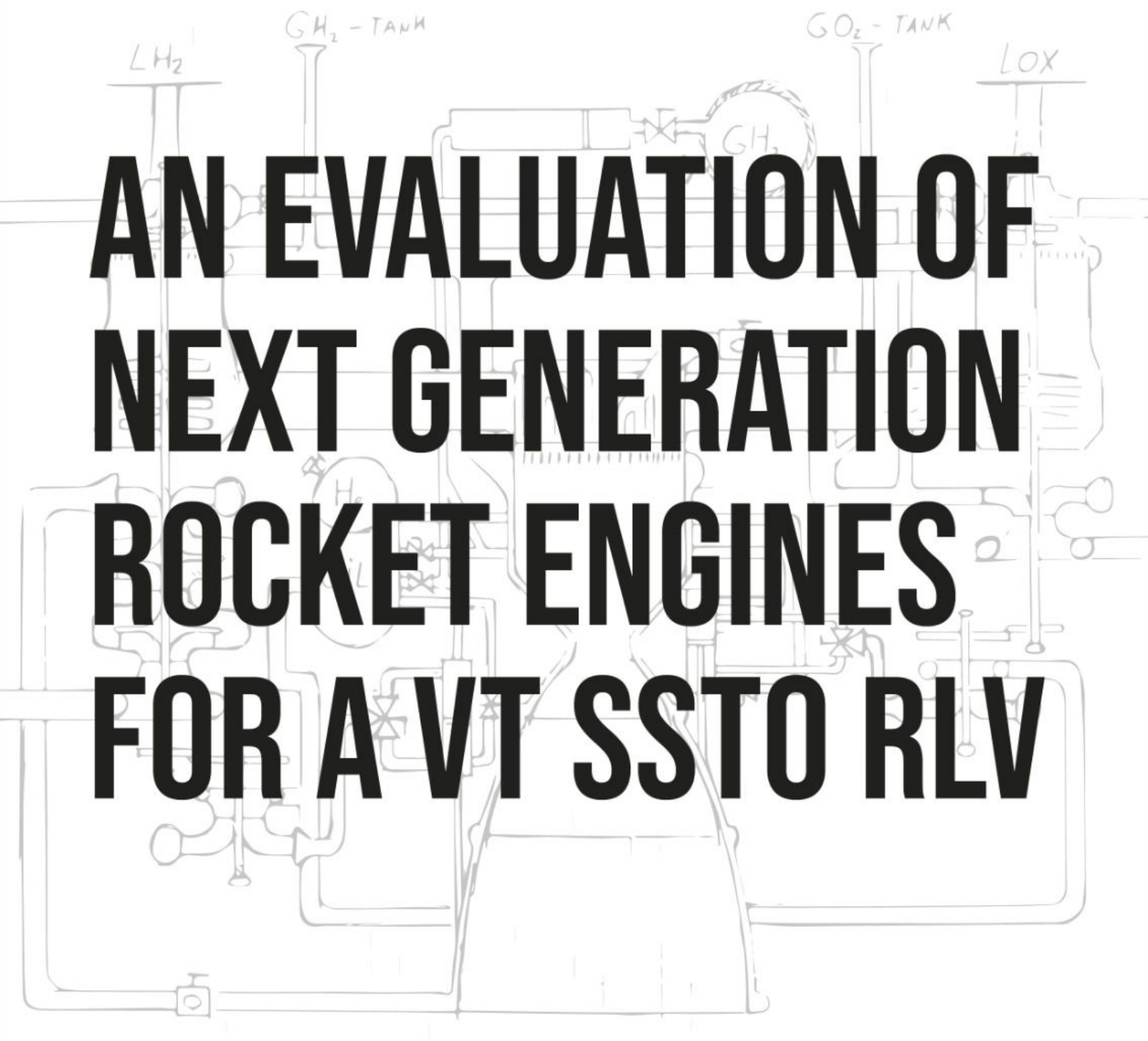

AN EVALUATION OF NEXT GENERATION ROCKET ENGINES FOR A VT SSTO RLV

A two-level evaluation on next-generation rocket engine and the propellant pallets for an SSTO vehicle developed by the private launch market. The first level is a literature evaluation, while the second is a performance analysis throughout the VT SSTO LV ascend trajectory.

TU Delft

Douwe Sonneveldt
Faculty of Aerospace engineering
Master thesis

An Evaluation of Next Generation Rocket Engines for a VT SSTO RLV

by

D.A.W. Sonneveldt

to obtain the degree of Master of Science
at the Delft University of Technology,
to be defended publicly on Tuesday Oktober 27, 2022 at Faculty of Aerospace.

Student number:	4485343	
Project duration:	November 9, 2021 - October 27, 2022	
Thesis committee:	ir. M.C. Naeije,	TU Delft, supervisor
	Dr. ir. E. Mooij,	TU Delft, Chair
	ir. B.T.C. Zandbergen,	TU Delft, Examiner

This thesis is not confidential and can be made public

An electronic version of this thesis is available at TBD.

TU Delft

Abstract

Observing that the majority of SSTO programs failed due to the propulsion system being far ahead of its time. Furthermore, acknowledging the that the private launch markets is increasingly dominated by partly reusable TSTOs. This thesis aims to evaluate whether next generation rocket engines make an SSTO viable within a foreseeable economical time frame, for the increasingly privatised space industry. From the market analysis it follows that the VT SSTO RLV developed by the private launch industry, with a payload capability of 15-20 tons to a LEO with an altitude of 200-400 km, is most likely. The evaluation is performed by a two level trade-off. Initially, a literature trade-off is preformed on elaborate range of potential next generation rocket engine, which are subdivided into pure rocket engine and breathing engine. All engines are evaluated on the market requirements, performance, and achievability. Only three engine types are selected. Upon evaluating the propulsion literature it was noticed that no literature cross evaluated advanced propulsion systems with high performance propellant pallets. Therefore, a literature propellant trade-off is performed.
For the aerospike, the pulse detonation engine and the precooled hybrid airbreathing rocket engine with the propellant pallets H2/O2, CH4/O2, C2H2/O2, and C2H4/O2 a performance analysis is performed. The performance analysis is done by both optimising the engine configurations and the ascent trajectory for a 15 ton payload delivery to an orbit of 400 km altitude. To simulate each engine, three performance analysis are developed, which are all derived from the continuity equations to ensure a consistent comparison. The aerospike is simulated as a continuous optimal convectional via the frozen equilibrium method, although it is found an alternation is needed to account for directional losses. The open-end of the PDE is simulated via a CJ-detonation wave followed by an exponential decaying blowdown phase. The DC nozzle expansion is iteratively simulated via the frozen equilibrium method. The intake and HPC of the precooled hyrbid airbreathing engine is simulated with convectional aero engine performance analysis, while the precooler is simulated ass a counter-flow heat exchanger. The CC and CD nozzle are simulated via the frozen equilibrium method.
From the optimised trajectory the representative performance of each engine is extracted and five engine configurations are identified as viable VT SSTO RLV engines. These are the H2/O2 powered aerospike, the pulse detonation engine and the precooled hybrid airbreathing rocket engine operating on an H2/O2 pallet, and the C2H2/O2 powered aerospike and pulse detonation engine. The H2/O2 powered PDE is found to be the most promising, as it offers the best performance gain relative to its achievability. Therefore, it advocates that future VT SSTO RLV research utilises the H2/O2 powered pulse detonation engine as the main propulsion system.

Keywords: Single-stage to orbit, Reusable Launch Vehicle, Aerospike, Pulse detonation engine, Precooled hybrid airbreathing rocket engine, literature trade-off, performance trade-off, Market research, Next generation rocket engines.

Contents

List of Tables

List of Figures

Preface

Before you lies the master thesis "The Evaluation of Next Generation Rocket Engines for a VT SSTO RLV" which is the culmination of my five years study of aerospace engineering, where I specialised in rocketry propulsion systems in particular. Yet, before pulling the reader into the content of this thesis, it might be better to explain the reason why it has been written from a author's point of view.
When initiating the research phase, the age of true reusability in space launchers had been properly established. SpaceX regularly uses Falcon 9, a partly reusable launcher, for human and non-human missions. Furthermore, competitors are rushing to catch up. It made me wonder about earlier reusable concepts. While, current reusable launchers are of the VT TSTO PRLVs type, originally it was believed that SSTOs would be the future of reusable launchers. Hence, the question arose would SSTO RLVs ever be a part of the reusable launchers, or would they merely be interesting vehicles reserved for science fiction? To answer this question I had to understand why prior SSTO concepts had failed.
It turned out that throughout all endeavours the propulsion systems were to advanced and complex for their time. However, the Venturestar, the last serious attempt at an SSTO RLV, was cancelled at 98% completion. Since then technology has advanced even further, thus the thinking became if it would be possible to meet past engine requirements with current technology.
To avoid getting carried away too much, as countless possible SSTO concepts exist, I decided to identify how an SSTO would be developed given the current launch market. The findings of this market analysis formed the fundamental drivers for SSTO type and, consequently, is the bases for all evaluations done in this thesis.
This thesis includes an elaborate overview of many possible next generation engine. It is from this overview that suitable engines are selected that do not only make VT SSTO RLVs a possibility, but are also most likely developed by the private launcher market. However, an odd phenomenon was detected as the research progressed, on no occasion were high-potency propellants combined with the more innovative SSTO engines. Therefore, I added an elaborate overview of potential propellant pallets for advanced engines too.
To evaluate the viability of VT SSTO RLVs I developed an optimisation model that optimises the engine configurations and ascent trajectory for a given vehicle powered by one of the selected engine configurations. I believe the complexity of this model is what is required to ensure that the extracted performance parameters are a realistic representation and that all the engines are evaluated on an consistent bases. To ensure the latter all engine performance analysis are derived from the three continuity equations.
I want to thank my supervisor who entrusted me with directional liberty to erect this thesis. Furthermore, I want to thank those and my roommates in particular, who vigorously helped with proofreading and illustrations. Lastly, I want to commemorate my grandfather who inspired me to become an engineer.

D.A.W. Sonneveldt
Douwe Anton Willem Sonneveldt Delft, October 2022

Nomenclature

Abbreviations

BC	Ballistic Coefficient
BFGS	Broyden–Fletcher–Goldfarb–Shanno
CC	Combustion Chamber
CD	Converging-Diverging
CG	Centre of Gravity
CP	Centre of Pressure
DC	Detonation Chamber
DFP	Davidon–Fletcher–Powel
F	Fuel
FFSC	Full-Flowed Staged Combustion
GG	Gas Generator
GTOW	Gross Take-Off Weight
HEDM	High-Energy Density Matters
HGO	Heuristic Global Optimisation
HL	Horizontal Landing
HPC	High Pressure Compressor
HRE	Hybrid Rocket Engines
HT	Horizontal Take-off
ISS	International Space Station
LACE	Liquid Air Cycle Engine
LH2	Liquid Hydrogen
LHC	Liquid Hydrocarbons
LOCE	Liquid Oxygen Cycle Engine
LOX	Liquid Oxygen
LPC	Low Pressure Compressor
LRE	Liquid Rocket Engines
NEWAC	New Aero engine Core concept
NPR	Nozzle Pressure Ratio
O	Oxidiser
PDE	Pulse Detonation Engine
PMF	Propellant Mass Fraction
PRLV	Partly Reusable Launch Vehicle
R&D	Research and Development
RFNA	Red Fumic Nitric Acid
RK4	Rung-Kutta 4
RLV	Reusable Launch Vehicle
ROI	Return Of Investment
RP-1	Rocket Propellant 1
SABRE	Synergetic Air Breathing Rocket Engine
SRE	Solid Rocket Engines
SSME	Space Shuttle Main Engine
SSTO	Single Stage To Orbit
STEP	Space Transportation Engine Program
TNRE	Thermal Nuclear Rocket Engines
TPR	Total Pressure Ratio
TPS	Thermal Protection System
TRL	Technological Readiness Level
TSTO	Two Stage To Orbit
UDP	Unutilized DeltaV Potential
VL	Vertical Landing
VT	Vertical Take-off
WFNA	White Fumic Nitric Acid

Greek Symbols

ϵ	Error term [-]
γ	Specific heat ratio [-]
$\kappa_{expansion}$	Reduced expansion ratio [-]
λ	Lapse rate [Km^{-1}]
μ	Viscosity [$kgm^{-1}s^{-1}$]
Ω	Angular velocity [s^{-1}]
Π	Pressure Ratio [-]
π_e	Ratio propellant mass/initial mass [-]
π_f	Ratio final mass/initial mass [-]
ψ	Momentary thrust load [-]
ρ	Density [kg/m^3]
σ	pitch rate [-]

Alphabetic Symbols

$\dot{m}$	Mass flow rate [kgs^{-1}]
A	Area [m^2]
Ar	Aspect ratio [-]
C	Aerodynamic constant [-]
C_D	Drag coefficient [-]
C_L	Lift coefficient [-]
c_p	Specific heat, constant pressure [kgm^{2}s^{-2}K^{-1}]
c_v	Specific heat, constant volume [kgm^{2}s^{-2}K^{-1}]
D	Force due to drag [kgms^{-2}]
dv	Delta velocity [ms^{-1}]
E	Effective conductivity [-]
e	Eccentricity [-]
G	Gibbs Energy [kgm^{2}s^{-2}K^{-1}]
g_0	gravitational acceleration [ms^{-2}]
H	Enthalpy [kgm^{2}s^{-2}]
h	Specific enthalpy [m^{2}s^{-2}]
I_d	Density specific impulse [s^{-1}]
I_{sp}	Specific impulse [s^{-1}]
L	Force due to lift [kgms^{-2}]
M	Mass [kg]
M	Molar mass [mol]
n	Placeholder for an unspecified number [-]
p	Pressure [kg m^{-1} s^{-2}]
q	pitch rate
R	Specific gas constant [kgm^{2}s^{-2}K^{-1}mol^{-1}]
S	Entropy [kgm^{2}s^{-2}K^{-1}]
S_e	Travel distance [m]
T	Force due to thrust [kgms^{-2}]
t	Time [s]
t_b	Engine burn time [s]
T_n	Temperature at n [K]
U	Flow velocity [ms^{-1}]
V	Volume [m^3]
v	Velocity [ms^{-1}]
W	Force due to weight [kgms^{-2}]
X	Mass fractions of a substance/mixture [-]
Z	Initial mass ratio SSTO/TSTO [-]

Subscripts

$\parallel$	Normal or parallel
$\perp$	Tangent or Orbital
a	Ambient
D	Drag
e	Exit
f	Final
gen	Generation
i	Initial
L	Lift
n	Arbitrary point
p	Periapsis
pay	Payload
pop	Population
$prop$	Propellant
ref	Reference situation

1

introduction

In 1957, the first man-made object reached space, ushering in the space race. Never before did mankind advance so rapidly in one particular field, the sky was not the limit. In the span of 12 years, mankind went from launching an object with the mass of a man into LEO, to landing two humans on the moon. After the space race ended, NASA assumed that this level of progression would resume, focusing their attention on the accessibility of space, by having multiple reusable vehicles to shuttle between multiple trajectories or orbits. However, as the space race ended, the development slowed, and the available resources diminished as a result the shuttle program, and the first SSTO program, was cancelled. The Shuttle program was too advanced for this new age.
Even though the shuttle program was cancelled, the idea of an fully reusable SSTO persisted and over the decades many designs were proposed, including the DC-X, X-30, and Venture Star. Unfortunately, none was ever completed, as the challenges of an SSTO RLV were too advanced at the time. Most Failure can be contributed too an over ambitious propulsion system to overcome all SSTO challenges, ramping up costs beyond an acceptable level. The technological leap, largely motivated by the pace of the space race, proposed to overcome the gravity drag, the atmospheric drag, and achieve orbit were simply too large for their time.
Furthermore, with the arrival of the partially reusable TSTO the concept of an SSTO RLV has rather disappeared into the abyss. However, with the privatisation of the space industry the sector once again sees rapid development. In addition, engine technology has progressed substantially, evidenced by the X-33 which was able to build an engine prototype. This observation raised the research question *To what extend can next generation rocket engines make a VT SSTO RLV viable within a reasonable development time frame?*
The relevance of the question now is that, even though an SSTO might be technologically possible in the future, economic forces could prevent this from happening. With the substantial developments in TSTO PRLVs, the initial competitive edge of SSTO RLVs, also referred to as the economical incentives, is diminishing. Hence, now could be the last change for the launch industry to develop an SSTO RLV, as it is increasingly less likely for the launch market to do so.

This thesis starts with begging the research question, to identify the need for, and how and what type of SSTO could naturally be developed in the current space market, as described in Chapters 2 and 3, respectively. This includes a market analysis and design choices based on the market requirements, which form the bases for the following trade-offs. The literature trade-off consist of a two-step approach. To start, an elaborate literature trade-off evaluates a large variety of possible next generations engines. The engines are evaluated on the previously established market requirements, the performance, and the achievability within an foreseeable time frame (TRL), as discussed in Chapter 4. An additional literature trade-off is performed which identifies high performance propellants for the selected engines, which is provided in Chapter 5. The absent in literature of such a cross evaluation motivated the inclusion of such a trade-off. The trade-off considers accessibility, handleability, and potency.
From the literature trade-offs certain engine types and their corresponding propellant pallets. While, all these engines can be developed within a reasonable time frame, it cannot be said whether these make VT SSTO RLVs viable yet. To determine the viability of each engine a simulation model is constructed that optimises the configuration of the selected engines and optimises the ascent trajectory for an VT SSTO RLV. How the

model is constructed and what VT SSTO RLV specification are used for the simulation is elaborated in Chapter 6.
To simulate each engine this thesis establishes three performance analyses for all the selected engines, which are elaborated in Chapter 7. The three performance analyses correspond to the aerospike engine, pulse detonation engine, and the precooled hybrid airbreathing rocket engine. As Chapter 8 will illustrate, the performance analyses provide a good indication on the performance of the engines, without the need for very complex models that require many engine design details. In addition, these model provide a far more accessible method to compute/evaluate the performance throughout the ascent trajectory, identify engine criticalities, and obtain initial design aspects.
Next to the need to evaluate the viability of the VT SSTO RLV when powered by one of the selected engines, the model allows for a direct comparison between engines. Such comparison cannot be done from literature as theses performance parameters are computed under different conditions, with different tool and capabilities, and with different levels of complexity. The model ensure a level of consistency, which due to the simulation of an ascent trajectory, is also a realistic representation of that particular engine when powering a VT SSTO RLV.
Hence, the viability and performance of each of the selected engine with its corresponding propellant pallets is computed, it is this data from which the research question can be answered. The thesis ends with identifying the most promising next generating rocket engine for an VT SSTO RLV, which logically follows from the performance evaluation. Future research can utilise the values and models of this thesis to size, evaluate, and preliminary design propulsion system, which can be topics for future studies. Furthermore, in Chapter 10 some suggestion are made on what these future studies can be. In addition, recommendations are made on how the performance model can be improved to incorporate more vehicles and how it can be expanded to an elaborate design model.

2

The Economical Justification of an SSTO RLV

At the time of writing this research, it is well established that the space industry has entered an era of private corporations dominating the launch sector. With Falcon-9, a TSTO partly reusable launch vehicle (PRLC), being the pinnacle of this movement having launched the first privately developed piloted capsule to the International Space Station (ISS). This era was mainly achieved through the effort of the Commercial Orbital Transportation Services (COTS) program, which significantly dropped the development cost and thus proved COTS effectiveness [44]. The COTS program has reshaped the space industry. Instead of being heavily involved in the development, governmental institutions now take a mature approach to the market, in that they only wish to tender the ascent vehicle, in which they are willing to invest. This approach has renewed the interest in Reusable Launch Vehicles, as such vehicles offer great economic benefits. The crown jewel of these efforts is the previously mentioned Falcon-9, which received less than USD 500 million from NASA, a fraction compared to previous development costs [44]. This amazing feat is evidence for the business case for commercial launch services, which is a continuing trend.
Therefore, it is extremely likely that future ascent vehicles will be developed by private corporations. Hence, the question this chapter aims to answer is, *what are the economic justifications for an SSTO ascent vehicle?*.
Yet, as good as the Falcon-9 is, the launch price of SpaceX has stagnated in the last few years, indicating a bottom limit for TSTO PRLVs launch cost [83]. The rapid growth in satellite launches in space and over 50.000 LEO satellites planned for 2025 [19], means that a launch costs reduction is required that TSTO RLVs might not be able to offer. For this reason, some people have once more reverted their attention to SSTO RLVs as the next milestone for a more accessible space, as these vehicles offer even greater reusability, thus increasing the economic incentive.
This chapter provides an overview of the space industry market and the overall trends. Additionally, this chapter explores the opportunities for an SSTO. The opportunities can then be translated into a mission profile.

2.1. The Space Industry in 2020

As early as 2015, the commercialisation of space was already widely expected [16], given the rapid growth together with active policy changes, like the Launch Act of 1984. The combined space industry had an estimated worth of USD 345 billion in 2016. It grew to USD 415 billion in 2018 [5][6], with 9% stemming from commercial organisations. The incredible growth is the result of other factors too. Firstly, more private money in the form of venture capital is entering the market. Unsurprisingly, eight new launch related start-ups were founded compared with two in 2000 [16]. Secondly, the general economy is transforming into a data-driven economy, increasing the need and diverse applications for communication and observation satellites [5]. Lastly, programs like COTS were successful in using public money to leverage private money, thus increasing the commercial interests [44]. This forces other governments to implement advantageous space policies too. This is evidenced by the UK government, taking a majority share in OneWeb, which had bankrupted earlier

on.

The space industry consists of three major sectors satellite manufacturing, the ground equipment (services and manufacturing), and the launch industry. The latter is the smallest in terms of worth USD 8 billion in 2018 [16]). Figure 2.1 illustrates a more detailed chart of the subdivision of each sectors in the space industry. This thesis primarily discusses the launch sector. Even though, the space industry would not exist without the Launch sector, the launch sector is driven by the needs of all other sectors. As such, the foreseeable needs of the entire industry should be carefully studied.

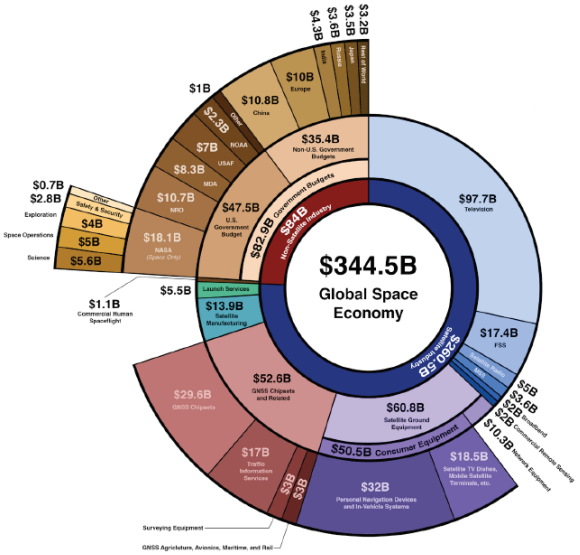

The global space economy at a glance (2016).

Figure 2.1: Illustration how the space market was compromised in 2016

Trends in ride sharing

The planning had been to launch 262 satellites in 2015, out of which 86 actually took place (2 launches failed). Out of the 86 launches, roughly one third involved commercial suppliers [10]. These numbers indicate that an average launch includes three satellites. This seems to increase, considering the trend presented in Table 2.1. The average trend is misleading. If one were to distinguish between commercial and non-commercial flights, one would discover that the number of commercial flights increases significantly more. One explanation is the nature of governmental institutions. They are more risk averse compared to commercial organisations. Governments tend to have satellites with more backup systems, so they are bigger, and they practice less in ride sharing[1]. Moreover, government institutions often have very specific missions, limiting the options for ride sharing.

Ride sharing tends to increase super linearly, as the decreasing size of the subsystems has increased of the possibility of swarm deployment. The current record is held by New Delphi with 104 satellites.

Trends in System Design and Manufacturing

Just like any other maturing industry, the industry is standardising. Rockets used to rely on different systems for each stage (unique boosters, unique 1^{st}, 2^{nd} and 3^{rd}.), current launchers reiterate their bottom stages (Falcon-9, New Shephard) and many of the subsystems like the engines. It is crucial to design systems that can be implemented at multiple levels, reducing many design and production cycles. Moreover, higher production levels lead to lower overhead costs.

SpaceX is a prime example, using an array of similar engines on the first stage, rather than fewer more powerful engines. As such the engines are easily converted to other crafts and upper stages.

[1] Ride sharing is when 2 or more satellites are launched via the same system, for which the ascent trajectory is optimised for all ride sharing satellites

Year	N°	Year	N°	Year	N°	Year	N°	Year	N°	Year	N°
1957	2										
1958	8										
1959	14										
1960	20	1970	130	1980	129	1990	168	2000	121	2010	120
1961	38	1971	156	1981	158	1991	135	2001	87	2011	129
1962	77	1972	133	1982	145	1992	130	2002	97	2012	134
1963	72	1973	138	1983	154	1993	108	2003	88	2013	210
1964	107	1974	128	1984	163	1994	123	2004	74	2014	242
1965	163	1975	156	1985	165	1995	105	2005	72	2015	223
1966	145	1976	158	1986	134	1996	100	2006	96	2016	221
1967	159	1977	137	1987	135	1997	152	2007	111	2017	453
1968	140	1978	165	1988	145	1998	157	2008	109	2018	382
1969	138	1979	124	1989	139	1999	129	2009	125		

Table 2.1: The number of spacecrafts that were put into space per year, since Sputnik, taken from [10]

Satellite Demography
Out of the current 2666 operational satellites, 1918 are in LEO, 554 in GEO, and 135 in MEO, with the remaining operating in an elliptical orbit [4]. However, programs like Starlink are expected to trigger a significant rise in LEO satellites over the next decade. Most of these satellites have been put in space by Ariane, Falcon, and Soyuz, each holding a 56%, 26%, and 11% market share (2016), respectively [5]. This is quite remarkable, as over 60% of the space industry is situated in the USA, whereas Ariane, a European launch agency, has launched over half of all commercial satellites. As all the rockets previously mentioned are able to serve all orbits, they logically dominate the market due to their market reach.

All in all, the space industry has become a more mature industry, attracting more private capital and standardising systems. Even though established sectors in the space market are still experiencing a moderate growth, many underdeveloped sectors are growing rapidly or expected to grow rapidly [19]. One of those maturing sectors is the launch service, which is experiencing a surge in commercial alternatives. Notably, the most successful launch services provide the ability to be deploy over a variety of orbits, just like their government counterparts.

2.2. Established Market Sectors

2.2.1. Television and Navigation

Satellite television and GNSS still make up the majority of the industry, with the television consisting of one third of the entire market value, see 2.1. Even though the satellite television sector is slowing down, it still grew by 11% over the period 2012 till 2016. The GNSS industry grew by 60% over the same period. The estimated worth of both was USD 98 billion and USD 85 billion, respectively. Including down stream markets, i.e., markets that are critical to but not necessarily part of the space market, would raise these values to well above USD 100 billion.

Because household dishes can only connect to stationary satellites, television is restricted to using geostationary satellites. GEO satellites have seen some miniaturisation, yet remain some of the larger satellites. Currently, 402 operational GEO satellites are in orbit, with an average lifespan of seven years. Each year roughly 50 to 60 of them have to be replaced. GEO satellites are only placed at three locations: above the middle of North America, the middle of Europe, and China. All this makes GEO satellites unsuitable for swarm deployment, yet ride sharing of 2-3 satellites is sometimes done. Note that even though ride sharing diminishes costs, it is helpful for competitors too. As the satellite television market has completely matured, it harbours many competitors.

GNSS has experienced some the of largest growth in the space market over the past decade. Furthermore, GNSS dependent devices are expected to reach a total of nine billion by 2023 [5], due to cheaper and more accurate GPS chips. This will consequently, increase their application in all fields. For instance, in agriculture GNSS is used to guide and automate all sorts of machines, and the mining industry uses similar technologies. Lastly, the wealth increase in Asia allows wider access of GNSS dependent devices, like cellphones.
Historically, GNSS used MEO satellites. However a trend to LEO satellites emerged in recent years. The disadvantage of LEO is the many more satellites that are required, which was simply not affordable. Moreover, the shortened lifespan of LEO satellites combined with the cost of GNSS satellites resulted in an even larger economical burden. However, the rise of ride sharing, miniaturisation, and reduction of manufacturing costs (standardisation), have mitigated those disadvantages, evidenced by the grown interest in LEO GNSS satellites[2].

2.2.2. Earth Observation

Rather unexpectedly, earth observation satellites have seen the largest growth in commercially owned satellites. This is due to the current economy becoming increasingly more data driven, thus increasing the demand for newer and faster data. With satellites becoming smaller and thus cheaper, they are increasingly used as data sources. Parties such as investors for instance use satellite observations to determine how fast cities and industries physically grow, to determine whether to invest in those economies. Alternatively, satellite imagery is used to determine the size of lithium deposits present in quarries, which can than be used to determine future market prices. The same has already been done for the oil reserves of OPEC. The implementations are wide and limited only by the operators imagination.
Earth observation satellites are commonly used for weather reporting, natural disaster forecasting, climate research, and other established research fields. With such a wide range of applications it comes as no surprise that LEO satellites roughly make up one-forth of the entire satellite population, namely 710 units in 2019 [10]. Even though, the Earth observation sector is a more established sector, it experiences some of the larger investments [5].

2.2.3. Exploration of Space

Arguably the oldest segment of the space industry, this sector has mostly remained withing government institutions. Programs like COTS were initiated to allow NASA to focus more on deep space exploration. That being said, NASA did put out a public contract for the moon landing in 2024. Yet, NASA did state that deeper space exploration missions will be done in house, as is in line with their current strategy. Furthermore other competing agencies, ESA, Roscosmos, and the CNSA, have not even implemented any programs to move (part of) the launch service to the commercial markets.
Even though, government organisations might not buy off the shelf rockets for deep space missions, they do outsource many of the manufacturing jobs and subsystem development.

2.3. LEO and MEO Operations

LEO is currently the most occurring orbit type, due to lower cost and better accessibility. The LEO satellites can be differentiated into the following categories, commercial observation, scientific (testbed, tech demonstration, other forms of measuring, etc.), and civil satellites. Although further distinctions can be made, they are unnecessary for the analysis of this study. Most of LEO satellites have remained relatively unchanged. It

[2] Many parties are investing in LEO based navigation, Boeing, OneWeb, Orbocomm, Globastar, and Iridium to mention a few.

logically follows that the launch systems have kept the same performance parameters.
Historically, civil satellites were launched by NASA. However NASA's new strategy aims to completely outsource all reoccurring LEO and MEO flights to the private market [44]. This is advantageous for launch suppliers, as NASA remains the largest customer in the space market. Other government agencies are unlikely to adapt similar policies (in the foreseeable future, that is), as their current rockets are still highly competitive, as witnessed by Ariane's 56% market share.

2.4. Upcoming Market Sectors

2.4.1. Satellite Radio

Oddly enough, satellite radio is the second of the space industry's fastest growing sector. This sector has experienced an annual growth of 7% [5]. Furthermore, it has shown the most consistent growth of the space market. The growth arose mostly from consumers in the USA. The satellites used for radio operate in elliptical orbits, due to their relative long exposure to one specific area. The orbits vary between MEO to HEO and LEO to MEO.

2.4.2. Nano/Micro-Satellites

The mass of satellites has been steadily decreasing ever since 2012 (currently ~3600 kg). In 2019, over half the satellites sent to space had a mass of less than 10 kg [6]. As was previously mentioned the majority had commercial origins. The commercial space industry generally uses more and smaller satellites. Moreover, it tends to be faster in changing to smaller and cheaper satellites, opposed to government owned satellites. The major driver is costs. Smaller vehicles, for one, can piggyback ride or rideshare, which reduces their launch cost. Furthermore, because they are expendable small, satellites often use cheaper components. Components used for Nano/Micro-satellites were often developed in other markets. These markets have a higher throughput and are often not designed to deal with the harsh space environment. Thus, the development costs are lower and can be spread over far more products. Light sensors/chips for phones are produced in the millions, whereas as only a few satellites are launched each year. The components not having been developed for space, can be seen as a disadvantage. However, the components are much cheaper and come in such variety that it is cheaper to buy many different types and test which of them are suitable for space. Note that it is possible that no type passes the test, yet testing represents only a fraction of the would be development costs.
The method described above is deemed too risky for government institutions to be widely implemented, due lower acceptable risk levels. Nano/Micro-satellites have less mass for back up system and ride sharing tends to be more risky to the overall launch. For this reason most Nano/Micro-satellites operate in LEO, for which transit is relatively cheap and commercial presence is higher. Note that government institutions sometimes use Nano/Micro-satellites as tested.

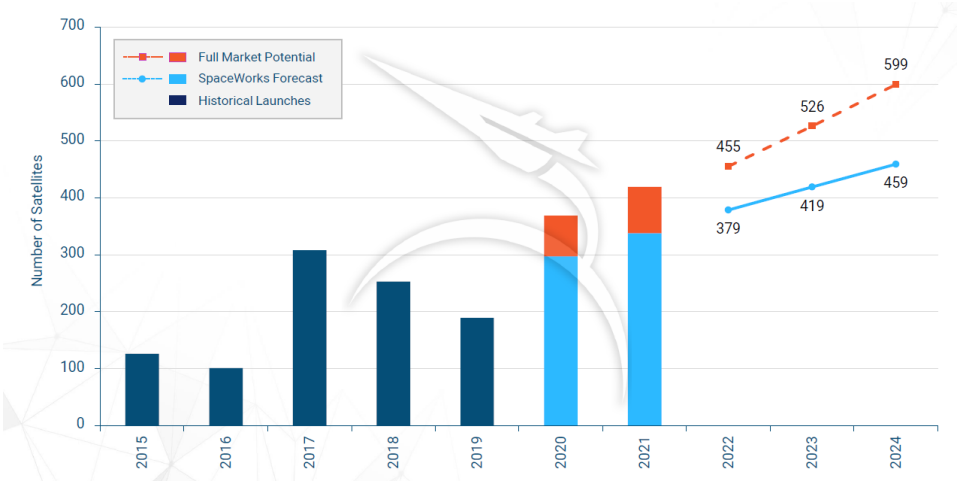

Figure 2.2: Illustrates the number of smaller satellites launched and a future prediction, taken from [72].

Even though the development in the field of micro satellites have been plentiful and predictions have been more than optimistic, the number of Nano/micro-satellites peaked in 2017 and has been decreasing ever since, see figure 2.2. Note that figure 2.2 gives the impression that substantial growth will occur. However, while previous reports showed similar predictions, a decrease was observed. Even the report by the Australian government [5] and McKinsey [19] remain sceptic and were uncertain how this sector will develop.
Even so, SpaceX launched 420 small satellites for their Starlink project last year. Their main competitor, OneWeb, launched 74 satellites over the same period. Both programs want to build an extensive constellation of small satellites.

2.4.3. LEO, MEO, and NGSO

Even though most satellites are operating in LEO, high altitude satellites have performed communication and navigation services. Yet, Non-Geostationary Orbit communications (NGSO) systems have reemerged with reasonable developments, as some organisations had already tested the concept in the 1990s. The key differences compared to 20 years ago, is the miniaturisation of the required technology to establish such connections, thus reducing the size and mass of the satellites. This has consequently resulted in smaller launcher or swarm deployment, reducing launch costs. Moreover, components are cheaper too, as was explained in 2.4.2. Yet, cost, especially launch costs, must be reduced further to make LEO GNSO viable in the long term [19]. The demand for greater bandwidth, due to te data driven economy, has increased the total of potential clients [5]. Whether the bandwidth of those satellites will be sufficient to ground-based alternatives remains to be seen.

As was briefly discussed in the previous section, the direct LEO satellite market knows two serious contenders. SpaceX and OneWeb. Both plan to use constellations consisting of 12,000 (Starlink) and 650 satellites, respectively. Both have deployed 420 and 74 satellites, respectively. If all direct LEO constellations succeed, 50,000 of these satellites are expected to be launched in the next ten years [19].

These LEO constellations will operate at altitudes between 500 km and 2000 km, with a shortened life span of 5 years. These systems offer a lower latency and higher bandwidth [19], being competitive to pre-5G wireless connections and sufficient for current data transfers. The cost to implement large LEO constellations ranges from USD 5 billion to USD 10 billion and would require another USD 1 to USD 2 billion for the annual replacement costs. Even though this might seem a lot, players such as Amazon, Facebook, and Apple have taken or are taking steps to enter the fray. These organisations have enough capital to the develop and implement such systems without any additional investments. Direct LEO connection offers consumers worldwide coverage for probably same price. From a provider's standpoint, this has a higher client reach and less legal blockades, as the infrastructure will not be present on the ground.

Currently, satellite communication is purely business to business based. Even if NGSO constellations can compete with alternative data transfers methods, growth will be limited. However, if the technology is accessible to consumers, an annual growth of 65% can be achieved [19]. Yet, this all depends on cutting costs, getting it close to the alternatives. Otherwise the services would only be suitable for clients who cannot accept the latency and who require a coverage greater than what current systems have to offer.

The engineering specifics of these satellites remain largely classified, but it has been derived that their masses lie mostly between 150 kg and 250 kg. Furthermore, it is expected that due to outsourcing companies with their own launch capabilities, like SpaceX, launch at cost price as opposed to market price. Especially for swarm deployment super heavy reusable lifters would be ideal. Such lifters, are currently only used for deep space transfers.

2.4.4. Space Debris Removal

Space debris increased from 8840 tracked parts in 2001 to 18640 tracked parts in 2017 [5], neglecting all untraceable parts. Even though space debris does not pose an immediate threat, it is widely accepted that this will become the greatest threat to spaceflight. As more and more satellites are put into orbit, more debris will be introduced, especially if any of the NGSO constellations bear fruit.

As of yet, no working space removal craft has been flown. However two concepts seem promising. Firstly, a relatively small expandable vehicle which attaches itself to the debris, after which it re-enters with the debris. Alternatively, there is a non-expandable vehicle which will attach itself to the debris, re-entering orbit. Afterwards it detaches and moves to the next object. Note that the former will be deployed into swarms or use some form of ride sharing.
Even though no space debris regulations have been implemented yet, with the increased commercialisation of space organisations are expected to be required to get rid of their debris. Currently, organisations only have to ensure the UNOOSA that they will either have their satellites re-enter or transition to a graveyard orbit. Failure to do so bears no consequences. Moreover, as more orbits get occupied, some organisations might be interested in occupying an orbit that is currently held by a defunct satellite. Such organisations might thus have an interest in a satellite removal vehicle.
The service of space debris removal is still in its infancy, yet regulations could make it develop very fast.

2.5. General Market Forces and Current Competitors

Before the place of an SSTO vehicle in the launch market can be determined, one must first know the competition and determine whether a market edge exists. The commercial launch industry can be divided into three segments: heavy lift launchers, conventional launchers, and small payload launchers.
The (super-)heavy lift launchers are often used for deep space missions of very heavy payload deliveries. Designs include Falcon heavy, the Space shuttle (retired), and SLS (in development). The price of the Falcon heavy is roughly USD 90 million per launch, which is a little below the market price. However, the heavy lift launchers operate in a niche market, dominated by government institutions. As mentioned before, they are likely to develop those systems in house. The Falcon heavy is an exception, due to te fact that it basically consists of three first stage Falcon-9s. This method is obviously unsuitable for an SSTO. Moreover, the low number of flights would make the return period too long, as developmental costs of SSTOs will surpass that of conventional rockets.
TSTO rockets (~20.000 kg payload capability) are the launchers mostly used for conventional satellites, with a mass between the 2000 kg and 6000 kg. Even thought the word conventional is used, there is a trend towards lighter satellites (a few hundred kg) using ridesharing/piggyback, swarming and dedicated smaller rockets (Electron rocket). Conventional rockets can deliver a variety of payloads to different orbits, up to GTO (the vehicle carries the last DeltaV for GSO). Typical rockets belonging to this category are Ariane 5, the Falcon-9, and the Soyuz. These three alone are responsible for over 80% of the annual launches, at a launch cost of USD 137 million, USD 62 million [70], and USD 66-81 million, respectively. Note that the prices for Ariane 5 and Soyuz are estimates, as government agencies do not publish their prices. One can thus expect government prices have higher margins. Furthermore, SpaceX has not completely taken over the market, so this would suggest that real prices might the significantly lower.
Notable is that Ariane 5 is being replaced somewhere next year by Ariane 6, which should cut launch cost by half. Even more notable is that Ariane 6 will have smaller payload capabilities than its predecessor.
Smaller rockets, such as the Rocket Lab's Electron and the Northrop Grumman's Pegasus, are used to bringing nano/micro-satellite into LEO. These rockets are typically under USD 10 million (USD 6 million for the Electron) and they deploy a payload of roughly 200 kg. These systems are typically used for satellites that cannot find suitable companion satellites, or require very specific orbits. Investors have shown a major interest in this type of launchers [19]. Investors tend to see these smaller rocket launch services as less risky, because they require less development capital and lower upfront investment. The lower initial capital comes with a smaller group of investors, thus investors remain relatively powerful, making it even more attractive to investors. Investors tend to see projects as less risky when they maintain a higher level of control.

2.6. Opportunities for an SSTO RLV

To summarise, for space to reach the accessibility required to make project like large LEO constellations viable, launch cost will have to be reduced considerably. SSTO RLVs offers a few key benefits. The main advantage being the shortened turn around time. Unlike the partially reusable TSTOs, they can be completely reusable, due to the construction of a new second stage. Given that conventional rocket construction is very expensive, most are build-to-order, with only few ready-to-go. An SSTO offers thus greater flexibility

to clients, by providing serves at a shorter notice. Consistent grounded periods[3] are avoided, as no systemic construction is required to make the vehicle launch ready. The other more obvious advantageous are a greater reusability, and thus a better economy of scale. Where both the turn-around time and higher reusability reduce the need for many vehicles to reach the same market size, therefore reducing the required overhead.
Even though, fully reusable TSTOs, like Starship, offer the same level of reusability, they come with the additional engineering challenge of reattaching the upper stage to the bottom stage. The reattachment process is a major point of failure which introduces a scrupulous endeavour. It is realistic to speculate that this process is similar to the refurbishing of the Space Shuttle, therefore the turn-around time and overhead argument hold against a TSTO RLVs.
Before considering which key benefits offer the most potential in the established and developing space market, lets first eliminate the sections for which it does not. To elaborate, an SSTO would be very unsuitable for deep space deployment (moon and beyond) as this would make the take-off vehicle to surpass any feasible size. Furthermore, the limited yearly launches would be insufficient to attain any reasonable earn-back period. On the contrary SSTOs might be able to serve a supporting roll delivering payload and propellant to an deep-spacecraft already in orbit, much like Starship when launching to mars. However, such rolls can never be the primarily purpose of the SSTO proposed here.
For similar reasons, the micro & Nano launch industry is eliminated too, due to its limited economic size. Even though, the sector is rapidly growing most utilise swarm deployment or piggybacking, which has half the USD kilo price than that of small launchers. Furthermore, the limited number of micro satellites that are launched by small launchers have very specific deployment requirements (e.g. polar orbit).
While, an SSTO can perfectly serve as a supply vessel for the ISS, which would come with a reliable income stream, NASA has invested heavily in Boeing and SpaceX to specifically fulfil this task [44]. Hence, it is unreasonable to focus on this segment, as it is unlikely that NASA will commit to new endeavour of this kind. Furthermore, initial investment would increase substantial, due to te added safety requirements complementary to ISS resupply and crew missions.
Considering the remaining market with their respective sizes and the discussed key benefits, an SSTO RLV will initially enter lower segment of the conventional launcher. This will give it a LEO payload capabilities of 15,000 - 20,000 kg for an altitude of 200-400 km, which is in line with the paylaod reduction trend of newly developed launchers [83]. Which, makes it a competitor to the likes of Falcon-9 (SpaceX), Soyuz, and New Shepard (Blue origin). Logically it follows that it is more likely that an SSTO development relies on an already established markets, than one that is still underdeveloped. This launch market segment is were a privately developed SSTO can achieve an acceptable earn-back period, due to the potential cost reduction and turn-around advantage, especially given the already limited amount of available cheap rocket launchers.
The specifications allow the vehicle to carry 2-3 conventional satellites, thereby able to serve the majority of the launch industry. Furthermore, the mission profile does allow for future swarm deployment, even if it is at a lower scale than Starship or other heavy lifters[4].
Even though the vehicle will have reduced payload GTO capabilities, it will not have heavy lift capabilities nor aim to increased LEO paylaod capability. It is believed that such aims will complicate the vehicle beyond attainable levels and should only be attempted in future versions. Therefore, the heavy launch sector will be dominated by TSTOs a while longer.

2.7. Economic Requirements for an SSTO RLV

It is clear that if SSTO vehicles want to stand any chance in the space industry they must be reusable. Take SpaceX as an example: it dropped the rocket price form USD 175 million to USD 62 million over a period of five years [83]. SpaceX was able to achieve this feat by leveraging already proven technologies and operations. It is largely due to this reduction that SpaceX was able to expand its market share so rapidly. Therefore, an privately SSTO will rely on as many proven technologies as possible, unlike the failed X-33, which is further discussed in Section 3.1.
One of the major changes in the market is the demand for "fixed services", this is further supported by NASA committing to the same strategy [16]. The main challenge for the SSTO, and any new ascent vehicle for that matter, is to achieve an operational prototype as soon as possible. An operational vehicle will ensure a revenue stream and gain initial market share. The launch costs are then reduced by continuous development,

[3] Operations that require (re-)construction of certain (sub)systems or excessive maintenance, that goes beyond refuelling, general maintenance or replacements (unsystematic).
[4] Whether the use of heavy lifters in this particular instance is economically viable remains to be seen.

like the Falcon-9.
The vehicle should aim to reach launch cost between USD 80-100 million upon entering, even though if this is higher than that of other suppliers. This forms no issue due to the lack of sufficient relative cheap rockets to serve the entire market need. Currently, similar programs to COTS do not exist, hence a fast entry before the prices become even more competitive due to the arrival of more TSTO PRLV is desired.
The aim should be to get the final launch cost down to below USD 60 million, such that one can undercut the market. With the faster turn-around time, higher utility levels can be attained. Consequently, SSTO stand to achieve a more rapid market growth compared to organisations operating TSTO PRLVs/RLVs given the same number of vehicles.
To conclude, this chapter has established in what launch segment the SSTO will operate and what requirements it must meet. Furthermore, an economic prediction is made about how it should go about achieving those requirements. All in all, an SSTO abiding by the requirements mentioned in this section would truly bring a disruption to the space industry, reducing the price per kg to USD 2000 (currently USD 3000-4000). Thereby, making space far more accessible than before and possibly allow other potential clients to enter the general space market.

3

An Economically Driven SSTO RLV

Although Earth's size makes it theoretically plausible that a chemically fuelled SSTO is marginally the better launch system from Earth, many principal complications exist. Factors like the high orbital velocity (~7400 m/s at 200 km), Earth's gravity especially in the early stages of the launch, and the flight through Earth's atmosphere. Neglecting other aspects, many possible SSTO concepts exist that aim to reduce, circumvent, and reduce the mentioned factors.
Furthermore, as discussed in Chapter 2, the space industry is maturing due to an influx of private capital. As the industry is privatised, development will be based on profit-driven decisions. SSTO reusable launch vehicles (RLVs), as discussed in Chapter 3, are no exception to this rule. The potential to drastically cut launch costs is the primary reason to develop such vehicles. Therefore, to summarise Chapter 2, privately developed SSTOs must be, 1) highly reusable 2) able to carry a payload of about 15-20 tons 3) able to operate over the range from LEO up to GTO. All in all, this still leaves many SSTO concepts possible.
However, the propulsion system is widely seen as the most critical component of a launch vehicle. It alone accounts for 70% of the manufacturing costs [5], attributing to the engineering complexity of the system. In a free economy driven market, entrepreneurs will thus try to mitigate this complexity as much as possible, while retaining the required performance. The propulsion system is the heart of the launch vehicle, thus its characteristics are highly aligned with and influenced by the vehicles characteristics, and vice versa. Such reasoning offers an elimination approach to the many SSTO concept.
To determine which engines enable SSTO RLVs, it is crucial to better understand on what SSTO RLV it is implemented. Hence, *To what extent does a private market developed SSTO influence the SSTO design choices?* Answering this question will make it possible to deduce fundamental design aspects of an economically driven SSTO.
This chapter discusses multiple concepts and designs, including a TSTO configuration and even a take-off assist vehicle. Trajectory procedures such as vertical or horizontal take-off and landing are considered too. All these aspects will be assessed for their innovative advantages, their achievability, and their development costs. When such a vehicle has been identified, the requirements for the propulsion system are established.

Beware that all launch systems are highly integrated vehicles, meaning that the engine choice is closely related to the overall design. One can thus expect that not all aspects and details of SSTO vehicles will be provided. Rather, a variety of design aspects that follow from the use of a certain engine is provided. Therefore, the complete vehicle design is linked to the engine trade-off.

3.1. General SSTO RLV Concepts

The concept of an SSTO RLV, ferrying cargo and personnel to space has been around ever since humans landed on the moon. Originally, NASA theorised about using multiple vehicles to ferry personnel between different trajectories. Spaceplanes playing a crucial role in this system. However, due the defunding of NASA the system never progressed past the Space Shuttle. Eventually, the project was skilled down, stagnating at the Space Shuttle. The Space Shuttle never reached the ambitions of the original goals and remained a refur-

bishable launch vehicle.
Very few RLVs have reached a stage beyond concept designs, let alone an SSTO RLV. Designs like the VentureStar and DC-X were proposed, yet both were cancelled after technical difficulties. Both designs had very similar design criteria, comparable to the ones established in Chapter 2. The X-33 is arguably the only SSTO design that came closest to actually flying.
The following paragraphs will briefly discuss the more notable SSTO RLVs. Thereby, providing a baseline in SSTO design philosophies.

The X-33 VentureStar
The X-33 was a very revolutionary craft for its time, with a total take-off mass of roughly 130,000 kg. Furthermore, two linear aerospikes engines would be used as its propulsion system. The X-33 served as a testbed for VentureStar, which would be able to carry a 20,000 kg paylaod to LEO, with a total take-off weight of 1,000,000 kg [82]. This made it a relatively heavy vehicle compared to Falcon-9, with 549,054 kg. VentureStar would be powered by 7 LOX/LH2 RS2200 linear aerospikes, take-off vertically and land horizontally. The latter would be possible due the high lifting body.

The Mcdonnel Douglas DC-X
Originally proposed as an alternative to VentureStar, the DC-X or Delta Clipper was a far more conventional design and is somewhat similar to current reusable rockets. The delta clipper would use four LOX/LH2 RL10 engines (conventional rocket engines). The vehicle would both take-off and land vertically. The landing would be done via a suicide burn. Unfortunately, the vehicle was never further developed, after losing the contract to Lockheed Martins X-33. As its development was stopped, specific design parameters for the final vehicle were not established. However, the vehicle was expected to have a similar payload capability of 20,000 kg. The delta clipper, would have followed a very similar flight trajectory as conventional rockets, as the lack of a lifting body prevents it from utilising a lifting trajectory.

Skylon
The Skylon concept is currently begin developed. It involves airbreathing engines. Skylon stays remarkably close to the early spaceplane design philosophy. The vehicle would be powered by two newly designed Synergetic Air Breathing Rocket Engines (SABRE). The engine would use liquid hydrogen and switch between LOX and air as an oxidiser. Skylon aims to carry 17,000 kg to LEO and up to 7,300 kg to GTO. Unfortunately, the project is still in its infancy, as the SABREs are still under development. The development of such engines requires a high level of funding, namely GBP 200 million for a full scale prototype [1]. Sceptics are dooming the project due the complexity of the engine, yet the project has raised enough investment to continue. The completed vehicle would both take-off and land horizontally.

Starship
Even though this is not a vehicle designed to ferry cargo to LEO it does illustrate the highest level of reusability that a TSTO can achieve. The vehicle will have two reusable stages, bearing much resemblance to current reusable first stage rockets. The first stage will not have to re-enter, as it does not leave the atmosphere eliminating the need for a TPS. Both stages land using a suicide burn. The upperstage would bear great resemblance to vehicles like the Space Shuttle. The upper stage will have wings for control throughout the re-entry phase. Starship aims to deliver a payload of 100-150 tons to LEO, with a GTOW of 5,000,000 kg. SpaceX has claimed that cost per launch would be USD 2 million, yet this has widely been disputed.

Many more concepts have been proposed, even concepts as odd as "black horse"[2]. The ones above provide the most important design philosophies. It was established that an RLV can both be an SSTO or TSTO, the vehicle could utilise lift trajectory or a conventional rocket trajectory, and that airbreathing engines and non-breathing engines are possible. More aspect do exist and will be elaborated in later sections. Yet, the previous three form the core of all design philosophies.

[1] https://www.bbc.com/news/science-environment-23332592
[2] An SSTO spaceplane that would be refueled mid flight

3.2. Vertical Take-off versus Horizontal Take-off

An important design parameter is the maximum producible thrust level, generally experienced at ignition, which is directly determined by whether the vehicle launches vertically or horizontally. The same reason is valid for the landing, as a suicide burn requires a short but high thrust burn.
A horizontal take-off is nothing new and has been proposed in many concepts. The general idea is to mimic airliners, who have a far shorter and less intense (thus cheaper) transit time. Well established infrastructures, such as airfields, could be utilised.
GTOW (low mass vehicles are often cheaper to manufacture) and achievability (reasonable return of investment/development costs) largely determine what would ultimately be the best configuration. Luckily, an extensive trade-off has been done by Dissel, Kothari and, Lewis [22]. In their paper, multiple configurations of airbreathing SSTOs are performed, together with a TSTO Space Shuttle like vehicle. Moreover, a consideration between LH2 and LHC was included too. It was assumed that the main engine for the SSTO would be either a 2D scramjet or an inward 3D scramjet, as are illustrated in Figure 3.1. Note that a 2D scramjet relies on 2D shock physics, whereas a 3D scramjet utilises all spacial dimensions.

Figure 3.1: Illustration of a 2D scramjet and an inward 3D scramjet, taken from [22].

The observant reader might argue that this analysis only applies to the specific scenario in which airbreathing engines are used. However, closer investigation would show that the weight of tanks, multiple propulsion systems and a different propellant for the SSTO, is roughly equal to the weight of the propellant and single engine/tank for the TSTO. This, indicates that both propulsion systems are interchangeable with a minimal impact on the other subsystems. Furthermore, by keeping the engine specifications the same, only the weight of the support systems for HTHL and VTHL affect the mass.
In Figure 3.2 the results of the GTOW and dry mass, the vehicles are configured for a payload of 20,000 lb (9072 kg) delivered to an orbit of 100 nmi (185 km) [22]. The study computes which vehicle can achieve this feed with the lowest GTOW and dry mass. Studying the vehicles, the conclusion is that the best configuration is a VTHL configuration, similar to VentureStar.
The two primary drivers for this conclusion, are the atmospheric drag and the support systems for the HTHL configuration. Firstly, the HTHL ascends much slower than the VTHL, thereby spending more time in the lower atmosphere, where the relative drag is much higher. Secondly, the supporting subsystem like the landing gear must be reinforced to deal with. Additional structural mass must be added to ensure the structural integrity latitude and longitude.
Notably, any airbreathing SSTO will require some sort of rocket propulsion to get into orbit, regardless the take-off procedure. As such, for a minimal mass addition the rocket propulsion system can be scaled up to allow VT. Furthermore, some airbreathing engines do require rocket system regardless (scramjets usually start to operate at ~3 Mach), reducing synergy even further.
Considering all aspects, using a heavier but more powerful propulsion system for vertical take-off is the superior design choice. The weight gained outweighs the slower descent (increase both gravity and atmospheric drag.)

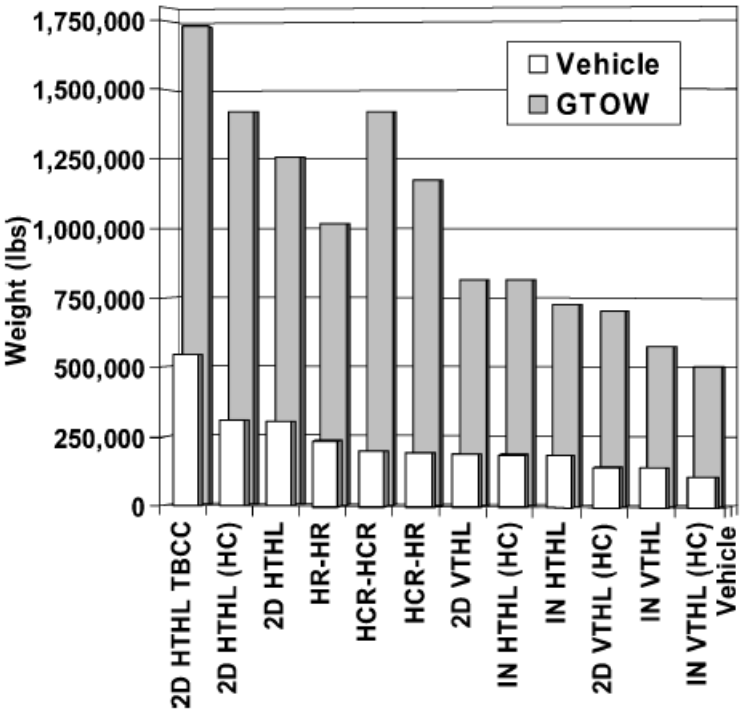

Figure 3.2: Provides the GTOWs of various SSTOs vehicles and TSTO space shuttle like vehicles

3.3. Re-entry Procedure

The re-entry procedure is the most hazardous phase, and as such the most damaging. It was the damage to the TPS that was the driver of the prolonged ground operations on the Space Shuttle. Two re-entry procedures exist, nose re-entry and base re-entry, each with their own advantages and disadvantages. This section is limited to the most relevant ones, for more insight the reader is encouraged to read [54].
Under the assumption that the base is wider than the tip, the base will have a larger radius, thus distribute the heat over a larger area. Yet, a base has a lower ballistic coefficient BC and as such experiences a higher peak heat [48]. On the other hand, a nose re-entry vehicle has a higher fineness ratio and a sharper point, producing a lift that reduces the peak heat. However, the cumulative heat flux for a nose re-enty is larger. Furthermore, lift allows for a guided descent allowing more flexibility in the re-entry window, as the vehicle has to return to the facility. Even though the cumulative heat is lower for the base re-entry, where and how much heat is applied at time t is important too. The peak load that the base experiences, where the engine is located, must not surpass failure levels. For the above reasons re-entry requires a careful balance between ballistic and lift re-entry [8].
Generally a base re-entry is preferred, as this provides manageable peak heats and peak deceleration, the cumulative heat load is lower, resulting in a less severe TPS. In addition, no 180^o manoeuvre is required in case of VL. In general, the engine of a base re-entry for an SSTO from lower altitudes, is likely to survive the peak heat fluxes [54].
In Chapter 2 it was established that to attain sufficient competitiveness, the SSTO has to reach GTO trajectories, surpassing the lower altitude limits set in [54]. Therefore, the base of the vehicle will require a TPS to protect the base. The presence of the engine means that a passive convectional heat shield cannot be applied. The TPS would either be a deployable heat shield or an active TPS. The former could either be a mechanically moved heat shield or an inflatable heat shield. The latter would be significantly more difficult as the cooling system for the engine operates using the rocket fuel while firing. It remains to be seen whether such a system can be adapted to operate during re-entry.
Both TPS systems are of low TRL as neither has successfully flown, thereby adding another level of complexity to an already very complex vehicle. Therefore, it is more likely that the enterprise will avoid this risk and choose for a nose re-entry, utilising a more conventional TPS design. Note that a nose re-entry does not exclude a base landing, yet this would require a manoeuvre as illustrated in Figure 3.4. In short, if the base can

be made such that the peak heat and peak g-forces remain within acceptable levels, then a base re-entry is preferred due to lower cumulative heat, shorter blackout window (the time during which communication is closed due the plasma surrounding the vehicle), and simply because this method has been developed further.

Considering the likelihood of a lifting trajectory, the vehicle will have a lifting body/devices. Analysis shows that without these lifting devices the GTOW would be 1.5-2.0 million kg to meet the required DeltaV for LEO. This together with the challenges of base re-entry and the advantages of a nose re-entry, the nose re-entry appears to be the logical design choice.
Another advantage of a nose re-entry, comes from the inevitability of the higher fineness ratio. This not only results in better guidance, downrange, landing capabilities, but add superior abort possibilities too [54]. Lastly, given the fact that both the Space Shuttle and Starship use nose re-entry adds more validity to this conclusion.
Note that a nose re-entry does not exclude top or bottom entry. To elaborate, non-symmetric vehicles like scramjet-propelled vehicles will have their bottom part defined by the location of the engine. Due the high heat fluxes upon re-entry, the vehicle might re-enter with a nose-top re-entry, as illustrated in Figure 3.3. This protects the engine and relieving the need for additional complex TPS.

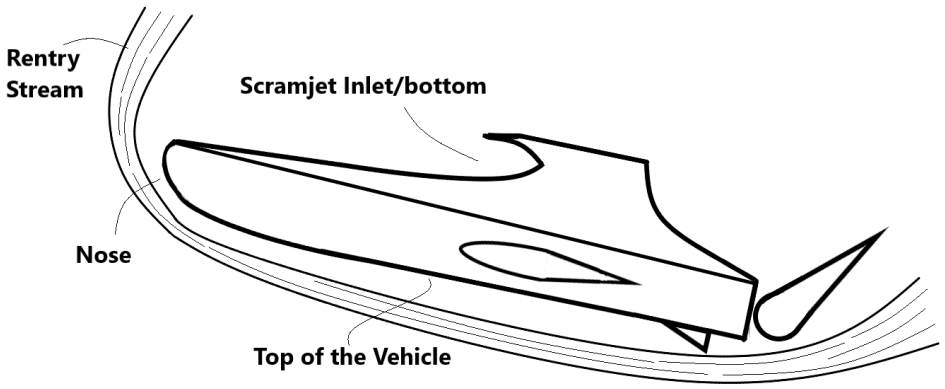

Figure 3.3: Illustrates a scramjet powered SSTO vehicle reenter via its topside.

3.4. Vertical Landing versus Horizontal Landing and its Consequences for Re-entry

The trade-off in Section 3.2 assumes a horizontal landing. However, as advantageous a horizontal landing might appear at first sight, when it comes to ground operations the vehicle will take-off vertically, as was established in Section 3.2. A vertical landing might thus be more advantageous, as the vehicle will not have to be raised. Considering all other ground operations no method possesses any direct advantage over than other, as the operations will largely depend on what the subsystems require in terms of maintenance. Take the TPS of the Space Shuttle, which trumped the time it took to raise the entire vehicle.
Ever since the Space Shuttle has been retired horizontal landing development has stagnated. Unlike vertical landing, which has seen immense development leaps. Currently, all reusable rockets use a suicide burn to land. There are two main reasons why vertical landing is the preferred method. The required lateral strength is already present, whereas often the horizontal strength is lacking and insufficient to hold its own weight. Horizontal landing, would require a structural strengthening, resulting in more structural mass.
In terms of facility, an SSTO vehicle would require a longer landing strip than conventional landing strips, which limits the possible facilities. That is assuming that conventional landing strips would make their facility available. However, such a lease would not come cheap, as the facility would be inoperable for all other aircrafts (because the airspace would have to be closed). Hence, new facilities will most likely have to be constructed.
On the other hand, vertical landings are less fail-safe, as even a partially failed landing will damage the engine (the most expensive component of the system [5]). A partially failed horizontal landing, will damage the

bottom yet the engine could still be salvaged.
Even so, as a vertical landing in the form of a suicide burn is the more developed technique, this is preferred. Such a landing will not require any systems to be refitted (unlike a parachute landing). Furthermore, theoretical equilibrium velocity reached by a nose re-entry vehicle (namely 65 m/s) is sufficiently low to be managed by conventional rockets systems [54]. However, the greater concern is the rotational manoeuvre to be executed by the vehicle, as illustrated in Figure 3.4. Dynamic stability has to be maintained, while the centre of gravity (CG) remains in front of the centre of pressure (CP). The challenge lies in retaining this stability while the vehicle is rotating. The CP must move forward as the angle of attack increases, crossing the CG at some point. The vehicle will thus reach a point of dynamic instability, as such the stability must be artificially maintained. It has been shown that this challenge can be overcome with certain design choices. However, would come at great performance loss during accent [54].

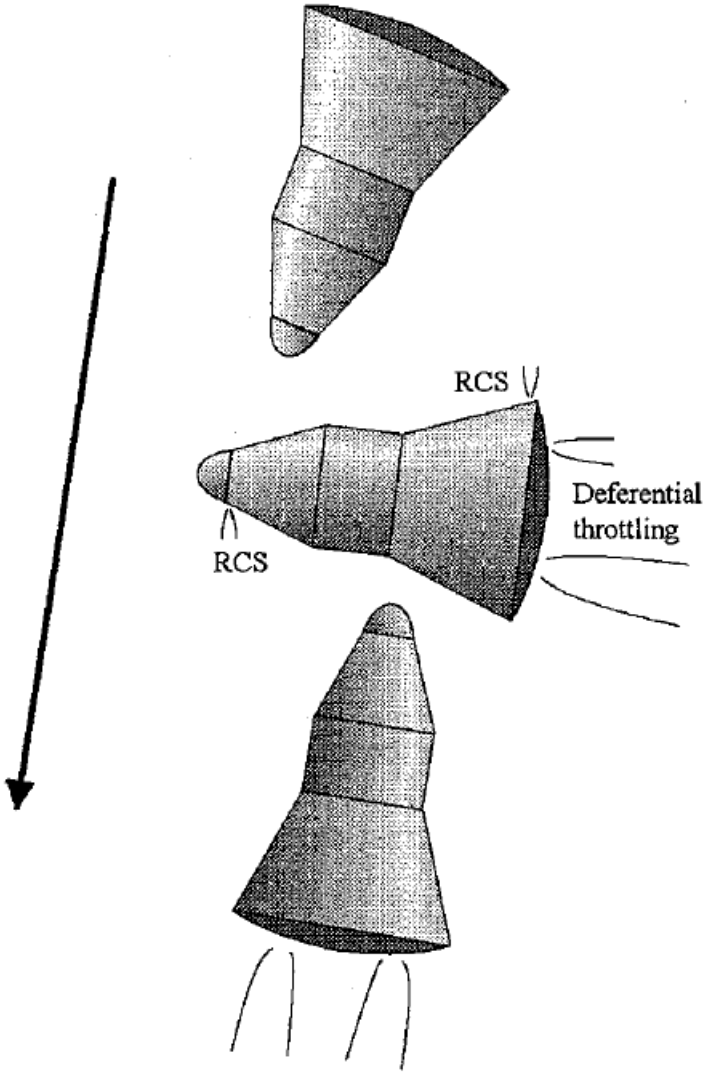

Figure 3.4: Illustrates the rotational manoeuvre required for a nose re-entry and vertical landing, taken from [54].

Yet, the most compelling argument might be due to the economical aspects, as the construction for a new vertically landing site is much cheaper than that of a horizontal landing site. Alternatively, a vertical landed vehicle could use pre-existing rocket facility, which would come at a cheaper lease. Yet, this is limited to the transport reach of the vehicle. Vertical landings are cheaper to develop and can potentially even be outsourced. The Space Shuttle used many different vehicles to predict aerodynamic behaviour and train/develop their crew and guidance systems. SpaceX and Blue Origin, used fewer vehicles and did not have to model

aerodynamic behaviour as the thrust of the engine was of greater influence. This is most probably due the higher similarities with the ascent guidance system.
All in all, the superior design appears to be the vertical suicide burn. However, the section fails to consider the engine. A suicide burn requires an easily reignitable engine, which can produce sufficient thrust in a very short time. As such, these requirements put additional constraint on the design space of an SSTO engine. Given that the engine is the most challenging/expensive system when it comes to R&D, it is better to maintain a larger design space and let the landing procedure be determined by the engine's capabilities.

3.5. SSTO versus TSTO

Whether an SSTO or a TSTO is the better launch vehicle has been the subject of much back-and-forth, ever since the development of the Space Shuttle. For some the comparison is a pre-concluded contest given the current state of launchers, yet the comparison is more complicated than one might think. Whereas it is true that SSTOs of the 1960s would be more than three times heavier than their TSTO counterparts, SSTOs have proven to be more sensitive to weight reducing technological advances [58]. Further supported by the fact that some SSTO concepts in [22] were lower in weight than the TSTO concepts.

Theoretically, an SSTO has the higher propellant mass fraction (PMF), therefore more efficient with its empty mass [58]. In short, a higher PMF means that with an SSTO and TSTO of similar mass and similar technologies, the SSTO will have a lower empty mass. An SSTO requires one engine, no staging mechanisms, one set of tanks, etc., resulting in a larger fraction of the total mass being used as a propellant. The sensitivity comes from the fact that a TSTO sheds part of its empty mass during the ascent. As such, the remaining propellant has to accelerate less empty mass. However, as the ejected empty mass becomes smaller the benefits reduce. There thus exists a point where it is more beneficial to replace the shed empty mass for propellant, as the SSTO experiences the mass reduction over a longer part of the trajectory.

From a more practical point of view, in 1996 the mass of an SSTO was estimated to be 920,000 kg for a payload of 12,700 kg [58], which is still significantly worse than the Falcon-9 with a 22.800 kg payload capability for a 549,054 kg GTOW [58]. Yet, the weight of the SSTO has substantially reduced compared with the 1970s estimates, with a 3,000,000 kg estimations [58]. Furthermore, the estimate 1996 is a lot closer to launchers like Ariana and Soyuz. The additional weight might not be so severe, given the advantages.

The most important advantage and driving design factor is the reusability, as there is strong evidence that current partially reusable TSTO rockets (Falcon-9 & Shepard) are limited to a minimal operation cost of USD 60 million (see Chapter 2). These rockets are considered the current baseline throughout this thesis. As such, only TSTO RLVs and SSTO RLVs are considered. Note that the TSTOs do exclude assist vehicles, launch systems like Pegasus or boosted spaceplanes are thus excluded, and will be discussed in Section 3.6.
To continue, throughout the trade-off it is assumed that both the TSTO and SSTO are on the same technology level. For instance, if the SSTO uses an airbreathing engine, then by default the TSTO operates using the same engine. Such a comparison will lead to the same performance parameters and allows for a fair comparison. This is necessary, as a more efficient engine might be better suited for a TSTO. As similar technologies are used, the development and manufacturing cost should bear great resemblance and should only depend on the size and/or mass of the vehicle.
With these conditions, the same method as presented in [30] can be used. This study assumes, as both vehicles use the same technology, that both vehicles have the same performance ratios. Namely, π_e (final mass/initial mass) and π_f (propellant mass/initial mass). Furthermore, it is assumed that each stage of the TSTO delivers half the specific energy, as is shown in [31] that for a given payload the initial mass is minimally influenced by the energy delivered per stage. These assumptions allow for the relations 3.1 and 3.2.

$$\Gamma_{\text{ssto}} = \frac{m_{\text{i,ssto}}}{m_{\text{p,ssto}}} = \left(\frac{1}{\sqrt{1-\pi_f} - \pi_e} \right)^2 \tag{3.1}$$

$$\Gamma_{\text{tsto}} = \frac{m_{\text{i,tsto}}}{m_{\text{p,tsto}}} = \frac{1}{1-\pi_f-\pi_e} \tag{3.2}$$

Using the relations 3.1 & 3.2, the trade-off parameter Z can be established 3.3. Note that when Z is below 1 an

SSTO has the better performance ratio. Given that the payload mass is equal for both vehicles, this illustrates which vehicle will have a lower GTOW and thus a lower manufacturing and development cost.

$$Z = \frac{m_{i,ssto}/m_{p,ssto}}{m_{i,tsto}/m_{p,tsto}} = \frac{\Gamma_{\text{ssto}}}{\Gamma_{\text{tsto}}} \tag{3.3}$$

Solving 3.3 for multiple fixed values of Z, leads to Figure 3.5. Note that the figure illustrates two curves where Γ_{ssto} and Γ_{tsto} are equal to inf, in this case $\pi_f \geq 1 - \pi_e$. The designs above these curves are forbidden design spaces for an SSTO and TSTO, respectively (due to negative payload).

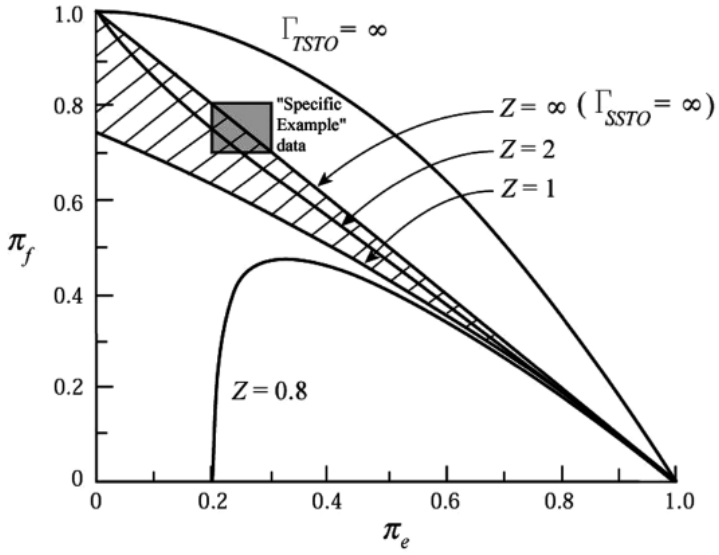

Figure 3.5: Illustrates the relation of π_e & π_f for multiple values of Z, taken from [30].

When studying figure 3.5, one should realise that reducing the π_f, thus reducing the propellant ratio compared to the empty/initial mass, will determine whether an SSTO is the better alternative. Reducing the propellant ratio is largely determined by three factors: 1) The engine performance in terms of the $I_{\text{sp,avg}}$ 2) How much the DeltaV can be reduced due to a lifting trajectory. 3) whether the engines use a fully/partially breathing cycle (compresses air to be injected in the rocket cycle, see section 4.1). Even though, the latter might seem contradict previous assumptions, it is unlikely that a TSTO, as described here, can operate an breathing cycle due to the location of the inlet.
The above criteria show that the engine is of great importance, supported by projects like the X-30, which failed due to a too complex engine design for its time.
Even though, this section does not provide a direct superior concept, it does provide a clear criterion, namely the Z parameter. Note that the preference is under the assumption that only the initial/empty weight is considered. In reality, a Z of near 1, even exceeding 1 might still be in favour of an SSTO, simply due the prolonged ground procedures of a TSTO RLV. In short, a TSTO requires two stages to be inspected and refitted, rather than one. Furthermore, the two stages have to be brought together and reattached (most likely by a non-reusable mechanism).
To conclude, [30] provides an quantitative measure to evaluate whether an SSTO with a certain mass budget is not better converted to an TSTO. This measure is incredibly valuable when sizing an SSTO and evaluating its viability. Furthermore, it is concluded that the viability of an SSTO is dependent on the current level of weight reducing technologies.

3.6. Assisted / Psuedo SSTO's Vehicles

Assisted SSTO vehicles, sometimes referred to as pseudo SSTOs, where largely popularised in the late 1990s. It was thought that the minimal empty mass was mostly optimised, leaving TSTOs as the preferred vehicles, see

Section 3.5. It was deemed that pure SSTOs would only be viable if they were highly reusable and have truly low operating costs per flight, to be even remotely economically competitive. Therefore, a pseudo SSTO was deemed a better competitor to TSTO [58]. Even though clear boundaries between pseudo SSTO and TSTO vehicles are difficult to identify. As a rule of thumb, a pseudo SSTO, is a vehicle that largely draws its DeltaV from one stage and only relies on supporting to stage either provide the payload with the last bit of DeltaV or a supporting vehicle that carries the SSTO in the early stages of its flight, like the Pegasus. Unlike a rocket stage, the supporting vehicle is used to position SSTO for an ideal ascent. Lastly, a booster/assist starting vehicle booster might be used, which is used to accelerate the vehicle to a certain velocity. All three concepts will be discussed in the following paragraphs.

SSTO with an Expandable Upper stage
A more popular design is the spaceplane concept, which rather than to continue to LEO, separates the payload at much lower altitudes. A non-reusable booster craft is used to accelerate the payload to the final orbit. These type of vehicles are suggested to be superior to pure SSTOs by [58], under the assumption that SSTOs have neither achieved sufficient reusability nor sufficiently low operation cost (namely, below USD 62 million [70]). However, this conclusion includes two main issues. When the paper [58] was written it did not consider that TSTOs would become reusable in the next two decades. Therefore, it is highly doubtful that a spaceplane with an expandable upper stage will pose any advances in the operational costs. This is largely due to concerns raised before, like the new facility costs (as most designs are HTHL concepts). Furthermore, the high development costs associated with space planes (the test vehicle for VentureStar costed USD 1.3 billion) with little promise for large operational advantages, eliminate any large economical incentive to develop such vehicle. Many attempts are made to circumvent these issues, designing for smaller payloads (1000-2000 kg). A similar prediction was made in [58]. However, decreasing the payload prolongs the ROI, making the vehicle less economically viable as described in Section 2.6.
Lastly, difficulties could arise when the upper stage separates under hypersonic conditions [48]. The aerodynamics must be carefully studied and understood, to prevent hotspots or undesired shockwaves, raising the R&D costs. To conclude, insufficient evidence exist to assume that such SSTO RLV will naturally develop in this way. However, the advances made by those organisations are more likely to be adapted by organisations that do design a more pure SSTO like vehicle.

SSTO with Supporting Vehicle
In this case, an SSTO vehicle is carried to a certain altitude where it is released at around 25,000 feet (7620 m)[67]. At first sight it can be shown that such vehicles offer a big advantage to pure SSTO vehicles, as initial mass is significantly reduced. [67] illustrates that an SSTO with a payload of ~11.4 tons would weight 445,000-612000 kg compared to 1,320,000 kg, for when a supporting vehicle is utilised (release at 0.85 Mach). Note that the SSTO weight estimate was done prior to the X-33, which would suggest that previous numbers are widely overestimated. Even though a supporting vehicle might appear to be a viable option, further analysis will prove the concept unviable with set requirements. If one assumes that the weight for the SSTO in [67] remains the same for double the payload mass, which is a very lenient assumption given the advances in weight reduction technologies. This would then require an aircraft with a lift capacity of ~600 tonnes. To put this in perspective, this is roughly what an A380 can lift, including fuel. Given such requirements an aircraft would have to be developed with performance similar to the A380 (A380 cannot be refitted as they have not been designed to carry such a large vehicle). The development of the A380 costed USD 15 billion. On top of the USD 15 billion would come the development cost of the spaceplane, which for a scramjet powered craft are estimated to be close to USD 10.7 billion [55]. For this reason this concept is only developed for smaller SSTO launchers, which can utilise pre-existing aircrafts.

SSTO with Take-Off assist
In this instance a vehicle, sledge, or even booster is used to assist the SSTO in the first phase of the launch. Unlike the first stage of a TSTO or a supporting vehicle for that matter, the aim is not to position the vehicle or deliver part of DeltaV. Rather, the assist simply serves to achieve the appropriate starting conditions for the vehicle. Take for instance a scramjet powered vehicle, these engines typically only operate at a Mach numbers $M > 3$. In such instance, a small and cheap solid rocket booster might be used to speed up the vehicle. In this example, analysis might have shown that the use of an expandable solid rocket booster is economically more advantageous than developing a scramjet hybrid engine able to take-off at $M = 0$.

A feasibility study was performed to reach a more reusable design utilising an erkanoplane [74]. An erkanoplane utalises the ground effect to produce the majority of its lift, thus has a higher lifting capability for the same wing area. The SSTO is initially accelerated by the erkanoplane vehicle thus require a smaller wing area to take-off (saving mass). The study even researched the feasibility for the HTHL-SSTO to land on the erkanoplane too, which would result in even more wing reduction (high speed landing). The optimal configuration by [74] (tripropellant engine) had an initial mass of 500,000 kg and could deliver a 7,000 kg payload to LEO. Yet, the entire system would require an erkanoplane of 1.5 million kg. Even though an erkanoplane is able to carry a greater payload, compared with aircrafts of the same size due to ground effect, it would face similar development cost as the supporting concept. Furthermore, there is the additional challenge of replacing the vaporised LOX/LH2 in the SSTO vehicle, as the erkanoplane phase is estimated to last 3 hours.

3.7. General Shape

Even though the shape generally has little effect on the engine it is briefly considered anyway (engines more often drive the shape). A rough description might provide the reader with a greater insight into the workings of an SSTO like vehicle. Most certainly, the vehicle will experience a lower fineness ratio, due the necessity to produce lift upon re-entry and to lower gravity drag. The lift is required to reduce the max peak load, such that the TPS is more achievable (T larger than 3000K require ablative or active cooling [48]). Furthermore, a lower fineness ratio possesses an economical advantage as the vehicle is more weight efficient reduces complexity and idle volumes.
To continue a nose re-entry vehicle with a descent fineness ratio will require a body flap and most likely wings for stabilisation and control [38]. In terms of general shape the vehicle will most likely be more crude in nature, unlike the Space Shuttle. One of the Space Shuttle's major issues involved the 10,000 unique heat tiles, contributing in its failing to be reusable. the design will be more similar to vehicles such as the X-33, FESTIP [42], and SHEFEX [12], utilising a series of simple and similar tiles. This method will result in larger synergy, as tiles can be placed on different spots, and reach higher levels of economy of scale. As a final remark, the simplistic design has the advantage that the shock is less complex, reducing uncertainty in shock behaviour and interaction. As a result the vehicle becomes is easier to model and less prone to errors [8].

3.8. Aerodynamic Characteristics

As was briefly mentioned in Section 3.4 and 3.7, the vehicle will have some form of lift generation to reduce the peak loads. Furthermore, a lifting body/device could reduce the 9400 m/s DeltaV required for LEO. Another complementary advantage to having high L/D is due to ferry operations and cross range capabilities, furthering the competitive edge of the vehicle [8].
To understand how the DeltaV can be reduced, one must realise that DeltaV is not an energy equivalent. Even though DeltaV contains the orbital velocity (Kinetic energy), it includes acceleration to overcome atmospheric drag and gravity drag too. Although the latter has a physical minimum, they are largely determined by the trajectory. As such, a trajectory can be chosen that requires more atmospheric drag DeltaV, yet saves on gravity drag DeltaV. It was computed that by optimising the lifting ascent of the X-33 an additional ~450 kg of payload could be taken [73], which is equivalent to reducing DeltaV. Figure 3.6 illustrates two almost identical rockets, the difference being that the left vehicle has a lifting body whereas the right is a non-lifting (symmetric) body. To elaborate, the drag coefficient is related to the lift coefficient via Equation 3.4. Note that both the AR and e are the the aspect ratio and the efficiency ratio of the lifting body. As C_{D_0} is largely determined by skin friction and the shape of the nose (largely determined by the re-entry requirements) it is assumed that this is the same for both vehicles, the extra drag is purely caused by the lift coefficient C_L.

$$C_D = C_{D_0} + \frac{C_L^2}{\pi ARe} \tag{3.4}$$

With the found relation and Figure 3.6, a relation can be established as to how lift can save DeltaV. For the vertical situation illustrated in Figure 3.6 a lifting body can lower the DeltaV given that condition in Equation 3.5 is kept for most of the ascent.

$$\frac{C_L^2}{\pi ARe}\frac{1}{2}\rho v^2 A_{\text{ref}} < C_L \frac{1}{2}\rho v^2 A_{\text{ref}} - Mg \tag{3.5}$$

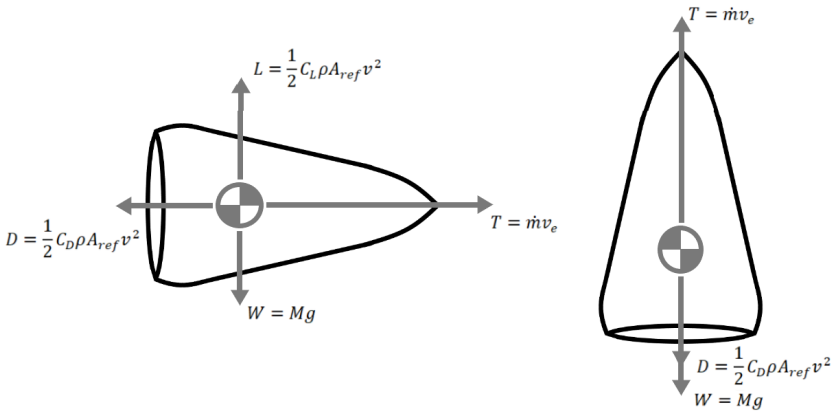

Figure 3.6: Illustrates the forces on both a horizontally (lifting body) and a vertically flying rocket

In short, equation 3.5 states that as long as the net lift is larger than the added atmospheric drag, a lifting body is beneficial. Furthermore, the equation does favour a vertical take-off, because one g will reduce faster (even though, this is a small factor). However, more importantly as the engine will provide more thrust during the vertical launch compared to horizontal, it will not only overcome the gravity faster, it will lose mass faster (as higher throttle, requires higher mass flow). Due the faster reduced mass the term Mg reduces faster, surpassing the requirement 3.5. Note that relation 3.5 can only be satisfied if $C_L > C_L^2/\pi ARe$.
As a final remark, relation 3.5 did exclude the benefits of an airbreathing engine. Such a vehicle would only have to satisfy relation 3.6, as it uses the air as oxidiser. Relation 3.6 is rather straightforward and simply states that if the added drag is larger than the weight, it would be more beneficial to directly thrust against the gravity, rather than staying in the atmosphere and using it as oxidiser.

$$\left(\frac{C_L^2}{\pi ARe} + c_{D_{\text{inlet}}} \right) \frac{1}{2} \rho v^2 A_{\text{ref}} < Mg \tag{3.6}$$

Beware that this is a first level analysis and a more in-depth analysis should be used to arrive at a better estimate on how much DeltaV could be saved. This evaluation can be added to the model proposed in Chapter **??**, to evaluate the gains and viability of an lifting ascent trajectory, which uses a 2D ascent model. The aim would be to reach orbital at +160 km, with the minimal amount of propellant. It is decided not to perform this analysis in this thesis, as this would put too much emphasis on the aerodynamics of an SSTO vehicle. Evidently, if the gain of lifting body were to be included in trade-off analysis s this would require an optimised trajectory simulation.

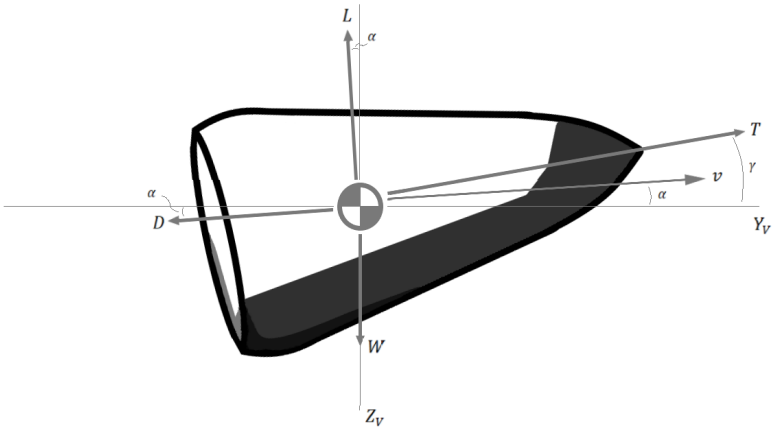

Figure 3.7: Illustrates the forces acting on an ascent vehicle with a lifting body

3.9. SSTO Engine Requirements

In this Chapter key aspects about the fundamental design aspect of an economically driven SSTO have been identified, which are listed below. These aspects are driven by the economical requirements established in Section 2.7. In addition, important vehicle aspects and other relevant findings are listed too.

1. It was established that the engine in the first phase of the launch should have a $T/W_{vehicle} > 1$. This came from the fact that a vertical take-off is the superior design choice, regardless whether a pure rocket engine or airbreathing engine is used.
2. Furthermore, it was established that the engine would not have to withstand the heat load imposed during the re-entry, as this would increase the complexity, therefore the economic risk, beyond acceptable level.
3. Regarding the landing, the preference lies with vertical landing. However it was determined that the landing should be influenced by the engine choice, so as to retain a larger design space[3].
4. In respect to an SSTO vs a TSTO the trade-off, the Z parameter is provided as a trade-off measure. The Z parameter acts as a relevant vehicle sizing compression measure to determine whether the technology is most suitable for an SSTO or a TSTO vehicle. , therefore requires an vehicle mass budget.
5. Through the use of an lifting trajectory, due to the presence of lifting surfaces, a reduction in DeltaV budget can be achieved.

The above aspects and their corresponding influence on the propulsion system form the driving requirement, considered in the literature engine trade of in Chapter 4. The translated requirements can be found in the lis below.
Beware that the listed elements are the result of the assumption that the vehicle is designed in a competitive and private market. If the vehicle were designed as a testbed or demonstrator different conclusions/designs choices could be reached.

1. The engine shall produce sufficient thrust to facilitate a vertical launch ($T/W_{engine} \gg 1$).
2. The engine shall drive the landing procedure (e.g. suicide burn) .
3. The engine shall only has to withstand the heat loads that follow from the thrust production.

The above vehicle requirement are in addition to the economic requirement set in Chapter 2.

[3] At the time of writing SapceX's Starship had not demonstrated the prospect of the flip manoeuvre required during the landing phase.

4

Literature Evaluation of Next Generation Rocket engines for VT SSTO RLVs

Earth is in the unique situation where the gravity well is too small to render SSTO concepts implausible, but it does require the very best technological capabilities. Therefore, an SSTO can only be realised by an extraordinary propulsion system, which has a very high I_{sp}. This is why an economically driven VT SSTO RLV cannot use conventional rocket engines, as current rocket engines lack the required performance.
This raises the question, *What are the next generation rocket engine for an economically driven VT SSTO RLV*?. The next generation engines in the question refers to unconventional engines, which can plausibly be built within one engine development cycle (~ 10 years see Table 6.2).
The engines proposed for VT SSTO RLVs can be divided in two categories: airbreathing engines and pure rocket engines (non-breathing). The distinction differs from study to study, because airbreathing engines have more rocket like features than typical aircraft engines. The distinction made in this thesis is more straightforward: airbreathing engines utilise air intake in some capacity, whereas the pure rocket engines solely use pre-stored oxidiser to complete the combustion cycle.

Airbreathing engines, or breathing engines, have a higher I_{sp} thus (by the rocket Equation 4.1) require less propellant mass to reach the same DeltaV, as illustrated in Figure 4.1. Liquid oxygen makes up over 80% of the propellant mass for hydrogen powered engines and about 70% for hydrocarbon powered engines. Therefore, airbreathing engines could significantly reduce the oxidiser mass. However, technological difficulties, such as the low thrust/weight ratio, limited Mach number, and an ascent trajectory with high dynamic pressure, resulted in many failed concepts.

$$dv = g_0 I_{sp} ln\left(\frac{M_0}{M_f}\right) \tag{4.1}$$

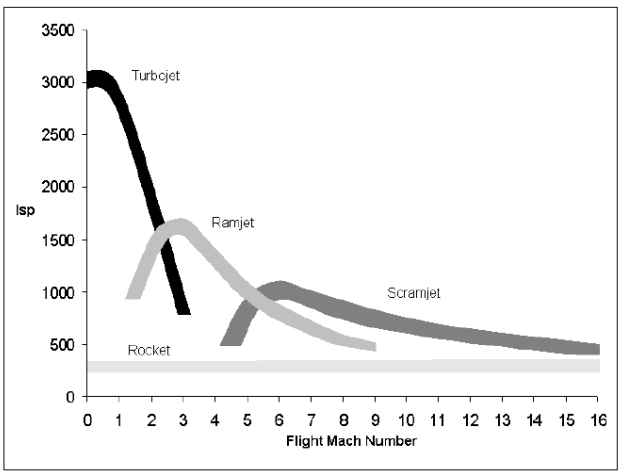

Figure 4.1: Illustrates theoretical I_{sp} per engine over the Mach number, taken from [66].

On the other hand, pure rocket engines are not constrained by the intakes and can reach higher T/W ratios, crucial for a vertical take-off. Nevertheless, pure rocket engines have lacking I_{sp} levels, with the highest record set at 442 s by the SMME [58].
This chapter will discuss most conceived propulsion systems for an VT SSTO RLV. An VT SSTO RLV requires minimum weight and maximum engine performance. Throughout this chapter it will become apparent that some propulsion systems are simply impossible, while other concepts are deemed highly improbable, both are the result of an inconceivable technological leap or because the concept carries too many economic risks.

Lastly, the review largely excludes solid (SRE) and hybrid rocket engines (HRE), their performance was significantly lower such that no serious contenders to liquid rocket engines (LRE) were identified. Furthermore, SREs lack any reignition ability, while such capability is limited to only a few HRE concepts. Lastly, this thesis will eliminate certain concepts, due to political and environmental constraints a government might have with such propulsion systems, such as but not limited to nuclear powered propulsion.

4.1. Breathing engines

The idea of using the atmosphere as an oxidiser, as opposed to pre-stored propellant is nothing new. Conventional rockets use the ejection of the pre-stored propellant to accelerate, whereas breathing engines largely depend on accelerating the atmosphere to generated thrust. Therefore, it comes as no surprise that the I_{sp} is generally far greater than pure rocket engines. The reason the I_{sp} is higher is because $\dot{m}_{\text{propellant}}$ is smaller, as it excludes the oxidiser (the atmosphere is not part of the propellant), see Equation 4.2. The impact on the final mass for utilising a breathing engines is illustrated in Figure 4.2.

However, the thrust remains of concern, as the exhaust velocity of the ejected mass is substantially lower. Simply scaling or adding the breathing engines, would impose more intake drag and initiate the snowball effect. Given the nature of a rocket one wants to minimise the atmospheric and gravity drag, often by leaving the atmosphere as fast as possible. A breathing engine which need the atmosphere must be carefully balanced, such that the increased drag does not trump the saved oxidiser mass.

$$I_{sp} = \frac{T}{g_0 \dot{m}_{\text{propellant}}} \tag{4.2}$$

Each of the following sections will deal with one type of breathing engine, which will be discussed as a general

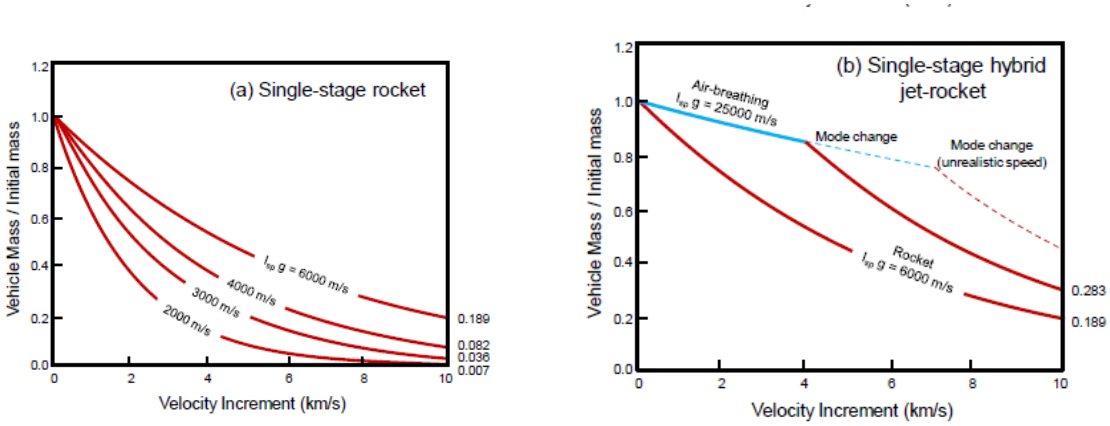

(a) (b)

Figure 4.2: Illustrates the correlation between ISP and the weight fraction over the DeltaV budget for both an pure rocket (a) and breathing rocket (b) configuration, taken from [8].

concept, the advantages, and disadvantages. Yet, more importantly the plausibility of the engine is discussed, from perspectives which include economic feasability, overall performance, current technological challenges, and the TRL.

4.1.1. Scramjets

The scramjet is the hypersonic version of the ramjet and often considered the holy grail of hypersonic flight. The principal of a scramjet is to avoid the dissociation limit of a ramjet [75], as such combustion occurs at supersonic conditions. Scramjets can only operate using a hydrogen combustion cycle, as most hydrocarbons have a to low flame velocity. The only decrease and compression of airstream velocity is done by the intake, therefore the intake is very sensitive to the performance and requires a very precise shape, utilising many oblique shock waves. For this reason scramjets are often inseparable from the launch vehicle, which make them more like flying engines, as illustrated in Figure 3.1. The complex vehicle shape, due the intake,

results in an inefficient volume use.
From a thermodynamic point of view scramjets are very simplistic, using a Brayton cycle [75][56]. Yet, in practice they are incredibly complex from an engineering standpoint, as illustrated by vehicles like the X-43 and X-51. Because the performance is highly sensitive to the intake, therefore little freedom exists in trajectory control. Hence, active CG management is required (possibly by propellant relocation). Furthermore, the high Mach numbers give rise to high pressures, causing substantial heating, deforming the intake. These engineering challenges become even more unmanageable given that none of the current facilities have the capacity to able to imitate the hypersonic flowfield at representative conditions.
All of the above challenges can only be dealt with by using test vehicles, ramping up development costs. Costs estimates range from 10.7 billion USD [55] to 25 billion USD [75]. Even though, lower estimates were produced in 1999, development has stagnated and this thesis does not identify major cost reduction breakthroughs. Given the launch industry's maximum annual value (in 2020) of 10 billion USD (Chapter 2), one has to conclude that a scramjet is economically unviable. Even if successful one would need to perform all launches to even have a reasonable Return-Of-Investment (ROI).
Even though a scramjet will not be developed for an VT SSTO RLV, it might still be developed for hypersonic transport. These scramjets operate at constant velocity, which is easier to develop [75]. This sector might provide the breakthroughs required to make scramjets for SSTOs cheaper to develop.

4.1.2. Turbine Based Combined Cycle (TBCC)

TBCC engines come in many forms. TBCC combine the higher I_{sp} of turbine engines with the higher thrust/weight ratio of pure rocket engines. The engines safe propellant mass, by using compressed air as oxidiser in the initial phases of the launch. The initial designs proposed to operate a turbojet alongside a rocket engine, interchanging heat flows to boost performance, as is illustrated in Figure 4.3. Later designs used adaptable intakes, such that the engine could be manufactured as one entity, increasing complexity to save engines mass.

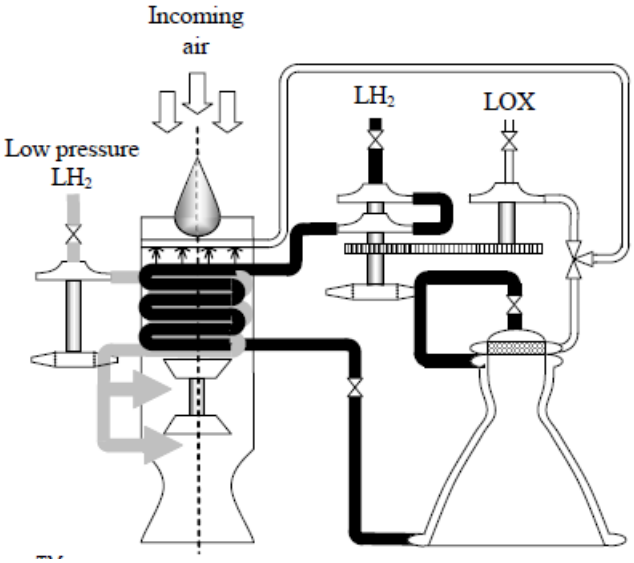

Figure 4.3: Illustrated the KLIN architecture, a TBCC dual engine using a interheat exchanger, taken from [66].

Turbojet Rocket Engine
The turbojet rocket engine uses a ram intake, according to Figure 4.4, sharing many similarities with the Blackbird engine. The ram intake is required to counter the rapid thrust decay above Mach 3. However, the intake flow is limited by the static exit temperature of high pressure compressor (HPC), referred to as the choke limit. A ram bypass is used to redirect the flow around the core at higher Mach numbers surpassing some of the compressors, to allow for an extended breathing period. The turbojet with ram intake and surpass can utilise breathing up to Mach 6-7 [75], after which it will proceed like regular rockets. The turbojet variant, adds significantly more mass and complexity for minimum propellant savings [75], which is why the

engine has seen minimum development over the years.

Turborocket Engine
The turborocket is a variant that deals with the choke limit by deviating further from the turbojet, thus putting greater reliance on the rocket aspect to deliver the thrust. The turborocket still uses the ram intake, yet it only uses a single compressor stage as opposed to the conventional 2 stage, as illustrated in middle engine of Figure 4.4. As the engine only operates one turbine the static exit temperature is far lower and thus the single turbine can operated to higher velocities (longer breathing phase). However, due to the lower air pressure additional LOX has to be added, such that a sufficient level of thrust is maintained. The turborocket is significantly lighter compared to the turbojet, yet comes at the cost of lower I_{sp} at low Mach numbers.

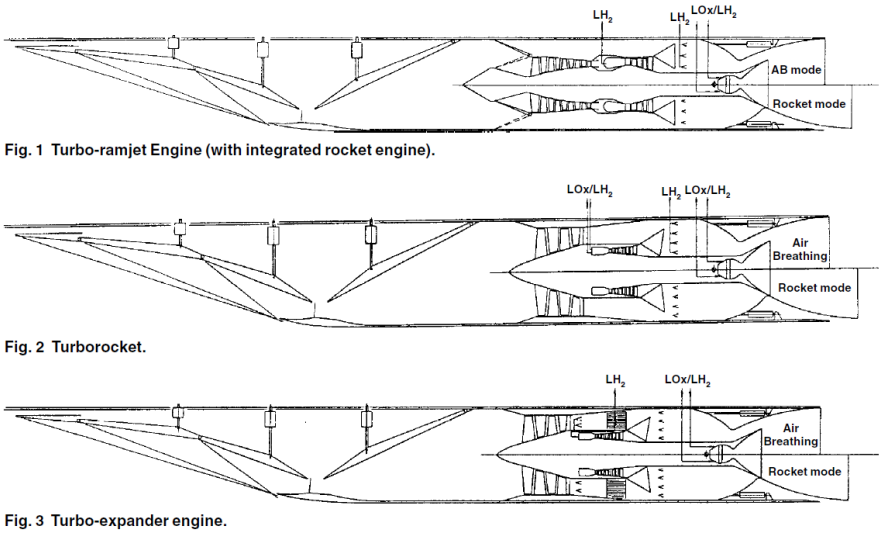

Figure 4.4: Illustrates various TBCC designs each utilising different mechanics, taken from [75].

Turbo-Expander Rocket Engine
Lastly, the turbo-expander engine, which replaces the HPC with a heat exchanger, as illustrated in the bottom engine of Figure 4.4. The heat from the LH2 which is used to cool the engine raises the pressure of the air after the LPC, resulting in higher static temperature, thus eliminating the need for additional LOX. Yet, the pressure loss is concerning, given studies performed during the NEWAC program by MTU aero engines in collaboration with the EU. The IRA engine (from the NEWAC program) is an intercooled bypass turboshaft engine developed to researched the use of heat exchangers in current aero to increase the efficiency. Yet, the study concluded that the heat exchanger caused more drag loss than the benefit provided by heat exchangers. Furthermore, the added mass was concerning, due snowball effect. Even though the LH2 exchanger operates at far higher temperatures, and no exchanger has to be placed in the ejected flow as was the case for IRA (as the cooling is done in the nozzle skin), both concerns render the concept less favourable over other designs proposed in this chapter. Lastly, such an engine would have a less efficient combustion cycle, as the LH2 is less preheated.

4.1.3. Rocket Based Combined Cycle (RBCC)

A reader might find many overlapping concepts between RBCC and TBCC and be of the opinion that some engines should appear in both categories. this thesis makes the distinction whether the state of the air is changed. To elaborate the following designs, partly or completely converts the air vapour into liquid form.

Liquid Air Cycle Engines (LACE)
LACE aims to maintain a high T/W ratio, while boosting the I_{sp} (estimated at ~800 s [75]). The LACE, illustrated in Figure 4.5, uses the cryogenically stored propellant (LH2) to cool the air, liquefying the air via a condenser. The liquefied air is used in combination with pre-stored LOX. The need for additional LOX is

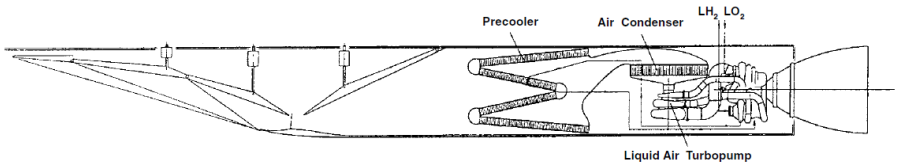

Fig. 4 Liquid Air Cycle Engine (LACE).

Figure 4.5: Engine design of a typical Liquid Air Cycle Engine with a ram intake, taken from [75].

simply due thermodynamics. In short, there is not enough cryogenic hydrogen to supply enough liquid air to reach LEO [75]. Evidently, the LH2 mass flow has to be many times above the stoichiometric levels[1] (namely 12 times), to cool the air sufficiently. Even though combustion above stoichiomtric levels is beneficial to I_{sp}, the ideal O/F ratio is around ~5.5. The higher LACE F/O ratio (namely 0.35) gives an inefficient combustion cycle, alternatively heated LH2 could be re-stored (low TRL). Further complexity arises from mass gained due the condenser, requiring even more performance gain. Air is a multi-species gas, liquefying the required O2 will cause CO2 to freeze causing clogging in the condenser [75].
The liquid oxygen cycle engine (LOCE) aims to circumvent the clogging by adding an O2 separator. However

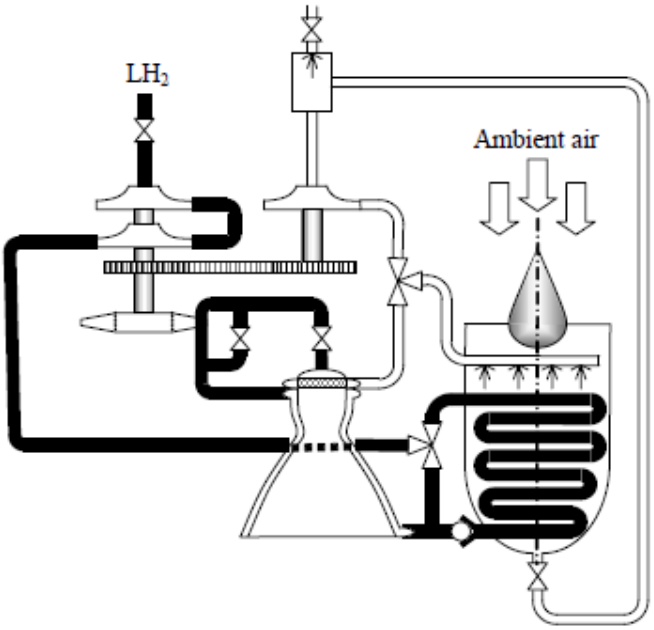

Figure 4.6: Illustrates the engine architecture of an RBCC engine, taken from [66].

this iteration of the LACE engine proved to contain a too large mass penalty [66].

Precooled Hybrid Airbreathing Engine (RB545)
These engines are specifically designed for SSTO vehicles, with desirable characteristics like; 1) acceleration from rest, 2) the breather phase lasts until the vehicle reaches a Mach number no lower than 5, 3) the T/W ratio is higher than LACEs and ramjets, while in the breathing phase. The first proposal was the RB545, borrowing concepts from both LACE and TBCC engines. Unlike, LACE or LOCE the intake conditions come close but do not surpass the vapour boundary, significantly reducing the cooling requirements. More over, the pinch point of CO2 is avoided, eliminating clogging.
The stored LH2 is pumped through the precooler, located after the intake. The airstream is cooled to a fixed temperature, via mass flow rate control. Due the constant inlet conditions, the thrust loss due increasing Mach number is eliminated [75]. The precooled air is compressed via a turbocompressor, which does not

[1] Stoichiometric combustion is when there exactly enough oxidising molecules for the given amount of fuel molecules, resulting in complete combustion without any unused/partially used molecules.

suffer from increasing static exit temperature($T_{0,\text{intake}}$=const.). The final pressure is close to inlet pressures of conventional rocket engines. Approximately 2/3 of the heated hydrogen is expanded to power the turbo-compressor, whereas ~1/3 is used for the preburner. The preburner powers the LH2 turbopumps and adds additional heat to the propellant (advantageous for the combustion).
The RB545 has a higher I_{sp} compared to the LACE, yet has a similar mass. The F/O ratio is reduced to 0.1 operating far closer to the optimum I_{sp}. However, the ratio does erode as the Mach number increases (increased precooling). Unfortunately, no engine architecture of the RB545 could be found. However, it is speculated to bear close resemblance to the SABRE engine, as illustrated in Figure 4.8.
Even though the RB545 offers great advantages, early cancellation of the HOTOL spaceplane caused many aspects, including the RB545, to remain in the concept phase. Sufficiently cooling the airstream, while keeping pressure losses to a minimum, remains the main engineering challenge. Lastly, it is uncertain whether the RB545 can support a VT, as the RB545 was designed for an HTHL vehicle.

SABRE Engine
The SABRE engine is currently developed by Reaction Engines (see Figure 4.7), which bears great resemblance to the RB545. Yet, rather than using the hydrogen as precooler fluid, helium is used (stored for control & guidance or SAS). The helium utilises a Brayton cycle, in which the helium is continually heated, expanded, cooled and eventually compressed, see Figure 4.8. The other aspects of the engine operates similar to the RB545, with the exception of the extra turbocompressor. The helium cycle reduces the F/O ratio to 0.08. The gain does not result from better thermal conductivity (as hydrogen is a better conductor), yet comes from better matched turbine stages and implementation of superior alloys [75]. The SABRE engine utalises a 2 shock intake (1 oblique and 1 normal shockwave). Lastly, the system has a bypass ramjet (labelled 6 in Figure 4.7) which uses the excess air of the main CC.

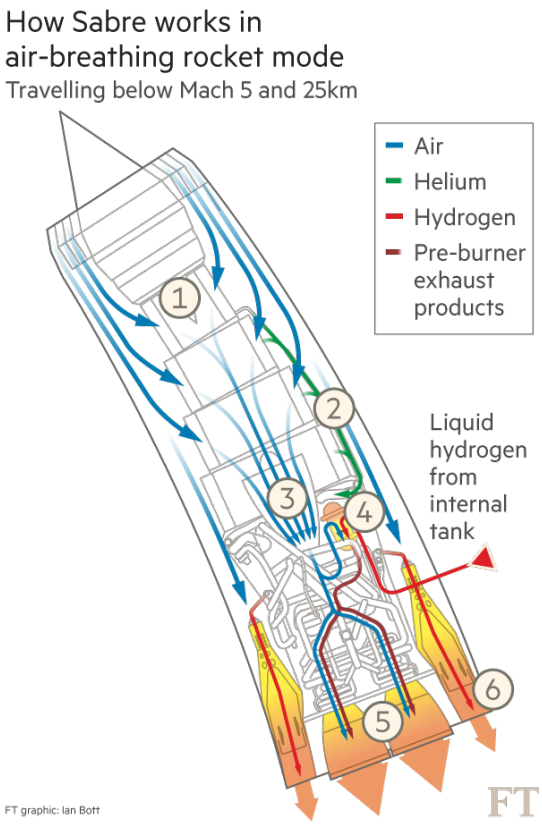

Figure 4.7: Illustrates the SABRE engine and various flows through the engine during the breathing phase, taken from [34]. The number refer to: 1.) the precooler 2.) the bypass 3.) the high pressure compressor 4.) rocket propellant injectors 5.) converging diverging nozzle 6.) bypass afterburners.

Sabre and RB545 offer the unique mix of high I_{sp} (average of ~2000 s), while maintaining T/W ratios well above 6 [75]. The breathing phases lasts up to Mach 5.1-5.5 after which it becomes a regular rocket engine. However, both engines were designed for an HT rather than the superior VL (Section 3.2), raising concerns about the thrust levels. The precooler remains the largest engineering challenge. Reaction Engines aim to use micro tubing, at the size of a hair. The micro tubing keeps the pressure loss low and provides enough surface for heat absorption. The challenge lies in the manufacturing were the welding of the tubing causes clogging, because the tubing melts.
Currently, the precooling technology has been demonstrated in a test facility, yet the test was only limited to the cooling lacking any combustion cycle. The low TRL and complexity of the engine make it such that performance is hard to verify.

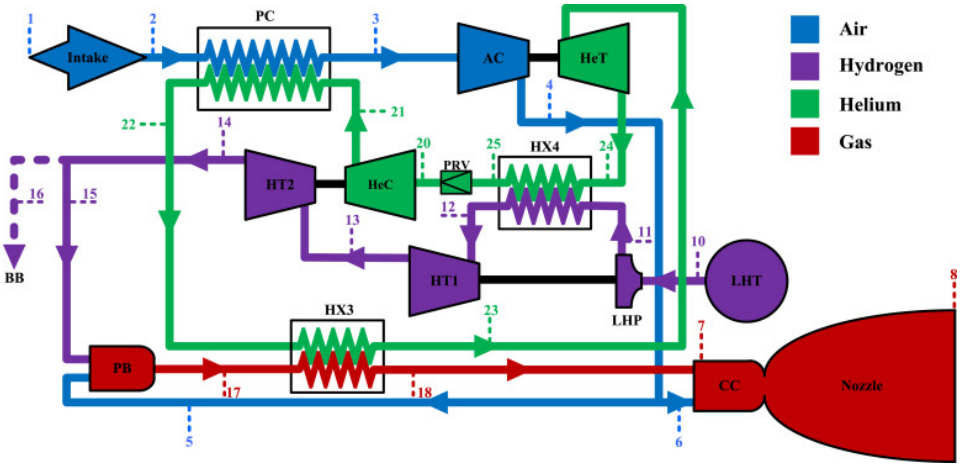

Figure 4.8: Illustrates the engine architecture of the SABRE engine, taken from [34].

4.1.4. Discussion on Airbreathing Engines

At first sight, airbreathing engines offer great advantages compared to the pure rockets, as airbreathing engines reduce the oxidiser mass, offer higher I_{sp}, and have cross range capabilities. With all I_{sp} levels of all discussed engines illustrated in Figure 4.9, the gain in payload mass fraction is significant, as was illustrated in Figure 4.2. Note that some of the levels may be off, as the estimates were made in 2003.

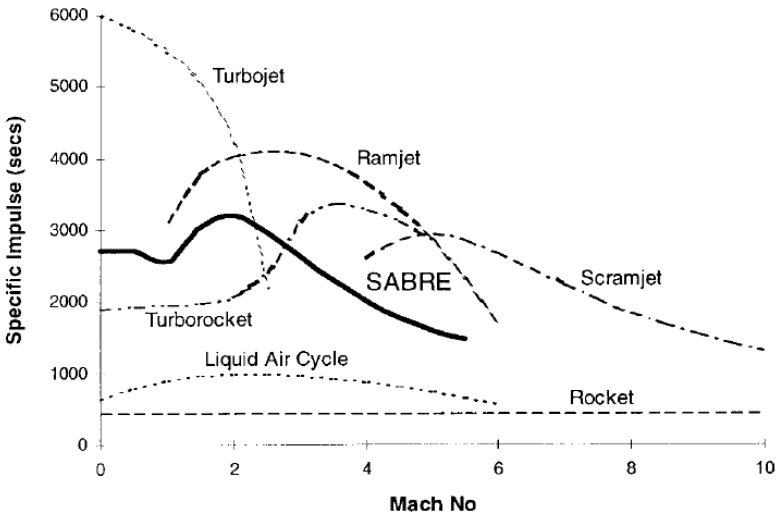

Figure 4.9: Illustrated the I_{sp} for various engines over Mach number, taken from [75].

However, most fail to flourishing due to the mass penalty of the additional (sub)system, with most of the performance gains made in the early launch phase. Furthermore, most lack significant levels of thrust, and therefore accelerate too slowly. The slow acceleration leads to lower velocities resulting in a prolonged atmospheric transition, increasing the atmospheric and gravity drag.
Out of all the airbreathing engines considered only the ramjet, turbojet, and precooled hybrid airbreathing engines have seen continued development. However, only the turbojet and precooled hybrid engines are worth considering further. Even thought the turbojet has seen more development, due to vehicles like the blackbird, the engine has limited thrust loss (due to the increase Mach number) and the choke limit. Therefore, engines like SABRE should be explored first. Furthermore, different aspects of different engines might be combined to reach better alternatives. One such concept would be a precooled hybrid engine, which would pre-mix air with hydrogen to cool the airstream, rather than relying on conductive means.

4.2. Pure Rocket Engines

One might think that rocket engines are by definition not an option for an SSTO, as a more efficient rocket engine can easily be implemented on current TSTOs. However, this assumption only holds true if performance gain is too small as was established in Section 3.5. In other words, if the weight penalty of one efficient propulsion system is relatively small, thus increasing performance enough, than the staging (ejection of empty mass) becomes less beneficial.
Having one propulsion system (multiple engines possible), limits the nozzle optimisation. To elaborate, a nozzle has an optimal expansion ratio (ϵ), the optimum is achieved when the exhaust pressure (p_e) is equal to the ambient pressure (p_a) [85]. While the rocket ascends the nozzle either deviates further from the optimum or is approaching the optimum. Therefore a nozzle must be carefully designed, such that it underexpands in the early phase and overexpands in the latter phase avoiding flow separation. An elaborate explanation can be found in [69] which deals in-depth with expansion compensation.
To summarise, a pure rocket engine for an SSTO must provide a significant gain in performance (I_{sp} level) for a minimum weight gain. Furthermore, the engine must be fully reusable and re-ignitable, eliminating concepts like ablative internal nozzle Layers and solid rocket engines.
Various designs are discussed, ranging from engines like the SMME to Aerospikes. Each will be discussed in a similar order as the breathing engines.

4.2.1. Convectional Rocket Engines

Development on the X-33 showed that current pure rocket technologies are insufficient in their performance [73], as also illustrated in Figure 4.2. Therefore, conventional engines in their current form are unsuited for SSTO. However, advanced engines like the RS-25 or SMME might pose a solution. The SSME has continually been improved ever since its introduction as the Space Shuttle's main engine. The SMME (LOX/LH2) has a vacuum I_{sp} of 442 s [58], yet only achieves a I_{sp} of ~366 s at sea level. The SSME uses two Full Flow Staged combustion cycles, both the LOX pressure pump and the LH2 pressure pump are powered by the preburner turbines. It was found that current SSTO would have a dry mass of 103648 kg for a payload mass of 13700 kg [76].
With the SMME and a conventional DeltaV budget (9400 m/s), the GTOW would be 1257575 kg. The SSTO would thus weigh more than twice the weight of SpaceX's Falcon-9.
Furthermore, the SMME has seen many years of development to reach the high efficiency, attributed to the complex cycles involved. The continued development process makes it very unattractive option from a market perspective, as a similar period would be required to reach the same results. Companies like Blue Origin and SpaceX prefer simpler cycles like the gas generator cycle, upgrading the engines over the years. Such a philosophy is unsuited for an SSTO engine, as it requires a higher initial performance.
Conventional engines using LHC have a I_{sp} 50% lower compared to LH2 engines, for this reason they will not be further discussed.
All in all, even highly efficient conventional engines are unsuited for SSTOs.

4.2.2. Tripropellant Engines

Tripropellant engines are unique due to the use of 3 propellants rather than the conventional 2, not to be confused with spiked propellants (adding radicals). The idea originates from the trade-off between LH2 and LHC.

In general, LH2 has a higher I_{sp} yet requires a large volume, thus causes more atmospheric drag, whereas the LHC has a lower I_{sp}, yet a higher volumetric density, resulting in lower atmospheric drag [76]. Therefore, a careful analysis must be made in which situation one is superior over the other. Tripropellants aim to combine the best of both, such that a perfect balance between minimum atmospheric drag and I_{sp} performance can be engineered.
Tripropellant engines include many different cycles and propellant combinations. From more nuanced variations inclusion of preburners, to more radical changes utilising a dual (co)annular CC configuration. The following paragraphs will discuss all prominent variations. Most of these designs have an LH2/RP-1/LOX combustion cycle.
Currently, one tripropellant engine has been fully constructed, this is the Russian RD-701, which used a single full-flow staged combustion (FFSC) cycle [77]. The preburners in tripropellants are sometimes referred to as initial CCS as the combustion happens closer to stoichiometric ratios than conventional preburner [74]. The preburner are fueled by LH2, therefore utilising both fuels throughout the ascent.

Single Combustion Chamber
Arguably the most conventional design, is the single CC tripropellant engine, see Figure 4.10. Operating a single CC does put limitations on the engine modes. When one propellant flow is reduced/stopped, voids are formed at its injectors, as injectors cannot be multipurpose without serious efficiency losses [85]. Voids in the CC lead to a lower chamber pressure , thus a loss in thrust[28]. More often than not, a single CC tripropellant engine operates under a constant mixture with a higher system integration (F/O tends to be optimum around 6).

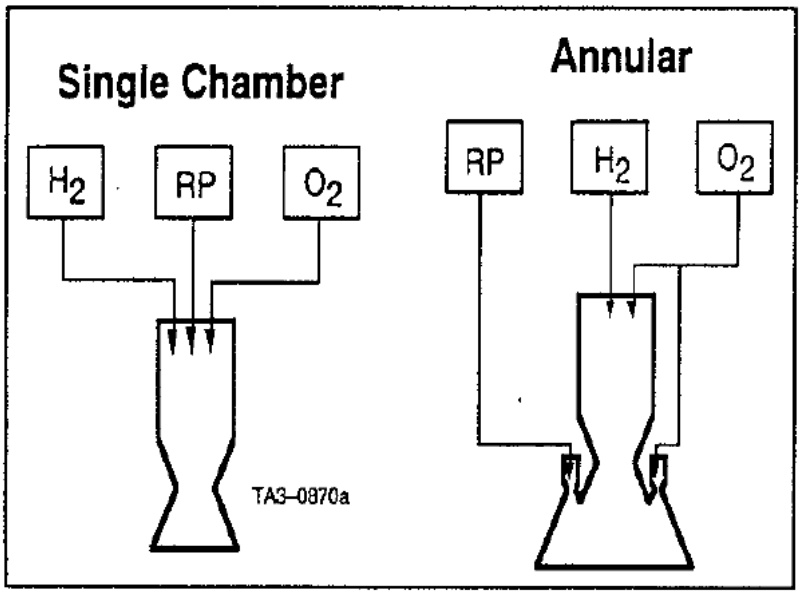

Figure 4.10: Illustrates the tripropellant configurations, namely a single CC on the left and an annular CC on the right, taken form [28].

Dual Annular Combustion Chamber
Opposite to the single combustion chamber, is the dual annular CC shown in Figure 4.10. The main advantage of an annular CC is that both chambers can operate independently from each other and eliminate void creation. Furthermore, both chambers can operate at conventional F/O ratios, so no new optimums have to be researched. This configuration operates using a LH2/RP-1/LOX cycle in the lower atmosphere (reducing atmospheric drag) and a LH2/LOX cycle in the upper atmosphere (maximising the $I_{sp,vac}$).

Dual External Co-annular Combustion Chamber
This configuration divides the combustion over two chambers an internal conventional combustion chamber and a external co-annular combustion chamber, see Figure 4.11. The main advantage of using such a

co-annular design is that the flow outside the combustion pots in the co-annular CC help cool the internal CC. The engine can be operated with the internal CC turned off, the outer flow will then fill the entire nozzle. Note that configurations where the co-annular CC has its own throat like the annular CC, in Figure 4.10, are possible too.

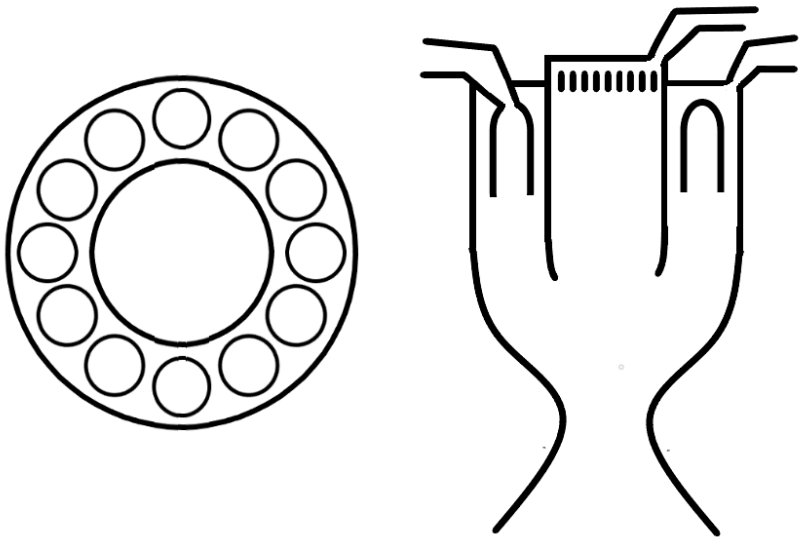

Figure 4.11: Illustrates the tripropellant engine with an interior annular CC and an external co-annular CC.

Power Cycles for Tripropellant

A tripropellant requires a minimum of two power cycles, as the aim is to switch between both fuels. Using hydrogen in the early phase to accelerate, and switches to a LHC (most likely RP-1) for which the size of the stored hydrogen would cause too much atmospheric drag. While the FFSC/FFSC cycle has a small edge over the FFSC/GG cycle [76], due to more efficient fuel use, it does come with more complexity.
Originally, tripropellants were theorised with expander power cycles to minimise the engine mass due the two power cycles. However, [76] indicated that the saved mass did not justify the loss in performance.
Alternatively, one could choose to operate in constant mixture mode. In this scenario only a single power cycle is required. A dual split expander cycle is one of these cycles. In this cycle only one of the propellants (LH2) is used as the coolant, after which the coolant is run through a turbine powering the pressure pumps. It was illustrated that such a design would have an empty mass of 115700 kg, opposed to the 125000 kg for a FFSC/FFSC cycle. Both vehicles were designed for a payload of 13700 kg [28].
A more general power cycle description is provided in Section 5.1.3.

Discussion

Even though tripropellants use 3 propellants their operation is very similar to conventional rocket engines. The operational mixture ratio is more limited for a single CC and co-annular CC, as the cooling system is dependent on minimum mass flow. Therefore, further analysis is required to indicate whether reduction in bulk density versus the loss in I_{sp} is advantageous.
Such comparison is made in Table 4.1. The study considered two bipropellant engines, with a GG and FFSC, and two tripropellant engines, with a single CC and annular CC. For the tripropellant various combinations with FFSC and GG cycles were tried. Mode 1 is a mixture of LH2/RP-1, whereas mode 2 is a pure LH2 combustion. Table 4.1 does not show a superior design in terms of I_{sp}. A fact even more benevolent when the empty mass is considered. Study [28] found that all optimum masses were around 80,000 kg for a payload of ~11,300 kg, with variations well within the uncertainty margins. The study concluded that engine parameters, like the mixture ratio, chamber pressure, etc, are far more influential than bipropellant versus tripropellant.
[76] found an optimum empty mass of 115,700 kg for a 13,700 kg payload, for dual split expander, a LH2/RP-1 ratio of 1/3 LH2 and 2/3 RP-1, with a CC pressure of 10.34 MPa. This is further proof of the engine parameters

	Single Chamber Tripropellant	Bell Annular Tripropellant	Bipropellant Closed Cycles	Bipropellant Gas Generator
Thrust, Sea Level, lbf	421,000	421,000	421,000	421,000
Thrust, Vacuum, lbf	477,630	478,701	484,585	486,706
Specific Impulse, sec				
Mode 2 Vacuum	450.69	461.13	451.43	445.28
Mode 2 Sea Level	339.18	267.33	392.19	385.16
Mode 1 Vacuum	406.26	369.33	451.43	445.28
Mode 1 Sea Level	358.09	324.81	392.19	385.16
Chamber Pressure, psi				
Mode 1	4,000	4,000	4,000	4,000
Mode 2	1,966	4,000	4,000	4,000
Area Ratio				
Mode 1	63.56	59.60/64.54*	69.77	69.84
Mode 2	63.56	226.73	69.77	69.84
Engine Weight, lbm				
FFSCC	4,176	4,201	4,242	—
ORSCC	4,295	—	—	—
FRSCC	4,040	4,187	4,049	—
Hybrid Cycle	4,026	4,227	4,058	—
Gas Generator Cycle	—	—	—	3,629
	FA3-1129			

* $(O_2/H_2)/(O_2/RP)$

Table 4.1: Performance indicators of various tri/bipropellant engines configurations, taken from [28].

being more influential in terms of vehicle performance.
Taking the average I_{sp} of the single CC at sea level mode 1 and at vacuum mode 2, gives 404.39 s. This would result in an initial mass of ~1,383,564 kg, for a standard DeltaV budget (9400 m/s). As the atmospheric & gravity drag is anywhere between 1300-1800 m/s, a lower bound of ~1,219,724 kg can theoretically be reached. The lower bound would put it in the same range as the SMME propelled SSTO.
Given the above arguments it is unclear whether tripropellants are indeed better than highly efficient conventional engines. The only major advantage tripropellants have over highly efficient engines is that they can be constructed with off the shelf technologies [28]. However, the similar performance makes them unlikely contenders.

4.2.3. Advanced Adaptable Nozzles

As was briefly touched upon, the largest loss factor of current rocket engines is due to the nature of static nozzles. Thrust is generated via momentum of exhaust mass and pressure differential, see Equation 4.3. The further a gas is expanded the higher the exhaust velocity (higher momentum), yet the lower the exhaust pressure. As the level of expansion is determined by the nozzle exit area (A_e), the A_e can be optimised for the optimum p_e and U_e (some studies use ϵ). The relation between P_e and exhaust pressure is non-linear, yet it should be clear that the first term ($\dot{m}U_e = \rho_{\text{prop}} A_e U_e^2$) in 4.3 grows faster for an increase in A_e than the second term grows for a decrease in A_e. Thrust is highest for ideal expansion ($p_e = p_a$ [69][85].

$$F = \dot{m}U_e + \left(p_e - p_a\right) A_e \tag{4.3}$$

By the above definition static nozzles can only be optimum for one set altitude, causing efficiency losses of up to 15% [26]. Adaptable rocket nozzle aims to completely or partially reduce this loss, by changing the adapting the exit area, such that p_e is closer to p_a. The following paragraphs will discuss designs that aim to achieve this feat.

Extendable Nozzle Design

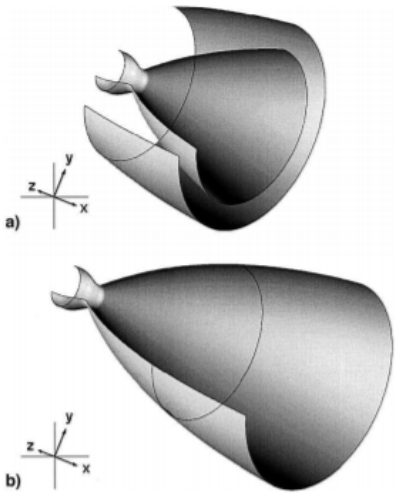

Figure 4.12: Illustrates a 2 stage nozzle a) 2nd stage is not extended b) 2nd stage is extended, taken from [26].

Illustrated in Figure 4.12, is an inherently simple adaptation. The nozzle in essence is divided into two stages: a lower altitude stage and a higher altitude stage. This would allow the same nozzle optimisation as TSTOs, without the need for two sets of engines. the concept would come at some contour losses, as the contour cannot be optimised to the same extend.

The lowering of the lower bell is done by hydraulics, which potentially could be powered by the engine turbines.
The concept has been flight proven (TRL 7), yet it was primarily used to overcome packing issues. However, the development and performance of such a concept can be achieved using current technologies. Yet, the simplicity comes with the fact that the design offers only limited altitude compensation, at best equal to TSTOs. As such the design seems very unlikely to make SSTO like vehicles a reality.

Dynamic Shock Ring

The Dynamic shock ring is a subsystem added to a high altitude nozzle to improve sea level performance. It offers performance gains like the Extendable Nozzle, yet is does not include mechanical components and can operate in multiple stages.

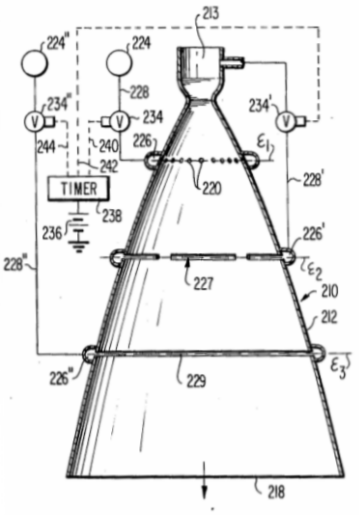

Figure 4.13: Design of multiple dynamic-fluid shock ring nozzle system, taken from [49].

In principle, a secondary flow is introduced in the nozzle via pores in the nozzle walls, inducing separation, see Figure 4.13. The secondary flow acts as an artificial atmosphere, preventing overexpansion. A high altitude nozzle can thus operate at lower altitudes without the undesired effects.
Preferably the pores inject an inert gas, like helium. Yet, such a configuration would result in larger SAS tanks. Alternatively, the fuel could be used, yet this would come at cost of lower propellant efficiency.
The main advantage is the multiple pore canals allowing for a more staged expansion, as is illustrated in Figure 4.13. More staged expansion results in a higher average I_{sp}. Yet, each canal would require a blast valve, which can resist the high heat, to prevent entry of the primary flow. Furthermore, when a canal is operational it acts as a bleeding cooling system. However, the moment a canal is turned off, cooling the canal becomes a challenges. Even if the secondary flow is used as a bleeding cooling system, the closed off pores are still exposed without little room for proper cooling channels. Lastly, The dynamic shock ring has never prototyped, giving it a TRL of 4-5.
To conclude, the dynamic shock ring does give a boost to I_{sp} performance, yet comes at a cost of additional coolant (inert gas or fuel), therefore further analysis is required to determine whether a performance gain exists.

Breathing Nozzle

The breathing nozzle gets its name from its opening flaps that appear to resemble gills of a fish, see Figure 4.14. Much like a fish the engine uses these 'gills' to allow air to enter the engine. The air entering the nozzle with the interior lacking a smooth transition surface, causes the exhaust gases to separate. The breathing nozzle is the mechanical version of the dynamic shock ring, as it operates in multiple stages too. As the rocket assents the exhaust gases are allowed to further expand down the nozzle, enlarging the exit area A_e.

The challenges for this system reside in the mechanical system, exhaust flow management, and cooling system. For the mechanical system, weight becomes a serious concern. The number of mechanical components and actuators would be many more than the conventional space standard, as each stage must be powered separately. Furthermore, each stage does not consist of a single flap due to the circular shape of the nozzle. Even though such systems exist and are not in the realm of fantasy, the overall weight could outdo the gained performance.

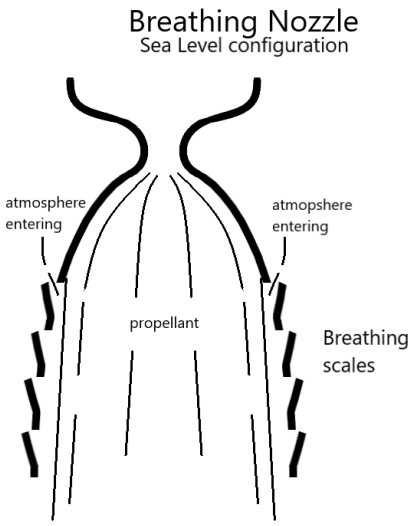

Figure 4.14: Illustrates the concept of the airbreathing nozzle at sea level configurations, taken from [69].

A smaller concern is that the system must be configured correctly. As the rocket ascends, the exhaust flow in the interior in Figure 4.14 becomes wider. If the flaps close too late and the flow becomes too wide or the shockwaves expand too far outward, they will hit the interior of the nozzle, causing hotspots and unwanted vibrations, causing wear and potential failure.

The most challenging element of this nozzle is the cooling system, due to the many moving flaps. Each closed flap must be cooled, and connecting them all would require many flexible pipes or many 180° turns. Even a dump cooling rather than a regenerative cooling system would face many of the same problems. Alternatively, insulating or ablative cooling could be an option. However, the former would make the design not meet the requirements of sufficient low TRL. The latter would be a good solution if the renewal of the ablative layer were effortless enough.

The breathing nozzle eliminates the need for additional gases to induce separation. However, it increases the initial mass. Lastly, the TRL of the breathing nozzle is significantly lower, namely 2-3. All in all, the breathing nozzle just like the dynamic shock ring could possible provide the additionally required performance, yet it is unsuited on its own.

Adaptable Afterburner Nozzle

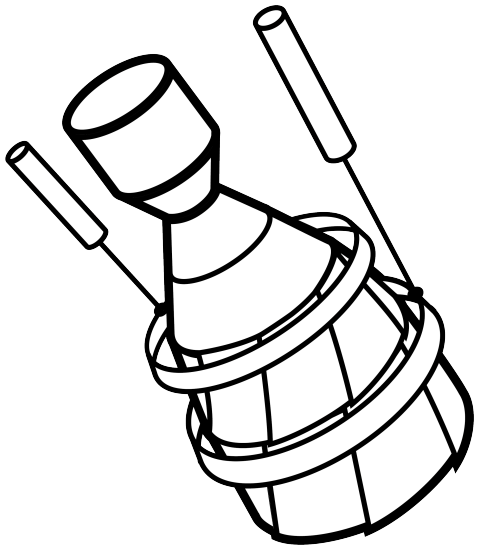

Figure 4.15: An Adaptable Afterburner Nozzle, only showing 1 piston per stage instead of the required 3, taken from [69].

The adaptable afterburner nozzle, was originally proposed in [69], and aims to reduce the altitude losses for the first stage engines of a TSTO. The adaptable afterburner nozzle utilises hydraulic pistons to change the exit area and contour of the nozzle, throughout descent. The hydraulic pistons are connected to a circular beam, which in turn is connected to the flaps via a rails 4.15. The flaps are segments of the entire nozzle, as illustrated in Figure 4.15. The concept bears great similarities with afterburners used on jet engines, from which the name originates. For a more in-depth analysis the reader is encouraged to read [69].

The adaptable afterburner nozzle has never been flown as it is a relative new concept, yet it is achievable using of the shelf components. Therefore, the design is achievable within a reasonable time frame. However, the performance gain by an adaptable afterburner nozzle is limited by the initial exit area. The final exit area can only be four times larger than the initial exit area [69], due to the packing of the unextended flaps. If every flap could store a flap size equal to its length then the circumference can increase by a factor of 2 (radius by 2, thus area by 4). The adaptable afterburner nozzle can only do some altitude compensation, resulting in a gain of ~10% [69].
As such, the adaptable afterburner nozzle might be a good concept for the first stage of a TSTO, as it is less complex than the breathing nozzle nor does it require additional propellant (or inert gases). Yet, for an SSTO the gain is too insignificant.

4.2.4. Aerospike

Aerospikes aim to overcome the static nozzle losses too. In essence an aerospike is a bell shape nozzle turned inside out, see Figure 4.16. The exhaust flow is ejected at the exterior of the nozzle as opposed to the interior. The oddly shaped nozzle offers three key benefits compared to bell shape nozzles [63]. Firstly, spike shaped nozzles offer altitude compensation by exploiting plume physics, improving lower altitude performance. Secondly, they produce lower base area drag, as the cross-section reduces less abruptly. Thirdly, aerospikes have a better base utilisation, as such a larger area ratios (ϵ) can be achieved (better vacuum performance). Additionally, thrust is transmitted over a larger area (reducing structural mass). Note that aerospikes come in two varieties, namely the circular aerospike and the linear aerospike.

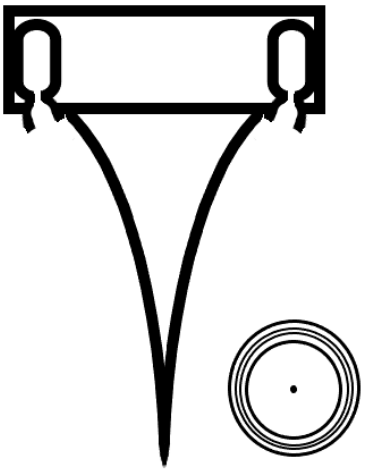

Figure 4.16: Illustration of cut-through of a circular Aerospike design

Aerospikes generate thrust similarly to conventional nozzles, by producing a net thrust on the nozzle and CC walls (p_w>p_a). Yet, aerospikes artificially increase the area ratio throughout the ascent, remaining at ideal or close to ideal expansion [63]. With the outer plume not being enclosed by a nozzle wall, it adjusts to the ambient pressure, as illustrated in Figure 4.17. The p_a acts as an outer nozzle and expends the flow to the ideal p_e. At lower pressures, see a in Figure 4.17, the plume does not expand much and the ϵ is relatively small. For higher altitudes the opposite is true. The expansion shocks in the plume impinges on the aerospike surface generating local high static pressure through recompression. The reflected expansion waves form the outer free jet boundary, creating compression waves forming the envelope shock. The interactions of the shock waves are the physics behind the altitude compensation characteristic, further illustrated in Figure 4.17.

When the ambient pressure decreases (due to ascent), the recompression travels down the aerospike surface, due to the envelope shock moving outwards, the compensation stops the moment the recompression reaches the nozzle base (after which it behaves like an overexpanded bell nozzle). Note that true spike nozzles are very uncommon among launch concepts, as the point would fail due to heat exposure. Fortunately, the first quarter of the spike produces the majority of thrust. in general the later three quarters (which add significant weight) can often be removed for net performance gains [63].

At the base of a plug aerospike, due to recirculation, a base pressure p_b is formed (subsonic region). p_b increases while exposed to the decreasing ambient pressure. However, the moment the envelope surround the entire subsonic region, including the inner shear layer, the base becomes insensitive to the ambient pressure and p_b remains constant thereafter [63], illustrated at c in Figure 4.17. At a in Figure 4.17 the compression

shocks hit the contour drastically increasing the profile pressure and p_b. However, most aerospikes will be designed such that the compression waves do not hit the contour, preventing hotspots. Furthermore, base bleeding can further increase p_b, leading to a thrust increase[63][85].

Yet, the same physics responsible for altitude compensation, causes the nozzle to be sensitive to local freestream. While in the transonic stream the freestream expands around the base of the vehicle, lowering local pressures. The plume of the aerospike overexpands, moving the outer jet free boundary outward, resulting in a wider envelope shock. How a slipstream influences an aerospikes performance is a complex study on its own. Luckily enough, the effects are only significant in the transonic flight regime. The slipstream effect could partially be mitigated using a circular cowl geometry [63].
Furthermore, for larger nozzle pressure ratios (NPR) the slipstream effects are less severe [63]. The NPR is larger when an aerospike engine passes through the transonic regime and beyond, limiting the freestream effects(overall performance loss is 4% [63]). This is partially the reason why the VentureStar took off vertically to reach the transonic stage faster and reduce the ambient pressure faster (increases NPR).

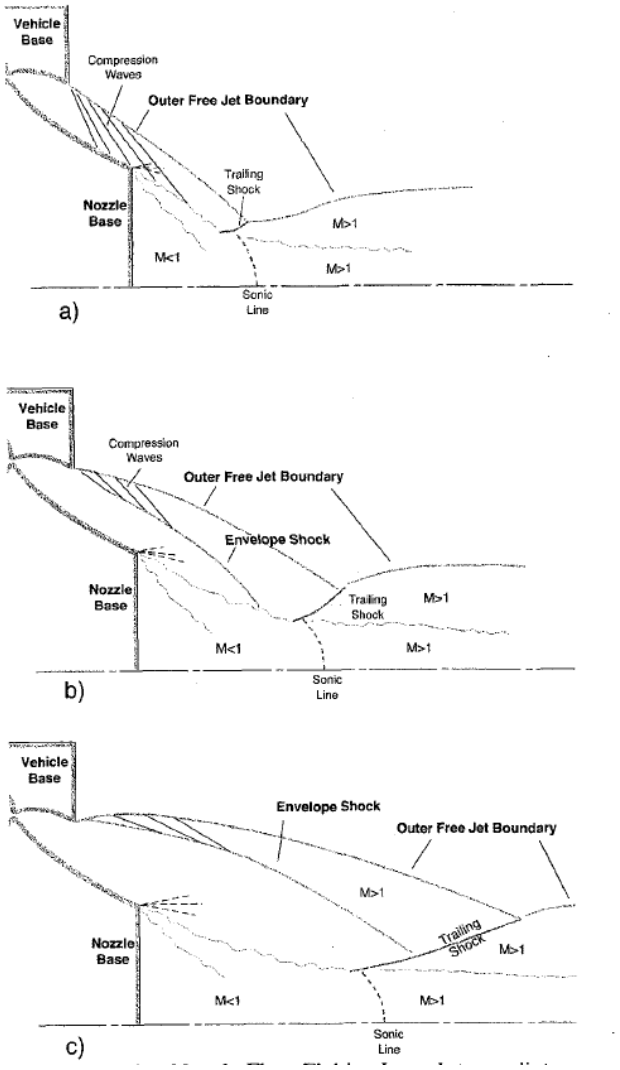

Figure 4.17: Illustrates the flow physics of a plug aerospike, taken from [63].

To continue, aerospikes have several challenging aspects [41], most notably heat management. An intensive cooling system is required, as the nozzle is completely enveloped in the exhaust gas. Alternatively, the nozzle wall can be made thicker at the cost of a weight penalty. Note that a more intense cooling system could result in a higher combustion efficiency, given that the cooling systems preheats the fuel. The fuel will enter the chamber with a higher temperature, requiring less energy for combustion, resulting in more complete combustion. In essence, the system uses more of its otherwise wasted heat, lowering reaction threshold. On another note, an aerospike uses a doughnut shape CC, a multiple smaller CCs, or a linear CC, introducing more complexity to the combustion process. However, the use of multiple combustion chambers allows vector thrusting, synergizing the propulsion system with the control system, potentially eliminating gimbal devices. Lastly, the contour of the aerospike remains unchanged, which will lead to some efficiency losses. Yet, it will most likely be developed for the highest ϵ possible, as this is more advantageous for the I_{sp} near vacuum.

All in all, aerospikes offer a unique performance increase compared to other pure rocket designs, as illustrated in Figure 4.18. The average I_{sp} lies between 400-420 s. Even though many challenges have been brought up, the fact that linear aerospikes have been developed by companies like Lockheed Martin and ARCA space, illustrating the short term achievability (TRL 6-7). The aerospike concept is worth considering further.
As a last remark the base bleeding could possibly be turned into a small propulsion system, which was done for some bell rocket nozzles using bleeding as cooling mechanism [85].

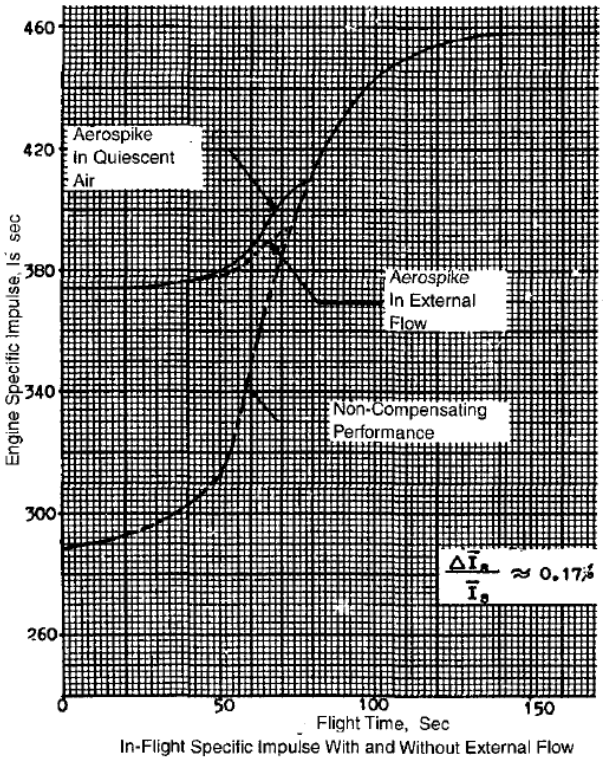

Figure 4.18: Illustrated the I_{sp} values under certain conditions over the flight [63]

4.2.5. Thermal Nuclear Rocket Engines (TNRE)

Unlike what the title might suggest nuclear engines neither use nuclear explosion (like the Orion) nor fusion. On the contrary, these engines are flying nuclear power plants. They superheat the coolant (the propellant) and eject the coolant. This process is reverted too, as an open cooling cycle. In short, hydrogen is pumped through the core, containing enriched uranium or plutonium. The core would be a slow neutron reactor. The moment LH2 enters the core, neutrons are slowed, causing more collisions, resulting in heating. Due to this characteristic, the core can be controlled by two means, namely via the mass flow control of LH2 and the control rods (absorbing neutron). The core heats the propellant to 3000 K - 5000 K, depending on the material properties of the engine. The superheated hydrogen is ejected through a nozzle.
Even though the concept might seem science fiction, NASA has actually considered and built a nuclear powered engine to be used in the second stage of the Apollo mission. The advantage of using a nuclear powered hydrogen rocket, is that the I_{sp} is at the highest levels achievable by pure rocket engines. I_{sp} depends on two factors: the exhaust velocity and the molar mass of ejected gas. I_{sp} increases for a higher exhaust velocity and a lower molar mass [85]. The temperatures referred to above can be achieve the same ejection speed as conventional rockets. However, as H2 is ejected rather than H20/H2 the molar mass is far lower. Therefore, the I_{sp} can easily reach level twice as high as conventional rockets, namely 850-1000 s.
However, the implementation of Thermal Nuclear Rocket Engine in an VT SSTO RLV, is very unlikely. A private company would have to go through a great deal of heavily restricted legislation, and deal with the possible risk of nuclear waste leakage. Not to mention the possible backlash from society. Even though technically possible, economically and socially it is highly unlikely that a private organisation will develop an TNRE.

4.2.6. Pulse Detonation Engine (PDE)

Pulse engines were among the first jet propulsion created, yet they have remained relatively unknown. Just like scramjets/ramjets, mechanically pulse engines are inherently simplistic. However, contrary to scramjets the pulse jet depends on shock compression, rather than ram compression. A pulse engine is simply a shaft (a small CC can be placed in front of the shaft), which allows fuel and oxidiser to enter. Once the propellant has entered the beginning of the shaft, the ejectors/valves are closed, followed by the ignition of the propellant. The CC/shaft is designed such that the propellant detonates, similar to scramjets. Unlike scramjet/ramjets the PDEs can generate thrust while at rest.
Due to the nature of a detonation, the propellant cannot leave the shaft before it has completely combusted. Therefore, the process happens at constant volume rather than constant pressure, as illustrated in Figure 4.19. As constant volume combustion is more efficient, more chemical energy is transformed into usefull heat. Theoretically, all chemical energy is transferred into internal energy. The gas is expanded via a nozzle at the end of the shaft, which causes an under pressure at the front of the shaft. Oxidiser and fuel are rushed into the underpressured front, which is ignited again. This process has been seen to reach 80 hz to 150 hz [14], depending whether breathing or stored oxidiser is used, respectively.
The difficulty of pulse engines lies in maintaining the ignition cycle, which requires good understanding

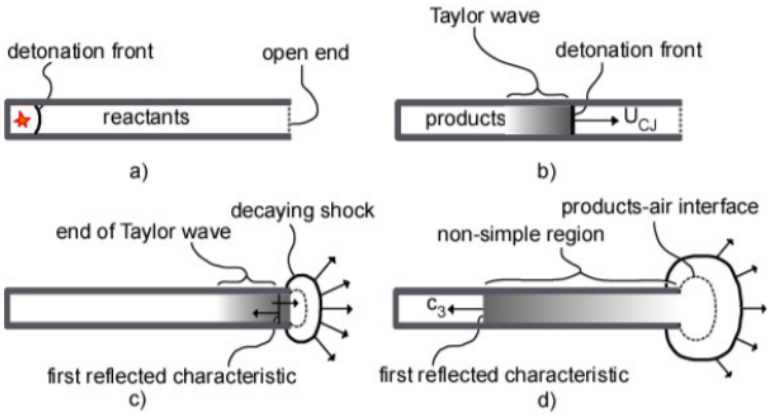

Figure 4.19: Illustrated the combustion cycle of a PDE, taken from [81].

of the fluid and shock dynamics involved. Continued combustion while keeping vibrations and heat at a minimum is key [43] (more heat is produced compared to conventional rocket engines). Originally pulse engines were breathing devices, which used one-way valves to allow air to enter the shaft/CC. However, these could only reach a maximum Mach number of 5. Furthermore, these engines required the hot gases to ignite the injected propellant, as they would also be pulled back into the underpressured front.
To reach higher Mach numbers the Pulse detonation Engine was proposed, which used an ignition system to stimulate or initiate the detonation. When air is used as oxidiser the I_{sp} could be anywhere between 2000 s and 8000 s, depending on the mixture ratio, as is illustrated in Figure 4.20. However, when LOX is used the I_{spf} drops to 1000 s up to 3000 s [81]. Yet, these levels are significantly higher than any other rocket engines considered so far. Furthermore, the Russian Advanced Research Foundation tested a pulse detonation rocket engine, giving the design a relative high TRL (6-7).
Due to the higher heat, a more demanding cooling system is required. Suggestions have been made to build the tank around the shaft, such that the stored propellant cools the shaft, where the absorbed heat keeps the tanks pressurised. Yet, such configuration must be carefully studied to prevent overstressing the tanks. Nor must the extra structural mass surpass the mass of an active cooling system. Alternatively, bleeding in the shaft could be used, as this could potentially increase the I_{sp} [81]. In such instance the combustion would be closer to the stoichiometric value, yet additional LH2 is added in the shaft via bleeding, lowering the specific mass [85].

All in all, the PDE has immense advantages over other engine concepts discussed in this chapter. The high I_{sp} performance together with the relative high TRL, makes this concept worth considering. Furthermore, the possibility exists to partially use air in the initial stages of the ascent, saving oxidiser mass.

Lastly, an even more potent but also complex PDE configuration exist, which is the rotating detonation en-

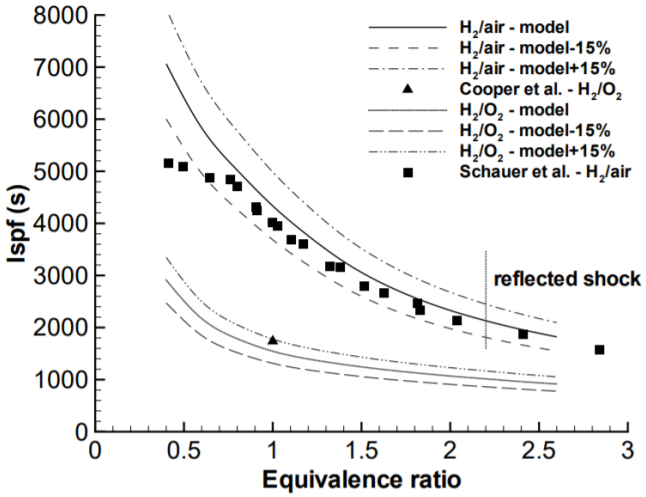

Figure 4.20: /illustrates the I_{sp} value of an LH2 powered PDE over various equivalence ratios (both modelled and test data), taken from [81].

gine [68], one was even proposed with an aerospike nozzle [39]. It is even speculated that the failure of the F-1 was caused by a very powerful rotating detonation occurring in the CC. Although, these engines illustrate great potential, they are still in there infancy (TRL 2-4). Adding the fact, that non-altered PDEs already offer significant performance gain, little economical incentive exists to add additional risk/complexity for potentially unnecessary performance gain. For the same reason and a weaker performance detonation turbojets are excluded [81].

4.2.7. Discussion on Pure Rocket Engines

Even though pure rocket engines have a significantly lower I_{sp} than airbreathing engines, they are considerably easier to achieve. Yet, the main concern is that most pure rockets are easily implemented on TSTOs, which would simultaneously raise the baseline for SSTO. Therefore, careful considerations must be made throughout the design process, as a proposal of a pure rocket engine could be more suitable for a TSTO RLV.
No conventional engine was identified in this thesis or during the research process of this thesis, that would suit an SSTO. Conventional engines are unsuited due to their low performance. They are better suited for the current TSTO launch vehicles.
On the other hand, concepts like the aerospike and pulse detonation engines offer promising concepts. The aerospike engine offers passive altitude compensation and superior vacuum performance (due to better base utilisation). Furthermore, the aerospike has seen significant development within the X-33 program, making it economically more appealing, which had an estimated average I_{sp} of ~420 s and the possibly reduced GTOW due to a lifting body, making a pure rocket powered SSTO a possibility.
Pulse detonation engines (PDE) have seen moderate development and are arguably on the same TRL as aerospikes engines. Yet, still many aspects of the implementation remains undecided. However, the increased I_{sp} performance (~1000 s) is one of the highest considered throughout this chapter. Furthermore, the possibility of partially functioning as a conventional pulse engine during ascent, could reduce oxidiser mass.
Even though tripropellants or advanced nozzle designs are insufficient on their own, they are easily implemented in the considered engines. Tripropellants with an LH2/RP-1/LOX mixture offered no advantage, yet a more potent mixture might yield better results. Furthermore, the aerodynamic drag reduction, by using (partially higher density fuels, might provide additional performance gain to considered engines.
When it comes to concepts like the dynamic shock ring, it is easily implemented on any engine with a conventional nozzles.
Continuing in this thesis, only the aeropsike engine and PDEs are considered pure rocket engines suitable for VT SSTO RLVs. As was mentioned before some of the previously discussed designs could be merged with the aeropsike or PDE, if it is believed the additional performance is needed.

4.2.8. Conclusion

To conclude, three engine designs are identified to be suited for an economically driven VT SSTO RLV. Out of these concepts one identifies as an airbreathing engine, whereas the remaining two are pure rocket engines. The selected engines are listed below.
The literature only provides a limited insight into the performance of the selected engines in the VT SSTO RLV setting, as discussed in Chapter 3. Fortunately, Chapter 6 provides a model to evaluate and compare the performance of the selected engines.

1. Aerospike engine
2. Pulse detonation engine
3. Precooled Hybrid airbreathing engine

Even though the literature and latter performance trade-off will refrain from utilising more complex engine configurations, due to economical incentives, future trade-offs or engine design do not have to be limited by these purer engine configuration. For these studies it is recommended to re-evaluate the current technological capabilities. At that time it might be possible to merge any of the selected or mentioned concepts in this chapter, which could provide additional performance or lead to future generations of engines.

5

Propellant Pallet for the Selected Engines

Throughout the groundwork for this research, the influence of the combustion chamber pressure (P_{cc}) was identified as a major performance factor. Evidently, comparing the large performances differences between the baselines of [17], [61], and [28] to name a few, were due to varying P_{cc}. The performance in some instances even surpassed the performance gains of the proposed concepts and propellant pallets in this research. The performance here refers to some sort of thrust derivative.
The exact relation between the thrust and combustion chamber pressure (p_{cc}) is not straightforward and to some extent unknown. However, a basic understanding explains that a substance with a higher pressure is more energetic, resulting in a more energetic engine and thus a more powerful engine. Consequently, increasing the energy level of a given engine is in some sense equally relevant as determining the overall concept. This depends on two aspects, namely the potency of the substance, also known as the propellant, injected into the CC, and the physical limitation on the amount of set substance that can be injected.
In the early days of rocketry [20] such reasoning was the driving force behind propellant innovations, which primarily focused on the former aspect. Extensive research has been done to increase the potency of LHC, due to the preferable operational characteristics, which also concluded that these engines should operate at higher chamber pressures (~155 Bar) [61].
Even today, propellant pallets are an intricate part of rocket engine innovation, demonstrated by the Raptor 1 (SpaceX) and BE-4 (Blue Origin) engines utilising the unconventional LCH4 and LNG fuels. Therefore, this section sets out to answer, *What are viable propellant pallets for the selected next generation rocket engines?*.
To determine what are viable propellants, requires an understanding of what makes an high performance propellant. This is elaborated throughout the explanation of the rocket engines power cycles. The power cycle includes the second aspect, namely the injector pressure limit. The chapter continues with the discussion on the propellant requirements including the those driven by economic forces, which are equivalent to the performance requirements. The chapter then proceeds with the consequential evaluation of the possible fuels and oxidisers. The chapter concludes with the overview of viable propellants for each engine.

5.1. Rocket Engine Power Cycle

5.1.1. Thrust in relation with the Combustion Chamber

The relation between the performance, namely the thrust, and the combustion chamber is not straightforward, especially when considering unconventional engines. However, two analysis methods exist for conventional engines. Each relies on different assumptions, thereby providing an upper and lower bound. The first method, the frozen equilibrium method, is the more commonly used and yields Equation 5.1, taken from [85]. For ideal expansion ($p_e = p_a$) Equation 5.1 offers a direct relation between thrust ($T = \dot{m}U_e$) and specific impulse ($I_{sp} = U_e / g_0$). The frozen equilibrium approach offers a conservative (lower) estimate for the exhaust velocity (U_e), its derivation is discussed in Section 7.2.2.

$$U_e = \left(2 \frac{R\gamma}{\gamma - 1} \frac{T_{cc}}{M} \left(1 - \frac{p_e}{p_{cc}}^{\frac{\gamma-1}{\gamma}} \right) \right)^{1/2} \tag{5.1}$$

Equation 5.1 is divided in the most inner (brackets) term and the outer term. The inner term is referred to as the efficiency term, as the upper value is 1. It is the inner term that relates to the physical limitations of the engine. While, the outer term relates to the propellant potency, which determines the maximum magnitude of U_e in Equation 5.1.
Ignoring all the species properties for now, as these will be discussed more extensively in Section 5.1.2, and focusing on the efficiency term. The ratio P_e/P_{cc} should be minimised. The exhaust pressure (P_e) can only be minimised to a certain extent, independent of the energy level. Hence, it should rather be seen as a quasi design parameter(through A_e). Yet, P_{cc} is completely unrestricted from external effects.
Logically P_{cc} should be as high as possible, which one can argue is achieved with more potent propellants. However, p_{cc} is determined by the propellant rate limit of the injector. For example consider a CC with a very potent propellant, as the propellant combusts pressure levels rise. To continue the combustion new mass has to be injected, which requires at least a injector pressure equal to the current CC pressure.
Ergo, the limiting factor for p_{cc} in rocket engine is the injector pressure produced by the turbo-pump. Evidently, it was the the turbo-pumps[1] in the development of the SSME that were the limiting factor for the performance.
To conclude, it is the power-cycle that sets the maximum energy level a CC can obtain. While, it is the propellant that determines how much mass is required to reach that maximum, this mass efficiency is measured as the specific impulse (I_{sp})

Ultimately, increased pressure requires more structural mass to contain the combustion, for which a limit exist too. However, if this is necessary for SSTOs they should strive to implementing newer materials that are lighter yet stronger, like metallic-carbon matrices, metallic glass, or super alloys. Whether this is required is left for future material and design studies.

5.1.2. Propellant impact on the Combustion Chamber

To evaluate the impact of the propellant on the performance the second method, namely the shifting equilibrium method, is introduced too, provided in Equation 5.2. The derivation is found in Section 7.2.2 too. In essence Equation 5.2 computes the exhaust velocity by adding all the entropies of the species entering the CC (H_{cc}), and subtracting the entropies of all the ejected species H_e. However, the ejected entropies require estimates of the exit conditions (temperature, pressure, etc). An infinite reaction rate is assumed to resolve this circularity, which makes the method an overestimation, thereby providing a upper bound for U_e.

$$U_e = \left(\frac{2(H_{cc} - H_e)}{M}\right)^{1/2} \tag{5.2}$$

M is the weighted molar mass of the exhaust gas (specific mass), which for both Equation 5.1 and 5.2 is optimal when minimal.
Whereas, T_{cc} in Equation 5.1 indicates a high energy release, the numerator in Equation 5.2 reveals how this is achieved. Hence, potent propellants are those which have a high internal energy, in the form of high energetic chemical bond (high enthalpy), yet easily breaks down into smaller less energetic chemical bonds. Such reasoning indicates that simpler molecules, with an increased likelihood to combust completely are more desirable too, as a lower H_e can be achieved before ejection.
Lastly, Equation 5.1 can be rewritten into Equation 5.3 [20], where H is the weighted enthalpy of all presents species.

$$U_e = (2H/M)^{1/2}\left(1 - \frac{p_e}{p_{cc}}^{R/C_p}\right)^{1/2} \tag{5.3}$$

Equation 5.3 makes previous findings even more apparent, as it highlights the distinction between the influence of the power-cycle and the propellant potency. The propellant properties H and M are now well isolated in the outer term, whereas the power-cycle efficiency term is maintained.
Furthermore, Equation 5.3 provides additional interesting insides into the propellant properties. Starting with the efficiency term, notice that R/C_p should be maximised as R is a constant, a propellant with a low heat capacity (C_p) is preferred. A low C_p can be interpreted as a propellant that is easily heated, hence reaches higher T_{cc} and easier self-ignites.

[1] More powerful turbo-pumps resulted in more weight reducing the T/W ratio, therefore the performance.

All in all, a potent propellant fulfils three criteria 1) it has a high enthalpy 2) it has a low specific mass 3) it has a low specific heat.

5.1.3. Power Cycle Impact on the Combustion Chamber

Next to powering the injector turbo-pumps, the power cycle is responsible for driving the turbo-cooling pumps too. Both pumps are powered by turbines which can operate in one of the three power cycles, namely an expander, a Gas Generators (GG), or a Full-Flow Staged Combustion (FFSC)[2]. The words single or dual are placed in front, to indicate if only the fuel/oxidiser or both operate a particular cycle.
The expander, and by far the simplest power cycle, merely uses the propellant used to cool the engine. The coolant is expanded into a heated gas which drives the turbines. The FFSC uses a preburner where all the propellant is partially combusted in a fuel rich or oxidiser rich environment. The preburned propellant is expanded through the turbine(s) to power the pump(s), losing some of the heat. The entirety of the preburned propellant is injected and combusted in the CC. On the other hand, the GG cycle takes some of the heated fuel (previously used as coolant) and completely combusts this in the GG, which powers all the pumps. The exhaust gases from the GG are ejected separately.
Unsurprisingly, [76] and the SMME show that full-flowed staged combustion (FFSC) or gas generator (GG) cycles have better performance. In general, GG cycles have 11% less engine mass compared to FFSC, yet this result in an overall vehicle mass gain of 8%, due to the lower performance [28]. However, the elimination between between FFSC and GG is less obvious.
To elaborate, preburners operate at the rich and lean ends of propellants, which is required to ensure enough unburned propellant remains for the CC. To efficiently power turbines, a detailed understanding and control of the combustion of the propellant is required, which also is needed to prevent combustion in the plumbing and turbines. This is simply far more challenging if not impossible for non-homogeneous propellants. Therefore, large LHC powered engines, like Merlin 1-D with RP-1, use the GG cycle. Whereas, homogeneous propellants, like LH2 and LCH4, operate the FFSC cycle. Hence, FFSC are more easily developed for propellants that reach complete combustion easier.
In addition, GG are more easily developed and operated. However, a GG engines can be upgraded although this is a challenging endeavour.

As is evident by now FFSC cycles are substantially more challenging, which is why only three have been developed so far (RS-25, NK-33, Raptor). But, FFSC are clearly the better operation cycle with a significant performance advantage. Therefore, it is most likely that corporation will strive for a FFSC cycle, were the initial version may temporarily operate on the GG cycle.

To summarise, for the selected engines to operate on more powerful FFSC cycle, a homogeneous propellant type is required with a relative simple structure so complete combustion is guaranteed in the preburners.

5.1.4. Propellant requirements and design considerations

Propellant potency driven propellant requirements
The from the previous sections 5.1.1, 5.1.2, and 5.1.3 derived requirements are formalised below.

The propellant shall have a high enthalpy
In essence, rocket engines are large heat generators, which convert the reaction heat (H or ΔH_R) into kinetic energy. ΔH_R can be calculated via $\Delta H_R = \sum \Delta H_{\text{fp}} - \sum \Delta H_{\text{fr}}$, where ΔH_{fp} and ΔH_{fr} are the heat of reactants and heat of products, respectively. From databases like JANNAF[3], NIST [4] or Cantera [27]. Hence, the higher the enthalpy, the more potent the propellant.

The propellant shall have a low specific mass and low relative specific heat
The correlation $I_{\text{sp}} \propto (T_{\text{cc}}/M_{\text{cc}})^{1/2}$, derived from Equation 5.1, indicates that the above properties benefit the heat transfer into kinetic energy.

[2] Some literature refers to GG as an open-cycle and to FFSC as an open-cycle.
[3] JANNAF Digital Online Collection : https://www.jannaf.org/
[4] https://webbook.nist.gov/chemistry/

Economically driven propellant requirements
Like the engine requirements, the reasoning of Chapter 3 provides economic requirements for the propellants too.

The refuelling cost of the SSTO is similar to current ascent vehicles
This is rather straightforward, as the entire launch industry is rapidly moving to more manageable and easier acquirable propellants. It is only logical for an SSTO to do the same. Preferably, multiple suppliers exist and a minimal amount of complex manufacturing processes are needed.

The selected propellants must be widely attainable in the amounts needed for a launch
Propellants like metallic hydrogen are superior to all other propellants, yet they have only been produced in milligrams. Therefore, to keep the SSTO within current reach, only propellants whose chemical industry is well-established are selected.

Other driven Propellant Requirements
Other characteristics that must be taken into account are heat transfer rates, cooling properties, temperature sensitivity, storability, toxicity, and oxidation. All must be within acceptable levels to even be considered as an alternative and are relatively standard propellant requirements. The most noteworthy are stated below.

One of the propellant components must be able to fulfil the cooling requirements
One of the selected propellants must have an adequate heat conductivity coefficient, while refraining from being to corrosive or reactive (due to the reusability). This is a larger constraint for the hybrid engine propellants, as the precooler requiring a substance that can cool the air quick enough.

The propellant cannot be hazardous due to toxicity during the ascent
Some of history's most potent propellants have used fluorine or mercury. Even though, LH2/LF is a high-energy propellant [85], it creates highly toxic hydrogen fluoride gas. As such, it cannot be used in large amounts in during the early ascent phase.
Furthermore, hypergolic oxidisers like ClF3 have been proposed but proved too much of an engineering challenge to be stored safely [20]. For mercury spiked engines, the health of the engineers is a major concern [20]. Further complications arise when government institutions are considered. Therefore, this review will refrain from selecting too hazardous propellants.

The required ignition energy is preferred to be low, enhancing the (re)ignition process.
Throughout the ascent the engines need to be reignited at least ones (deorbit burn), Due to the fact SSTOs have one set of engines. Hence, a propellant that is easily reignited is preferred to ensure operational reliability. This is especially true for the PDE.

Propellant Requirement overview
The general propellant requirements are considered too, however the discussion of these is excluded from this research. For an elaborate explanation a reference is made to [85].
Table 5.1 provides an overview of the combined requirements parameters, both stated and general.

Requirement Category	Requirements Parameter
Propulsive Performance	Enthaply, specific heat (ratio), specific molar mass, homogeneous substance, Reactivity
Economic viability	Availability, Price, Suppliers, TRL
cooling qualities	Heat of vaporisation, boiling point, thermal conductivity, corrosiveness
Handling qualities	Explosiveness, toxicity of reactants, corosiveness, (re-)ignitability
Storability	High density, embrittlement, stability, Cubic expansion ratio, vaporisation
Other properties	Toxicity of product

Table 5.1: provides the an overview of all parameters that are important for a propellant trade-off.

5.2. Fuels for SSTO RLVs

Throughout the research it was noticed that the more innovative engines never considered more potent propellants. Whereas, more potent propellants limited themselves to more conservative engine designs. The following sections dedicates themselves to the more potent propellants, identifying the ones that could increase performance of the selected engines.

5.2.1. Liquid Hydrocarbons (LHC)

Hydrocarbons have been used ever since the birth of space flight. LHCs have lower I_{sp} values than LH2, yet have a more compact energy/volume ratio, thereby reduce reduce atmospheric drag [76] and Thermal Protection System (TPS) size [22]. Both factors result in a lower vehicle dry mass, reducing the required propellant mass.
LHCs are generally far easier to store and operate (no cryogenics), reducing costs. Furthermore, LHCs have lower leakage and higher availability of raw materials (more suppliers), further reducing costs.
Generally, the disadvantage of LHCs is the impurity of the fuel, often consisting of many different species. Multi species combustion have more complex reaction patterns, these combustion interactions are difficult to model if not impossible, due to the many unknowns. Engine optimisation is therefore limited in the design phase, leading to larger deviations between theoretical I_{sp} and achieved I_{sp}. More over, these impurities lead to incomplete combustion (soot), causing deposits. The deposits alter the contour and clog the engine, resulting in prolonged and expensive ground operations.
Fuels like Propane and Methane (partly) evade the impurity issues, as both gasses are far purer than alternative LHC fuels. Theoretically synthetic hydrocarbons avoid the same issues, yet require more complex production procedure. Only a few companies can produce the required volumes of synthetic fuels.

Highest Specific Impulse Hydrocarbon Fuels

Hydrocarbon	Formula	I_{sp} (seconds)
Acetylene	$C_1 H_1$	370.3
Allene	$C_1 H_{1.333}$	356.7
Bicyclo(1,1,0)-butane	$C_1 H_{1.5}$	356.3
Methylacetylene	$C_1 H_{1.333}$	355.6
1,5-Hexadiyne	$C_1 H_1$	353.5
Ethylene	$C_1 H_2$	353.1
Cyclopropyl-acetylene	$C_1 H_{2.0}$	353.1
Spiro(2,2)pentane	$C_1 H_{1.6}$	351.7
1,6-Heptadiyne	$C_1 H_{1.143}$	350.6
Cyclopropane	$C_1 H_2$	350.1
Baseline		
Hydrogen (liquid)	H_2	432.9
Methane	$C_1 H_4$	350.0
Propane	$C_1 H_{2.667}$	343.7
RP-1	$C_1 H_{2.0}$	337.0

Table 5.2: Illustrates the I_{sp} levels of various LHCs at a CC pressure of ~155 bar and an expansion ratio of 40, taken from [61].

RP-1
RP-1, a more purified form of kerosene, belongs among the oldest rocket fuels to date. RP-1 is still widely used in Launchers like the Soyuz. Even though some variation in RP-1 exists between producers the behaviour of RP-1 is well understood allowing higher optimisation compared to less common LHCs. The large availability of RP-1 allows for lower restrictions in allocation and refuelling, reducing the settling/operational costs. RP-1 is lacking in performance (337 s), making it unsuited to power an SSTO on its own. Note that RP-1 is unsuited for the precooler, as it is stored at ambient T.

Propane
Propane offers a cleaner combustion compared to RP-1, a higher density than LCH4 and is widely available, offer the advantages of both RP-1 and LCH4. Even though propane is still plagued by some multi species presents, this is insignificant compared to RP-1. As such propane is a better alternative to RP-1 boosting performance, yet retaining much of the economical advantageous. Moreover, propane can be cryogenically stored (for the precooler).

Liquid Methane LCH4
In recent years liquid methane (LCH4) has increased in popularity, new launchers use a LCH4/LOX cycle. Evidently, LCH4 has even replaced RP-1 in the Falcon-9. Methane is the simplest hydrocarbon molecule and is the purest LHC available, thus producing a very clean burn and eliminating clogging or deposits. Furthermore, LCH4 has the highest concentration of hydrogen (high r value) and thus, a low specific mass (thus increases I_{sp}). Another advantages is that methane gas can self pressurise, eliminating the need for a pressure gas. However, LCH4 is less energetic than other LHCs, producing lower T_{cc}. Furthermore, LCH4 is less dense and has a lower I_d than other LHCs. I_d is a measure that partly weights the density and consequently the atmospheric drag. Given the presented advantages, combined with the wide availability (produced from natural gas), makes it a very attractive candidate for any rocket engine. Note that LCH4, too, can be stored cryogenically.

Acetylenic fuels Ethyne (C2H2) and Ethylene (C2H4)
Acetylene or ethyne has the highest I_{sp} (370.3 s) of all currently tested LHCs [61]. This is largely due to the far higher chemical energy levels (due to double/triple c-bonds), thus a low r value (H/C ratio), yet the product still has relative low specific mass (M). Acetylenes have the highest adiabatic flame temperatures known in combustion, due to its rapid ignition and high reaction rates. Ethyne and Ethylene produce the highest flame temperatures, respectively, when excluding the more dangerous nitric varieties. Note that acetylene can refer to both the molecule ethyne or acetylenic molecules. The latter being hydrocarbons with only double and/or triple C-C bonds ($r \approx 1$).
Ethyne could potentially reduce the atmospheric drag, due to its higher density and boiling point. Furthermore ethyne has properties very similar to LCH4. However, the availability comes with a catch. Even though ethyne is widely used for high temperature welding it is not currently used for any rocket propulsion system. Alternatively, the equally available, Ethylene could be the better option. Ethylene is marginally less energetic, yet has twice the r value (lower M). Acetylene and Ethylene are both manufactured using petroleum as starting resource.
Acetylene saw much development in the early days of rocketry, yet were mostly abandoned due to storability difficulties. Whereas, other LHCs yielded faster results [20]. However, the storage of acetylenic propellants is less challanging than that of LH2 [64], therefore not impossible to overcome.

All in all, ethyne and Ethylene are highly promising fuels for an SSTO propellant. Yet, is supplied by industries other than the space industry. Acetylenes will be elaborated in more detail in Section 5.4, due to mostly being hypergolic.

High density LHCs
Even though high density carbon fuels logically lead to lower I_{sp} (low r ratio), the density specific impulse I_d is increased [61]. The I_d is a measure used to quantify volumetric penalty. High density LHC have an abundance of C atoms, often near a 1-to-1 ratio with H, some I_d are illustrated in Table 5.3. Yet, the validity of using I_d is ill defended. As such, the further evaluation is required to determine the performance gain of these high density LHCs. This means that the severity of the volumetric penalty is not established.

5.2.2. Spiked LHCs

Throughout the space transportation engine program (STEP) NASA researched many high density fuel options, some of these studies included spiked propellants. In essence, spiking fuel, simply refers to adding radicals (often metals) to the fuel to increase the heat generation. The metals act as some sort of catalyst, benefiting the combustion process.
The potency of using spiking propellants, was illustrated by the LH2/LF/Li engine, yielding an I_{sp} of ~542 s, making it the most powerful chemical engine to date. The metals researched include aluminium, beryllium,

Highest Density Specific Impulse
Hydrocarbon Fuels

Hydrocarbon	Formula	I_d (seconds)
H-COT-Dimer	$C_1 H_{1.25}$	382.1
RJ-5	$C_1 H_{1.286}$	377.3
Tetrahydrotri-cyclopentadiene	$C_1 H_{1.467}$	368.0
RJ-6	$C_1 H_{1.417}$	366.1
B-4[11]	$C_1 H_{1.2430}$	364.0
Dicyclopropyl-acetylene	$C_1 H_{1.25}$	361.4
C-9[11]	$C_1 H_{1.0656}$	361.1
cis-trans Perhydrofluorene	$C_1 H_{1.692}$	360.9
COT (Cyclooctatetrene)	$C_1 H_1$	360.4
Baseline		
RP-1	$C_1 H_{2.0}$	341.7
Propane	$C_1 H_{2.667}$	309.3
Methane	$C_1 H_4$	283.5
Hydrogen (liquid)	H_2	156.7

Table 5.3: Illustrates the I_d levels of various LHCs at a CC pressure of ~155 bars and an expansion ratio of 40, taken form [61].

lithium, magnesium, and in some instances mercury. The adding of metals originates for solid propellants. However, for liquid propellants the challenge is in how to properly mix the radicals. The LH2/LF/Li engine heated the lithium to a liquid injecting it separately. Alternatively, the insides of the CC could be covered with an epoxy containing the radicals. Such a configuration would prolong refuelling of the vehicle, yet would reduce the cooling requirements of the CC (due to ablative effects) and is inherently simpler.

The effect on I_{sp} for adding Al is illustrated in Figure 5.1. Figure 5.1 illustrates the effect of the more common and high performing LHC. Note that the results are at an ideal fuel weight percentage and at the optimal O/F ratio. The optimum weight percentage of Al is typically 5% (for some 10%). Furthermore, the O/F increases compared to the neat variants. It was shown that low I_{sp} HCs are more sensitive to aluminium additives, compared to high I_{sp} HCs [61]. Aluminium is an important base line as only metals like boron (produces toxic fumes upon combustion) have higher heats of formation. Therefore, from a pure thermodynamics perspective aluminium radicals are among the best additives [17]. Notably, fuels like Acetylene showed no increase. Furthermore, the increase in density was marginal at best, therefore lacking any indication of atmospheric drag decreases.

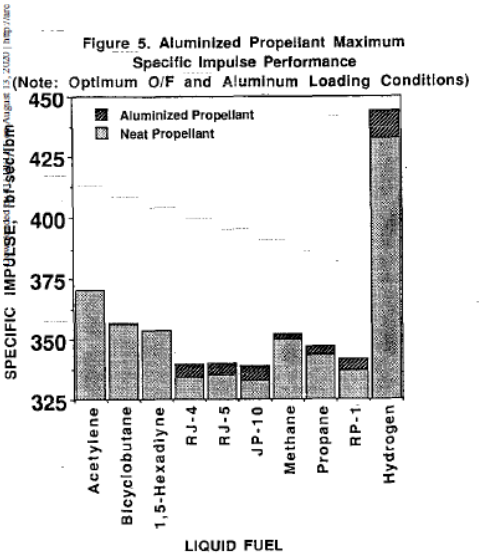

Figure 5.1: Illustrates the I_{sp} gain by adding aluminium to the propellant, taken from [61].

To conclude, the addition of metallic radicals, although showing marginal improvements, is trumped by other alternatives like Acetylene. Even though metals like boron and beryllium might pose a more significant improvement, the complexity due to toxicity makes them unworthy to explore. Catalytic effects were largely ignored in Figure 5.1, since to properly would require excessive testing in representative environments. Such testing would be expensive, with little theoretical indication of success.

5.2.3. hydrogen

In terms of specific mass hydrogen is the superior fuel, yet the density leaves much to be desired (1/10 that of RP-1 [61]). Therefore, H2 is stored cryogenically and under high pressure. Currently only two main forms of hydrogen fuel have been tested, namely LH2 and SH2. Both are discussed in the following paragraphs.

Liquid Hydrogen (LH2)
LH2 has historically been the preferred propellant for American launchers. Hydrogen is the smallest natural molecule, and with high reactivity, it is an ideal rocket propellant. Those properties result in a I_{sp} of 366 s at sea level and reach 452 s in vacuum. LH2 is the highest performing pure liquid rocket fuel, only some alternations which add radicals have a better theoretical performance.
Yet, LH2 has some disadvantageous most notable, the liquefaction, where gaseous H2 is cooled to cryogenic temperatures of 22.7 K[85]. Liquefaction is costly and requires stored fuel to be constantly cooled, eliminating long time storage. To continue, the low specific mass is a double edged blade as hydrogen escapes through most containing vessels, daily losses of 10% are common. During the launch of the Space Shuttle the LH2 tanks were constantly refuelled, up to the moment of ignition. Lastly, LH2 has a terrible volume density[85].
In terms of cooling, LH2 has some of the best thermodynamic properties, namely high specific heat and high heat transfer coefficient , making it an ideal absorption coolant. The effective cooling, allows for far higher CC temperatures, leading to higher yields. Note that a high specific heat does mean that LH2 requires more heating energy, thus resulting in lower injection temperatures.
Lastly, unlike LHC propellants hydrogen is much purer, thus leading to higher optimisation levels. On the other hand, difficulties might arise from the fact that H2 has a high flame speed, many times faster than LHCs. The high flame speed makes it engineering wise more challenging to maintain stable combustion, as the flame is more sensitive to the combustion conditions.
All in all, as a high performance propellant hydrogen is worth considering for all engines. Thermodynamic properties are ideal for the precooled engine, while the fast flame speed increases detonation frequency in the PDE.

Spiked Hydrogen
Al spiked hydrogen only marginally boost performance but triples the density, thus decreasing the mixture ratio to 0.6 [61]. The lower mixture ratio decreases the bulk density, reducing atmospheric drag. The 10% bulk density increase(41% in LH2) and 2% thrust gain is insufficient to justify the added complexity, eliminating LH2/LOX/Al from further consideration. Currently, no solution exists to keep the Al homogeneously mixed with LH2.
Radicals must provide a significant gain in performance to make up for the density loss, therefore only metals like magnesium or lithium could pose a solution. Yet, lithium is in high demand, so this is economically unsustainable.
Three injection methods exists for metallic radicals. Firstly, premixing the radicals with the hydrogen. Nevertheless, this would lead to separation issues, resulting in a non-homogeneous fuel. Secondly, radicals are attached to the wall of the CC or throat via an epoxy. The radicals are mixed through the ablation of the epoxy. However, the amount of ablation will vary, as it is almost impossible to properly control during combustion. Lastly, the metals can be brought to melt, like the LH2/Li/LF engine[20]. Yet, having melted metals on board poses another risk.

Solid Hydrogen (SH2)
SH2 was developed during the high-energy density matters (HEDM) NASA project, aimed to overcome the low density of LH2. Note that SH2 differs from metallic hydrogen (SH). SH2 with a 69 bar CC would at sea level conditions perform similar to LH2, at 389 s [17]. Yet, the SH2 is more densely packed than LH2, namely 0.086 g/cm^3 versus 0.071 g/cm^3. The smaller volume would decrease the drag area by ~12%, resulting in lower atmospheric drag. However, the increased pressure would add structural mass, therefore an overall gain in performance is uncertain. Furthermore, SH2 does raise concerns when dealing with the plumbing as the hydrogen will have a slush form rather than being liquid. This requires stronger pumps. Cooling could be reduced, due to the tubing resistance that reduces the flow rate.
Under HEDM SH2 was further developed, including the concept of trapping radicals in the cryogenic solid, eliminating the need for additional mixing systems. However, this method is limited to a maximum mass fraction of ~8% [17]. However, a loading of 5% is recommended to prevent clustering, which is significantly

lower than the optimum of 60% found for LH2 [61].
Study [17] computed the I_{sp} for various atomic and diatomic radicals, as illustrated in Tables 5.4. Even though beryllium and boron yield the highest performance, lithium and aluminium are preferred due to their none toxic exhaust gases. Note that Carbon does boost performance significantly, yet it is highly unstable in this form. The values presented in Tables 5.4 should not be taken literary, as they vary depending on the computation method, rather focus on the performance gain. In reality effects like clustering, catalyticity and other molecular interactions cause I_{sp} deviations. All in all, SH2 seems to offer a minor advantage over LH2,

Species	I_{sp} 5% w/sH_2 (sec)	Increase over LH_2\LO_2 (sec)	(%)
H_2 (s)	389	-1	0
H	407	17	4
Li	401	11	3
Be	452	62	16
B	472	82	21
C	469	79	20
N	414	24	6
Mg	398	8	2
Al	425	35	9
Si	432	42	11
Ti	404	14	4

(a)

Species	I_{sp} 5% w/sH_2 (sec)	Increase of solid over LH_2\LOx (sec)	%
LiH	402	13	3
BeH	458	69	18
BH	453	64	16
CH	436	47	12
MgH	409	20	5
AlH	418	29	7
Li_2	420	13	3
LiBe	486	97	25
LiB	496	107	28
LiC	467	78	20
LiMg	417	28	7
LiAl	450	61	16
Be_2	529	140	36
BeAl	483	94	24
B_2	493	104	27
BC	483	94	24
C_2	462	73	19
CAl	459	70	18
Mg_2	410	21	5
Al_2	445	56	14

(b)

Table 5.4: I_{sp} levels of solid hydrogen with both atomic (a) and diatomic (b) radicals, taken from [17].

yet this is most likely offset by the operational complexity and the added structural weight. Adding radicals could make it worth the trouble, yet much more development would be needed. Therefore, SH2 is only worth considering if no other alternatives are available.

5.3. Oxidisers for SSTO RLVs

5.3.1. Liquid oxygen (LOX)

Liquid oxygen is the go-to oxidiser for all current launch vehicles. The only time vehicles refrain from using LOX is for deep or prolonged space missions. LOX is unfit for those scenarios, due to the cryogenic storage and consequent leakage.
LOX is one of the most potent oxidisers and if made to ignite results in extreme adiabatic flame temperatures. Generally, pure oxygen results in an adiabatic flame temperature far above 3000 K (air ~2500 K). Cryogenically stored LOX is kept at a temperature of 54.36 K, therefore LOX is heated to properly ignite. Solutions include preburners and regenerative cooling, although the latter is rarely used due to the corrosive nature of LOX [85]. Most LOX systems have been widely developed, and should pose no problem during development (off the shelf technology). Hence, engineering challenges concerning storage, plumbing, and general substance behaviour are well understood. Similarly, methods and tool to deal with the hazards of LOX have been firmly established minimising the risks.
Unfortunately LOX still has to be stored close at 1-4 bar and 54.36 K, resulting in evaporation under atmospheric conditions. Therefore, LOX can only be loaded shortly before launch and is unsuited for prolonged ground storage.
Ywt, in most instances LOX offers the best performance results with any other fuel and it does not produce

toxic exhaust gases. Lastly, LOX is a well established oxidiser, with many suppliers on the market.

5.3.2. Ozone

Given the performance of LOX, logically some chemists reckoned that molecules containing even more oxygen atoms would yield even better results. This logic lead to ozone (O3), a far more reactive oxidiser than LOX. Ozone is inherently unstable and randomly decomposes, which can vary from a few days to hours, depending on the conditions. When decomposition occurs a radical oxygen atom is released, which is extremely reactive. Therefore, O3 is just as toxic as fluor.
The main advantage of O3 is that it is significantly more dense than LOX. The presence of the radical oxygen atom benefits the combustion, which releases energy upon decomposition [20]. Ozone can be stored at higher temperatures as it has a boiling temperature of 161 K (93 K for O2).
Due the inherently unstable nature of O3, ozone is often mixed into LOX or LF (not considered in this study). However, mixing liquid ozone with LOX must be carefully monitored as the two substances will partly separate under certain conditions [20]. Note that some species can be introduced (OF2 or F2) to eliminate separation, yet this will result in toxic exhaust gases.
Yet, the largest challenge with ozone, is the tendency of engines exploding during and even after firing. The reason for the explosion is still unknown, yet explanations vary from a build up of organic peroxide, to oil residues in the oxygen, to build up of radicals in the plumbing. The latter can be resolved through extensive purge systems. Ozone has seen some minor development over the years, yet still has not come into its own. Even though some suppliers exist, they are few compared to LOX suppliers.
All in all, ozone has some very attractive characteristic which could yield an incredible performance,given that the engineering challenges can be overcome. One could dilute the ozone with LOX to circumvent some of the engineering challenges, yet a purity below 25% would make the whole endeavor unfruitful [20].

5.3.3. Hydrogen Peroxide (H2O2)

Hydrogen peroxide (further referred to as peroxide) was primarily developed as an alternative to oxidisers, like nitric acid. Unlike the acidic oxidisers peroxide produces no toxic exhaust gases (for most fuels that is). Yet, unlike the acidic oxidisers peroxide only has a single oxidising nucleus. However, the addition of hydrogen atoms by the oxidiser lowers the specific mass, potentially increasing the I_{sp}.
Yet, peroxide is inherently unstable and decomposes exothermic (decomposition is self accelerating), although H2O2 is more stable than ozone. Therefore, the tanks must be very well sanitised, as almost any molecule is a catalyst for peroxide [20]. Peroxide has a high freezing/boiling point, eliminating the need for cryogenic storage. However, this limits H2O2 use in regenerative cooling and useless as a precooler. However, H2O2 has a higher oxidation potential than most oxidisers including chlorine, making the adiabatic flame temperature reach ~2800 K when burned CH4 (stoichiometric) [18]. Even though 2800 K is impressive LOX is about 1000 K hotter (LCH4). Alternatively, through the use of a catalyst peroxide can be transformed into 2 OH molecules. These molecules are only beaten by the reactivity of fluorine, enhancing the combustion process significantly.
Even though peroxide is not considered hypergolic with all substances, it will ignite upon contact with most (HC) fuels, further discussed in Section 5.4. The mixture will simmer, yet after some time it will detonate [20]. This phenomenon is explained by the fact that peroxide decomposes violently for temperatures above 723 K [18], releasing radical oxygen atoms, increasing heat release, releasing more radicals (positive feedback loop). Peroxide is widely available, due to its use in mostly hygienic products, the stability has largely been dealt with by increasing concentrations to 98%. It appears that the higher the concentration the more stable H2O2 becomes. Yet, peroxide does not pose a direct alternative to LOX, for one because the energetic performance is significantly lower. Secondly, the technology is less developed (for large launchers that is). Yet, H2O2 provides an advantage over LOX when it comes to carbon heavy fuels (like acetylenic HCs), where H2O2 can significantly lower the specific mass of the exhaust gases. Lastly, H2O2 does bare a storability edge over LOX, the vehicle can stay in space over prolonged periods of time. More over, H202 can be kept on hand, reducing turnaround times and allow last moment launches, given that the fuel holds similar properties.

5.3.4. FLOX Liquid Fluorine (LF), Liquid Chlorine (LCl)

FLOX is the mixture of LOX and Liquid Fluorine, variations have been tried from 30% O2 to up to 70% O2. Even though,FLOX and LF outperform LOX, they are extremely toxic and cannot be used during launch. Only when a sufficiently high altitude has been reached might the use of Fluorine or Chlorine in some amounts be tolerable. Yet, both are less dense than LOX, and would add atmospheric drag. Furthermore additional tanks and plumbing would be required. Therefore, it does not seem worth the effort.

5.4. Hypergolic propellants

Hypergolic propellants are some of the most potent reactions out there, due to their igniting nature upon contact. Yet, as hypergolic propellants can both be oxidisers or fuel, they are discussed in this separate chapter to avoid confusion.
Hypergolic propellants are advantageous, the short ignition delay results in a more complete combustion. Hypergolic propellants eliminate the need for ignition systems, and can easily be reignited. Yet, most hypergolic substances are highly toxic, erosive or explosive, leading to storability and workability issues.
It was found that hypergolic fuel with tertiary amines or triple bonded (alkynes) were mostly hypergolic [20]. Combinations of amines and acetylene with white or red fumic nitric acid (WFNA/RFNA), nitric acid, and oxygen were researched. Nitric acid was unsuited for acetylenes as it detonated upon contact. Most impressive was the combinations of dicyanoacetylene with ozone, achieving a steady state temperature of 6000 K [20].
The later and now more commonly used hypergolics fuels are UDMH, MMH, hydrazine and aniline, whereas the more common oxidisers include hydrogenperoxide, nitric acid, and nitrogen tetroxide (NTO). Even though these fuels can be stored easily and over extended periods of time, the I_{sp} for all is around 270-290 s at sea level and 320-340 s in vacuum[5]. Furthermore, they are highly hazardous to work with and produce toxic exhaust gases. With these disadvantages common hypergolic fuels can be excluded for SSTO engines as the performance with much cheaper and safer fuels (like methane) is superior.
Acetylenes have proven to be more potent, with an estimated I_{sp} of 425 s, and are far denser than LH2 or LCH4. Yet, the explosive nature, shock-sensibility, and the fact that most acetylenes are unstable pose many challenges. However, acetylenes have been developed outside the field of rocketry, leading to more stable and workable compounds, like diacetylene. Alternatively to LOX, ozone or hydrogen peroxide could be used as oxidisers. Moreover, current acetylene compounds produce adiabatic flame temperatures similar and higher than LH2, dicyanoacetylene reaches temperature ~5300 K (note that this component does have many challenges for it to be used as a rocket fuel).
The theoretical potential of acetylene has already been shown in [61] and [71], the latter illustrating the benefit of using acetylene in a pulse jet. Acetylene should mix better with air and evidently with LOX as it is closer to the density of the oxidiser than kerosene[71]. The most common used acetylene, ethyne, has a boiling point of ~188 K. Hence, ethyne is less suitable for intensive regenerative cooling. Furthermore, HCs often have inferior thermal characteristics compared to hydrogen, as such the acetylenic compounds are probably unfit in the precooled hybrid airbreathing rocket engine. The same issue could arise for high pressure combustion chamber, which reach higher temperatures. Alternatively, LOX regenerative cooling could be used for the engine, yet this comes with corrosion challenges.
To summarise, acetylenic compounds, like ethyne, have performance similar to LH2. However, regenerative cooling for high pressure CC might be jeopardised. The advantage that some Acetylenic compounds are hypergolic with LOX, will eliminate a complex reignition system. Even if the compound is not hypergolic with LOX, small amounts of peroxide or nitric acid (HNO3 or N2O4) can be injected to start ignition.

5.5. Propellant Selection for Each Engine

Previous sections discussed fuels and oxidisers, elaborating on performance, availability, and TRL. Many more propellants exist or are under development. Yet, this thesis is limited to Propellants that have seen significant development and are most relevant. Some new and far superior propellants might already exist, yet these would undermine the aim of developing an SSTO engine within a reasonable time frame, see Chapter 2.

[5] http://www.astronautix.com/h/h2o2udmh.html

5.5.1. Aerospike Engine

The aerospike is the least propellant sensitive engine of the three, and likely works with any combination. Yet, there are some combinations which are more worthy to pursue, see Table 5.5. Note that not all fuels and oxidisers are equally understood as LH2/LOX are, therefore the performances should be taken as indications and need to be verified when designing an ascent vehicle utilising one of these propellant pallets.[6] [7].
Most tank pressures are in the range of 1 to 4 bar, this is the typical pressure of liquid propellant tanks. The actual pressure is decided with a sizing analysis, and depends on storage capabilities, structural mass, and presence of a pressure structure.
RP-1 is absent in Table 5.5 as acetylenes are far more potent. Therefore, the reasoning goes that if acetylene is not sufficient, RP-1 would not be sufficient either. The development of ozone has mostly been abandoned, adding the fact that engines tent to explode even after termination, excludes ozone from consideration. If, however, a reader can find breakthroughs, dealing with the instability, LO3 might be worth considering.
I_{sp} levels provided in the last row are taken form the literature at sea level with mostly a P_{cc} of 69 bars. For combustion cycles with H2O2 as the oxidiser, the I_{sp} is based on the energy difference between LOX and H2O2. Note that this is not a one-to-one relationship.
Note that if it is possible to use catalysts to transform peroxide into OH, the combustion will be enhanced, resulting in a higher I_{sp} [61].

Propellant Pallets	LH2/LOX	LC2H2/LOX	LC2H2/H2O2	LCH4/LOX	LCH4/LH2O2	LC2H4/LOX	LC2H4/LOX
Storage properties fuel	22K	~189.15 K[6]	~189.15 K[6]	90 K	90 K	~169.45 K	~169.45 K
storage properties Oxidiser	54.36 K	54.36 K	+273 K[7]	54.36 K	+273 K[7]	54.36 K	+273 K[7]
Regenerative cooling fluid	LH2	C2H2	C2H2	LCH4	LCH4	C2H4	C2H4
I_{sp} indication (SL)	430	370	~310	340	~290	350	~290

Table 5.5: Provides the properties of the selected propellant pallets for the aerospike engine, both fuel and oxidiser are stored at 1-4 bar.

5.5.2. Pulse Detonation Engine

Many jet and rocket pulse engines have operated using LHCs. Furthermore, paper [71] computed that ethyne (C2H2) would be better than kerosene. It can be concluded that almost all HCs are suitable for pulse detonation engines. Yet, for hydrogen based detonation pulse engines the amount of tests are limited. Even though enough literature exists, the technology has matured less than its HCs alternatives.
The incredibly short detonation time of hydrogen, makes consistently maintaining combustion cycles challenging. However, if made to work the amount of ignitions per second can significantly be increased, resulting in higher thrust. Furthermore, hydrogen can be added in the extended throat to decrease the specific mass, thus increasing I_{sp} even further.

Propellant Pallets	LH2/LOX	LCH4/LOX	LC2H2/LOX	LC2H4/LOX
Storage properties fuel	22 K	90 K	189.15 K	169.45
Storage properties oxidiser	54.36 K	54.36 K	54.36 K	54.36 K
Regenerative cooling fluid	LH2	LCH4	LC2H2	LC2H4
I_{sp} estimates (SL)	4335[8]	1598[9]	1711[8]	~1650

Table 5.6: Provides the properties of the selected propellant pallets for a non-breathing pulse detonation engine, both fuels an oxidisers are stored at 1-4 bar.

All in all, the same fuels that were considered for the aerospike are valid and recommendable for the PDE, see Table 5.6. Yet, H2O2 is deliberately excluded from the Table 5.6. Whereas, H2O2 has illustrated promising detonation properties outside the field of rocketry [62], it has never been utilised as the primary oxidiser in an PDE. Therefore, even though H2O2 remains a promising candidate for an PDE, it remains to be seen if such an engine can be developed within the reasonable time frame. For this reason and the reasons discussed

[6] Even though, acetylenic compounds have been widely lab tested, yet lack any references of actual rocket storage, therefore only a range for the liquid Acetylene compound C2H2 and C2H4 is provided
[7] Peroxide has been used in many deep space launches, yet lacks any experience as a launch propellant, therefore the minimum storage properties are provided.

later, H2O2 is not further considered for the PDE.
Additionally, unlike the aerospike engine the PDE can be made to operate with air intake. As such, the Propellant Pallets for an launch with an initial breathing phase are illustrated in Table 5.7[8][9].
Ozone is excluded for the rocket phase for the same reasons described before, see Section 5.5.1.

Propellant Pallets	LH2/Air	LCH4/air	LC2H2/air	LC2H4/air
Storage properties fuel	22K	90 K	189.15 K	169.45
oxidiser additives	LOX	LOX/H2O2	LOX/H2O2	LOX/H2O2
Regenerative cooling fluid	LH2	LCH4	LC2H2	LC2H4
I_{sp} estimates (SL)	4335[8]	1598[9]	1711[8]	~1650

Table 5.7: Provides the properties of the propellant pallets for a breathing pulse detonation engine, both fuels an oxidisers are stored at 1-4 bar.

Paper [18] concluded that adding peroxide to the LCH4/air combustion, the combustion became more energetic. Therefore, a pure air mixture for the initial phases might not be ideal, adding a small amounts of the oxidiser could lead to better performance overall. The combustion of LH2 with LH2O2 is illogical, as it provides no reduction in specific mass, excluding it from the trade-off.

5.5.3. Precooled Hybrid Airbreathing Engine

As has been extensively discussed in Section 4.1.2, the Precooled Hybrid engine requires a cryogenic fluid to cool the inlet airstream. Therefore, the propellant pallets are limited, eliminating all combinations with H2O2.
Whether, LOX would be able to precool the airstream depends on two aspects. Firstly, whether heat transfer rate is sufficient to precool the airstream. Second, whether the LOX is capable of cooling the air throughout the airbreathing phase, due to heat buildup. Even though the first challenge can be overcome by using a transfer cooling fluid, like helium. The latter is of greater concern, as it was the case for the LACE engine (4.1.3), the mass of the oxidiser required to meet the precooling conditions, might surpass the mass required for the DeltaV bugdet. That is not to mention the corrosive challenges that come with a LOX based cooling system. In short, before any LHC can considered these challenges will have to be dealt with, yet given the concept studies on the LACE engine this seems unlikely [75].
When it comes to LCH4 based precooled hybrids, LCH4 can be used for the precooling. The LCH4 is being used throughout the airbreathing phase, less cumulative heat buildup. Yet, whether LCH4 can be directly used as the precooling fluid (cryogenically stored) or whether a cooling fluid is required, is left for future analysis.
In Table 5.8 one can see the selection for the Precooled Hybrid Airbreathing Engine. The I_{sp} indications are provided for the rocket phase, as no good estimates were identified for the breathing phase. However, a reader can safely assume that the I_{sp} for the breathing phase is a factor 4-6 higher.

Propellant Pallets	LH2/LOX/Air	LCH4/LOX/Air
Storage properties fuel	22 K	90 K
Storage properties oxidiser	54.36 K	54.36 K
Precooling fluid	LH2	LCH4/He
Regenrative cooling fluid	LH2	LCH4
I_{sp} indication (VAC)	450	380

Table 5.8: Provides the properties of the propellant pallets for the precooled hybrid airbreathing rocket engine, both fuels and oxidisers are stored at 1-4 bar.

[8] The presented I_{sp} levels are taken from the appendix E. of [81].
[9] The I_{sp} of Methane/air is a very rough estimated derived from $I_{sp} \propto (T_{cc}/M_{cc})^{1/2}$ and the I_{sp} of acetylene.

Additions of Additives
As was discussed before B2 and Be2 allow for the highest I_{sp} gain and might be worth exploring if the current proposed engines require the extra performance. However, it might be more advantageous to start with additives like aluminium and lithium, as they do not produce any toxic fumes. Even if boron and beryllium only produce insignificant toxicity, getting approval poses too much of an obstacle to be economically worth considered.
The above additives are not considered in the performance analysis as it is believed that these are ether implemented as an upgrade to an well developed engine or as a last resort to make SSTO possible. The latter would likely extend the development beyond a reasonable time frame.

Exclusion of H2O2 from the Performance Trade-off Module
Even though, H2O2 is suggested in the conclusion of this chapter it will not be further considered outside the literature trade-off. The reason is rather straight forward and due to the constrains of the performance trade-off model. H2O2 was chosen for its easier handling properties and increased density, which could justify the I_{sp} performance reduction.
At room temperature H202 is 27% more dense than cryogenic oxygen. In the absence of a cryogenic oxidiser less complex system can be utilised, thereby reducing mass and increasing T/W, a phenomenon further elaborated in Section 6.2.4. Furthermore, the increased density can reduce the overall tank size, depending on the F/O and fuel density. Given that the tank size are the largest volumetric components, a size reduction the overall drag area, thereby reducing the aerodynamic drag losses lowering the DeltaV budget.
However, as will be evident in Section 6.2.4 the current performance model excludes the sizing of the ascent vehicle. Therefore, the advantages of the H2O2 cannot be evaluated in the current model and only the reduced performance is considered. Therefore, in advance it can be concluded that the model will undervalue the performance a reject H2O2 propellants pallets as the ideal configuration.
A CH4/H2O2 powered conventional engine at a 0.33 F/O has a computed I_{sp} value of ~295 s, whereas an equivalent CH4/O2 at a 0.275 F/O has a computed I_{sp} of ~330 s. Hence, the sizing advantageous have to justify a performance loss of roughly 10%.
As a final remark the H2O2 oxidiser is included in the performance trade-off model, via the propellant module as described in the upcoming Chapters 6 and 7. Consequently, future research can easily evaluate the viability of H2O2 given a dedicated sizing module is developed and implemented.

6

Performance Trade-off Model

The literature engine trade-off, in Chapter 4, identifies the aerospike engine, the pulse detonation engine, and the precooled hybrid airbreathing rocket engine as most likely candidates for a foreseeable SSTO RLV. While, Chapter 5 identifies the possible propellant pallets for the selected engines. Even though the literature provides great insights, it fails to provide a direct one-on-one comparison. Furthermore, the limited performance analyses performed are all based on different methodologies and assumptions. Some concepts even rely on large technological advances across many rocket systems. As discussed in Chapters 2 and 3, this should be avoided and should only be reserved for the propulsion system. The conclusions derived from these sources are biased and inconclusive for this thesis. Consequently, the next logical question is *How to evaluate the selected engines in a realistic, unbiased, and consistent manner?*. This Chapter answers set question with a performance trade-off between the selected engines.

To extrapolate any meaningful conclusion from the performance trade-off analysis, the model must reflect a realistic scenario. Furthermore, the model must analyse the performance on a consistent and unbiased basis. The vast differences in the engines architectures, engine operations, and engine-vehicle interaction dynamics complicates such an analysis and eliminates parameter based methods like I_{sp}, fuel rate, thrust, etc.

To achieve the above phrased model requirements it is ideal to compare the performance of each engine in their respective optimal SSTO RLV configuration. Where all other (sub-)systems are of the same relative size, weight, etc. the configuration refers to both physical and non-physical aspects, like the ascent trajectory, which is equivalent to the entire SSTO RLV design. Vehicle design requires many iterative design loops between the system engineering disciplines[1], which is infeasible for a performance analysis and far beyond the scope of this thesis. To prevent having to design eight separate SSTO RLVs, while still ensuring the required model flexibility, a reduced system design loop is required, as proposed in [84]. This serves as the foundation for the performance trade-off and incorporates the propulsion, trajectory and sizing design disciplines.

Consequently, the performance trade-off model is a multidisciplinary optimisation model, which provides the performance of the corresponding engine, with the respective sizing parameters. This is achieved by utilising two joint optimisation loops. The outer loop iterates the propulsion system with the respective vehicle sizing, while the inner loop finds the optimal trajectory for the provided propulsion and ascent vehicle. The model is elaborated in more detail later on this chapter.

As described, certain system engineering disciplines are excluded from the reduced system engineering loop. Hence, some aspects from frozen disciplines required for the model will need certain assumptions. These assumptions, like the C_L, follow from design choices, which for C_L depends on the shape of the vehicle and other lifting surfaces, e.g. wings. This thesis will refrain from making as many design assumptions as possible, as these condition the conclusion. Thereby, introducing the same pitfall as the literature trade-off. However, some aerodynamic and vehicle sizing aspects cannot be avoided, in these instances choices will be made based on the argumentation presented in Chapter 3.

As previously mentioned, this chapter will provide a general description on the model layout, followed by a more detailed explanation. The performance trade-off model is compartmentalised into segregated modules, which each handle a different aspect of the trajectory optimisation. The modulation ensures a plug-and-play

[1] The system engineering disciplines for an ascent vehicle are configuration, aerodynamics, propulsion, trajectory, sizing, operations, safety, economics [84].

model set-up, were modules can easily be replaced, which is needed due the three different propulsion modules. Additionally, the modularization allows future research to expand upon the model by replacing and adding (more detailed) modules. The chapter continues by elaborating each individual module, with the exception of the propulsion modules which is left for Chapter 7.

6.1. The Performance Trade-Off Model

Understanding the performance of the selected engines is less about the isolated engine performance, than it is about the performance of the corresponding engine in an SSTO setting, which is what the rocket motion module provides. Evaluating the isolated engines is insufficient due to the realistic representative, consistent model and unbiased model requirements. this is best explained by an example.
Consider the breathing phase of the hybrid engine. The air intake is dependent on the trajectory, hence the optimal trajectory of a hybrid powered SSTO might have an extended period in the lower atmosphere. Even though such a trajectory has more drag loss (increased DetlaV budget), it can still result in reduced oxidiser use (increased payload delivery). Additionally, without the trajectory it is impossible to determine the effective I_{sp} for the hybrid engine, which to some extent holds true for the other two engines (due the changing expansion conditions).
Furthermore, it is improbable that all the engine have the same relative weight, commonly measured as the Thrust-to-Weight (T/W) ratio. It is likely that the T/W ratio for the PDE is higher due the absence of heavy turbo-pumps, whereas the T/W for the hybrid engine is likely lower due the addition of the intake. As will become evident in Section 6.2.4, knowing the exact T/W ratio of the selected engines is next to impossible. As such, the model must be flexible enough to account for alterations in the T/W ratio.
For the performance trade-off to account for the above engine aspects while fulfilling the model requirements, the ascent and configuration optimisation of an SSTO operating one of the selected engines is utilised. Such methodology ensures that findings have great relevance to reality and allows the engine of the optimised ascent vehicles to be compared directly and consistently. Additionally, such model allow for the sensitivity evaluation of underlying assumptions/parameters, which will provide better insights in the feasibility of the SSTO and the importance for the success of the evaluated engine[2]. The sensitivity analysis is reserved for Chapter 9
To summarise, the optimisation is tasked with finding the optimal engine configuration and finding the corresponding optimal trajectory settings. Both are separated in their own optimisation loops that are joined to form the overall performance trade-off model. The optimum ascent trajectory provides the data from which the performance can be extrapolated.

6.1.1. Problem description

In essence, the performance analysis is the optimisation of an ascent trajectory to delivering a payload of 15.000 kg to an orbit of 400 km. Even though it is easy to describe the goal of the optimisation, quantifying this to an optimisation is more challenging. To start with, an understanding of the optimal trajectory is established. This is best understood by treating the propellant as a currency, where propellant is spent to gain altitude, increase velocity, and overcome both gravity and drag losses. The more efficient the propellant is spent, the less is required, which reduces the M_0 (reversed snowball effect) or increases the payload capability. Hence, the first quantified problem can be derived, as illustrated in Problem Function 6.1.

$$\begin{aligned} \max_{\{\vec{\theta},\gamma(t),\dot{m}(t)\}} \quad & M_{prop,surplus} f(\vec{\theta},\gamma(t),\dot{m}(t)) \\ \text{s.t.} \quad & v_{\perp} = v_{target} \equiv \epsilon_{\perp} \geq abs(v_{\perp} - v_{target}) \\ & h = h_{target} \equiv \epsilon_h \geq abs(h - h_{target}) \end{aligned} \tag{6.1}$$

$\vec{\theta}, \gamma(\mathrm{t}), \dot{\mathrm{m}}(\mathrm{t})$ in problem 6.1 refers to the optimisation variables, defined in Section 6.1.2, Where ϵ is the error term and $\mathrm{h_{orbit}}$ and $\mathrm{v_{orbit}}$ refer to the target orbit altitude and corresponding orbital velocity.
Crucially, Problem Function 6.1 is not a single unified function. Furthermore, Problem Function 6.1 lacks any equation that directly relates to the aforementioned aspects that determine efficient propellant usage. Therefore, conditions are added that quantify the efficiency and minimise the losses. These loss conditions

[2] Design and/or sizing parameter that are highly influential to the performance of the engine are considered bottle neck parameters, and their achievability lies hand in hand with the viability of the respective engine.

are illustrated in Problem 6.2 where h_p refers to the altitude at the periapsis. Each conditions in Problem 6.2 relates to one of the spending aspects, where the first two minimise the altitude overshoot and the second two conditions each minimise the tangent and the normal velocity overshoots, while the combination of 1^{st} and 4^{th} relates to the gravity losses, and the 2^{nd} and 3^{th} relate to the aerodynamic losses.

$$\begin{aligned} \text{s.t.} \quad & \epsilon_h \geq abs(h - h_{target}) \\ & \epsilon_h \geq abs(h_p - h_{target}) \\ & \epsilon_{v,\perp} \geq abs(v_\perp - v_{target}) \\ & \epsilon_{v,\parallel} \geq abs(v_\parallel) \end{aligned} \tag{6.2}$$

However, most optimisation algorithms are unsuited resolve an constrained problem function. Therefore, the conditions are integrated into the maximisation function via the Lagrange multipliers, which subtract the condition multiplied by a weight from the maximisation function [52]. Since the weight values are problem specific and not determined by an exact science, they are derived through trial-and-error. As the altitude and tangent overshoot constrains are equivalent to the conditions posed in Problem 6.1, only those of Problem 6.2 are integrated.
Additionally, the maximisation function is turned into an minimisation function, as this is required by both the optimisation algorithm and the Lagrange multipliers. Furthermore, to better understand the relative weights, the conditions and function are normalised. Consequently, this results in the final problem 6.3, further referred to as the fitness function.

$$\min_{\vec{\theta},\gamma(t),\dot{m}(t)} w_{prop}\left(1 - \frac{M_{prop}}{M_{0,porp}}\right) + w_h \frac{|h - h_{target}|}{h_{target}} + w_p \frac{|h_p - h_{target}|}{|h_{target} - h_{p,0}|} + w_\perp \frac{|v_\perp - v_{target}|}{v_{target}} + w_\parallel \frac{v_\parallel}{v_{target}} \tag{6.3}$$

w_n are the respective Lagrange multiplier weights as discussed above. The optimisation prioritises the conditions with the relatively larger Lagrange multiplier, as it is more beneficial to reduce these to zero. The subtraction of $h_{p,0}$ in the denominator of the periapsis aspect is due to the fact that at t=0 $h_{per,0}$=~6300 km. With that, the problem has been quantified into Fitness function 6.3, which is the driving equation for the optimisation, and consequently for the performance trade-off too.

6.1.2. Definitions for the Performance Trade-Off

Before embarking on the detailed model and individual component descriptions, it is good to establish a few definitions and specification of certain wordings to prevent any misunderstanding and enhance readability. The definitions are listed below:

Selected Engine(s) : one or all of the Aerospike engine, Pulse Detonation Engine, and/or Precooled hybrid air-breathing rocket engine, identified in Chapter 4.
The performance trade-off : refers to the actual performance comparison between the selected engines and possible propellant pallets.
Model : Refers to both the complete code and overarching methodology used to simulate and obtain the performance of a selected engine with corresponding propellant pallets. The model consists of individual modules that operate together to form the model and perform the analysis.
Module : is defined by its particular task in the model and the overarching physical/scientific category that comes with that task. The distinction between overarching categories and sub-categories depended largely on the packages available and what their capabilities are. Each module forms it separate python class.
sub-module : are the same as modules. However, they have a significantly smaller operational task and singular interactive nature. Therefore, sub-module are integrated into the module class.
Function : A function is a sub-component of a module and is defined by a single transformation, a single set-up or aspect specification. Hence, they form the smallest task segment in the model. Each function is a python class function.

In addition, to the model descriptive definitions, distinctions are made between certain variables and parameters defined as follows:

Operation parameters Σ : Is the overarching category under which all parameters and variables required to simulate an ascent fall. It includes sizing, design and optimisation parameters and variables.
Optimisation variables : Are all variables optimised by the model, which include the sizing variables, burning settings, and trajectory settings

Optimisation parameters : Specify the optimisation operation e.g. population size, number of generation, precision, etc.
Trajectory (optimisation) variables $\vec{\gamma}$ & $t_{\vec{\gamma}}$: Are all specified angles and time interval that (partially) define the orientation of the ascent vehicle at a particular time instance. The Trajectory optimisation variables are optimised by the inner or trajectory optimisation loop.
Trajectory settings $\gamma(t)$: Are both the trajectory optimisation variables and the method with which the angle at all time instances is extrapolated.
Burning (optimisation) variables $\dot{m}$ & t_b : Are both the specified propellant mass rates and their corresponding burn time. The burn variables are optimised by the configuration or outer optimisation loop
Burning settings $\dot{m}(t)$: Are the burning variables combined with the method to extrapolate the fuel and oxidiser mass rates at each time instances.
Sizing parameters : Refers to any specified parameters that can be deliberately chosen when designing an engine or vehicle, which sizes or configures the engine or vehicle.
Sizing (optimisation) variables $\vec{\theta}$: Are all engine sizing parameters that are being optimised by the outer optimisation loop[3].
Design parameters : are rather achieved and in some sense performance specifications. These are efficiencies and effectiveness ratios and are the consequence of the design and the manufacturing. By definition design parameters cannot be chosen.

6.1.3. General Description of the Performance Trade-Off Model

As will be further elaborated in Section 6.2.2, the model is a multidisciplinary non-linear configuration and trajectory optimisation simulation, which aims to attain the ideal SSTO configuration for each selected engine. How the simulation is designed and operates to achieve this is described in this section. The inner workings are visually best understood by studying the code architecture, illustrated in Figure 6.1.

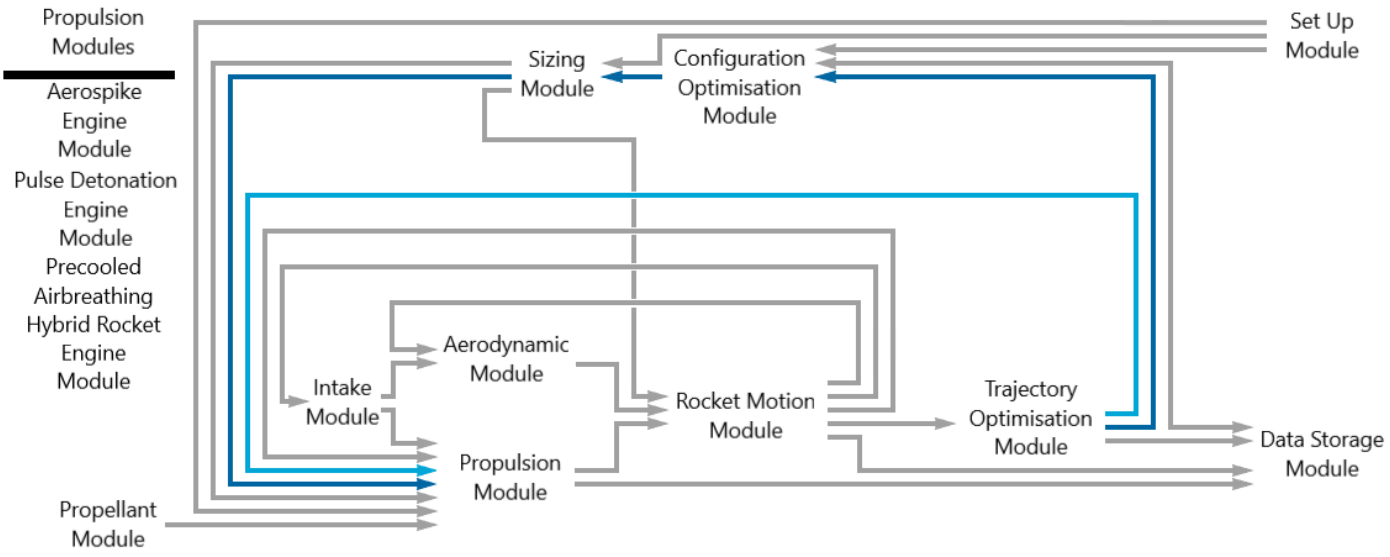

Figure 6.1: Illustrates the overall code diagram of the optimisation model, where the arrows illustrate the main data flow (grey), the inner (light blue), and outer (dark blue) optimisation loops.

General Model Overview
Evaluating the code architecture, the internal processes are best understood by dissecting the optimisation loops. The two optimisation loops are illustrated in Code architecture, Figure 6.1, by the dark and light blue arrows. with the dark blue arrows are the configuration optimisation loop, also referred to as the outer loop

[3]Technically, the mass rate is also an sizing variable. However, due to its significance it has been allocated to its own category, making it an exception.

and the light blue arrows being the trajectory optimisation loop, also referred to as the inner loop.
The inner loop is best understood starting from the trajectory optimisation module, which provides the control settings. The settings are used by the propulsion module (steering sub-module) to continuously provide the guidance and thrust direction for the rocket motion module, which in turn simulate the trajectory. The simulated data is provided back to the trajectory optimisation module, which extrapolated the fitness, thereby completing one iteration loop.
The outer loop is best identified by starting from the configuration optimisation module, which provides the burning settings and sizing variables to both the sizing and propulsion module. The sizing module provides the necessary vehicle specification to the rocket motion module to simulate an ascent trajectory. The burning settings and sizing variables, combined with the trajectory settings from the inner loop, complete the required operational parameters for propulsion module. just as in the inner loop, the propulsion module provides the thrust magnitude and guidance to the rocket motion module, it is here were the inner and outer loop overlap. After the trajectory optimisation module has found a sufficiently good trajectory for the given burning settings and sizing variables, the fitness and corresponding data is passed back to the configuration optimisation module, thus completing the outer loop.
The outer loop as the name suggests configures the vehicles, including the engine, which includes the sizing. Whereas the inner loop optimises the trajectory for the given configured vehicle. As such, every single outer loop iteration contains multiple inner loop iterations.

To resume, some modules are excluded from the above explanation, as their inclusion is not necessary to gain a general understanding of the model operations. How the excluded modules are interlinked and operate within the module is described in Section 6.1.4. A detailed explanation of the inner workings for each individual module can be found in Section 6.2.
Please beware that, for the sake of clarity, Figure 6.1 only contains the main data stream and module interactions. Hence, minor interactions are excluded.

Model Assumptions
With the model described, the conditions and/or assumptions to which the model is bound have not been defined yet. Hence, these are defined here.
The purpose of the model is to evaluate the performance of the selected engines in a realistic scenario on a consistent basis. Therefore, a definitive ascent trajectory and configuration do not need to be found, as this would be equivalent to designing the SSTO RLVs. From this premise all assumptions and model conditions are derived, which are discussed below.
Given that no actual trajectory is designed any orbit inclination and launch location can be chosen as long as they are kept consistent throughout the trade-off, an equatorial launch to an 0° inclination orbit is chosen. Consequently, the trajectory ascent becomes a 2D earth model.
Similarly, a point mass gravity model can be used, as the detail for J2-model is only needed for the definitive trajectory design. Therefore, it would have little benefit to the trade-off.
A flat earth model was considered, but given that the curvature of the earth is ~60 km for a flight of 800 km, equivalent to some of the smallest 1st stages, this is an unreasonable assumption. Therefore, unsurprisingly a spherical earth is used.
Additionally, Earths rotation, which provides ~ 460 m/s of initial orbital velocity, cannot be neglected as this translates to ~6% of a LEO DetlaV budget (9400 m/s).
Furthermore, weather effects like heavy wind, GNC errors, or other non-engine/vehicle related performance losses were considered to be of minor importance to this study. Such losses are accounted for by the propellant margin, set to 1% of the M_{prop} in this study.
All in all, the assumptions are believed to not favour any of the selected engines disproportionately. Furthermore, the assumptions are reasonable to still reflect a realistic scenario without complicating the module more than necessary. A visual diagram of the model is illustrated later in Figure 6.2.

6.1.4. Overview of the Individual Modules

The perceptive reader might question the heavy focus on modularization, which is a the result of a plug-and-play design philosophy. Each individual module is its own python class, with its own confined task/purpose. All classes are imported by the module highest in the module hierarchy, namely the configuration optimisation module, making it easy to swap or replaced modules, a feature required for the varying propulsion

modules. It is also preferable to first construct simplified modules because they can easily be replaced with more complex modules if this is required. The aerodynamic module is such an example where a simplistic module is implemented, which can be upgraded if more detail aerodynamics is required. Moreover, it allows future research to quite easily modify or replace individual modules, such that other aspects can be evaluated or optimised in greater detail. The model has the ultimate potential to be converted into a complete vehicle design tool. However, this would require extensive development and many iterations, which is not required for the current research question.

Module	Code Package	Output purpose
Set-Up Module	config file	Σ
Configuration optimisation module	Pygmo	$\vec{\sigma}, \dot{m}(t)$
Trajectory optimisation module	Pygmo	$\vec{\gamma}, \vec{t_\gamma}$
Rocket Motion	Tudatpy	Trajectory simulation
Intake Module	Custom	$\dot{m}_{intake}, p_{intake}, \rho_{intake}$
Aerodynamic Module	Custom	C_L, C_D
Propulsion Module	Cantera/ Custom	T, $\dot{m}(t)$,
Propellant Module	Cantera/ Custom	X_f, X_{ox}
Data Storage Module	Custom	Save all data
Sizing Module	Custom	M_0, M_{prop}
Steering Sub-module	Custom	$\gamma(t)$

Table 6.1: Provides the code package and the output parameters of each individual module.

An overview of all the modules is provided in Table 6.1. Additionally, Table 6.1 provides the program package used for each module. Even though, the code is constructed in Python 3.8 entirety, the major computations are done by the respective packages in the background. Hence the python packages are interaction tools between python and the actual programs, which utilise the more powerful C++ language. The particular programs are Tudatpy, Pymgo, and Cantera.
In addition to program driven modules, there are the custom-build modules and configuration files. The custom-build modules run all their computations in python, however are referenced to as custom in Table 6.1, as python is the base code for the entire model. Lastly, Table 6.1 provides the shortened output or purpose of all modules.

A step-by-step approach, starting from the set-up module following the outer and than inner loop, is used to describe the task of each individual module and their interactions with other models, illustrated with the arrows in Figure 6.1. Additionally, the minor interactions are discussed too.
To start with the set-up module. This provides the operational parameters for the engine and sizing module, while it provides the optimisation parameters for both optimisation modules. The set-up module is a configuration file which contains all the manual model inputs, resembling a look-up table.
Continuing with the configuration optimisation, which is tasked by providing each run with a set of sizing variables and a burning setting. After a population, set of runs, is completed the module is responsible for providing an improved set of sizing variables and burning settings. The combined set is passed to both the sizing module and the propulsion module.
The sizing module computes the initial vehicle mass and propellant mass. The dry mass without the engine mass is provided by the module itself whereas the engine mass is extrapolated from the maximum thrust provided by the propulsion module.
Before continuing with the propulsion module, lets discuss the propellant module. The propellant module is a library which contains the python instructions on how to create the selected propellant as a Cantera mix-

ture. which propellant type is used is specified in the setup module.
As the name suggest, the propulsion module provides the thrust magnitude and mass rate used for set thrust generation. Additionally, the Propulsion module contains the steering sub-module tasked with providing the flight path angle (γ), which together with the previous two attributes is passed to the rocket motion module. The thrust is assumed to be inline with the CG and in the direction of the vehicles orientation, hence via the γ the thrust direction is extrapolated.
The rocket motion contains all aspects necessary to simulate the trajectory. The module computes the aerodynamic and gravity force and the respective direction. Together with the propulsion module, they are iteratively used to propagate the ascent vehicle.
Backtracking, to the aerodynamic module, which in the current model is a pass-along for the constant aerodynamic coefficients, specified in the set-up module.
Next to the aerodynamic module is the intake module, which extracts the ambient conditions from Rocket motion module. The module is tasked with and contains all functions, such as cooling, ramming, compressing the air, before it enters the CC. The intake module is excluded from the module for any non-breathing engine, namely the Aerospike engine and PDE.
Continuing with the last module of the inner loop, namely the trajectory optimisation. As the name suggest this module optimises the trajectory, by optimising the trajectory settings passed to the propulsion module and utilised by the rocket motion module. After completing the specified amount of generations, the trajectory module passes the best fitness value to the configuration module, which represents the best possible performance of that particular configured vehicle. The vehicle is configured by the variables the configuration module generates. Hence, having discussed all modules except for the data module, the outer loop is completed.
From a methodology standpoint, the data module is irrelevant. However, it illustrates the issue of operating multiple programs that perform their computations in C++. Consequently, these programs have difficulty communicating especially when one wants to extrapolate data. Therefore, the data module is constructed, which is a custom code that extrapolates all relevant data from the individual modules, primarily the optimisation modules, Rocket motion module, and propulsion module.

6.2. Modules for the Performance Trade-Off Model

Each of the following subsections will contain a detailed description of a module in the performance trade-off model. The propulsion modules are the exceptions as these are discussed in Chapter 7. The module sections will discuss the motivation about the set-up choices, the chosen methodology, and how they are implemented into the code. The modules are the configuration and trajectory optimisation, The rocket motion, the sizing, and the aerodynamic module, in chronological order.

6.2.1. Configuration and Trajectory Optimisation Modules

Due the joint nature, the configuration optimisation and trajectory optimisation are discussed together, yet both are their separate modules. Prior to discussing the justification for a two loop optimisation architecture, the underlying optimisation processes are elaborated.

Optimisation Setup

Both optimisation are done using Pygmo, a C++ powered program [7]. The configuration optimisation module is tasked with optimising the $\{\vec{\theta}, \vec{m}. \vec{t}_{\mathrm{b}}\}$ variables, whereas the trajectory optimisation module is tasked with optimising $\{\vec{\gamma}, \vec{t}_{\gamma}\}$. Pygmo is the python interface for the scientific library PaGMO. PaGMO was developed by ESA to solve, among others, non-linear constrained astrodynamic problems. For the optimisation the Differential Evolution (DE) algorithm is used for both optimisation loops. As this is a single-objective unconstrained Heuristic Global Optimiser (HGO)[7], it is well suited to resolve the quantified problem type of posed in Section 6.1.1 [13]. Furthermore, it is the default algorithm used in collaboration with Tudatpy, which gives great confidence in model convergence.
The DE algorithm requires a population(minimal size of 5) from which to derive the pseudo derivatives for variables, and a specified number of generations to optimise over. For the inner loop 3 trajectory generation ($n_{\theta,\mathrm{gen}}$) with a population size ($n_{\theta,\mathrm{pop}}$) of 5 are found to be sufficient to extrapolate the potential of a single configuration. The population size ($n_{\dot{m},\mathrm{pop}}$) and number of generation ($n_{\dot{m},\mathrm{gen}}$) for the outer loop varied per

selected engine and are provided in Chapter 9.
The aware reader might wonder why no precision driven optimisation is used, which would force the model to optimise until an sufficiently optimal ascent trajectory is obtained. However, such method cannot be used, as it is not guaranteed that all selected engines with their corresponding propellant pallets are able to do so.

Two Loop Optimisation Architecture
In theory, a double loop optimisation offers no reduction in the number of iterations required to find the global optimum. While this holds true for independent variable problems, it is less valid for problems with codependent variables [52]. Hence, in practise a segregated loop set-up can offer a computational and convergence advantage. The isolated influence of a codependent variable on the problem function depends on the values of the variables it is codependent with. To simplify, an optimal steering set with a poor burning set, will produce a bad fit. As a result, the model associates the optimal steering variables with a poor fit, and thus diverges from the optimum.
By splitting the optimisation loop, the codependency issue is circumvented. The increased independence ensures convergence by the DE algorithm. Yet, codependency between the time stamps ($t_{\vec{\gamma}}$&$t_{\dot{m}}$) and the flight path angle ($\vec{\gamma}$) or mass rate ($\dot{m}$) variables remains. Yet, these codependencies are not severe enough to justify further segregation of the optimisation. However, this does have some consequences for the model output, as will be discussed in Section 9.1.1.

The configuration potential is sufficient for the aim of the model, as its goal is to find a realistic representation of the performance. Therefore, for a given configuration, it is more desirable to optimise the trajectory over a few generations, where the best fit is passed to the configuration loop (outer loop). The inner loop only needs to find a good indication for the potential, which requires far fewer iterations than the outer loop.
However, to guarantee that no large swaths of potential are excluded, a super optimisation loop is used after the joint optimisation. The super optimisation loop is the repetition of the inner loop for the best burning settings and corresponding sizing variables. The optimisation last until the performance gain is less than 0.5% and performance is equal or better that the joint optimisation.

It is essential that the model determines the potency in as few iterations as possible. The two loop set-up might appear sub-optimal, as even bad configurations go through multiple inner-loop generations. Whereas, this is true, the added benefit outweighs the added inefficiency. With the two-loop set-up each successive configuration generation is closer to the optimal configuration variables. Therefore an increasing number of good configurations occupy the population. Moreover, bad configuration variables will cause the ascent vehicle to crash regardless of the trajectory variables, preemptively terminating the run, which makes the inefficiency of many bad generations a lesser issue than it originally appears.

6.2.2. Rocket Motion Module

The rocket motion module is the most essential module for the performance trade-off, as it simulates the ascent of the vehicle from which the performance is extrapolated. Each simulation provides the final altitude, final vehicle mass (payload + dry mass + leftover propellant), and the states throughout the ascent. The methodology of the trajectory optimisations has been discussed in the previous Section 6.2.1.
In this section an explanation of the rocket motion module is provided, combined with an overview of the set-up. As was previously mentioned the rocket motion dynamics are done using the Tudatpy module. The first two subsection discusses the general model and Tudatpy package. The following three subsections discuss the simulation set-up. While, the last subsection discusses how the simulation is terminated.

General Module
The rocket motion module combines the three forces acting on the vehicle, which are the thrust, gravity and the aerodynamic forces. Tudat uses these forces to propagate the state of the ascent vehicle, as the forces induce an acceleration, which results in velocities, which in turn drive the motion. By the *principle of solidification* [21], the states are iteratively updated throughout the ascent as instantaneous rigid bodies with constant mass. Note that the state refers to both the position and velocity of the ascent vehicle.

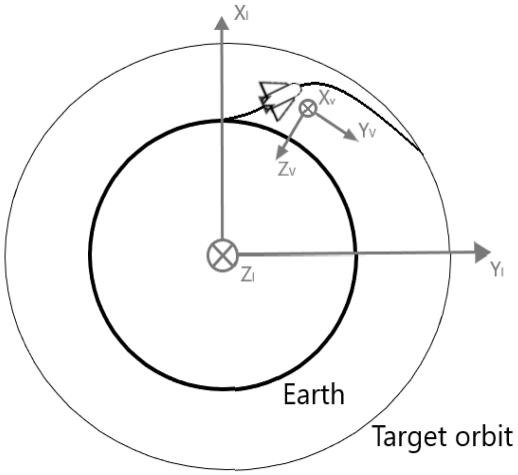

Figure 6.2: Illustrates a visual diagram of the optimisation model, viewed from the south as this ensures the rotation is in the clockwise direction.

However, to update the state, the instantaneous vehicle orientation and force directions direction are required. To achieve this Tudat takes all of the aforementioned forces, which are in their respective reference frames, and translates these to the specified coordinate system. It is in the specified coordinate system that the propagation is done. The translation in this model is illustrated in Figure 6.2, in which the vehicles orientation is specified in the vertical body reference frame and translated to the specified coordinate system, namely the Inertial Earth reference frame, all the reference frames can be found in Appendix A.1.
As was previously mentioned the trajectory optimisation is a 2D motion problem. However, by nature Tudat is a 3D program. Therefore all motions are restricted to the equatorial plane, as is illustrated in Figure 6.2.
With a basic understanding of the rocket motion provided, the need for the rocket motion can be argued. Most obviously, the output data is required to evaluate the fitness, defined in Equation 6.3. Additionally, the feasibility of the trajectory can be evaluated from the flight data. Furthermore, engine operation data is obtained through ascent simulation, which is a very good proxy for the real operations. It is this engine data that forms the bases of the analysis, which is evaluated in Chapter 9. Even though adding all output data to the appendixes is impossible, a list of the optimisation variables is given in Appendix H.

Tudatpy Program
All rocket motion calculations are done via the Tudatpy package, which translates the python inputs to Tudat. Tudat is a C++ simulation program developed by TU Delft, which is capable of simulating any astronomic motion in the solar system. To provide an impression on how Tudat operates a top level code diagram is provided in Figure 6.3. To elaborate, Tudat operates with a dynamic simulator, which is like an instruction manual for Tudat on how and which objects to propagate. Hence, it is from the dynamic simulator that the trajectory data is obtained, illustrated with the "state & dependent variable history" output in Figure 6.3. In turn, the dynamic simulator is configured with three inputs, namely the environment set-up, propagator set-up, and the integrator set-up. With inputs defined and integrated the simulation can be initiated and an output is generated. Each of the inputs is discussed in more detailed further on in the section.
The class contains all required functions to set-up the inputs and create the dynamic simulator. Furthermore, it contains functions to run the trajectory simulation, plot and label the output variables, and the trajectory optimisation problem. The latter is used by both optimisation problems. As discussed in Section 6.2.1, the functions can be divided in three categories: add, set, and get, each with a distinct interaction. the add functions are used to 'add' or replace output variables. the 'set' functions are used to provide used to set the conditions of the dynamic simulator, which include the masses, propulsion and aerodynamic forces. The 'get' functions are used to extract the inputs, simulator, optimisation problem, or output variables.

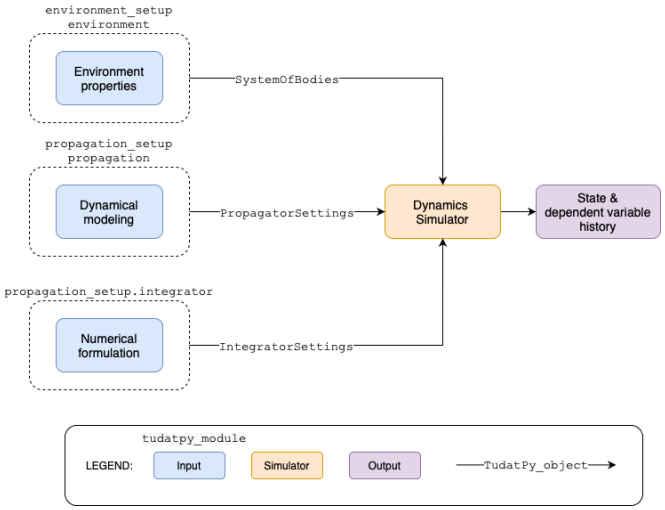

Figure 6.3: Figure illustrates a top level code diagram of the Tudat code set-up.

Environment Setup

As the name suggests the environment set-up defines in which environment the simulation is done. Hence, all objects, reference frame, initial state, atmospheres and time are defined. The objects include the celestial bodies (Earth) and the propagated objects (ascent vehicle). All bodies except for the earth are neglected, However this is editable in the set-up module. Earth is integrated with the default Tudat settings. For the ascent vehicle, the mass and initial state must be defined. As such, for each configuration iteration (outer loop iteration) the mass is updated via the sizing module, which also provides the propellant and cutoff mass.
Additionally, the atmospheric interactions between the celestial bodies and propagated object are activated in the environment set-up. The standard built in earth atmosphere is used.
The initial position of the ascent vehicle is set on the earth's surface in the equatorial plane on the Y_C-axis, the resulting coordinates are $[r_{earth}, 0, 0]$. The initial location can be edited thought the function *add_initial_state*. However, if the vehicle is not placed at the equator, additional alternations to the Steering sub-module are required. In addition, the coordinate system is defined. Evidently Earth is taken as the origin, with an Earth-centred, Earth-fixed reference frame, see Appendix A.1.

Propagator Set-up

The propagator instructs Tudat which objects have to be propagated, what dynamics drive the propagation, and how to compute the dynamics . The dynamics include the aforementioned forces, namely the gravity, the thrust and the aerodynamic forces. The latter includes lift and drag. However, it includes any other dynamic aspect too, like the decreasing vehicle mass.
To start with the forces, Tudat computes the magnitude and direction of each force in their respective reference frames. Tudat translates the forces to the specified coordinate system, with which the total induced force is obtained. The same procedure is performed for induced moments.
As mentioned before, the celestial induced gravity forces are simulated as point masses, as this is sufficient for a performance analysis. The magnitude and directional of the gravity forces is computed by Tudat internally, unlike the aerodynamic and thrust forces.
It is through the propagator that both the aerodynamic and propulsion modules are interlinked with the rocket motion module, which is done by the *set_aerodynamic_model* and *set_thrust_model* functions.
The aerodynamic force is computed in the aerodynamic frame. Tudat requires the aerodynamic coefficients and reference area to compute the magnitude of the lift, drag and side lift. The coefficients are defined in the same Aerodynamic frame, and are provided by the aerodynamic module, see section 6.2.5.
The Thrust is defined in the vertical body reference frame, where the magnitude is provided by the propulsion module and the direction in the vertical body reference frame is provided by the steering sub-module.
Lastly, the ejected mass rate has to be included in the propagator, which is again provided by the propulsion module.
The perceptive reader may have realised, that a new dynamic simulator is required for a different engine or vehicle configuration, which means that for each iteration of the outer loop a new dynamic simulator is created.

Integrator Set-up
Whereas the propagator instructs what drives the propagation, the integrator instructs how to propagate the state. the integrator is constructed within one function, namely *get_integrator_settings*. The Rung-Kutta 4 (RK4) is selected as the integrator method, which relies on a constant time step (dt) to evolve the vehicle state. Other more complex methods (higher order or variable step size) are investigated, but negligible effect the outputs. It is believed that the truncation errors are too insignificant to form a significant factor over the relative short duration of the ascent. Moreover, the inaccuracy in the optimised mass rates ($\dot{m}$) are of greater effect. Therefore, RK4 is found sufficiently accurate and requires relatively low computational effort [15]. The latter is required as the combined optimisation requires anywhere from a few 1000 ascent simulations, were each instance is evaluated 2 to 4 times because of RK4.
dt is by default set to 1 s, but this is changeable in the set-up module. The integrator has to be changed in the rocket motion module, but requires minimal effort.

Termination Conditions and Orbit Reached Conditions
Even though the termination conditions are technically part of the propagator set-up, they form an essential part of the model. If the termination conditions are too restrictive the model may not be able to converge, whereas if they are too flexible they will prolong simulation time reducing the optimisation efficiency. Therefore, the following termination conditions were set: a max ascent time of 4000 s, a minimal altitude of -100 m[4], a minimal mass dependent on the dry and wet mass, and an orbit reached condition.
The latter is a custom function in which the vehicle needs to be above the target altitude (h_{target}) with corresponding target orbital velocity (v_{target}). The instantaneous orbital velocity is computed via Equation 6.4.

$$v_{\perp} = \| \vec{v} - \frac{\vec{v} \cdot \vec{r}}{\vec{r} \cdot \vec{r}} \vec{r} \| \tag{6.4}$$

As an individual might have noticed that Equation 6.5 is not necessarily a reflection of an actual orbit. In other words, the condition does not purely present an actual sustainable orbit, due to the exclusion of the normal velocity. The exact implications for the performance model are discussed in Section 9.1.1. However, as argued here, it is not useless in evaluating the orbital capabilities.

$$\begin{aligned} &Orbit\ is\ True: \\ &\quad if\ h_t \geq h_{target} \\ &\qquad v_{\perp} \geq v_{\perp,target} \end{aligned} \tag{6.5}$$

The quasi-orbit conditions is utilised as it achieves its purpose, yet provides some key advantageous over more constraining conditions. As stated, the purpose to the model is to evaluate the performance of the selected engines. Which includes the evaluation whether a particular configuration is able to reach orbit, to this end the condition suffices. To elaborate, if the quasi-orbit condition is met with negligible normal velocity an actual orbit is achieved. Whereas, if the conditions are met with a large overshoot in normal velocity, actual orbit might not be achieved. In such instance the configuration is capable of achieving actual orbit, as it merely spend to much DetlaV on reaching the h_{target}.
Note that an undershoot, the conditions are met with a negative normal velocity, cannot occur as this is always preceded by an overshoot, which stops the ascent simulation.
Therefore, the quasi-orbit method is a better method to evaluate orbit capabilities of engine configurations. More over, faster single run completion is achieved using quasi-orbit. Stopping the run early, at quasi orbit, is not an issue as a better fit cannot be achieved, see Problem Function 6.3. Only the next iteration with a faster pitch or a reduced normal burn can increase the fit. Additionally, fewer generations are necessary for the model to converge to a consistently reach orbit.
As a final remark, the level of overshoot (or undershoot) can be minimised via the Lagrange multiplier $w_{\|}$, as described in Section 6.1.1.
Furthermore, an orbit condition based on the Tudatpy provided periapsis was considered. However, the periapsis is not an accurate depiction of the altitude at periapsis and is not inline with the required orbital capabilities. Therefore, periapsis based orbit conditions were dismissed.

[4] Using a value of 0 m would prematurely terminate the simulation even if sufficient thrust is generated.

6.2.3. Steering Sub-Module

The GNC generally ensures, with all available means, that the vehicle is heading to the predetermined control state. However, Tudatpy only requires the instantaneous moments and directional forces, for which only the vehicle orientation is relevant. Therefore, a detailed GNC that obtains the desired orientation with adjustment by the aerodynamic devices and thrusters is excluded. Such minor adjustments are only relevant for trajectory finalisation and redundant for a trajectory evaluation. The γ normally follows from the GNC inputs, but because the development of an SSTO GNC is outside the scope of this study, perfect control is assumed. Which implies that the vehicle at any instant can overcome any force or moment to achieve the ideal orientation. Note that in a 2D model the orientation is specified by a single control angle, which in this thesis is the flight path angle γ. How the flight path angle orients the thrust is illustrated in Figure 6.4. The remaining forces gravity and drag are orientated towards the centre of the earth and opposite to the airspeed, respectively. Lift, as is described in section 6.2.5, is excluded from this thesis.

Perfect control should not affect the conclusions validity, if the obtained trajectory is realistically achievable. A realistic trajectory is one that is absent of manoeuvres outside the physical or engineering capabilities of any GNC system e.g. heading changes of $d\gamma > 14°$ at $M > 5$ [47].
Given that in the current version only the thrust requires the vehicles orientation and the fact that the model is not a dedicated GNC module, it was made a sub-module in the Propulsion Module, under the parent class. However, just as regular modules, the sub-module is easily replaced by a dedicated GNC Module. This would only be required in the presence of a detailed aerodynamic module.

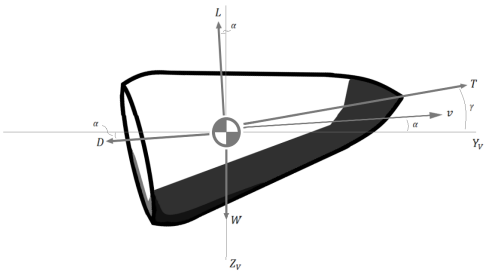

Figure 6.4: A smaller version of Figure 3.7, which illustrates the orientation of the vehicle w.r.t. γ and α in the vertical body reference frame, elaborated in Appendix A.1.

Steering of the Flight Path Angle
It is impossible to specify the angle at each instance, as it would result in an infinite set of variables, which would cause dimensionality and is impossible to solve. To prevent dimensionality an additional variable is introduced, namely time intervals ($t_{\gamma,n}$), hence creating trajectory nodes. A trajectory node is a defined γ_n at time interval $t_{\gamma,n}$. To obtain the instantaneous γ ($\gamma(t)$) the built in cubic spline interpolator of Tudatpy is used. The cubic spline interpolator provides a smooth transition between two specified angles. Although other interpolator have been considered the cubic spline is chosen as it is relatively easy to define, yet offers detailed characterising capabilities.
each individual γ_n and intervals $t_{\gamma,n}$ are variable to ensure the greatest flexibility in the optimisation space. An variable $t_{\gamma,n}$ allows the model to increase the node density at phases where greater γ control is required, while the density can be reduced for phases with minimal manoeuvring.

Implementation
To elaborate, the number of nodes is defined by the amount of γ_n's, which is specified in the set-up module and is therefore changeable. However, the number of $t_{\gamma,n}$ is specified separately, as such the number of $t_{\gamma,n}$ variables can be below the number of nodes. Hence, nodes can share the same t_γ, yet cannot share the same γ. Such approach simplifies the trajectory optimisation and thus improves efficiency (less optimisation variables), when higher levels of complexity are unnecessary. Both the number of γ_n and $t_{\gamma,n}$ are tailored to achieve the highest potential performance, while still ensuring a reasonable convergence time. The number of nodes and how many variables are allocated to each node will vary per engine and are specified in Chapter 9.

6.2.4. Ascent Vehicle Sizing Module

The sizing of SSTO RLV, or any ascent vehicle for that matter, is not an optimisation problem but rather a consequence of the optimisation parameters (design choices). As such, the sizing is derived from the optimisation of (sub-)systems, which in this thesis is limited to the propulsion system. Therefore, the sizing can be

seen as separated in two successive tasks, namely the engine sizing and the overall vehicle sizing.
Even though the sizing in system engineering refers to both the mass profile and configuration of the vehicle, for the purposes of this thesis the sizing module will primarily focus on the mass budget. The configuration aspects for which only the shape is relevant are discussed in Section 6.2.5, the aerodynamic module.

Sizing of the Engines
Engine sizing on a performance level is done by means of the T/W ratio with the next step being the engine design itself. This would provide a more accurate mass of each component. However, as the aim of this thesis is to identify the engine that is most worth pursuing, designing the engines would defeat that purpose. Therefore, the engine is sized via the T/W method.
To size the engine two parameters need to be identified. They are the reference thrust T and the thrust-to-weight ratio T/W. The thrust can be computed at any altitude given that the sizing and burning parameters are provided. These optimisation parameters encompass the $\dot{m}(t)$, F/O, $F/O_{breathing}$, and ϵ. The thrust computation is described in Chapter 7, for now it is only relevant to know that for a set of optimisation parameters a thrust can be computed.
The T/W ratio stipulates which thrust measure has to be taken as the reference thrust. The T/W ratio is measured by dividing the maximum possible thrust at sea level (SL) an engine can produce divided by the dry mass multiplied with g_0. Hence, in the performance model it is the thrust at sea level with $\max(\dot{m}(t))$. This implies that even if the real $\dot{m}$ at SL is lower than the maximum $\dot{m}$, the latter is still used to compute the reference thrust at SL. For the hybrid engine two thrust levels are computed, with which the maximum is used as the reference thrust. The first reference thrust is computed for the pure rocket phase with $\max(\dot{m}(t))$. The second reference thrust is computed for the breathing phase with $\max(\dot{m}(t)) : t < 100s$ and an intake velocity at 100 m/s, which is the minimal airflow velocity due the compressor suction [59].
Which leaves the identification of the T/W ratio. Usually, the T/W is extrapolated from historic engines with the same propellant pallet. However, as one might expect this thesis deals with unusual engines. Therefore, historic T/W ratios from conventional engines with similar propellant pallets as the ones selected in Chapter 5 are not representative values of the selected engine. Moreover, some of these ratios date back decades and are not an inaccurate representation of the current technology levels.
However, the historic T/W can serve as an indication for the actual T/W ratio. Table 6.2 the T/W ratio of engines that are identified as most representative to the respective propellant pallet. The engines chosen for Table 6.2 include engines that have at least had a full scale hot ground test. Hence, theoretical T/W ratios of the papers [75][76][65], are excluded.

Engine	Propellant pallet	T/W_{SL} ratio	P_{cc} [bar]	development period
SSME/RS-25	LH2/LOX	73.1	206.4	1970-1980
XRS-2200	LH2/LOX	80	58	1990-2000
NK-33	RP-1/LOX	137	148.3	1960-1970
Merlin D	RP-1/LOX	176	97	2005-2015
Raptor	LCH4/LOX	200[5]	300	2015-2022+

Table 6.2: Provides the propellant pallet, Thrust-to-Weight ratio, P_{cc}, and the decennial over which the engine was developed.

Table 6.2 hints at 3 interesting trends. The first two are rather obvious, namely that the T/W increases for increasing P_{cc} and T/W increases as the years progress. The increase with P_{cc} follows logically from relations 5.1 and 5.3, which illustrate that a higher P_{cc} results in a higher velocity.
However, to understand why the pressure is closely related to the second trend. As previously mentioned, the limiting factor for the P_{cc} are the tubro-pumps. As turbo-pumps are developed and utilised in many other fields, it can be concluded that rocket engines use many carried over technologies from other fields. This is further evidenced by the fact that all engines were developed by vastly and sometimes previously inexperienced organisations. Hence, the performance (T/W ratio) of rocket engines increases with the general technology development trend.
Compensating for the discussed patterns, it appears that cryogenic propellants have a reduced T/W compared to none cryogenic propellants[5]. Even though this pattern is not as evident as the previous patterns, it

[5] Note that the raptor engine is still being developed, the test flown prototypes had a T/W ratio of 140.

can logically be explained by the added complexity, due to prevention sloshing due to phase changes in the cryogenic flow [45][6]. The increased complexity of the turbo-pump translates to a higher engine mass. Additionally, non-cryogenic LHC engines are powered by the less heavy GG power cycle, as discussed in 5.1.3.
As no definitive T/W value can be found for any of the selected engines, three values will be considered for the performance trade-off model. These values are chosen to account for the above pattern, while still giving enough flexibility to derive an adequate conclusion. The first value of 200 is equivalent to current conventional engines. Given that it is unlikely that a prototype for the selected engine will exist before 2025, technology might have advanced far enough to make this value attainable for the selected engines. The second value is the lower estimate, namely 100. Which is equivalent to the XRS-2200 if one accounts for minor technological improvements. Additionally, it is inline with the overall T/W ratio estimated for the hybrid engine in [75]. Lastly, the mid value of 150 is chosen, which is roughly the average of Table 6.2.
Introducing the T/W ratios as presented above makes the conclusion a conditional one. Therefore the findings of this thesis are exposed to the achievability of these T/W ratios. It will only be during the design phase that an accurate T/W values is obtained. If the value is found to be below the initial value to reach a satisfactory performance, then the engine is not a viable option for a foreseeable SSTO RLV.

Sizing of the Ascent Vehicle
Sizing of the ascent vehicle is rather straightforward, as it will be largely derived from Falcon 9. As a detailed and fully flexible SSTO RLV sizing module can be a thesis on its own, it is beyond the scope of this thesis. However, the Module is developed such that a sizing module can easily be implemented. All that needs to be replaced is the ascent vehicle sizing function, named *configure_ascent_vehicle*.
Next to Falcon 9 other reference vehicles were considered, namely the McDouglas, X-33 venture star, and Lazarus [84]. However, all are deemed unsuitable due the following reasons. Firstly, all designs are outdated and do not represent the current technology level. Secondly, none have reached the phase of a full-sized ascent vehicle, with Lazarus remaining in the conceptual phase. Therefore, using these sizing methods introduce additional assumptions, constraining the extent of the conclusion. Thirdly, some of these vehicles require very specific SSTO implementations. Besides the additional sizing complexity, caused by the aerodynamics, the specifications go against the findings in 3. All of the above arguments, not even mentioning the absence of detailed mass budgets, make it impossible to derive any meaningful sizing module form these vehicles.
On the other hand, Falcon 9 has actually been flow, is build with the newest technologies, and for which a detailed mass budget is available in [3] and [51]. The mass budget is provided in Table 6.3. More over, using the mass budget of Falcon 9 implies that all other systems of the ascent vehicle are technologically equivalent to the Falcon 9. As such, by definition the ascent vehicle considered in the performance trade-off is achievable within a reasonable development time frame. Moreover, Falcon 9 is a TSTO PRLV with a fully reusable 1st stage. Therefore, all systems are designed to be reusable and sized accordingly.

Mass Budget Falcon 9	Mass [kg]
Total mass	549054
1st stage	
Propellant mass	395700
Empty mass	25600
Empty mass without the engines	21370
2nd stage	
Propellant mass	92670
Empty mass	3900
Empty mass without the engine	3530
Other	
Total engine mass	4700
Fairing mass	1564
Payload mass GTO	4020

Table 6.3: Contains the mass budget of the Falcon 9 Rocket, taken from [51] and [70].

Note that Table 6.3 specifically provides the engine mass rather than the total propulsion system mass. However, the engine mass does include the actuators and hydraulics. The base mass (26,364 kg[7]) of the ascent vehicle is then derived by adding the propellant mass and empty mass without the engines of both stages, with the addition of the fairing mass to account for the TPS. The total mass is than derived by

[6] How much added mass results from cryogenic turbo-pumps or whether these penalties have been mitigated by technological advances is not further explored in this thesis.
[7] Which is remarkably close to the Lazarus [84] vehicle and X-33.

adding the payload (15,000 kg) and engine mass ((T/W_{SL})) to the base mass.
The mass percentage of the engine mass is close to what would be expected for an SSTO, namely 13-15% [84][65], further supporting the use of the Falcon 9 Budget. Additionally, the mass budget of Falcon 9 contains a landing gear and complementary landing systems to make the vehicle reusable. Even though, the landing gear is only designed for the 1st stage, it is expected that the propellant reserves and margins of the 1st stage are substantial and surpass the mass of the empty 2nd stage mass.
While it is true that the Falcon 9 lacks the lifting devices and TPS more typically seen on an SSTO RLV, this is less severe than it might appear. The lifting devices are not considered in this thesis, as described in Section 6.2.5. Hence, it is only reasonable to exclude the mass of these system (up to 10% of total mass[84]).
The same cannot be said about the TPS, given the reusability requirement. However, using the mass budget of a TSTO for an SSTO does neglect the benefit of having one set of systems. That is to say that that an SSTO has more mass synergies, which reduces the overall total system mass. Therefore, the mass budget lacks the TPS mass, but overestimates the mass of all other systems. With the addition of the faring mass, it is believed that this accounts for the missing TPS mass. What's more, the performance of a lower T/W can be taken into account for the underestimated TPS mass, and vice versa. Note that the TPS relies on the lifting characteristics of the vehicle and whether bleeding or ablation is utilised.
Other ascent vehicles might exist that are better representations than Falcon 9. However, during the research of this thesis no vehicles could be identified that did not suffer from the same issues as those presented for McDouglas, Venture Star and Lazarus.

6.2.5. Aerodynamic module

Whereas it is certain that the ascent vehicle will have a lift coefficient (C_L) to manage the peak heat during ascent, as described in Section 3.8, it is unclear to what extend a lifting ascent trajectory (relative high C_L) is and can be utilised. Moreover, how the C_L, whether through a lifting body, a centre of mass offset or other lifting devices, is achieved is beyond the scope of this thesis and would condition the conclusion too.
As mentioned in Section 3.8, utilising a lifting trajectory can reduce the required DeltaV or equivalent increase the paylaod [73]. Understanding the influence on the performance of these aerodynamic effects would not only require extensive vehicle design, which could encompass a whole thesis on its own, it would restrict the findings of this thesis to set vehicle design. For the X-33 ~450 kg of additional payload could be taken on a 28,600 kg dry mass and a 129,000 kg wet mass, which is marginal compared to the engine performance gains analysed in this thesis. Such analysis would add great complexity to the already extensive performance analysis of the selected engines, with probably marginal effect on the trajectory. Furthermore, the added complexity is only relevant in the lower atmosphere (<20km) after which the influence of the aerodynamic forces drop significantly.

Note that the marginal effect is not due to the lack of the lifting trajectories potential, but rather due the limitations posed in Section 3. Utilising a lifting body to full extend as proposed by [84][66][55], would require an almost spaceplane vehicle generating high L/D across all sonic regimes. Such a vehicle was deemed too expensive and too technological advanced to be developed by the private market in the foreseeable future, see Section 3. Furthermore, vehicles utilising these lifting trajectories often did so, to benefit of because of the breathing propulsion system (e.g. ramjets).

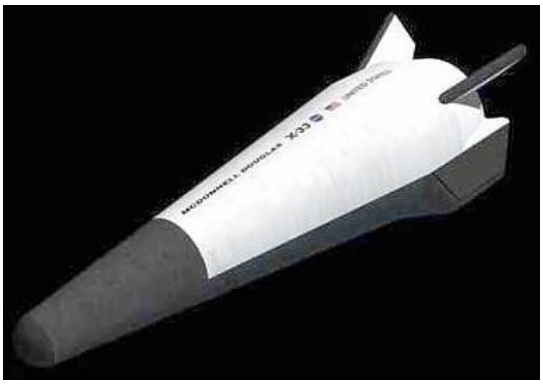

Figure 6.5: Illustrates what the McDouglass would have looked like if it had been selected for the X-33 tender.

Therefore, this thesis assumes a more conventional shape for the ascent vehicle, like the McDougals illustrated in Figure 6.5. Such vehicles have a L/D value more in the range of the X-33, namely 1.35 [73]. For the above reasons, the aerodynamic module is restricted to the standard Tudatpy Module (*aerodynamic_coefficients.constants*), The Tudatpy module specifies constant aerodynamic coefficients, for which only the C_D is defined (symmetric body). From the coefficients the aerodynamic forces are computed. In addition to the C_D a reference area A_{ref} is specified. C_D

is set to 0.25 representative to that of the Delta Clipper [37] and A_{ref} is set to 100 m^2, both are in line with the values presented in [73].
The above approach gives an advantage to the hybrid engine, which can be derived from Equations 3.5 and 3.6. The hyrbid engine has a less severe constrain to overcome, especially with the inlet drag $c_{D_{inlet}}$ being neglected. The advantage is evaluated in the C_D sensitivity analysis in Chapter 9.
In reality, the lift coefficients are a function of the angle of attack and Mach number. Future research can either derive these relations on its own or extract them from look-up tables as the one presented in [47] (pag. 80). Due to the modularity of the model, the aerodynamic model can easily be replaced, with little alterations to the overall code.

7

Performance Analysis Methods for the Selected Engines

This Chapter aims to answer the question *how to simulate the performance of the selected engines,* with the selected engines being the Aerospike engine, The PDE, and the hybrid engine [1]. The methods presented, as suggested by the question, are performance analysis rather than detailed engine simulation. Each engine follows a standardised and modularized simulation approach, which ensures trade-off consistency. Additionally, this chapter will elaborate and argue on engine design choices. The impact of these choices is briefly discussed too, where necessary these choices are further evaluated in Chapter 9.
The validation and verification of the methodologies presented in this chapter are done in Chapter 8.
The chapter will follow the structure by first providing the general simulation and methodology set-up, followed by an overview of the fundamental assumptions and consequential equations. Once the general approach has been established, the chapter will provide the simulation methodologies of all the selected engines. The general approach refers to the simulation methodology of a conventional engine, which forms the basic building block for all the other engines. Each propulsion module is dividend in transitions, in section 6.1.2 referred to a function, which are all discussed individually. Also, the limitations of each methods are discussed.

7.1. General Engine Simulation Approach

As previously described in Section 6.2, the overall model consists of many segregated modules, and so does the propulsion module. How these modules are structured is described in this section. By adding, configuring or removing individual propulsion modules, all three engines can be simulated. In addition, this chapter provides an overview of the assumptions made throughout the propulsion module. Lastly, the section provides the simulation of the conventional engine, which transitions serve as the base blocks for the other engines.

7.1.1. Transitions and stations

As described, the propulsion module consist of many individual modules. To structure these modules the aero engine number convection is used as presented in [59], see Appendix A.2. Although this is uncommon for rocket engines, it offers greater clarity when dealing with complex engines. Using this convention, each module can best be seen as a transition between engine stations, where each stations number specifies a location in the engine. All stations used in this theses are illustrated in Figure 7.1.
Note that the engine in Figure 7.1 differs from the hybrid engine. The single digits in Figure 7.1 are specified by convention.The specifications for the single digits that are relevant for this thesis are; 1.) Inlet interface, 2.) First compressor inlet, 3.) Last Compressor exit, 4.) Burner exit, 8.) Nozzle throat, 9.) Nozzle exit. The order is in the direction of the mass flow through the engine. The notation a or 0 often denotes the ambient conditions.

[1] Formally known as the precooled hybrid airbreathing rocket engine, yet for reasons of simplicity referred to as the hybrid engine

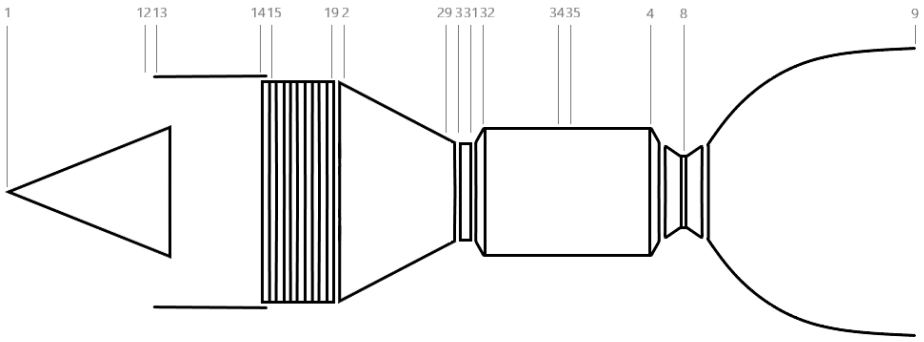

Figure 7.1: Illustrates the total number convection used in this thesis to refer to certain aspects or transitions in the an particular engine, as is by the convention presented in [59]

The double digits will follow the convention of [59] where possible. However, there were no specification exits, double digits are added to suite the applications in this thesis, which is more often the case for double digits.
Each transition thus forms its own block and deals with the mass flow from the previous station to the next. The engine specific transitions are discussed at the respective engine sections. General transitions are described in Section 7.2.2. All transitions contained in this thesis and their corresponding stations numbers are stated below.

1 -> 12	: Ram Intake
13 -> 14	: Intake
15 -> 19	: Precooler
2 -> 29	: High Pressure Compressor (HPC)
3 -> 31	: Injector
32 -> 34	: Combustion Chamber/Detonation Chamber
35 -> 4	: Wave Tube
4 -> 8	: Throat
4/8 -> 9	: Nozzle

The transition for the nozzle can be computed from station 4 or 8, depending on which method is used. In this thesis two methods were explored. Note that throughout this thesis 9 & e and 8 & t are used interchangeably, as both refer to the exit plane and throat, respectively.

7.1.2. Simulation Aspects and Overall Assumptions

As previously stated, the aim of this study is to compare the representative performance and capabilities of the selected engines. Therefore, a detailed and complex design simulation, like a CFD is unnecessary. Instead, the flow dynamics and thermodynamics are used to obtain a good initial performance estimate.
To use analytically driven methods, assumptions need to be made. The overall assumptions applicable to all engines are discussed below.

Adiabatic Flow
This assumption should not be confused with adiabatic combustion, which implies adiabatic flame temperature. Rather, it deals with the transfer of heat from the flow to the engine walls. Even though this might be unrealistic at a first glance, the fact that the flow is only in the engine for milliseconds and the formation isolating boundary layer at the engine walls make it a good approximation of reality [85].

Transitional Isotropic Flow
Isotropic flow is assumed throughout the transitions, with two exceptions, namely the combustion processes and compression shocks. Even though the flow is not inviscid, a boundary layer will quickly form, for which

the heat transfer and friction forces between the flow are minimal [9]. Therefore, isotropic flow can be seen as a reasonable assumption. Furthermore, multiple studies have used the assumption of isentropic flow to obtain performance analysis [85], [14], [24], and [59] to name a few.

Transitional Calorically Perfect Gas
Unlike the previous assumptions, this assumption is only kept throughout a single transition. A caloric gas has a constant specific heat ratio, whereas a perfect gas abides the perfect gas law (see Equation 7.1). These two assumptions are realistic if the species remain relatively constant and the temperature does not deviate too much. This is the case for an individual transition, but for multiple transition the deviation is to significant to ignore.

$$P = \rho RT \tag{7.1}$$

Steady State
For both the Hybrid and Aerospike engine steady state conditions can be assumed, implying constant equilibrium flow. Thus, the assumption states that flow or combustion fluctuation in the engine can be neglected, which from a performance level point of view is irrelevant. Furthermore, engines are optimised to minimise these fluctuations and often designed to return to stable states.
Obviously, for the PDE steady state cannot be assumed as the mass flow is unsteady, which makes it a mass tracking problem rather than the fixed volume tracking system.

Ignition System
Next to the assumptions additional simulation simplifications were made. These simplifications deal with the ignition and power cycle.
The ignition mechanism is outside the scope of this thesis and is more relevant when designing the engine. Additionally, simulating ignition adds little value in understanding the performance potential of the selected engines. Ignition is therefore achieved by setting the initial temperature of the combustion chamber at the self ignition point (1600 K) of the fuels and having it reach equilibrium. It was found that the initial temperature had negligible effects on the T_{cc}, given that it does not approach the equilibrium T_{cc}.
That being said, three ignition techniques were identified that are believed to be most suitable for an SSTO engine, as they have to prevent a hard-start and be able to have multiple operation cycles. These techniques are spark ignition, arc ignition, or hypergolic ignition. Ignition can be done in the CC or in a separate ignition chamber that can be sealed off to preserve the system. Plasma and laser ignition were looked at but are still in development phases at the time of writing.

Power Cycle and Plumbing
The plumbing and hence the power cycle of rocket engines is one of the most challenging aspects, as it is responsible for the cooling and the injector pressure. The latter being the limiting performance factor for conventional engines. The plumbing deals with the turbo-pumps, turbines, and preburners. As is described in Section 4.2.2, next generation rocket engines will operate a Full-Flow Staged Combustion power cycle. However, although simulating the power cycle is more relevant when designing the engine, it is of little value to the overall performance simulation. Therefore heat transfers between varying flows and pre-combustion is replaced by a fixed injector temperature of 500 K. This value was found by testing lean and rich combustion in Cantera for varying added heat from the cooling system. As will be illustrated later this seems to be in line with real world examples. Furthermore, injector temperature had minimum effect on the final T_{cc}.

7.1.3. Fundamental Thermodynamics and Fluid Dynamics For Rocket Engines

With the Assumptions specified and the simulation aspects defined, the engine can be seen as a unidirectional flow system. Implying that all flows, that is mass and heat flow downstream without any interaction with the upstream. For this system the fundamental equations are established and listed here.
To start with the continuity equations, for which two follow from flow dynamics and the last from thermodynamics. From the law of *conservation of mass Equation* 7.2. Subscript 1 and 2 refer two upstream and downstream respectively. U refers to the flow velocity and A refers to the cross section of the flow. For unchanged cross-section the ($A_1 = A_2$), the cross-sections can be divided out.

$$\rho_1 * U_1 * A_1 = \rho_2 * U_2 * A_2 \tag{7.2}$$

The second continuity equation follows from the law of *conservation of momentum*. The form given here was taken from [9], which gives Equation 7.3. The equation is in the unit mass form as such no mixture or additional mass flow streams should exist.

$$p_1 + \rho_1 * U_1^2 = p_2 + \rho_2 * U_2^2 \tag{7.3}$$

The last and probably most important of the 3 conservation equations is the law of *conservation of energy*. Many equations exist around this law, which all balance the energy. However, the form used here is the equation used in [9] and [85], given in Equation 7.4. Equation 7.4 tracks the enthalpy of the fluid, and is in the unit form. h stands for the unit enthalpy, which gives it the J/kg units (m^2s^{-2} in SI units). U is the flow velocity. Equation 7.4 forms the starting point for many of the methods presented in this thesis.

$$h_1 + \frac{U_1^2}{2} = h_2 + \frac{U_2^2}{2} \tag{7.4}$$

Other than the continuity equation, the above assumptions allow the use of other equations as well. The first of which is the previously provided *perfect gas law* 7.1. Note that the equations presented here are only valid throughout a single transition, but do not hold between transitions. The principal works much like the solidification, see Section 6.2.2. The second set of equations follow from the isentropic gas in combination with calorical gas. The isentropic relations explain the behaviour of a gas isentropic conditions, illustrated in Equations 7.5, 7.6, and 7.7. These equations are sometimes also referred to as the Poisson relations. γ refers to the specific heat ratio (c_p/c_v).

$$V_1^\gamma p_1 = V_2^\gamma p_2 \tag{7.5}$$

$$T_1 V_1^{\gamma-1} = T_2 V_2^{\gamma-1} \tag{7.6}$$

$$T_1^\gamma p_1^{1-\gamma} = T_2^\gamma p_2^{1-\gamma} \tag{7.7}$$

In addition to the isentropic relations the enthalpy of calorical gas can be written as $h = c_p T$, where T is in K. These equations will be further referred to as the transitional relations, because they are only valid within a transition.
Next to the continuity and transitional relation there is the speed of sound relation, see Equation 7.8. Note that the second relation in Equation 7.8 only holds if the perfect gas law holds. As such, the first relation is preferred.

$$a = \sqrt{\gamma \frac{p}{\rho}} = \sqrt{\gamma R T} \tag{7.8}$$

With Equation 7.8 all fundamental equations have been given to derive all methods presented in this chapter.

7.1.4. Ideal Rocket configuration and the Implications

Lastly, the propulsion module will be approached as an ideal rocket configuration. As is described in Section 6.2.4, a detailed sizing of the vehicle is beyond the scope of this thesis and would introduce to much speculation. The same holds true for the engine sizing, which would limit the extend of the conclusion too much.
Therefore, a goal driven approach is used, which for the performance trade-off is to identify the engine with the most potential. For this reason, the propulsion module is developed such that the engine at all instances operates at its optimum operations (100% throttle). Hence, the mass difference between nodes should roughly be a multiple of the mass rate at 100% throttle of a single engine. However, if losses due to lower of higher rates are minimal, a varying throttle range can be utilised to achieve the ideal burning program. However, such design aspects are left for future research.
To elaborate, the model will not specify the number of engines or the actual size. However, it will calculate the optimal sizing of the engine for a given mass flow. As such, the model will not compute how many engines must be operational at what time and at what thrust level. It will however, compute the total critical throat area required for a given mass rate at optimal thrust levels. From the throat area the rest of the sizing can be derived. This will be elaborated in more detail in Section 7.2.2.

7.2. Engine Simulation Methodologies

With the engine specifications, the building blocks, and assumptions established the engine simulation methodologies are presented. All performance methodologies are discussed perselected engine separately.
However, the aware reader might have noticed the conventional engine methodology in Section 7.2.2. While, conventional rocket engines were excluded in Chapter 4, here they serve as the building blocks from which the other engines are built. As one might have realised, every selected engine alters a single transition of the conventional engine. The aerospike alters the nozzle, the PDE alters the combustion chamber and the hybrid engine adds an intake, thus altering everything up to and including the injector.
Each section will discuss the transitions in chronological order, relative to the flow direction. Overlaps will not be discussed twice, but merely referenced.
Each engine module is programmed as its own Python class, were each transition is a class function. The transition functions are successively used to form the thrust function, for which the output is passes to the rocket motion module (Tudatpy).
Next to the burning program the engine class requires the other inputs to simulate the thrust throughout the ascent. It requires the fuel and oxidiser in the reaction *Mixture* object (propellant module), the mass budget, to identify the amount of propellant (sizing module), and the vehicle properties throughout the ascent, to identify when the propellant is depleted or to obtain the ambient air properties (rocket motion).

7.2.1. Propulsion Modules Utilised in the Model

In Chapter 6 the entire trade-off model is given, which leave the propulsion modules. The model directly measures the effectiveness of the engines purpose, which is to deliver as much DeltaV and as efficiently to the vehicle as possible. The propulsion system adds DeltaV by generating thrust, hence accelerating the vehicle. DeltaV can therefore be seen as the potential total acceleration of a propulsion system. In essence, the propulsion module is simply an elaborate thrust calculation.

Thrust Computation
Thrust operates like any other kinetic force by asserting pressure on one side of a system. The pressure differential over the system is what accelerates the vehicle. The back of ascent vehicles, which includes the CC and nozzle walls, experience high pressures due to the combusted gassed. The front of the ascent vehicle is exposed to the lower atmospheric pressure, which decrease with altitude. However, integrating the pressure over the entire surface is a tremendous procedure, which requires detailed information about the vehicle and engine.
Luckily, the rocket Equation 7.9 is a good alternative. This equation is a volume tracking approach, in which the volume of both the CC and nozzle form the system together with the vehicle. This simplifies the calculation substantially, as the atmospheric pressure cancels out, with the exception of the A_e. A_e forms the second component of the Rocket Equation 7.9, referred to as the pressure thrust. Where p_e and p_a are the exhaust and ambient pressure, respectively.
The first component is referred to as the impulse component, as its momentum change due to the ejected mass. For this reason, Equation 7.9 is sometimes referred to as the impulse equation, as it tracks the impulse change of the system. U_e and $\dot{m}$ refer to the exhaust velocity and mass flow rate at station 9.
Note that Equation 7.9 is a volume tracking system with steady state and does not hold for mass tracking systems or unsteady states, see Section 7.2.4.

$$T = \dot{m}U_e + A_e(p_e - p_a) \tag{7.9}$$

Even though Equation 7.9 is inherently simple to understand and compute, the individual p_e components are more tedious to extrapolate. The component, U_e, U_e, and p_e, need to be computed, the simulation of which forms the propulsion modules. Note that $\dot{m}$ is determined by the optimisation module and p_a is extrapolated from the Tudatpy, the rocket motion module, see Section 6.2.5.

Propulsion Modules
Each engine is its own propulsion module, which is its own Python class. All the selected engines have a parent class which provides the conventional transitions. This is described in Section 7.2. Additionally, this parent class contains the mass rate and guidance modules.

The purpose of the propulsion module is to compute all the variables of the rocket equation 7.9, given the operating parameters. The operating parameters can be divided into sub-categories, namely operation trajectory optimisation variables, sizing optimisation variables, sizing parameters, burning variables, and design parameters, as discussed in 6.1.2. The latter three are primarily important to the parameters in the Equation 7.9, where the former is indirectly relevant for the ambient conditions.
The exact definitions can be found in Section 6.1.2, for now a brief overview is provided. The sizing optimisation variables in this thesis are limited to the fuel-over-oxidiser ratio('s) and the expansion ratio, F/O and ϵ respectively. The burning variables via the burning settings provide the time dependent mass rate ($\dot{m}(t)$). The sizing parameters vary per engine but are the parameters an engineer designs for, e.g. p_{cc}. whereas the design parameters are a consequence of the sizing parameters and manufacturing capabilities. These entail the efficiencies.
Via the above parameters, the propulsion module computes all the variables of Equation 7.9, from which the thrust can be calculated. The transitions and the respective functions from which the variables follow these are discussed in Section 7.2.

7.2.2. Methodology for Convectional Rocket Engine Simulation

As stated before the conventional engine serves as the main module. However, the module is also used to from a baseline. For the baseline the Raptor engine will be used, which will indicate how much of a performance gain the selected engines offers.
Figure 7.2 has far less states than Figure 7.1, therefore less transitions. The transitions include, the injector, the CC, the Throat, and the Nozzle.

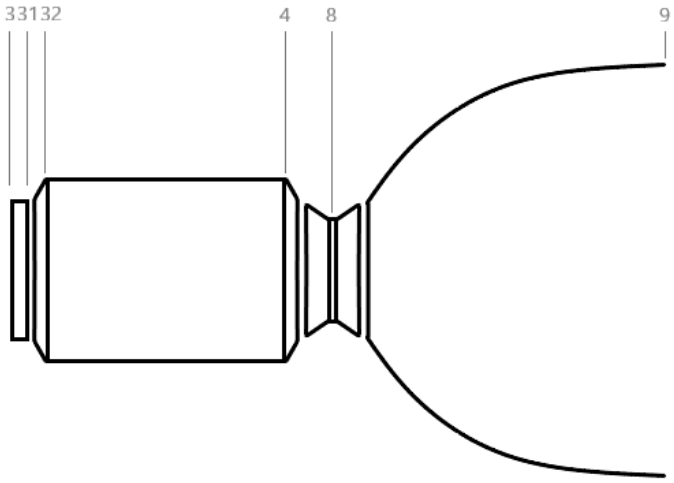

Figure 7.2: Illustrates the engine stations of a convectional rocket engine architecture

3 -> 31 Injector
To understand the injector, the chemical kinematic model must be explained. The chemical kinematic model is responsible for the reaction, hence combustion/detonation, of the propellant. For rocketry, the convention is to use RocketCEA to perform the kinematics. However, the code compiler for the python version of RocketCEA is broken at the time of developing. Additionally, RocketCEA is not configurable for the selected engines.
For this reason the Cantera package is used. Cantera is a general reaction kinematics tool with many implementations. Cantera creates reaction objects which are based on input files. The input files (.yaml files to be exact) contain all the species considered and all the possible reactions between set species. The yaml files act as a library for the reactor object, which enables the chemical interactions. In this thesis the build in *gri30.yaml* file is used, which contain all the selected propellant species.
Next to the yaml file, the reactor object needs something to react. Two methods exist: a closed system ap-

proach in which the substance is predefined, or to create substance via *Valves* or *MassFlowers*. The *MassFlower* function acts as the injector for the CC which is the reaction object.
The *MassFlower* function requires a Cantera *Reservoir* or reactor object from which it draws the injected mixture. In additions, it requires an injector pressure and mass rate. The mass rate is an optimisation parameter and a function of t. From F/O ratio the $\dot{m}_f$ and $\dot{m}_{ox}$ follow. The injector pressure determines the p_{CC}, making it a sizing parameter and is further discussed in the CC transition.
The *Reservoir* object can best be interpreted as the storage tanks or plumbing from which the fuel flows. The reservoirs are set to the specifications presented in Tables 5.5, 5.7, and 5.7. Before injection the temperature of both the oxidisers and fuel is raised to 500 K, as stated in Section 7.1.2.

32 -> 4 Combustion Chamber
For conventional combustion chambers the *ConstPressureReactor* function of Cantera is used, which performs isobaric reactions. Furthermore, no surface- or phase interaction models were introduced, thereby assuming perfect atomization of the propellant. Additionally, an exit *MassFlower* was introduced which allows the reactant to leave the reactor object. The reactants are dumped in a dump reservoir, to prevent mass build-up in the reactor object. The mass rate for the exhaust *MassFlower* is set equal to the total mass rate into the CC.
The CC is initially filled with argon gas at 1600 K, which serves as the ignition system, see Section 7.1.2. the reactants enter the CC reactor object, increasing the temperature due to the reactions. After <0.0018 s a pseudo-equilibrium state is reached[2]. The CC reactor object provides the parameters p_{cc}, T_{cc}, x_i, and y_i. The latter two refer to the mass and mole fractions of the product, respectively. From the composition all thermodynamic properties can be extrapolated.
Lastly, the CC is reset after each run and purged during a cut-off period, after which reignition occurs.

4 -> 9 Nozzle (Frozen Equilibrium)
To transition from stations 4 to 9, CC exit to nozzle exit respectively, the transitional relations are required. The assumptions make γ and R constants, thereby fixing the flow composition, hence the name Frozen Equilibrium. To simplify, no reactions take place after the CC.
The frozen equilibrium is derived from Equation 7.4, neglecting U_{cc} and using $h = c_p T$, which gives Equation 7.10.

$$U_e^2 = 2C_p(T_{cc} - T_e) \tag{7.10}$$

Equation 7.10 needs to be further transformed as the T_e is unknown. Therefore, T_e is replaced with p_e, which is via Equation 7.7. Even though the unknown parameter p_e is introduced, in reality only the ratio p_{CC}/p_e needs to be known. This ratio can be extrapolated from Equation 7.11. The derivation for Equation 7.11 is similar to the derivation for the frozen equilibrium and can be done with the provided equations. The equation and derivation can be found in [85].
ϵ is the expansion ratio, which is a sizing optimisation parameter. In the code the pressure ratio is found by using the *minimize* function from the *scipy* package. Note that A_t is found using Equation 7.16, found in the throat transition.

$$\epsilon = \frac{A_e}{A_t} = \frac{\Gamma}{\sqrt{\frac{2\gamma}{\gamma-1}\frac{p_e}{p_{cc}}^{\frac{2}{\gamma}}\left(1-\frac{p_e}{p_{cc}}^{\frac{\gamma-1}{\gamma}}\right)}} \tag{7.11}$$

Γ is the value of the gamma Equation 7.13 Additionally, rewriting C_p in terms of γ and R is preferred, as γ is less sensitive to temperature. Therefore, the assumption of calorical gas is less severe. This transformation can be achieved by using the algebra and the relations $\gamma = c_p/c_v$ and $c_p = R - c_v$. The above two transformations give the frozen equilibrium equation 7.12.

$$U_e = \sqrt{2\frac{\gamma}{\gamma-1}RT_{cc}\left(1-\frac{p_e}{p_{cc}}^{\frac{\gamma-1}{\gamma}}\right)} \tag{7.12}$$

Resolving Equation 7.11 provides the pressure ratio, with p_{cc} known the p_e can be computed. Filling in Equation 7.12 provides the U_{cc}. As the exhaust area can be found from the expansion ratio, all the parameters for

[2]The T_{CC} fluctuate with 0.2 K and the species only change a 1E-6 of a percentile.

the thrust calculation have been found.

$$\Gamma = \sqrt{\gamma}\frac{2}{\gamma+1}^{\frac{\gamma+1}{2(\gamma-1)}} \tag{7.13}$$

Some final remarks about the frozen equilibrium method. Firstly the method is derived for a steady state system, which means this method is not suitable for pulse detonation nozzles (unsteady process). Secondly, the frozen equilibrium method is an underestimation due to the calorical gas assumption. In Equation 7.10 c_p is assumed constant, however in reality c_p reduces with temperature. Hence, more chemical/internal energy should be converted into kinetic energy. Note that this phenomenon is partly remedied by replacing c_p with γ.

4 -> 8 Throat

For the second approach, namely the shifting equilibrium method, the state of the throat is required. Hence, the additional transition from the CC to the throat. Similarly to the frozen method, U_{cc} is neglected, as a consequence $T_{cc} = T_t$ and $p_{cc} = p_t$. Therefore, the total conditions equations from [9] can be used, given in Equations 7.14 and 7.15.

$$p_i = p_t\left(1+\frac{\gamma-1}{2}M_i^2\right)^{\frac{\gamma-1}{\gamma}} \tag{7.14}$$

$$T_i = T_t\left(1+\frac{\gamma-1}{2}M_i^2\right)^{-1} \tag{7.15}$$

i is a placeholder for an unspecified station. From the ideal configuration conditions it follows that the throat is optimal, thereby critical (M_{throat}=1). As the throat is critical, the critical flow Equation 7.16 taken from [85] can be used. Furthermore, Equations 7.14 and 7.15 simplify to Equations 7.17 and 7.18.

$$\dot{m} = \frac{\Gamma p_{cc} A_t}{\sqrt{RT_{cc}}} \tag{7.16}$$

$$p_t = p_{cc}\frac{2}{\gamma+1}^{\frac{\gamma}{\gamma-1}} \tag{7.17}$$

$$T_t = T_{cc}\frac{2}{\gamma+1}s \tag{7.18}$$

Where Γ is again the gamma equation 7.13. With two thermodynamic properties know the flow, a Cantera *Mixture* object, can be updated to obtain the remaining properties. Furthermore, the last dynamic property, U_t which is sonic, can be computed using equation 7.8.

8 -> 9 Nozzle (Shifting Equilibrium)

The alternative to the frozen method is the shifting equilibrium method. As the name suggests this method assumes the flow or mixture is in perfect shifting equilibrium, with the result that the assumption of calorically perfect gas is removed. The mixture is made to react till shifting equilibrium. However, this thesis uses the semi shifting equilibrium method, in which the mixture is allowed to react over a Δt time step, because reacting till equilibrium is found to be unrealistic.

The reason for a second nozzle model is twofold. Firstly, a second model offers greater validation to the overall model when in agreement. Secondly, the method presented here is a mass tracking approach, making it a viable method for unsteady processes.

Again, the method starts with Equation 7.4 and neglecting $U_{cc} = 0$, which leads to Equation 7.19. H_{cc} and H_e are the enthalpies of the gasses when entering the combustion chamber and once exhausted, respectively[3]. M is the weighted molar mass of the exhaust gas. In practise, the shifting equilibrium is less practical, due to its iterate and non-linear nature, which dismisses algebraic methods.

$$U_e = \left(\frac{2(h_{cc}-h_e)}{M}\right)^{1/2} \tag{7.19}$$

Equation 7.19 might seem simple at first, yet obtaining h_e makes the endeavour far more cumbersome. h_e cannot be computed algebraically as it introduces too many errors. Hence, an iterative approach is required.

[3] The enthalpy is not per unit mass hence the division by M

The flow is made to travel through the nozzle in steps. The flow mixture is updated after each step.
Furthermore, this iterative approach requires the contour to be specified. This thesis approximates the nozzle as proposed in [85], by using a parabola formula (Equation 7.20). x is the length of the nozzle (l) wheres y is the difference between the contour radius (r_c) and the exit radius (r_e), $y = r_e - r_c$.

$$y = ax^2 + bx + c \tag{7.20}$$

The parabola formula has to be resolved whenever the mass rate changes, as this provides a new A_t. y is equal to $r_e - r_t$ at x = 0, which leaves two unknowns with one relation for y = 0 at x=l. However, to get the steepest parabola the relation $a = -2/lb$ is used. This relation was found while analysing the coefficient sensitivities. However, it can be algebraically derived. The steepest parabola is preferred as it initially expands the flow rapidly after which it straightens the flow direction. The expansion of the flow is what converts the internal/chemical energy into kinetic energy (given that M>0)[9]. Mathematically speaking b must be as negative as possible as it is the derivative at x=0, while satisfying $y > 0$ for $0 < x < l$, that is to say the function is singularly decreasing.

With the radius known the effective nozzle plane can be computed at any length. The effective nozzle plane refers to all the nozzle planes combined, which is a problem as the number of engines is undefined. As such, the above method assumes a single large engine, which cannot be ideal for varying mass rates. Furthermore, it is economically unsound, as discussed in Chapter 2. However, this is only a problem when considering directional losses[4], which are neglected due to the ideal configuration approach. Therefore, the method is perfectly fine for computing the flow expansion, which is illustrated in Figure 7.3.

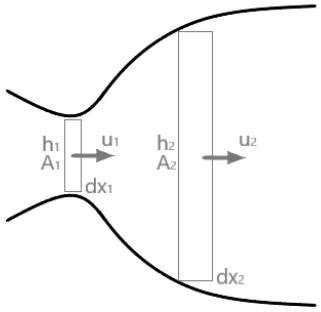

Figure 7.3: Illustrates an exaggerated step of the iteration shifting/frozen equilibrium method

Figure 7.3 illustrates the above method, with the contour defined by Equation 7.20. The iteration is done via the Euler method and relies on tracking a volume of mass to the nozzle exit (note that this is a mass tracking method). The mass expands in both the y and x direction. While, the expansion in y is due to the contour, the expansion in x is due to the flow acceleration. Each iteration uses approximately 1000 steps, by setting $dt = l/(1000U_t)$. The volume is calculated via Equation 7.21, where $dx_i = U_i dt$. The subscript i is the iteration number, with $U_0 = U_t$, $x_0 = 0$, and $y_0 = r_e - r_t$.

$$V_i = dx_i(r_e - y_0(x_i))^2\pi \tag{7.21}$$

x is updated via $x_{i+1} = x_i + dx$. With a method to update the volume between each iteration, one more thermodynamic property is required. From Equation 7.5 the pressure can be extrapolated. Hence calorical flow is assumed for a single step. Equation 7.5 can be used, as the initial pressure is equal to $p_t = p_8$. With two thermodynamic properties known the flow can be updated, via the *Mixture.PV* Cantera command. The *Mixture* can then be made to react over a specific dt or till equilibrium by creating a reactor object, using *ReactorNet.advance(dt)* or *ReactorNet.advance_to_steady_state()* respectively.
In general, the shifting equilibrium method is an overestimation, as the reactions are hindered by the supersonic turbulent flow. When testing both methods a U_e of ~3830 m/s and >3835 m/s are found, respectively. Here the equilibrium method is deemed unrealistic, as it fails to reach a steady state even after 1 s, whereas the flow is in the nozzle for less than 1 ms. Therefore, only the former method is used from here on out.
By allowing the mixture to react, the thermodynamic properties are updated for the next step. When the Thermodynamic properties are updated, the new enthalpy of the mixture (h_{i+1}) can be extrapolated. Via Equation 7.4 the new flow velocity (U_{i+1}) can be calculated, hence dx_{i+1} can be obtained[5].
The above steps are repeated until $x_i \geq L_{nozzle}$. Additionally, if the kinematics is switched off, the mixture is

[4]Exhaust flow is not ejected in the axial direction but has an ejection angle.
[5]The changing value of dx_i is the main cause for the iterative approach.

not made to react. This method finds a U_e of 3263 m/s compared to the 3279 m/s the frozen equilibrium method found. This suggest both methods are equivalent. The small difference is probably caused by the caloric gas assumption, which for the frozen method holds from 4 -> 9 and for the shifting equilibrium from 8 -> 9[6].

Conventional Rocket Engine Module

The conventional rocket engine module is set-up to both act as a parent class for the selected engines and to provide baseline. As a parent class all child classes, the selected engines, can use any function in the parent class. Additionally, any parameter set-up, like the propellants, get passed on too. Note that parameters defined in the child class overwrite the same parameters in the parent class.

The secondary purpose is to simulate the performance of the Raptor engine, which currently is the engine with the highest T/W. The purpose of the baseline is to see how much better the selected engines perform compared to the conventional engines. The higher the performance gain the more justified the development is.

The conventional engine requires one additional sizing parameter specification, namely the p_{cc}. The p_{cc} is set by the $p_{injector}$, as described above. Therefore, a p_{cc} must be chosen that realistically can be achieved by the turbo-pumps. Historically, this number was between 69 bar to 155 bar[17][61]. However, the newer engines, like the Raptor engine which was even tested at 330 bar, operate at a p_{cc} of 300 bar. Hence, p_{cc} is set to 300 bar.

Lastly, the sizing optimisation parameters ϵ and F/O can be overwritten to a fixed value. In performance simulations, namely Chapter 9, it will be stated when of these parameters are prefixed.

7.2.3. Methodology for the Aerospike Engine

The first of the selected engines, namely the aerospike engine, is very similar to a conventional rocket engine, i.e. from a thermodynamic perspective it only changes the nozzle interaction. The injector and CC transitions work according to the same thermodynamic principal as the conventional engine. From a design aspect the CC is very different. Aerospike engines utilise multiple CCs per spike, either in a linear of in an axial configuration. Using a single CC would not only give a compromised shape, it would be significantly harder to manufacture. The added benefit of this is that the engine can use thrust factoring, eliminating the need for gimbal system, as is illustrated in Figure 7.4. Explicitly, this thesis deals with an plug-nozzle (truncated aerospike), for which the optimal amount of tip is removed, due to the ideal configuration. The engine design parameters ϵ is the max expansion ratio ($\epsilon_{\text{eff,max}}$) for the plug-nozzle. In addition to the ϵ design parameter there is the F/O ratio.

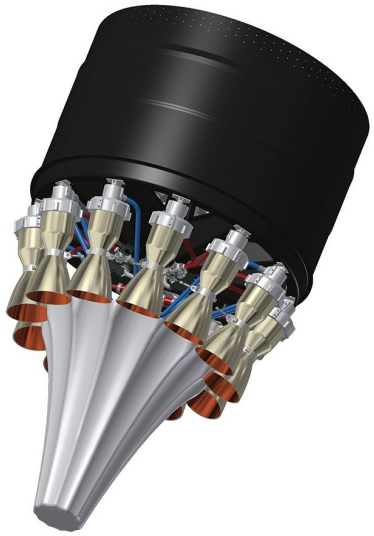

Figure 7.4: Illustrates a render of an Aerospike engine proposed by the Firefly company, taken from [53]

Lastly, it is largely accepted that aerospike engines operate a GG and FFSC hybrid power cycle, in which the gases of the GG cycle are used to base bleed. Base bleeding has been shown to improve the expansion capabilities of the aerospike, hence improving the performance of the engine [79][50].

Section 4.2.4 gave an elaborate description on the concept and operation of an aerospike. But to recapitulate an aerospike is a conventional nozzle turned inside out, thereby relying on the ambient pressure to expand and straighten the flow. In essence, aerospikes scale p_e in Equation 7.9 to p_a, such that U_e is optimal, as explained in Section 7.2.1.

Initially, a more complex method was proposed to simulate the aerospike expansion, which uses two tran-

[6] γ is higher for the frozen equilibrium method, which will result in a lower pressure at station 9, see Equation 7.5. A lower p_e results in a higher U_e.

sitions to simulate the aerospike nozzle. The first transition, from 4 -> 85, follows the conventional frozen equilibrium nozzle transition (4 -> 9), described in Section 7.2.2. Aerospikes initially use conventional contours to reduce the initial pressure difference. The flow will expand too rapidly in the radial direction if the pressure difference is too large, inflicting significant directional losses[7].
The transition from 85 -> 9 is more cumbersome due to the interaction with the ambient atmosphere, as illus-

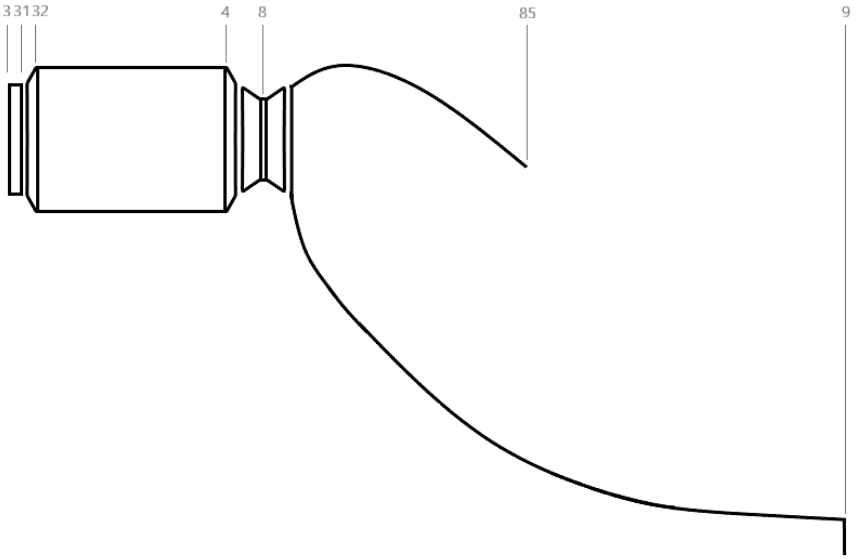

Figure 7.5: Illustrates the engine stations of an aerospike engine

trated in Figure 7.5. Therefore, most papers [36][87][79] utilise CFD[8] when evaluating aerospike performance, as no definitive algebraic alternative exists. However, paper [63] described the aerospike expansion as a series of expansion/decompression shocks, forming an expansion fan, illustrated in Figure 4.17. This expansion fan can be algebraically approximated by the Prandtl-Meyer method, illustrated in Equation 7.22. The Prandtl-Meyer method comes with its limitations as it assumes isentropic flow across the expansion shocks, which has the implication that the more significant the expansion shock is the more the Prandtl-Meyer method deviates from reality.
The method computes the flow direction $\sigma = \upsilon(\mathrm{M}_9) - \upsilon(\mathrm{M}_{85})$, with respect to the exit direction of the contour at station 85. This method comes with more constraints. To start, the contour of the spike must be defined. this thesis advocates the parabola-polynomial approach suggested in [79], which is an improvement of the convention set by Angelino [11]. M_9 is extrapolated by setting $\mathrm{p}_9 = \mathrm{p}_\mathrm{a}$ in Equation 7.14, which holds true until the outer expansion fan edge intersects with the spike's end. At that point, further expansion does not effect the flow on the spike anymore, $\epsilon_{\mathrm{eff,max}}$ is reached. In this instance, σ should be parallel to the axis of the ascent vehicle to minimise directional losses[7].

$$\upsilon(M_n) = \sqrt{\frac{\gamma+1}{\gamma-1}}\, tan^{-1}\sqrt{\frac{\gamma-1}{\gamma+1}\left(M_n^2-1\right)} - tan^{-1}\sqrt{M_n^2-1} \tag{7.22}$$

The above method is interesting to further explore and could become its own paper, which could evaluate the validity and limitations. However, initial testing showed that little additional value was added compared to using a conventional nozzle transition, while ample additional engine specifications need to be added. Such specification would limit the extent of the conclusion. Lastly, the Prandtl-Meyer approximation requires far more computational effort than the frozen equilibrium method. Hence, the trade-off was made to abandon this method in favour of an adapted frozen equilibrium method to be more time efficient. The method is still discussed as the author believes the method could provide better insights in aerospikes performance if developed properly. In addition, the method provides a deeper understanding of what drives the altitude compensation of an aerospike nozzle.
The next paragraphs elaborate on the transitions used in the simulation of the aerospike engine.

[7] Exhaust flow is not ejected in the axial direction but has an ejection angle.
[8] Often the Navier-Stokes equations with the lam-bremhost $\kappa - \epsilon$ turbulent model are used.

3 -> 31 Injector
The injector transition follows the same procedure as an conventional engine described in Section 7.2.2.

32 -> 4 Combustion Chamber
The CC's of aerospike engines are simulated like an isobaric process, which is thermodynamically identical to that of an conventional engine. Therefore, the same procedure is used as described in Section 7.2.2.

4 -> 9 Aerospike Nozzle and Base Bleeding
As previously mentioned, an altered frozen equilibrium method, as described in Section 7.2.2, is used. However, using the frozen equilibrium has additional implications for the aerospike simulation. The implications are in line with the assumptions and conditions presented in [79]. Logically, the effects of the relative velocity and turbulence induced by the ascent vehicle on the external flow are neglected. Additionally, a smooth transaction from the throat (8) to the aerospike (85->9) is assumed, that is to say that the conventional nozzle contour (8->85) performs in ideal conditions. These assumptions do not need to imply an overestimation, as the vehicle induced turbulence might benefit the performance of the aerospike [63].
Unlike conventional nozzles, the p_e is decreasing for aerospike engines, regardless of whether the operational settings are kept constant. Therefore, Equation 7.12 has to be recomputed for every time step in the rocket motion model, given that the engine is operational. Fortunately, p_e is obtained by setting it equal to p_a, then the effective expansion ratio ϵ_{eff} is computed via Equation 7.11, which results in the effective exhaust area ($A_{e,\text{eff}}$). Once the ϵ_{eff} is equal to the $\epsilon_{\text{eff,max}}$, p_e is kept constant and no more evaluations are needed.
The above method assumes ideal expansion ($p_9 = p_a$), which in reality might not be the case, as Figure 4.18 illustrates an aerospike effective of 93%-97% compared to the ideal convectional nozzle at that particular expansion[63]. It is speculated that the inefficiency is due to inefficient expansion ($p_9 > p_a$). The inefficient expansion is evaluated in Section 9.3.3, for which the exhaust pressure is computed via $p_e = p_a(1 + \kappa_{\text{expansion}})$, were $\kappa_{\text{expansion}}$ is the reduced expansion factor. For the base performance simulation $\kappa_{expansion}$ is set to zero ($p_9 = p_a$).
Research suggest that the use of base bleed increases the effectiveness of aerospikes. This can be achieved by replacing $\dot{m}$ with $\dot{m}(1 - \eta_{\text{bleed}})$, were η_{bleed} is the % of propellant mass used for base bleeding. The desired effect can already be achieved with 1% of the total mass rate [41].

Aerospike Module
The aerospike module is a python child class of the conventional module class (parent), as discussed in Section 7.2.1. The aerospike class is still a separate class. However, all convention transition functions are inherited from the parent class.
Moreover, both classes are very similar in set-up and design, as both have the same task of providing the thrust and mass change to the rocket motion module. The sizing parameters that need to be defined for the aerospike engine are the same, which is the p_{cc}. The p_{cc} is set to the standard of 300 bar, unless otherwise implied.
The module operates exactly like the standard module described in Sections 7.2.1 and 7.2.2.

7.2.4. Methodology for the Pulse Detonation Engine

As briefly mentioned in Section 4.2.6 detonation happens much faster than the acceleration of the flow. Hence, the flow cannot expand before combustion. The result is that pressure increases substantially, while volume is kept constant. Therefore, detonation is closer to an isochoric process, a thermodynamically more efficient process, than the isobaric process seen in Combustion Chambers (Also referred to as deflagration combustion). The thermodynamic cycle of a PDE is a Humphrey cycle [14]. Consequently, the combustion chamber transition established in Section 7.2.2 cannot be utilised.
Furthermore, as the name suggest PDE engines pulse, where a unit of mass is detonated in the detonation chamber(DC) and thereafter expanded and ejected before a new unit of mass is injected (a detailed explanation can be found in Section 4.2.6). Hence, the mass rate is discontinuous and $\dot{m}$ is the average mass rate for 1 s. The actual instantaneous mass rate varies between 0 to 2-4 times $\dot{m}$, depending on the ignition delay, filling and purging time. It should now be clear that this is an unsteady process, which means that using transitions 3 -> 31 and 4 -> 9 from Section 7.2.2 are invalid.
As such, alternative transitions need to be established for these stations. Additionally, the flow through the shaft (35 -> 4) needs to be simulated. Generally, it is true that performance estimation with CFD methods are more reliable. However, these models are unsuitable for the performance analysis required in this thesis. For this reason, the methodology presented will follow the model established by Endo Fuijware et al[24].
Note that this thesis explicitly simulates PDEs, which contrary to regular pulse engine rely on artificial ignition. As such, ignition is initiated rather than caused by the colaps of the hot gases. The latter is significantly more complicated to simulate as cycles cannot be treated as isolated processes.

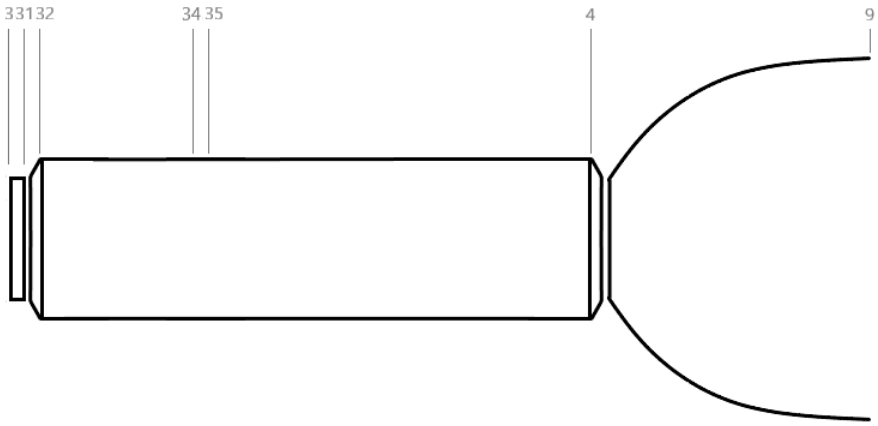

Figure 7.6: Illustrates the engine stations for a PDE.

3 -> 31 Pulse Injector

Previously, a *MassFlower* was utilised to provide a constant influx of propellant into the reactor object, which is the CC. However, PDEs inject propellant until a certain mixture mass is obtained (pulse mass), at which point the mass flow is stopped and detonation is initiated. In essence, the pulse injection transition only needs to provide the mixture before ignition. To achieve this, the *Quantity* function from Cantera is used, this function creates a new *Mixture* object by combining the content of multiple *Reservoir* objects. For reasons discussed later, the pulse mass is irrelevant, as *Quantity* only needs the proportion between $\dot{m}_f$ and $\dot{m}_{ox}$. These, are computed from $\dot{m}(t)$ and F/O. Furthermore, as previously mentioned Cantera regards all reactor objects as unit masses, hence only the relative ratios need to be known.
Besides a more efficient thermodynamic cycle, DCs have another distinct advantage over CCs. Whereas, the p_{cc} is limited by the turbopumps, which operate far above p_{cc} to overcome the friction losses in the cooling and plumbing [35]. Evidenced by the development of the HMMR, where the turbopump became a severe mass penalty to reach the desired pressures. DCs, on the other hand, can operate at far lower pressures and are limited by the DC and wave tube wall strength. As a result, DCs can operate at far higher pressures than their CCs counterparts.
As a result, the maximum DC pressure is set ($p_{DC,limit}$) as the limit condition, where the maximum deto-

nation pressure is equal to the Neumann pressure ($p_{DC,N}$). Next to the mixture's composition, the injector conditions need to be determined (T_{31} & p_{31}). Consequently, the injector conditions need to be such that $p_{DC,N} = p_{DC,limit}$. This is challenging because of the high sensitivity to the initial conditions, due to the unsteady nature of pulse detonation.
To find the injector conditions a customised golden section method is utilised. A description of the golden section method is found in Appendix B, here it is only relevant to understand that it minimises $abs(p_{DC,N} - p_{DC,limit})$. The method is found under *get_golden_injector_conditions* in PDE module. The method operates by injecting and detonating at a particular p_{31}, if this results in $p_{DC,N} \approx p_{DC,limit}$ the function has found the correct injector pressures. The golden method is customised to deal with the secondary input parameters, namely T_{31}. The model is customised such that the minimal detonation temperature is found, which is achieved by step-wise increase and decrease T_{31}.
However, an absolute minimal ignition temperature of 500 k is set. It is unrealistic to use a lower ignition temperature than conventional CCs, because the thermal loads in DCs are the more challenging aspect of PDEs [14][60]. Note that a lower T_{31} is more efficient as T_4 does not increase equivalently with T_{31}. Explicitly, using less energy for ignition results in a larger net energy output.

32 -> 34 Detonation Chamber
It is widely accepted that detonation combustion can be approximated by a constant volume process (isochoric) [33]. This reaction process is simulated by the *Reactor* function, which is a Cantera reaction object that simulates reactions at constant specific volume. Compared to the CC transition in Section 7.2.2, two distinctions exist. A new reactor object is created every time the operational settings change, due to the unsteady nature. The method is tracking the mass that flows from 3 to 4, rather than evaluating the volume properties of 32 -> 4. In addition, where, previously, the volume expansion accelerated the CC flow, the detonation shocks themselves accelerate and expand the flow. Whereas the former distinction is merely a simulation feature, the latter poses a problem as Cantera assumes stationary mixtures. Hence, no dynamic flow properties.
The state properties provided by Cantera cannot be used directly, as the flow is non-stationary. The dynamic flow properties are computed using the endo-fuijware method [24], which approximates the detonation as a Chapman-Jougout detonation wave. The Hugonoit relations are used to complete the equations. This method treats detonation in phases, namely the combustion, forward rarefaction, refers rarefaction and, exhaust phase. Figure 7.7 illustrates the pressure levels over the length of the CC and wave tube combined(L_{DC} for various phases.
Each phase has its own set of properties that describe the dynamics and state. However, all are dependent on the Chapman-Jougout (CJ) detonation speed of the mixture D_{CJ} and the Chapman-Jougout detonation Mach number $M_{CJ} = D_{CJ}/a_{1,DC}$, computed via equation 7.23. q is the energy relaesed per unit mass, which is extrapolated from the previously discussed Cantera *Reactor* function.

$$D_{CJ} = D_{DC,2} = \sqrt{2\left(\gamma_{DC,2}^2 - 1\right) q} \tag{7.23}$$

The subscripts of all DC equations with the addition of the prefixed $_{DC}$ follow the convention of [24] and refer to the different thermodynamic situations. The subscripts are; $_N$: von Neuman spike of detoantion wave, $_1$: the pre-combusted mixture, $_2$: 2 surface of the CJ detonation wave, $_3$ rear boundary of the forward detonation, and $_{ex}$: open-end boundary conditions of reverse rarefaction wave. Figure 7.7 Illustrates when properties of the subscripts are achieved.

Once detonation is initiated, the von Neuman wave travels down the DC and wave tube. The compression wave is what initiates the reaction of the mixture. The reaction powers the Neuman wave and forms the CJ wave. The von Neuman pressure is the maximum pressure and is computed via Eqaution 7.24. Besides the pressure the von Neuman wave has little relevance to thrust computations. The pressure is of very short duration and thus its contribution to the thrust is negligible.

$$p_N = \frac{2\gamma_{DC,1}}{\gamma_{DC,1}+1} M_{CJ}^2 p_{DC,1} \tag{7.24}$$

The CJ conditions can be found in Equations 7.25, 7.26, and 7.27. $\gamma_{DC,2}$ is the post-detonation specific heat ratio, which is extrapolated from Cantera. $\gamma_{DC,2}$ is assumed to be constant after detonation, $\gamma_{DC,2} = \gamma_{DC,3} = \gamma_{DC,ex}$. The CJ wave is what accelerates the flows, it is the first forward rarefaction wave that stalls the flow.

$$p_{DC,2} = \frac{\gamma_{DC,1}}{\gamma_{DC,2}+1} M_{CJ}^2 p_{DC,1} \tag{7.25}$$

$$\rho_{DC,2} = \frac{\gamma_{DC,2}+1}{\gamma_{DC,2}} \rho_{DC,1} \tag{7.26}$$

$$U_{DC,2} = \frac{1}{\gamma_{DC,2}+1} D_{CJ} \tag{7.27}$$

The CJ wave is followed by a rarefaction wave which decelerators the flow to $U_{DC,3} = 0$, which travels at half the CJ wave speed $D_3 = D_{CJ}$. The reverse rarefaction wave is what accelerates the flow again, which travels from open-end (4) to the closed/injector-end (31). Thus, between these waves is a period at which the flow is at rest. This period varies for different locations in the DC and wave tube (31->4), but decrease when approaching the open-end(4). The state properties of 3 are given in Equations 7.28 and 7.29.

$$p_{DC,3} = \frac{\gamma_{DC,1}}{2\gamma_{DC,3}} \left(\frac{\gamma_{DC,3}+1}{2\gamma_{DC,3}} \right)^{\frac{\gamma_{DC,3}+1}{\gamma_{DC,3}-1}} M_{CJ}^2 p_{DC,1} \tag{7.28}$$

$$\rho_{DC,3} = 2 \left(\frac{\gamma_{DC,3}+1}{2\gamma_{DC,3}} \right)^{\frac{\gamma_{DC,3}+1}{\gamma_{DC,3}-1}} \rho_{DC,1} \tag{7.29}$$

With Equations 7.28 and 7.28 all relevant state properties have been defined. With these properties the state at open-end(4) can be defined over the entire period of on pulse t_{cyc}. A curious reader might wonder why no properties for $_{ex}$ were given, which is explained in the wave tube transition.

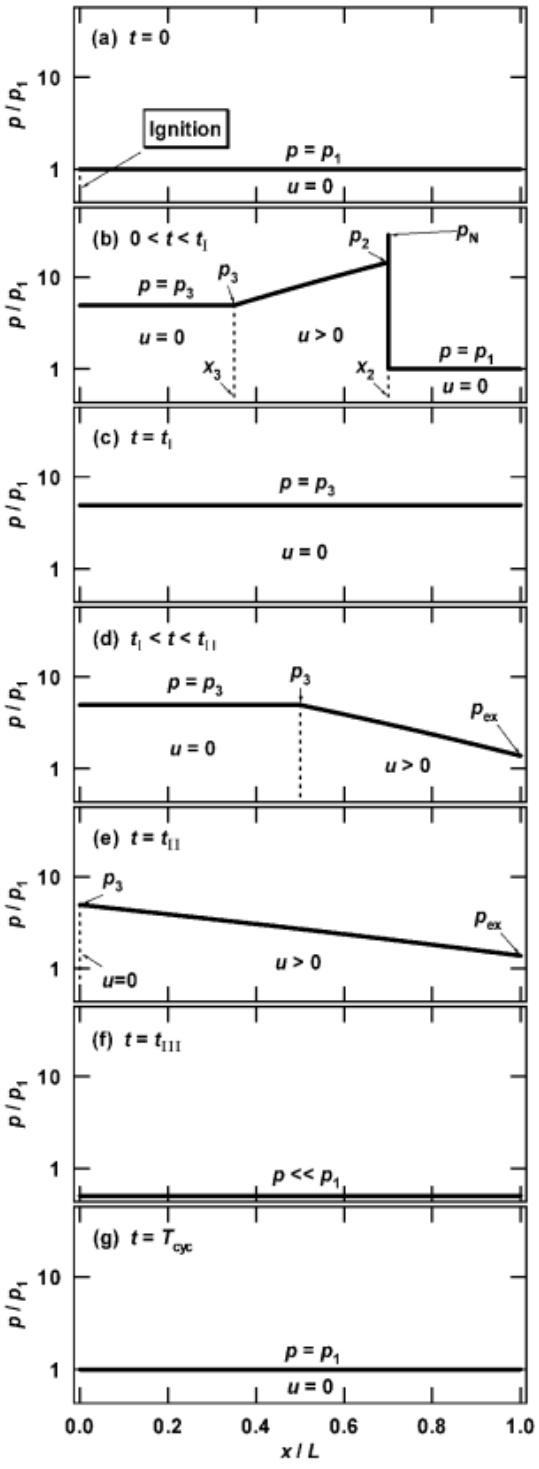

Figure 7.7: Illustrates the pressure distributions in a shock tube at the instants: (a) t = 0, (b) $0 < t < t_I$,(c) $t = t_I$, (d) $t_I < t < t_I I$, (e) $t = t_I I$, (f) $t = t_I I I$, (g) $t = t_{cyc}$, taken from [24].

34 -> 35 Wave Tube

In some research the wave tube is combined with the DC. However, from both an engineering and simulation point of view it is better to make the distinction. The DC is designed to transfer the deflagration to detonation

as fast as possible. Such modifications could be an enlarged radius or the addition of a Shchelkin spiral or obstacle blockage [57]. From a simulation perspective it is the CC that provides the relevant thermodynamic properties, whereas the wave tube provides the fluid dynamics during the pulse period.
Here the primary goal of the wave tube transition is to provide the p_4, ρ_4 and U_4 over the entire pulse period t_{cyc}. [24] provides methods for the exhaust properties, which would provide the conditions at 4. However, these estimations deviate too much to be a realistic. The reason for this is three fold. [24] provides an impulse equation for a no nozzle PDE. Hence, the pressure integral over the closed-end area (31) is equivalent to the thrust. As such, computing the conditions over the entire length ,especially at the open-end (4)(as the properties are not used for their final equation), is of secondary priority. Furthermore, there is the discontinuous pressure drop at the open-end from $p_{DC,3}$ to $p_{DC,ex}$ after which it remains constant, which both are not observed with test data, illustrated in Figure 8.1a. Lastly, there is the indirect estimation that both $\rho_{DC,1}$ and $\rho_{DC,3}$ occupy the same amount of volume with the same amount of mass, which is not an issue when computing only pressure thrust. However, this is an issue for the open-end where both pressure and momentum thrust exist. Therefore, it comes as no surprise that by the Endo-Fuijware method [24], the thrust at open-end and closed-end are not the same.
For the above reasons an alternative Quick-and-Dirty method was used, which is inline with the methodology presented in [60]. The equations derived in [24] are used such that they are best matched to test data, illustrated in Figure 8.1. Before the methodology can be provided the previously discussed phases need to be defined over t_{cyc}. To start with the detonation phase, this includes the ignition delay and the time for the detonation wave to reach the open-end ($t_{\frac{1}{2}}$). When neglecting the ignition delay, as it is only a small fraction of the wave travel time, $t_{\frac{1}{2}}$ can be calculated via Equation 7.30.

$$t_{\frac{1}{2}} = \frac{L_{DC}}{D_{CJ}} \tag{7.30}$$

L_{DC} is the length of the DC and wave tube, which needs to be defined to perform the method presented here. Luckily, the L_{DC} has no effect on the thrust level, as a shorter shaft will reduce the amount of thrust per pulse, but increase the amount of pulses equally [14][24]. Consequently, the value for L_DC is of little significance. However, a length of 2 m was chosen which is based on real PDE designs and results in frequencies found in test data. That being said, A_{DC}/L_{DC} ratio should not exceed 0.5, as the method presented here will be invalid [60]. It is even questionable if geometries will even operate, as a relatively long shaft is needed for the detonation pulse [57].
The second relevant time stamp is when the forward rarefaction wave reaches the open-end (t_I), see Equation 7.31. The t_I is more relevant for no nozzle PDEs. Furthermore, [24] states the stationary conditions $_{DC,3}$ are not valid for the open-end. Hence, there is validity in not using them.

$$t_I = \frac{2L_{DC}}{D_{CJ}} \tag{7.31}$$

The third time stamp is when the reverse rarefaction wave reaches the open-end(t_{II}). After t_{II} the ejection of mass is merely powered by the remaining pressure in the DC and wave tube, which is revered to as the blow-down phase.

$$t_{II} = \frac{4L_{DC}}{D_{CJ}} \tag{7.32}$$

Next is the time stamp at which point all mass has been ejected (t_{III}). When using a linear decay from t_{II} to t_{III} Equation 7.33 can be used. The proof can be found in [24].

$$t_{III} = \left(1 + \left(\frac{\gamma_{DC,3}+1}{2}\right)^{\frac{\gamma_{DC,3}+1}{\gamma_{DC,3}-1}}\right)\frac{2L_{DC}}{D_{CJ}} \tag{7.33}$$

Lastly, there is the purge and fill time (t_{fill}), which is set at 0.002 s, in line with literature [14][24][57]. Purging is usually required to prevent early ignition. However, purge and fill can be combined by initially only injecting fuel via wall pours and injector, after which a less rich mixture is injected, to together reach the optimal F/O ratio. Note that $t_{cyc} = t_{III} + t_{fill}$. With t_{cyc} found the detonation frequency can be extrapolated, which is typically around 150 Hz [14] for non-breathing nozzles. Simulations are in line with literature and found a frequency of 159 Hz for the LH2/LOX pallet. The pulse mass is then equal to $\dot{m}/f_{cyc}$. The A_{DC} can be found by dividing the volume with the length, $A_{DC} = \rho_{DC,3} * \text{pulsemass}/L_{DC}$.

With the time stamps 4 phases are created to simulate the properties at 4, 2 of which are relevant for the thrust calculations. The first phase is from $0 < t < t_{\frac{1}{2}}$ which is the detonation phase. It is only at the end of this phase that the open-end reacts. Hence, the conditions are $U_4 = 0$, $\rho_4 = \rho_a$,and $p_4 = p_a$.
The second phase is the first exhaust phase where the shocks power the exhaustion and last from $t_{\frac{1}{2}} \leq t < t_{II}$. The flow velocity U_4 is given by Equation 7.34. Equation 7.34 illustrates that the moment the detonation reaches the open-end the flow velocity is equal to U_{CJ}. However, as more mass gets ejected less energy remains to expel the remaining mass. Unlike, conventional engines no constant stream of mass, means no constant stream of energy. The same pattern can is seen in the pressure and density illustrated in Equations 7.35 and 7.36.

$$U_4 = U_{DC,2} - \frac{2}{\gamma_{DC,2}+1}\frac{D_{CJ}t - L_{DC}}{t} \tag{7.34}$$

$$p_4 = \left(\frac{1}{\gamma_{DC,2}} + \frac{\gamma_{DC,2}-1}{\gamma_{DC,2}}\frac{L_{DC}}{D_{CJ}t}\right)^{\frac{2\gamma_{DC,2}}{\gamma_{DC,2}-1}} p_{DC,2} \tag{7.35}$$

$$\rho_4 = \left(\frac{1}{\gamma_{DC,2}} + \frac{\gamma_{DC,2}-1}{\gamma_{DC,2}}\frac{L_{DC}}{D_{CJ}t}\right)^{\frac{2}{\gamma_{DC,2}-1}} \rho_{DC,2} \tag{7.36}$$

The last exhaust phase is the blow down phase, for $t_{II} \leq t \leq t_I II$. The blowdown phase is computed following the procedure presented by [60]. Which give Equations 7.37 and 7.38 for the pressure and density, respectively. The flow velocity cannot be updated directly but is updated via Euler iteration using Equation 7.39, which follows from the derivative of Equation 7.2. x refers to the location of the DC and wave tube, here equal to L_{DC}. The derivative $\delta\rho$ is derived from Equation 7.38 and computed using the *derivative* function from scipy. Both the derivative w.r.t. dt and dx are computed this way.

$$p_4 = p_a + p_4(t_{II})\left(1 - \frac{t - t_{II}}{t_{III} - t_{II}}\right)^k \tag{7.37}$$

$$\rho_4 = \rho_4(t_{II})\left(\frac{p_4}{p_4(t_{II})}\right)^{\frac{1}{\gamma_{DC,2}}} \tag{7.38}$$

$$\frac{dU}{dt}(x) = \frac{U(x)\frac{\delta\rho}{\delta x}(x) + \frac{\delta\rho}{\delta t}(x)}{\rho(x)} \tag{7.39}$$

k is the decay factor and can be altered to fit better to the test data. k for this thesis was set at 2 as it is a good approximation of the test data, which is elaborated in Section 8.3.2. Moreover, only a small proportion of the thrust is generated in the blow down phase, thus little influence on the overall thrust magnitude.
Note the blowdown phase as described here lasts until the pressure in the DC is equal to the ambient pressure. Alternatively, the blowdown phase can be shortened by injecting propellant earlier. The maximum pressure at which early injection can occur is $p_{injector}$. For this operation, the t_{III} serves as the theoretical time to reach ambient pressure. Consequently, $t_{cyc} = t_{p_{DC}=p_{injector}} + t_{fill}$, which is substantially shorter, due to the reduced blowdown phase. The PDE module is constructed such that it can operate a variety of pulse waves, like the $p_{injector} = p_{e,final}$ method see function *thrust_nozzle_Pin* in the PDE module. Such pulse wave is significantly more powerful, as it increases the frequency by reducing the duration of the low thrust blowdown phase.
This operation is not the default simulation method, as early injection is more of an engineering challenge, due to premature detonation which reduce efficiency and can damage the engine.
This leaves the fill and purge phase for $t_{III} < t \leq t_{cyc}$. The properties are once again set at $U_4 = 0$, $\rho_4 = \rho_a$,and $p_4 = p_a$. In reality, some reacted left over mass gets rejected and pressure increases to $p_{DC,1}$. However, these effects are negligible compared with the thrust generated in the period $t_{\frac{1}{2}} \leq t \leq t_{III}$ and hence, they are assumed to be zero.
With that the properties at 4 are defined over the entire pulse period.

4 -> 8 Throat for PDE

[40] shows that the DC pressure is increased with a contracted throat area, which accelerates the mixture faster though the throat area, thus results in an I_{sp} gain. However, [57] argues that a reduced nozzle area will inflict shock losses, reducing the efficiency of the engine. With no consensus found in the literature, it was decided to exclude a contracting throat. Hence the mixture state and fluid properties are unchanged ($U_4 = U_8$, $p_4 = p_8$, $T_4 = T_8$, etc.). Therefore, no throat transition is required.

4 -> 9 Pulse Nozzle and Pulse Thrust

As must be clear by now, the frozen equilibrium, that is Equation 7.12, cannot be used, due to the unsteady operation of PDEs. However, the shifting equilibrium method does not require steady state, as it tracks mass from the throat to the nozzle exit instead of volume. If the process is steady iterative shifting equilibrium only has to be done once. Alternatively, if the process is unsteady then the operation must be repeated.

Hence, the thrust of the pulse detonation nozzle is simulated using the shifting equilibrium method with the kinematics switched off. The method is implemented with a slight alternation compared with what is described in Section 7.2.2. To compute the thrust of a single pulse Riemann's estimation rule is used, to integrate thrust over period t_{cyc}. This is done for n step in the period $t_{III} \leq t \leq t_{\frac{1}{2}}$, consequently dt is equal to $(t_{III} - t_{\frac{1}{2}})/n$. For each step the throat conditions are calculated as described under the wave tube transition. Each throat condition is then translated to its respective nozzle exit conditions, via the shifting equilibrium method described above. The instantaneous thrust is calculated using the same Equation 7.9. Each instantaneous thrust is multiplied by the time step dt, after which it is summed to provide total pulse thrust. The pulse thrust is multiplied by the frequency to give the total thrust. This procedure is mathematically written in equation 7.40.

$$T_{PDE} = \sum_{(t_{\frac{1}{2}}, t_{III})}^{i} \left(\dot{m} U_{9,i} + p_{9,i} A_{9,i}\right)(t_i - t_{i-1}) - p_a A_{9,i}(t_{III} - t_{\frac{1}{2}}) \tag{7.40}$$

$A_{9,i}$ is found by multiplying the throat area, which is equal to the DC area, with the expansion ratio ($A_{9,i} = A_{DC}\epsilon$). Note that the expansion ratio of a PDE is significantly lower than conventional engines, because of the generally larger throat area and the low throat pressures during each pulse. Low throat pressures prevent additional expansion as the nozzle could stall, due to atmosphere entering the nozzle.

With the above procedure a PDE engine with a conventional rocket nozzle can be simulated. However, this procedure requires significantly more computational power than previous methods. Unfortunately, this cannot be avoided. While, algebraic methods do exist for no nozzle PDEs [24], a similar method has not been developed for nozzle PDEs yet. Initial analysis showed that for a no nozzle PDE it is significantly more difficult to attain orbital capabilities in an SSTO setting. Therefore, nozzle PDEs with their more demanding computation cannot be avoided.

PDE Simulation and Set-Up

Just like the Aerospike module, the PDE has the convectional Module as a parent class too. However, none of the conventional transition functions can be utilised by the PDE module, besides from the nozzle transition. Yet, the PDE still needs the guidance functions and mass rate functions that are contained in the conventional engine module.

The PDE has different sizing parameters compared to the other discussed engines, namely the $p_{cc,max}$ and the L_{cc}. Setting $p_{cc,max}$ to 300 bar would be an unfair comparison as the turbo-pumps are not a limiting factor for the PDE. Additionally, little information about the large scale ground test of the rocket PDE done by Russian Lab is available. Hence, $p_{cc,max}$ is set at 600 bar, in Chapter 9 the sensitivity of this parameter will be evaluated. If future research indicates that a lower of higher value is more realistic, one should then compare the performance for a higher or lower T/W value, respectively, of this engine compared to the other engines. The L_{cc} was set at a probable 2 m length, but then again it does not influence the thrust calculation, thus matters little.

Lastly, the upper expansion ratio limit has to be altered due to the bigger throat and lower exhaust pressure at the end of each pulse. It was found that a max expansion ratio of ≈5 is small enough to prevent early nozzle stall during the take-off pahse[9].

Even though the PDE is an unsteady process, the module does not need to recompute the thrust components at each instance. The computation for U_e, $\dot{m}$, and p_e mostly remains (mostly) unchanged provided the operation parameters remain unchanged.

7.2.5. Methodology for the Precooled Hybrid Airbreathing Rocket Engine

With two of the three selected engines discussed, all that remains is the hybrid engine. The Hybrid engine is the only breathing type among the three and operates a Brayton cycle [75], thereby the only engine with

[9] All PDEs will stall eventually as the DC gets emptier reducing the exhaust pressure.

an intake (1->3) making it the most complex engine of all the selected engines. The intake stations are illustrated in Figure 7.8. The precooled hybrid airbreathing rocket engine can have many configurations, which have great consequences on the simulation of such an engine. Fortunately, the configuration options can be limited by applying the logic of Chapter 2. To reiterate Chapter 2, the potential performance simulated in this thesis should be attainable, through upgrades and augmentations, in a foreseeable time frame. Additionally, The engine should have a T/W ratio well above 1.

Therefore, the task is to determine which technological developments can be achieved over such a time

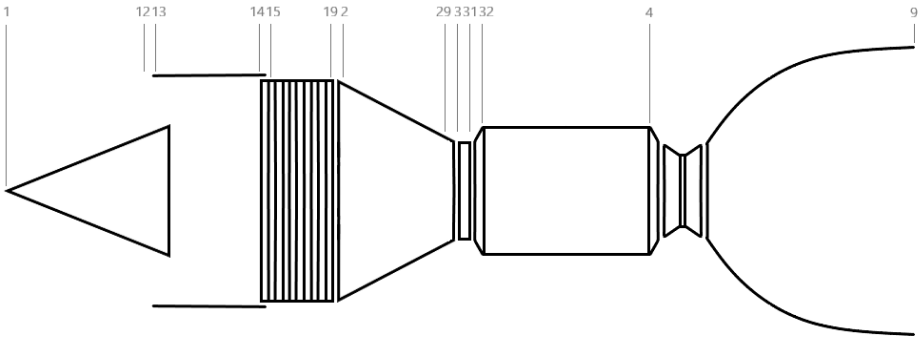

Figure 7.8: Illustrates the engine stations of a precooled hybrid airbreathing rocket engine.

frame. A major point of failure in the development of the X-30 was the integration of multiple propulsion systems into a single main propulsion system. This is the prime reason to exclude the integration of an afterburner, which is contrary to the proposed SABRE design, see Figure 4.7. Further arguments are, the substantially lower T/W ratios of afterburners (unsuited for VT) and the short operational range during the earlier/mid breathing phase M ≈ 3, were roughly 2/3 of the intake air is passed through the bypass afterburner. Hence, the precooled hybrid breathing rocket engine considers a homogeneous uniform propulsion system, where the homogeneous refers to a single propulsion type and the uniform refers all engines operating in the same phase.

Following the logic of Chapter 2, the design choice of each component (transition) is discussed, starting from the nozzle and working towards the inlet. The CC (32->4) and nozzle (4->9) are similar to that of a conventional engine. The exception is that the CC operates at the High Pressure Compressor (HPC) pressure (p_{29}), throughout the breathing phase. Furthermore, the injectors do not require any development, because they are based on off-the-shelf aero engine and rocket engine injectors.

Which leaves the intake (1-.29), the subsystem that is the driver behind the increased performance. The compressor (2->29) might appear as the most complex component, nonetheless it is actually the least complex. Rocket Reaction, the company behind SABRE, claims that an industrial standard HPC can be used, which is in line with other Turbine Based Combined Cycle (TBCC) concepts [75][66], of which some are described in Section 4.3.

The next component is the heat exchanger (15->19), which is also the most crucial component, because it directly controls the effectiveness of the engine and is the limiting factor for hybrid engine. The reason for this is, for the hydrogen to cool the substance to 80 K [75], the tubes need to be extremely narrow. Consequently, when the air gets too hot, the tubing might fail. This is exacerbated by hydrogen embrittlement [75]. Therefore, the more heat the tubing can resist and the better it cools the air, the longer the breathing phase lasts (HPC choke limit), the better the performance. This means that all foreseeable developments should be dedicated to the heat exchanger, which appears to be the development path of Rocket Reaction too. As a result, complexity in this component cannot be avoided and complexity of other components should be limited.

For the above argument, TRL and complexity of the inlet (1->14) is kept at a manageable level. Hence, a simpler intake is chosen than those proposed in [65] or [75]. Instead, the more achievable oblique-normal shock inlet, evaluated in [66], is chosen. The proposed inlet utilises two shocks, namely an oblique shock (1->12) and a normal shock (13->14), to slow down the flow and increase static pressure. The oblique shock is managed by an extendable ram inlet. The ram inlet is extended such that the oblique shock just avoids intersecting the edge of the outer wall at 12, as is illustrated in Figure 7.9. The normal shock makes the flow

subsonic which should slow the flow enough for the heat exchanger[10].
The closed intake drag should be minimised and not create an additional leading edge or high drag surface(s)

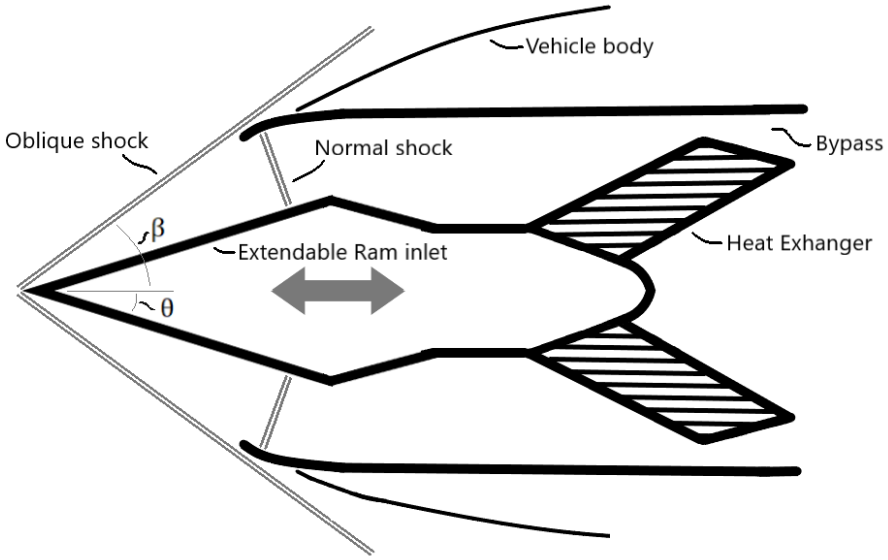

Figure 7.9: Illustrates the oblique shock and normal shock interaction for the intake of an integrated precooled hybrid airbreathing rocket engine.

for the vehicle [84]. Hence, the engine should be integrated into the vehicle's body, which should be imaged to have a similar shape as the X-33 or Delta Clipper, as discussed in Section 6.2.4. Additionally, the leading edge turbulence should not interfere with the intake, as this can disrupt the engine's performance[75]. Therefore, the intake should integrate into the leading edges, with the exception of the nose. The nose serves as the primary heat shield upon reentry, thereby experiences the highest heat peaks. Merging the two systems will reduce the TRL beyond a level for which it cannot be attained within a foreseeable time frame.
While, it might have appeared obvious to use a circular inlet geometry, like SABRE, a square inlet is more optimal, as this results in a larger intake area and would fit better in the leading edge of the vehicle.

1 -> 12 Ram Inlet or Oblique Shock Inlet
As previously discussed, the flow velocity needs to be reduced and the static pressure increased, for which the first step is an extendable ram inlet. As the Mach number increases the shock angle (β) decreases, the ram inlet is extended to prevent the shock from entering the inlet, as is illustrated in Figure 7.9. The shock entering the inlet can cause unwanted shock reflection interactions and hotspots, both diminish performance and can cause failure. As the intake extends the intake area gets smaller until the intake is completely closed off.
When the intake is closed-off the air intake mass is set to zero and the engine operates as a conventional rocket engine. If the mass flow is subsonic station 1 is equal to station 12 (1=12) and the ambient conditions are passed along.
Else, β can be found with Equation 7.41 taken from [9] and is known as the $\beta-\theta-$M equation. θ is the ram angle illustrated in Figure 7.9 and M is of course the Mach number, both of which are known. Therefore, β can be solved from Equation 7.41. However, one may have noticed that the $\beta-\theta-$M equation has two solutions. The solutions refer to the strong and weak shock, the former having the larger β. Luckily, strong shocks can only be artificially induced hence the algorithm is configured to always provide the lower solution. The algorithm uses the *minimize* scipy function, where the upper bound and initial guess are set by custom functions f(θ) that can be found in the intake module.

$$tan(\theta) = 2cot(\beta)\frac{M_1^2 sin^2(\beta-1)}{M_1^2(\gamma+cos(2\beta))+2} \tag{7.41}$$

Furthermore, a maximum β exist for a given M. This means that if θ is too small the shock will detach form-

[10] If the flow in the heat exchanger is too fast, the flow will stall between the tubes, causing hotspots and a significant increase in intake drag.

ing a bowl shock. In this instance $\beta_{\max}$ is used, which serves as an average shock angle[11]. Fortunately, the detached shock only lasts <10s and occurs when the vehicle transitions from subsonic to supersonic flight (M<1.3). Detached shocks should be avoided as this thesis approximates the average conditions behind such a shock, which therefore are less accurate than the attached shock conditions.
The β is important as it allows oblique shock to be approximated by a normal shock, for which the equations can be found in the next transition. To elaborate, oblique shocks have a normal component that can be treated as a normal shock [9], from which the normal flow properties behind the shock are computed. Next, the post-shock normal component is converted back to get the total component. To obtain properties of the normal component properties Equations 7.42 and 7.43 are used, where the subscript $_n$ indicates the normal flow with respect to the shock.

$$M_{n,1} = M_1 sin\beta \tag{7.42}$$

$$M_{12} = \frac{M_n, 12}{sin(\beta - \theta)} \tag{7.43}$$

With the parameters θ and β the intake area (A_{in} or A_1) is calculated using some simple algebra. The mass rate unsurprisingly scales linearly with the dimensions. The intake area requires a small area to achieve substantial mass rates, for an effective intake area of ~5 m^2 at Mach ~3 roughly 6000 kg/s of intake mass is reached. Note that the intake area decreases as the Mach number is increased, due to the shock angles decreasing, see Figure 7.9.
With Equation 7.42, $M_{n,1}$ is used in the normal shock Equations 7.44, 7.47, and 7.46, the latter two are provided in the next transition section. Replacing M_1 with $M_{n,1}$ does not change the other flow property conversion. Hence, the flow properties behind the shock are obtained, which are used to update the Cantera *Mixture*.
The reader needs to be made aware that the methodology provided here does have its limitation. Firstly, the $\beta - \theta - M$ Equation 7.41 only holds for 2-D dynamics and is therefore only valid for linear square intakes, like the one considered in this thesis. Secondly, the method tends to break down as hypersonic speeds are reached. In this instance the temperature difference break the assumptions of calorical gas and isentropic flow, which is not a problem in this simulation as the intake closes long before the hypersonic region (Mach 5.5). Thirdly, the above method assumes a sharp point ram intake. However, in reality the point is blunt. The level of bluntness is determined by the reentry conditions, which are beyond the scope of this thesis. This is mostly limited to blunt inlet point/nose, for which the effects are minor and can be ignored [9]. However, for larger blunt intake noses that substantially effects the intake shape, the effect is more substantial an can result in inlet efficiency losses.

13 -> 14 Normal Shock Inlet
The normal shock inlet transition simulates a normal shock if the flow is (super)sonic, otherwise the transition simply passes on the state (13 = 14), like the oblique shock inlet. A normal shock will always make the flow subsonic, therefore reduces the flow velocity to acceptable levels for the heat exchanger. The oblique shock is required to get a sufficient density[12]. The normal shock increases the density too, but not enough on its own.
To obtain the Mach number after the shock, Equation 7.44 is used, which was taken from 7.1.3. Equation 7.44 is derived from the momentum equation 7.3, which is rewritten into $p/(\rho U) + U = const$. Next is to replace p/ρ with the speed of sound, a, via Equation 7.8. Finally, the energy equation 7.4 is introduced with the alteration $h = a^2/(\gamma - 1)$. With some algebra Equation 7.44 can be obtained. For a step-by-step derivation one is referred to [9].

$$M_{14}^2 = \frac{1 + \left((\gamma - 1)/2\right) M_1^2}{\gamma M_{13}^2 - (\gamma - 1)/2} \tag{7.44}$$

To obtain the flow properties behind the shock transitional equations are required. Before these can be derived Equation 7.45 has to be given, with the subscripts up & down refer to the upstream and downstream with respect to the shock, respectively. The M^* is the characteristic Mach number and a pivotal parameter in the study of compressible flow dynamics. The implications and significance of the function is beyond the scope of this thesis, but elaborately discussed in [9]. For this thesis it is only relevant to know that M^* is a

[11] due to the bowl shock, all flow lines have different β's, which is required to accurately predict CFD.
[12] The oblique shock increase density before the flow enters the engine, therefore a smaller intake area is needed for the same amount of mass

characteristic of a specific flow, determined by the properties before and after the normal shock. Moreover, M^* is bound between 0 and $\sqrt{(\gamma+1)/(\gamma-1)}$ for M = 0 and M = ∞, respectively.

$$M^{*2} = \frac{U^2}{U_{up}U_{down}} = \frac{(\gamma+1)M^2}{2+(\gamma-1)M^2} \tag{7.45}$$

Starting from the continuity equation 7.2 it can be transformed to match Equation 7.45, illustrated in Equation 7.46. With Equation 7.46 the density ρ_{14} and flow velocity U_{14} can be computed, Which leaves one more state property to update the Cantera *Mixture*.

$$\frac{\rho_{14}}{\rho_{13}} = \frac{U_{13}}{U_{14}} = \frac{U_{13}^2}{U_{13}U_{14}} = \frac{(\gamma+1)M_{13}^2}{2+(y-1)M_{13}^2} \tag{7.46}$$

By starting from the momentum Equation 7.3 a pressure transition equation can be found with a similar procedure as the one used for the density and flow velocity, although it is slightly more tedious. Again, the step-by-step derivation is found in [9]. Thus, p_{14} can be computed via Equation 7.47.

$$\frac{p_{14}}{p_{13}} = 1 + \frac{2\gamma}{\gamma+1}\left(M_{13}^2 - 1\right) \tag{7.47}$$

With that that the normal shock inlet transition is completed.

The more aero engine familiar reader might have noticed the absence of the Total Pressure Ratio (TPR) for the inlet, which is generally the ratio between the total pressure after the inlet over the total freestream pressure (TPR = $p_{pri,0}/p_{aft,0}$). In this thesis the TPR is set to 1, as was the case in [25], which nullifies its effect. [25] neglected the TPR due to its minor effect on the SABRE engine, especially compared to the effect of the shocks. However, the TPR can be calculated with Equation 7.48, were $\eta_{k,inlet}$ is the kinetic efficiency ($\eta_{k,inlet}=U_{pri}^2/U_{aft}^2$). The subscripts $_{pri}$ and $_{aft}$ refer to the flow before and after the inlet, respectively. The TPR is discussed for the sake of completeness and for future research that aims to include more detail.

$$TPR = \left(1 + 0.5\left(\gamma-1\right)\left(1-\eta_{k,inlet}\right)M_{pri}^2\right)^{\frac{-\gamma}{\gamma-1}} \tag{7.48}$$

15 -> 19 Heat Exchanger
SABRE's heat exchanger is tasked with cooling the subsonic flow to the pinch point (≈ 80 K), within a fraction of a second (0.01 s). Thereby, cooling the air near the saturation point but not beyond liquefaction.
To compute the heat transfer between flows Equation 7.49 is used, which is the method presented in [80] and [23]. Equation 7.49 contains a minimise function as the heat flow is limited by how much heat can be given or by how much heat can be received.

$$q = E_{cooler}\,min(c_{p,air}\dot{m}_{air}, c_{p,f}\dot{m}_{fuel})(T_{15} - T_{f,storage}) \tag{7.49}$$

E_{cooler} is the effectiveness of the heat exchanger and therefore an additional design parameter. The computed heat is added to the fuel *Mixture* and subtracted from the air *Mixture*. As a result, the fuel flow into the CC has a higher injector heat than the preset 500 K. How much higher is determined by the heat transferred. Unfortunately, the heat exchanger forces the air past many small tubings, causing a pressure loss ($\kappa_{cooler,loss}$). p_{19} can simply be calculated by $p_{19} = p_{15}(1-\kappa_{cooler,loss})$.
With that the Cantera *Mixture* can be updated as two thermodynamic properties are known at station 19, namely h and p.

2 -> 29 High Pressure Compressor (HPC)
As described earlier in this section, TBCCs including the hybrid engine are meant to operate an off-the-shelf HPC that is amplified for higher pressure ratios. The amplification is possible as the intake air is far cooler than regular air HPC compress in conventional aero engines. Because of the use of a conventional HPC, general performance analysis method for aero engines can be used, as those described in [59].
The procedure starts with the assumption that the flow through the compressor has negligible velocity. Hence, the total conditions become the true conditions. The total conditions are be computed using Equations 7.14 and 7.15. The compressed pressure (p_{29}) is then computed with Equation 7.50.

$$p_{29} = \Pi_{comp}p_2 \tag{7.50}$$

Equation 7.50 introduces a new sizing parameter, namely the HPC pressure ratio Π_{comp}, which is a varying parameter in some studies [25]. However, Π_{comp} is fixed to cruise values in this thesis.
With pressure p_{29} the respective temperature can be computed using equation 7.51.

$$\frac{T_{29}}{T_2} = 1 + \frac{1}{\eta_{ise,comp}} \frac{p_{29}}{p_2}^{\frac{\gamma_2 - 1}{\gamma_2} - 1} \tag{7.51}$$

Equation 7.51 introduces the isentropic efficiency of the compressor ($\eta_{ise,comp}$). Note like the $\kappa_{cooler,loss}$, $\eta_{ise,comp}$ is a limitation of the design, thus a design parameter. If one were to remove $\eta_{ise,comp}$(=1) from Equation 7.51, one would see that Equation 7.51 is derived from the isentropic Equations 7.6 and 7.5.
With the flow having negligible velocity ($U_{29} = 0$), properties of station 29 have all been defined, rounding up the HPC transition.

3 -> 31 Injector
The hybrid injector uses the convectional method as described in Section 7.2.2, with the additional *Mass-Flower* for the compressed intake air. Luckily, the injector function is built such that any number of additional mass flows can be added. Each additional mass flow requires the mass rate and *Mixture* object which contain the composition.
Note that the mass flow of the LOX in the breathing phase is not necessarily cut off. This is left to the optimisation module. The reason for this is the requirement of sufficient thrust for VT, established in Chapter 3. To reiterate, the RB545 and SABRE are designed for HT vehicles and thus required lower thrust levels.

32 -> 4 Combustion Chamber
Even though the CC of the hybrid engine has to deal with an additional *MassFlower*, inherently it varies little from a thermodynamic perspective. Hence, the same reactor object approach described in Section 7.2.2 can be utilised. However, a slight alteration is made during the breathing phase. During breathing intake mass is compressed by the HPC after which it is injected into the CC. However, the compression pressure achieved by the HPC is far lower than the injector pressure achieved by the turbo-pumps of the rocket engine, as these inject a high pressure liquid. Hence, for the breathing phase the p_{cc} is equal to the pressure of the compressed air ($p_{29} = p_{32}$).
As discussed before, the bypass of the SABRE engine is not simulated. However, with the prior transitions it is relatively easy to implement and model an bypass afterburner. This alteration would require the addition of the bypass ratio, the ratio of intake air going to the bypass over the intake mass going to the precooler, and the bypass F/O ratio.

4 -> 9 Nozzle
The nozzle is simulated via the frozen equilibrium method described in Section 7.2.2. However, with a slight alteration to Equation 7.9. This is necessary as the derivation of Equation 7.9 only considered mass being ejected from the system. However, the breathing engine also collects mass. Therefore, Equation 7.9 is modified with the aero engine thrust equation from [59] to form Equation 7.52.

$$T = \dot{m}_{prop} U_e + \dot{m}_{intake}(U_e - U_a) + A_e(p_e - p_a) \tag{7.52}$$

Where $\dot{m}_{intake}$ is the air mass flow and U_a is the freestream flow velocity of the intake air, due to neglecting the effects of the angle of attack and wind speeds.

Precooled Hybrid Airbreathing Rocket Engine Simulation Set-Up
Unlike previous propulsion modules, the Hybrid module has far more interactions with the ambient atmosphere, which continuously changes the operational conditions. Hence, the thrust magnitude has to be recomputed every iteration during the breathing phase. In the non-breathing phase the hybrid engine module operates exactly as the conventional module.
Next to the engine cut-off conditions, described in Section 7.2.1, the hybrid engine contains intake-closed conditions too. Four intake-closed conditions are programmed into the module, which relate to the intake limitations or inefficient breathing operations. The HPC choke limit is achieved when T_{29} exceeds 1300 K. Whereas, the inlet has a maximum Mach number at which point it becomes ineffective (stall) or induces too large a drag penalty, for SABRE this is at Mach 5.5[25].

The remaining two intake-closed conditions deal with inefficient breathing operations and are introduced to ensure that the breathing phase is only commenced once sufficient thrust is generated. Therefore, a minimal intake mass rate equal to 10% of the propellant mass rate is required, as a lower mass rate does not justify the reduced p_{cc} accompanied with breathing phase. The last constrain is a minimal p_{cc} of 50 bar, at which point the reduced U_e does not outweigh the increase in total $\dot{m}$.
The inlet of the hybrid engine requires additional sizing parameters, and the consequential design parameters, to simulate the operations. The sizing parameters consist of the ram angle (θ), the HPC pressure ratio (Π_{HPC}) and the heat exchanger effectiveness (E_{cooler}). Whereas, the design parameters consist of the heat exchanger pressure loss ($\kappa_{cooler,loss}$) and the HPC isentropic efficiency (η_{HPC}). The respective value are set at $\Pi_{HPC} = 85$, $E_{cooler} = 0.8$, $\kappa_{cooler,loss} = 0.03$, and $\eta_{HPC} = 0.83$, which are taken fromm [25] and are based on the cruise conditions of the SABRE engine. [25] evaluated multiple intake areas (A_{intake}), ranging from 10.4 m^2 to 37.2 m^2. This thesis settled for an area of 11.0 m^2 equivalent to roughly 10% of the reference area. It is believed that a larger area would not only invoke too large a drag penalty, but it also does not transform the ascent vehicles into the flying engine vehicles that Chapter 3 excluded from consideration. The ram angle (θ) is set at 20°, which is extrapolated form schematics of SABRE, as the ram angle is not published. This ram angle ensures a prolonged attached shock, see Figure F.1, which would impose a drag penalty. Currently, a detached shock has no direct effect on the performance as the static aerodynamic module has no build in drag penalty.

8

Verification and Validation of the propulsion modules

To what extent are the performance analysis of the selected engines a realistic representation? This question must be answered after Chapter 7, due to the unconventional engines discussed in Chapter 7, it is necessary to verify each propulsion module. Most relevant is the verification and validation of the base module, the conventional engine simulation. Additionally, verification and validation tests are performed on the selected propulsion modules, even though these tests cannot always be done to the same extend as the conventional tests, due the lack of available flight performance tests/data.
The propulsion modules can be verified separately and independently, due to their modular nature, which leads to a better understanding of the individual limitations. Next to the verification and validation functions, numerous unit tests are included to verify each transition function. Only the most relevant unit, validation, and verification test are discussed in this chapter, the remaining tests can be found in the code.
The chapter will asses the verification and validation of each propulsion module, including and starting with the conventional engine module. The verification and validation process aims to validate the model to real-world examples. For those instances in which no direct observation data could be found, references from literature were used instead. After the discussion on the conventional engine module, the chapter proceeds the discussion on each of the selected propulsion modules in the same order as Chapter 7.

8.1. Verification and validation of the Base propulsion module

The conventional propulsion module contains two methods to compute the exhaust conditions, both of which will be verified and validated in this section. The verification and validation are done simultaneously and are done by comparing the exhaust conditions, which are U_e, p_e, and A_e.
The verification parameters are extrapolated from CEA [1]. CEA is a conventional engines propulsion simulator developed by NASA and widely used in the industry for performance analysis. The tool is versatile in the propellant selection, therefore all selected propellants can be simulated. Additionally, the tool contains both the frozen and shifting equilibrium methods. CEA is openly available and free to use, the URL can be found under [1].
CEA, like the methodology provided in Section 7.2.2, requires operation parameters to run the simulation. A range for each operation parameters can be given, CEA returns a text file containing the performance parameters for each set-up. Some of the operational set-up outcomes will be reported here, the other set-up parameters have been checked but are not reported on. The entire file extracted from CEA can be found in appendix C.
Real world engines are used for the validation of the conventional engine module. These engines are the SSME (or RS-25) for an LH2/LOX propellant pallet and the Raptor engine for an LCH4/LOX propellant pallet. Unfortunately, no acetylene/LOX flown engine exists, therefore validation to a real engine is impossible.
Each of the following section will cover one propellant pallet and present the findings.

8.1.1. Verification and Validation on an LCH4/LOX powered Engine

Table 8.1 provides the exhaust parameters for the frozen equilibrium method, the shifting equilibrium method, the CEA generated values, and the published values of the Raptor engine. Five values are presented, starting with the modules presented in Chapter 7, namely the frozen equilibrium method and the shifting equilibrium method. The values in the brackets under the shifting equilibrium method are the values with the reaction kinematics switched off.
To continue, the next two columns contain the values extracted from CEA. The entire output file can be found in Appendix C. The first column contains the frozen equilibrium, while the second column contains the shifting equilibrium approach.
The last column contain the publicly available data on the Raptor engine. The fact that it contains publicly available data must be stressed here, as these are performance specs published by the company SpaceX. Hence, the data has not been review on the correctness. Additionally, the question can be raised how beneficial it is for SpaceX to inflate the performance numbers. As such, the numbers should not be taken as an absolute, but rather a good indication of what to expect.
The values of Table 8.1 are computed at SL with the following found values; $\dot{m}_{LCH4} = 510$ kg/s, $\dot{m}_{LOX} = 140$ kg/s, the exhaust diameter $d_{cc} = 1.3$ m, $\epsilon = 34.34$, and a $p_{cc} = 300$ bar. Note that any discrepancy in these numbers will cause differences between the performance specs of the Raptor engine and the outcomes of the model. As can be seen in Table 8.1 the exhaust area's are missing for the CEA columns. Unfortunately,

Propellant Pallets	Frozen Equilibrium	Shifting Equilibrium (no kinematics)	CEA Frozen Equilibrium	CEA Shifting Equilibrium	Raptor Engine
Exhaust velocity [m/s]	3279	3830.40 (3263.89)	3236.5	3401.9	3210
Exhaust Area [m^2]	1.344	1.344 (1.344)	-	-	1.327
Exhaust Pressure [atm]	0.7825	0.660 (0.719)	0.723	0.967	-
Thrust [kN]	2102.67	2446.90 (2083.38)	2066.48	2206.76	2197.44/ 2268.59

Table 8.1: Compares the modelled raptor exhaust conditions to the actual exhaust conditions at SL, with the operational settings of p_{cc}=300 [atm], ϵ=34.34 [-], $\dot{m}$=650 [kg/s], and F/O=0.275 [-].

CEA does not compute any area's, rather it defines $A_r = 1$. Moreover, The thrust value for CEA was computed with Equation 4.1 using A_e from the Raptor engine column. Furthermore, the exhaust pressure for the raptor engine is missing, as this is not publicly available.
With the omitted values discussed, Table 8.1 can be analysed. To start with the obvious, the shifting equilibrium methods. Both methods are too optimistic (6% to 20% for the U_e) about what can realistically be achieved, which is expected from the shifting equilibrium. What is more remarkable is the difference between the two. At first, it appears that the frozen equilibrium method from this research has a higher U_e due the over-expansion compared to the CEA shifting equilibrium and thus the p_{cc}. However, the contrary is true. If the overexpansion were the culprit, the same phenomenon would also be seen between the two frozen methods when the kinematics are switched off. Furthermore, the thrust of the produced by the shifting equilibrium methods should be lower than the CEA shifting equilibrium, as the latter operates closer to the ideal SL settings due p_{cc} being closer to 1 atm.
Both observations point towards the kinematics of Cantera. As it turns out, Cantera computes a higher rate of reaction than CEA. Therefore, the mixture has a more complete combustion and a reduced presence of radicals, thereby converting more chemical energy into kinetic energy. Further evidence of the higher reactivity is found when comparing T_{cc}'s which were 3809 K and 3767 K for Cantera and CEA, respectively.
The overexpansion is a result of the higher energy conversion to kinetic energy, which increases the U_{nozzle}, therefore expanding the flow faster by increasing dx faster, see Section 7.2.2.

To continue, the U_e produced by the frozen equilibrium methods is within 0.5-2% of the each other and the available exhaust velocity of the Raptor engine. Additionally, the computed A_e is incredibly accurate and might be the true value, as the diameter from which the area was computed might have been rounded.
However, when studying the thrust the accuracy deteriorates. It is believed that this is due to the larger ex-

haust area, which causes a slight overexpansion in the model. As described above, before a lower p_{cc} is further from the ideal and thus results in a lower thrust. However, such reasoning would not explain the entire difference. Furthermore, the thrust levels are believed to be inflated. For the Raptor engine two thrust level are provided, the smaller follows from the 140 T/W ratio and the engine mass and the other coming from the given value of 510,000 lb_f. It is acceptable to presume these have been rounded up and do not present the actual values.
All in all, the frozen equilibrium and shifting equilibrium without kinematics are well within the uncertainly levels of the actual Raptor values, deviating only 1% and 2% from the actual CEA and actual value, respectively. Even though the impression can be caused by the slight overexpansion, this is compensated in the optimisation of ϵ. Besides, the ϵ found in this research should be taken as a good indication but not as a final design parameter. Hence, no problem should exist if the ϵ is off by a few decimal places. The deviation between CEA and the model is probably due to different injector temperatures, illustrating their minor effect.
Hence, the Cantera based methodology is sufficient accurate to simulate the combustion processes of rocket engines. Moreover, the base model is satisfactory to simulate the LCH4/LOX powered conventional engine too. Note that for reasons stated previously CEA cannot be integrated with python.

8.1.2. Verification and Validation on an LH2/LOX powered Engine

The analysis on the LH2/LOX propellant pallet follows the same procedure as in the previous section. In this instance the RS-25 engine is chosen as a reference. The columns of Table 8.2 contain the same computational methods as those presented in Table 8.1.
The values in Table 8.2 were generated with the following operational settings; a $\dot{m}$ = 514.49 kg/s, an exhaust diameter d_{cc} = 2.4 m, a ϵ = 78.1, a p_{cc} = 206.42 bar, and a O/F = 6.03. Unlike, the raptor engine, these values are decimal numbers published by a government organisation. Hence, they are more reliable in terms of being exaggerated or due to discrepancies. A more familiar reader, may recall that the RS-25 is the refurbished SSME for the SLS. However, it must be stressed that the values above are explicitly for the RS-25 set-up and they deviate from the SSME set-up.
When scanning the exhaust velocities, it appears that all the models are performing poorly. Yet, closer exam-

LCH4/LOX Propellant Pallet	Frozen Equilibrium	Shifting Equilibrium (no kinametics)	CEA Frozen Equilibrium	CEA Shifting Equilibrium	RS-25 Engine (SSME)
Exhaust velocity [m/s]	4321.96	4584.79 (4279.50)	4246.4	4398	3590[1]
Effective I_{sp} [s]	367.54	390.15 (359.40)	356.14	373.86	366
Exhaust Area [m^2]	4.524	4.524 (4.524)	-	-	4.524
Exhaust Pressure [atm]	0.190	0.150 (0.154)	0.157	0.183	-
Thrust [kN]	1855.04	1969.15 (1813.95)	1797.81	1886.93	1859.36

Table 8.2: The table above compares the modelled RS-25 exhaust conditions to the actual exhaust conditions at SL, operational settings are p_{cc}=206.42 [bar], ϵ=78.1 [-], $\dot{m}$=514.49 [kg/s], and O/F=6.03 [-].

ination reveals that the U_e of the RS-25 is the effective exhaust velocity[1]. Hence, the U_e's cannot be directly compared. Therefore, the additional row with the effective I_{sp} is added. The effective I_{sp} is calculated by dividing the thrust by the propellant mass flow and g_0. The cEA thrust values are calculated as in Section 8.1.1 using Equation 4.1. Studying Table 8.2 reveal the same patterns as in Table 8.1, which are discussed in Section 8.1.1. For the frozen methods, the U_e are all within 2% of each other. Moreover, the effective I_{sp} are all within 2% compared to the RS-25. Especially, the thrust and effective I_{sp} of the frozen equilibrium presented in this research is remarkably accurate. Furthermore, as the values of NASA are more reliable, it gives even greater confidence to the methodology presented in this research.
The shifting equilibrium present the same inaccuracies with the same reasons as for the LCH4/LOX propel-

[1]As far as the author is aware of, only the effective exhaust velocity of the RS-25 was published by NASA.

lant pallet, described in Section 8.1.1.
Only the pressures of the frozen methods of this research and that CEA, showed a larger difference than the one observed in 8.1. One explanation could be the difference in the Cantera and CEA reaction models, as the T_{cc} are 3647 K and 3604 k, respectively. Nevertheless, the frozen equilibrium method presented in this paper, seems to be the more accurate model.

8.1.3. Conclusion on the reliability of Conventional Rocket Module

All in all, the tables presented in this section give merit to the methodology described in Section 7.2.2. The accuracy by the presented frozen equilibrium method shown in Tables 8.1 and 8.2 give great confidence in the findings produced using this method.
Even though, the shifting equilibrium method with kinematics switched-off illustrated a lower accuracy, it deviated 1-2% in terms of thrust calculations. Hence, it is the author's believe that this method can still be used to as a potential performance indicator. More importantly, the deviation was always an underestimation. Hence, the modules that utilise the shifting equilibrium methods are more likely to be underestimates of the true potential.

8.2. Verification and Validation of the Aerospike

As described in Section 7.2.3, the methodology for simulating the aerospike follows the exact same procedure as the convectional engine. The only adaptation is that the ϵ is made to vary until it reaches an upper limit, which translates into an increasing I_{sp} with altitude. The I_{sp} flat-lines the moment the max ϵ is reached. This phenomenon can be seen in Chapter 9.
Considering, the above reasons the module is verified, which leaves the validation. The computed values are validated with parameters of the XRS-2200 engine. Such validation should give a better understanding how well the methods in this research represent reality.
The same parameters were used as those published by Boeing Rocketdyne [2], which are ; ϵ_{max}=58 [-], O/F = 5.5 [-], p_{cc} = 58.88 [bar]. The performance parameters in Table 8.3 were taken from [2] too. To obtain simulated parameters the mass rate is required, which unfortunately is not public information. Moreover, the provided I_{sp} are not the effective I_{sp}. Hence, the mass cannot be computed. While, the I_{sp} at SL should be equal to the effective I_{sp}, in reality losses can be up to 7% [78]. However, the $\dot{m}$ from $T_{SL} = 9.81 I_{eff.sp,SL}\dot{m}$ can be used as indication, which gave 276.38 kg/s. A mass rate of 260 kg/s, aligns with the approximated vacuum thrust. At vacuum the aerospike is almost 100% efficient, so the computed p_e and A_e are very close to reality, which were already validated in Section 8.1. Hence, all values in Equation 4.1 are known with high certainty except for $\dot{m}$.
Evaluating the vacuum parameters, the I_{sp} are incredibly close. As expected the computed value is a little

LCH4/LOX Propellant Pallet	Aerospike Method	XRS-2200 Aerospike
Thrust vac [kN]	1153.23	1161.88
Effective I_sp vac [s]	434.26	428.2
Thrust SL [kN]	949.41	917.22
Effective I_sp SL [s]	372.23	338.3

Table 8.3: Compares the performance parameters of the aerospike model to the XRS-2200, with the operational settings of $\dot{m}$ = 260, O/F = 5.5, p_{cc} = 58.88 bar, and ϵ = 58.

higher,as the model approximates an aerospike as an ideal CD nozzle and the XRS-2200 was a prototype. Hence, performance being less that optimal is to be expected. Evaluating the SL parameters, larger deviations are observed. The thrust is overestimated by roughly 3-4% and the I_{sp} is almost overestimated by 10%. Again the deviations expected to be caused by the approximation method and the fact that the XRS-2200 was a prototype. The error is exacerbated due to the engine being operated further from its design ϵ. It is expected that the aerospike does not expand the flow to the ambient pressure ($p_e \neq p_a$), which would reduce both the I_{sp} and thrust.

The deviations are within the maximum expected level as stated in [78]. An expansion factor (κ) could be introduced which would calculate the $P_e = \kappa \ p_a$. However, in reality this factor changes and approaches 1 as

the engine operates close to its design ϵ. Furthermore, the deviations are only large in the lower parts of the atmosphere, where an aerospike ascent vehicle is expected to only operate briefly.
Therefore, it is is decided to use the model with no expansion factor, with the consequence that the thrust is overestimated when the engine operates far from the design ϵ. If it is kept in mind that the results for the aerospike powered ascent vehicle will be overestimated, especially if the vehicle operates for a significant margin in the lower atmospheres far from its design ϵ, the model can be used to get a good indication what the theoretical performance of an aerospike powered SSTO should be.

8.3. Verification and Validation of the Pulse Detonation Engine

As described in Section 7.2.4 the PDE operates very different transition functions than the base module. Therefore, more extensive verification and validation will be needed. The verification will be done by evaluating the transitions. While, the validation will be done by comparing the pressure levels for a single pulse cycle. Recall that in Section 4.2.6 a quick-and-dirty approach was utilised for the simulation. Hence, Section 8.3.2 illustrates that combining the transitions functions in a particular way, the pressure over the duration of a pulse cycle can be imitated.

8.3.1. Verification Pulse Detonation Engine

Each transition functions provides key state parameters as described in Section 7.2.4 under the subsection DC and Wave Tube. Therefore, each of the transitions can be verified separately. Luckily, [24] provides a numerical example for others to verify whether the relations have been implemented correctly. The values of this numerical example is used to verify the transition functions. The outcome of the comparison are found in Appendix E. The values are all within reasonable levels, more so when one considers that [24] uses rounded number too.

8.3.2. Validation Pulse Detonation Engine

The validation is done hand-in-hand with the varying pulse pressure simulation, meaning that the method that best presents the data is chosen to simulate the thrust.
Three methods were considered and compared to experimental data. All methods start with the forward rarefaction wave, as this is clearly seen in the data [32][46]. The first implements the Chapman-Jouguet (CJ) detonation wave ($_{DC,2}$) followed by the stationary exit conditions ($_{DC,ex}$) and finished with the blow down phase. This is the method briefly proposed by [24]. The pressure profile produced by this method can be found in Sub-figure 8.1b.
The second method, treats the open-end as a midpoint in the DC. This method has some merit as the open end of the DC is followed by the nozzle. Hence, the nozzle is seen as a partial extension of the DC. Therefore, the method implements the CJ detonation ($_{DC,2}$), followed by stationary conditions due to the forward rarefaction wave ($_{DC,3}$), and ends with the blowdown phase, illustrated in Figure 8.1c.
The final method is based on the findings of [60], in which the stationary phase ($_{DC,3}$) is shorter for pressure profiles measured close to the open end. Consequently, the non-stationary phase should exist at the open-end. The states are initially defined by the CJ detonation ($_{DC,2}$), after which it directly proceeds to the blowdown phase, as is illustrated in Figure 8.1d
The three methods are compared to the test data of [32] which measured the pressure profile near the open-end. Hence, a small stationary phase does exist. The pressure profile of the test data is illustrated in Sub-figure 8.1a. The test data was performed with the following characteristics, $p_{cc,limit}$ = 22 bar, F/O=4, and a L_{cc} = 1.75 m. Unfortunately, the test data is in psi, whereas the simulated data is in atm. To overcome this burden a few transition values are given 280 psi = 19.0 atm, 180 psi = 12.24 atm, and 60 psi = 4.08 atm. From the Figures 8.1 it is evident that the method by [24] deviates the most from the observed data, due to the unobserved pressure drop. Note that the large spike of 280 pis in the observed data is the Neumann shock, which is not modelled due to its brief nature, see Section 7.2.4.
To distinguish which of the two remaining methods is the more accurate one, a more detailed analysis was performed. This analysis compares the performance parameters of each method to the results from the Endo-fujiwara closed-end method. The performance values are found in Table 8.4. Additionally, Table 8.4 contains the performance parameters for a rocket designed PDE too. The Rocket PDE has the following settings $p_{cc,limit}$=600 bar, L_{cc}=4 m, O/F = 4. The $\dot{m}$ for both set-ups is set at 1.275 kg/s, as this sets $\dot{m}_{ox}$=1 kg/s.

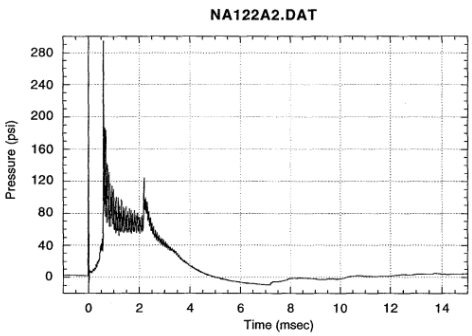

(a) Illustrates the pressure profile of a PDE close to the open-end, taken from [33]

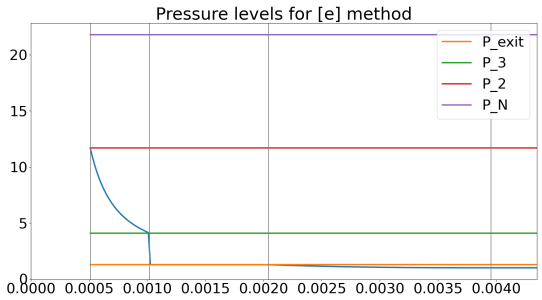

(b) Illustrates the pressure profile of a PDE close to the open-end computed by the method of Endo-Fuijware [24].

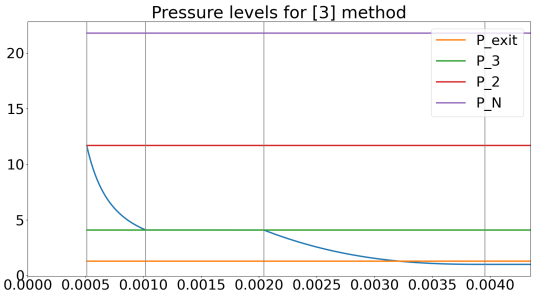

(c) Illustrates the pressure profile of a PDE close to the open-end simulated as a midpoint in the DC.

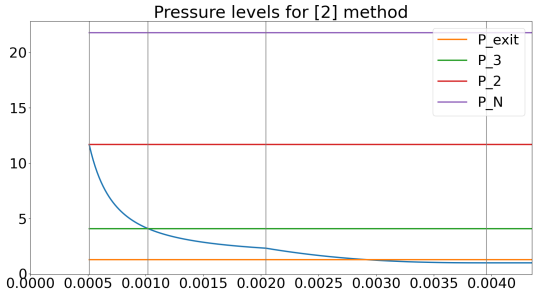

(d) Illustrates the pressure profile of a PDE close to the open-end simulated by the CJ wave + blowdown method.

Figure 8.1: Illustrates the pressure profile of a PDE close to the open-end with only CJ detonation wave and blowdown phase, for b till c the y-axis are the pressure in bar with time in seconds on the x-axis.

From Table 8.4 the following becomes clear, the Endo-Fuijiwara open-end method significantly underes-

PDE Simulation Methods	PDE Experiment Operation Set-up			PDE Rocket Engine Operation Set-up		
Simulation Methods	Pulse Thrust [N]	Mass rate [kg/s]	I_{sp} [s]	Pulse Thrust [N]	Mass rate [kg/s]	I_{sp} [s]
Endo-Fuijwara closed-end	24.15	0.0075	329	45.13	0.0134	343
CJ wave + Blowdown	28.81	0.0085	345	47.56	0.0133	365
CJ wave + Stationary + Blowdown	38.81	0.0114	455	66.51	0.0187	362
Endo_Fuijwara open-end	20.94	0.0062	346	31.83	0.0087	375

Table 8.4: Provides the performance parameters of all the PDE simulation methods considered in this thesis.

timates all performance parameters, compared to the established closed-end method. Furthermore, treating the exit as midpoint significantly overestimates the performance parameters. Moreover, both methods worsen as more energy is added to the detonation process.
Even though the CJ wave + blowdown still overestimates, one must remember that the Endo-Fuijwara closed-end approximation is an underestimation itself, as it neglects the initial pressure spike. Furthermore, as more energy is added to the system the method converges with the Endo-Fuijwara method.
It is by optimising the performance parameters that the value 2 for k is found. Values can be made to fit one instance better by optimising k even further. However, this is done at the cost of worsening the fit for all other instances. The value of 2 was found to be good for all instances.
Lastly, there is one more piece of evidence that prefers the CJ wave + blowdown method, which comes in the visual evidence of Figure 8.2. Figure 8.2 illustrated pressure profiles along the length of the DC, in which P7 is near the open-end. The figures were constructed from a PDE experiment with a C3H8/O2 propellant pallet. Figure 8.2 clearly shows there is no stationary period. Rather, the exponentially decreasing CJ wave pressure is followed by the blowdown phase. Additionally, the Neumann peak pressure is not observed, further supporting the choice of neglecting thrust contribution due the Neuman pressure.

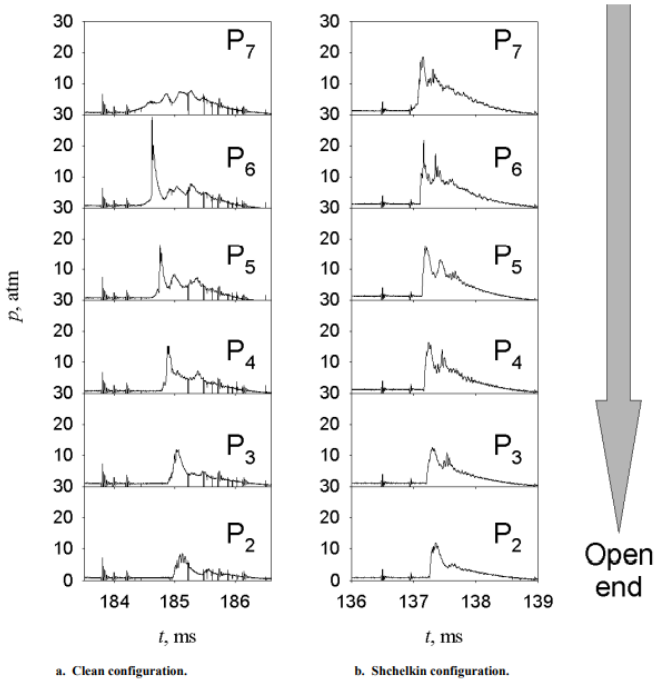

Figure 8.2: Illustrates the pressure profiles at locations along the length of a C3H8/O2 powered PDE for both a.) a delayed detonation process b.) a direct detonation process. The detonation was done stoichiometric at 6.9 Hz with P_{in} = 1 atm and T_{in} = 20 C°, taken from [46]

All in All, the CJ wave + blowdown method provides the best imitation of the exhaust conditions. Furtermore, [46] and [32] provide evidence for this methods being more than a pure quick-and-dirty approach, but has some physical merit too. Even though the method is an overestimation of the Endo-Fuijwara method, the Endo-Fuijware method itself is an underestimation. Hence, the method proposed here should be closer to reality. Moreover, the methods convert for increasing energy level, which are the levels the simulation will operate at. Therefore, the author believes that the method can be used for a performance analysis. However, if results offer little added performance or only make SSTO's a marginal possibility, then future research needs to operate more detailed simulations to substantiate the performance findings.

8.4. Verification and Validation of Precooled Hybrid Airbreathing Rocket Engine

Even though the hybrid engine is the most complex engine to engineer, the verification is rather straight forward. The back-end (3->9) of the engine has been verified and validated in the previous Section 8.1, which corresponds to the non-breathing/pure rocket phase. Therefore, only the breathing phase, implying the intake, needs to be verified and validated.

While verifying the intake module is easy, the validation is more challenging. This is because a complete module validation cannot be performed, due to the absence of both ground and flight testing data for either the RB545 or SABRE. At best the overall model can be verified and each transitions can be validated. As the transitions of the back-end have been verified before only the validation of the intake transitions needs to be computed.

However, the transitions used for the intake are all well-established relations in their respective fields. Therefore, each has been validated and scrutinised countless times. The shock transformations are well-established theories in the field of aerodynamics and are valid until the hypersonic region [9]. The heat exchanger and compressor are based on established performance analysis in the field of aero engines and are perfectly valid for an initial performance analysis. The aero engine transitions are valid for subsonic flow, which is guaranteed by the normal shock [9]. By verifying the transitions, the relations are implemented correctly and by the above arguments this makes them valid indications of the engine's performance. Hence, each transition only needs to be verified to validate the transitions. The verification data for the shock inlets and heat exchanger

& HPC are taken from [9] and [59], respectively.
The hybrid engine will go through more extensive sensitivity analysis in Chapter 9, to compensate for the absence of a complete module validation. Hence, the sensitivity to certain parameters will be a driving factor on how reliable the performance findings are.

8.4.1. Verification and Validation Shock Inlet

Oblique Shock Inlet (1 -> 12)
As mentioned in Section 7.2.5 the $\theta - \beta - M$ Equation has two solution, namely the strong and weak shock. The optimisation model described in Section 7.2.5, was extensively tested to consistently produce the weak shock angle. The intake is configured with $\theta = 15°$ and simulated at standard atmosphere conditions. At Mach 2 the two possible solutions are 45.3° and 79.8°, for which the model produced an angle of 45.359°. More tests were done at various Mach numbers, with which the solutions were taken from Figure F.1 in Appendix F.1.
Next to Figure F.1, Appendix F.1 contains two numerical examples taken from [9]. The results illustrate that the transition functions for stations 1 to station 12 are implemented correctly. Any discrepancies are caused by the temperature being updated via Cantera instead of the perfect gas law (see Equation 7.1).

Normal Shock Inlet (13 -> 14)
The verification of the normal shock transition is just like the oblique shock based on numerical examples presented in [9]. The results of the verification can be found in Appendix F.2. The results indicate the relations have been correctly implemented. Again, the discrepancies are cause by the Cantera update, as described above.

8.4.2. Verification and Validation Heat exchanger and High Pressure Compressor

Heat Exchanger (15 -> 19)
Equation 7.49 is inherently simplistic, which makes the verification of the heat exchanger transition more a of bookkeeping check. Unlike the previous transitions the heat exchanger is verified with a numerical example from [59]. The results can be found in Appendix F.3.
The example is a performance analysis of the NEWAC engine layout, in which the heat exchanger is located between the Low Pressure Compressor (LPC) and HPC. The intake air (flow that goes through the CC) is cooled by the bypass air flow (coolant). Unfortunately, there are few heat exchanger aero engines, let alone Rocket engines equivalent. The limited aero engine references is the consequence of NEWAC concluding that it offers inadequate performance benefits for aero engines, see Section 4.1.2. Furthermore, the RB545 and SABRE engines are the only engines with a layout as described in Section 7.2.5, for which no data is available. However, Reaction Engine has stated that the engine is operating an conventional HPC like NEWAC. Hence, the numerical example is relevant for the verification.

HPC (2 -> 29)
As mentioned multiple times, the HPC is a conventional HPC used in aero engines. Hence, numerous verification examples exist. An numerical example taken from [59] can be found in Appendix F.4. Only one example was provided, as the methodology used is a well established performance analysis in the aero engine technique. Hence, only the correct implementation is verified.

9

The Performance Simulations and Selected Engines Trade-Off

With all the components for the performance model established in the Chapters 6 and 7, the performance analysis of each of the selected engines can be performed. Consequently, this chapter evaluates *To what extend do the selected engines make an SSTO ascent trajectory viable?*. This chapter is categorised by three parts, namely the model setup, the individual engine evaluations, and the trade-off between the viable engines.
The first segment elaborates on how the performance model is set-up, and elaborates how the optimisation parameters were chosen, see Sections 9.1.2 and 9.1.3. The set-up segment includes a brief discussion on the model limitations, presented in Section 9.1.1. Furthermore, a segregated optimisation for the F/O parameters is presented. The F/O is optimised separately, as the F/O ratio is constrained by tanks sizing and separating F/O makes the performance model significantly more efficient. The set-up segment concludes with the establishment of a baseline, which is a conventional engine derived from the Raptor engine specifications. In the baseline Section 9.2, the general outputs of the model are discussed and explained.
The next segment are the individual evaluations of all the selected engines for different selected propellant pallets and at various specifications. The analyses are ordered by their engine type. The results of each engine type are analysed based on their performance and trajectory.
In addition, this segment evaluates the performance findings of each of the selected engines with multiple sensitivity analyses. The sensitivity evaluates the affect of the design and sizing parameters, discussed in Section 7.2, on the optimised trajectory. The optimised trajectory refers to the computed optimal vehicle configuration with corresponding trajectory settings by the model. The sensitivity analyses reveal the reliability of the performance results and identify possible critical parameters.
The last segment, summarises all the engines that make SSTO RLV viable ascent vehicles. Each of these viable engines is evaluated compared to the other viable engines, which results in the most viable candidate being identified. Lastly, a brief overview on promising engines that do not posses the orbital capabilities set in Chapters 2 and 6 is provided. Though, these engines are insufficient forA VT SSTO RLV they still might be interesting for future research, as the performance potential might be beneficial for either a TSTO or for a lesser capable SSTO.

9.1. Performance Analysis Setup

With the model for the performance trade-off established in Chapter 6 and the engine simulation methods elaborated in Chapter 7, the performance analysis can be performed. However, the conditions under which the performance trade-off is done have not been given yet. Although, some operation parameters are given in Chapter 6 including the aerodynamic parameters and none-propulsion system masses. This section provides the remaining operation parameters and the hyper-parameters required for the optimisation. The motivation on how these parameters are derived or extrapolated is provided too.
The section starts by establishing conditions under which the optimisation is done and how the findings are substantiated.

The Performance Optimisation Conditions
As mentioned in Chapters 5 and 6 the performance trade-off is done for varying engine performance parameters, namely the T/W and p_{cc} or $p_{DC,limit}$ in the PDE instance. As argued before, it is impossible to give any indisputable value to these parameters, which would not inevitability constrain the conclusion, thereby diminishing the robustness. Therefore, rather an array of possible values are evaluated and optimised.
Following the T/W argumentation presented in Section 6.2.4, the T/W values 100, 150 and 200 are evaluated. Whereas, the argumentation for the p_{cc} are found in Sections 5.1.1 and 5.1.3, and are set at 200, 250 and 300 bar. As mentioned in Section 7.2.4 the p_{DC} is not limited by the heavy turbo-pumps, but rather by the strength of the DC and wave tube walls. Therefore, DC's can operate at higher T/W ratio's and at higher combustion pressures. Unfortunately, no specifications are public about the PDE rocket test by The Russian Advanced Research Foundation, moreover most alternative implementations are military with limited information available. Hence, no representative values are available, however it is believed that the combustion pressure can be around twice as high. Consequently, the values 500, 600 and 700 bar are chosen to be evaluated.
Note that the optimisation for either T/W or the combustion pressure is done at a single value of the other variable, respectively. Performing an entire cross evaluation for all combinations is believed to add little value in terms of understanding the performance. Furthermore, in some instances not all values are evaluated for each selected engine or propellant pallet. This could be due to several reasons, e.g. when a previous lower value already achieved sufficient performance. Logically, a company would not develop an engine with better specifications than required, as this would unnecessarily increase costs. Another reason is that a value is unrealistic for the engine or propellant evaluated, as a consequence valuating such a value would not have any value (e.g. T/W of 200 for the hybrid engine).

Sensitivity of the performance
The performance findings are substantiated by varying the design and sizing parameter. Unlike, the performance conditions, no optimisation is performed. Rather, the settings of an optimal ascent from the performance trade-off is taken. The ascent with the optimal settings and the changed parameters is simulated. How the performance changes compared to the respective optimal ascent, serves as bases to evaluate the sensitivity.
For this reason the fitness value presented in the sensitivity tables should not taken as the predominant parameter, as no ascent optimisation is used. But, change in fitness should rather be interpreted as a measure indicating how much the optimum is affected by corresponding parameters. For most sensitivity parameters there exists a point where suddenly the fitness deviates significantly, which is referred to as the drop-off point (a change in fitness of over 100%). Depending on the deviation of the other performance parameters this can either be one of two things. In the instance the other parameters are significantly worse too, orbit capabilities are diminished making the respective parameter a critical one, whereas in the instance the other parameters are relatively unaffected, it indicates that the current trajectory is sub-optimal for the altered engine. Hence, ideally a new trajectory should be found, which can be done by the super optimisation loop. In the second instance, depending at what value the drop-off point occurs, the respective parameters should not be neglected when evaluating the true capability of currently evaluated engine. The same holds true when optimising a true ascent trajectory or in future design studies.

9.1.1. Quasi-Orbit Condition and the Relation to Orbit capabilities

Orbit is determined by the orbit condition (Equation 6.5) as described in Section 6.2.2. To recall, the condition neglects overshoots and the normal velocity w.r.t. Earth's centre. Consequently, it does not necessarily represents a true circular orbit, which is not an issue, as is discussed in Section 6.2.2. However, as a consequence of the orbit conditions, it has some implications on the model outputs.
The main implication and the primary limitation of the model is that very capable engines, produce worse fits than their less capable counter part (lower p_{cc} and/or lower T/W). The very capable engines offers more local optima, due to the quasi orbit conditions, therefore are more likely to converge to a local optima. These local optima often contain a larger overshoot, which explains why orbit can be achieved at varying values of DetlaV too, illustrated in Tables 9.7 and 9.11.
The overshoot is managed with the Lagrange weights, discussed in Section 9.1.3. Yet, the more powerful engines still present a substantial overshoot in the normal velocity, due to a thrust surplus in the early launch

phase. Thrust in the early launch phase is mostly contributed to reaching h_{target}. However, the model has difficulties reducing the early phase thrust by slightly reducing $\dot{m}_0$ or $t_{b,0}$, due to the codependency that exist between the individual burning variables and steering variables, as is discussed in Section 6.2.1.
In addition, and not restricted to the quasi orbit conditions, more capable engines are more sensitive to a change in $\dot{m}$ and t_b, as this proportionally results in a larger thrust change compared to a weaker engine. The increased sensitivity worsens jumping around the optima, which is a typical phenomena for chaotic black box models. Note that for the performance model is a chaotic black box model for the DE optimisation method.
For future research with the aims to find the actual optimal ascent, it is recommended to make the orbit conditions more strict, increase $w_{\parallel}$, and/or add a dedicated sizing module that removes excess propellant. The latter reduces the number of local minima. Alternatively, a third optimisation that takes the steering settings of the super optimisation and optimises the burning and sizing variables can be utilised. The burning and sizing values are constrained closely to the previously found variables, to allow only for slight alterations.

9.1.2. Optimisation Setup Parameters

This section provides the motivation behind the chosen values for the burning and steering nodes, trajectory population and generations, and the sizing population and generation. All the model hyper parameters excluding the weights of the problem function (see Equation 6.3) are presented in Table 9.1. These values provide the number of trajectories simulated and set the dimensional of the problem.

Nodes for the Steering and Burning Programs

The amount of nodes and corresponding variable time periods for each selected engine are provided in Table 9.1. Furthermore, the amount of generations and populations for both the outer ($\dot{m}(t)$) and inner ($\gamma(t)$) loop are provided.
The varying node numbers in Table 9.1 are increased or decreased according to the complexity of the trajectory/burn program. To elaborate, the hybrid engine will require greater control over its burning program and trajectory program in the early stages of the launch. During this early phase the intake mass is changing rapidly, consequently a greater control over the propellant flow is required. Additionally, the hybrid engine will stray further from a gravity turn, therefore require more complex steering nodes (more independent t_γ) in the breathing phases. Hence, the more complex hybrid engine trajectories requires more nodes and variable time periods.
Contrary, the conventional and pulse detonation engines require the least amount of nodes, as their trajectories should be closest to a gravity turn. The performance of the aerospike is more closely related to the trajectory, hence more trajectory nodes are used.
The minimum amount of burning nodes is 4 with 3 time periods. Which translates to a short full thrust take-off, followed by a prolonged high thrust period. After which a burnout with a period of not thrust occurs, which is than followed by an orbit burn. The described burning program describes the standard ascent burning program for current TSTO rockets. It is reasonable that SSTO's with similar engine operations operate similar/the same burning program.
The minimal trajectory nodes used are 4 with 2 variable time periods. This was found to be sufficient for a trajectory similar o a gravity turn.

Engine Type	$\dot{m}$	t_b	$\vec{\gamma}$	$t_{\vec{\gamma}}$	$n_{\dot{m},gen}$	$n_{\dot{m},pop}$	$n_{\vec{\gamma},gen}$	$n_{\vec{\gamma},pop}$
Conventional	4	3	4	2	17	10	3	5
Aerospike	4	3	5	4	17	10	3	5
Pulse	4	3	4	3	15	10	3	5
Hybrid	5	4	5	5	9	9	4	6

Table 9.1: Provides the optimisation parameters used in the model for each engine type.

Generation and Population Numbers

Logically, more variables require more data point for the DE algorithm to extrapolate how each variable effects the problem function. Consequently, the steering populations are scaled with the respective variables accordingly, as is illustrated in Table 9.1.
The number of sizing generations is chosen based on the trial-and-error, throughout the development of the

model. Even though such approach is rudimentary, it is sufficient for the goal of this thesis. Further research is recommended to proof a minimal required number of generations. Alternatively, other optimisation methods/algorithms can be explored to improve optimisation efficiency.
A trajectory generation number of 3 is found to sufficiently converge, such that the performance potential of a particular engine configurations is consistently determined. The hybrid engine is the exception, due to the increased complexity in the trajectory requires more generations to converge.
Even though the hybrid engine has a more complex burning program its generation number is decreased, due to computational limitations. To account for the reduced generation both the sizing population and generation number are increased. However, as will become evident the hybrid engine due to its continuous environment interactions requires exponentially more computational power. For reference the simulation of an aerospike ascent takes typically 6 s, while the hybrid engine can easily take 30 s (ideal) to 4.5 minutes to complete.

9.1.3. Lagrange Weights for the Problem Function

This section provides the motivation for the Lagrange multiplier weights, as is discussed in section 6.1.1. Each weight (w_{n}) in fitness Function 6.3 represents a different aspect of an efficient ascent. One might question the relevance of the weights, therefore advocate for a uniform evaluation. However, selecting the right weight values is equally important to the selected optimisation method [29], in the utmost cases wrong weights can result in a failed optimisation. Studying Fitness [-] Function 6.3 an example of a failure to optimise case can be identified.
Take the weights w_{m} and $w_{\parallel}$ which penalise no surplus mass and overshoot velocity, respectively. For instance, if these weights are made relatively large, the model will prioritise the minimisation of these aspects. Consequently, the rocket will not take-off, as a result the mass surplus is equal to the propellant weight and the normal velocity never gets above zero. Therefore, well evaluated weights both ensure the model converges with the imposed constrain and improves the rate of converges.
Unfortunately, the identification of weights is an ad-hoc science as no presiding method exist, therefore often done through trail-and-error. Hence, what weights in what combination are optimal and how these effect each other is a study on its own, and more in the field of quantitative sciences, like econometrics. The two common trial-an-error methods are grid-search and random-search. This thesis restricts itself to the quasi grid-search. However, for more extensive methods the reader is referred to [52] and [29].
In the quantitative fields the weights are better known as the hyper-parameters of the model. Note that the number of nodes and time set are part of the hyper-parameter set.

Trial-and-Error Grid-Search Weight Identification
Optimal weights are determined by evaluating the performance of the aerospike engine under varying weights. The aerospike is used as it has the shortest computational time, thereby allowing more evaluations over the same time period. The model was configured with the same aerospike optimisation parameters as the ones in Table 9.1, with a LCH4/LOX pallet. Before, the trial-and-error approach is commenced, the above example provides additional key information. Weights can be differentiated into two categories, namely problem evaluators and efficiency evaluators. The problem evaluators are w_{h}, $w_{\perp}$[1], and p, which all are direct measure on weather the goal (reaching orbit) is achieved. The efficiency evaluators are w_{m} and $w_{\parallel}$, and measure, given the goal is achieved, how efficient the goal is achieved. Furthermore, from the example it can be concluded that the weights of the problem evaluators must be substantially larger than the weights of the efficiency evaluators.

With this information Trail-and-Error tables, like Table 9.2, are created. From Table 9.2 the influence and effectiveness of certain weight setups is explored. The exploration leads to a new table until a satisfactory setup is found. Note that via such approach a found setup cannot be determined optimally.

[1] Note that $w_{\perp}$ is an efficiency evaluator too, as an overshoot in the tangent velocity inflicts unnecessary drag losses.

Run	w_h	$w_\perp$	$w_\parallel$	w_m	w_p	Fit	%	$M_{prop,surplus}$	$I_{sp,eff}$	DeltaV	Orbit
I	1000				1000	44	2.2	0	373	8752	T
II	1000	1000	500			25	1.0	0	376	8892	F
III	1000	1000		500		501	20.0	0	370	8934	F
IV	1000		500		1000	61	2.4	0	376	8709	F
V	1000	1000				1	<0.1	0	370	8897	T
VI	1000			500	1000	543	27.1	0	375	8778	F

Table 9.2: Provides the performance parameters for varying weight combinations used in Fitness Function 6.3.

From Table 9.2 it appears that the w_m severely worsens the optimisation effectiveness, however this is caused by the fact that the propellant aspects is measured relative to the total propellant available for the ascent. Therefore, it is expected that the fit is >500 when orbit is not reached.
Further, Table 9.2 shows that generally the addition of the efficiency evaluators (excluding $w_\perp$), reduces the relative fit and prevents orbit from being reached. Whereas, the w_m appears to only hinder the optimisation with no upside. However, the efficiency parameter $w_\parallel$ does increase the effective I_{sp}. It is most likely, that the weight for $w_\parallel$ is too large, thereby directing the focus on the efficiency rather than achieving goal of reaching orbit. Hence, a lower weight for $w_\parallel$ and the exclusion of w_m should be considered.
Lastly, both the problem evaluators drive the optimisation to its goal, with the $w_\perp$ driven sets generating far more DeltaV. The larger DeltaV is caused by either a higher $I_{sp,eff}$ or by generating a larger portion of the thrust in the latter launch phases. The latter is achieved by having a larger $\dot{m}$ at higher altitudes were the ϵ_{eff} is larger therefore a higher U_e is achieved. This observation has two interpretations. First it can be argued that w_p is more efficient in the sense that it reaches orbit with a lower DeltaV. However, such explanation would result in a propellant surplus, which is absent in Table 9.2. Thus, it can only be concluded that the w_p driven problems generate a larger portion of the thrust in slower lower altitudes.
The second interpretation is inline with the increased DeltaV observation, which argues that $w_\perp$ driven problem is more efficient with its propellant usage, by generating more thrust in the higher atmospheres.
Which ever interpretations is correct it suggest that the other generates an overshoot. The effect by the addition of $w_\parallel$ is relatively larger for the $w_\perp$ driven problem. This suggest it is the $w_\perp$ which generates the overshoot, however the effect is to small to be conclusive.

For the above trail-and-error Table 9.2 the previously discussed deductions are incorporated in the creation of the next trade-off matrix. Thereby, making the grid-search into a quasi grid-search.Such, approach is within merit as a trajectory deals with deterministic relations, were hyper parameters can be linked to real physical phenomena. Whereas, in quantitative fields the problem are stochastic, for which the hyper-parameters cannot be linked to physical phenomena [29].
Hence, the new table evaluates $w_\parallel$ at a lower weight and combines the problem evaluators $w_\perp$ and w_p to see if this improves consistency in reaching orbit.
The iterative procedure of the quasi grid-search is repeated for several evaluations, until a satisfactory set of hyper-parameters was found. Sets are foremost evaluated on the orbit reached consistency, which means orbit is reached in both the jointed optimisation loops (main model) and the super optimisation loop. Next preference is given to sets with low relative fit values (% fit) and high realised DeltaV. The lower fit value ensures that the difference between bad and good runs is more substantial, which is preferred. The higher DeltaV is an efficiency indicator, although important it is of second relevance. All relevant optimisations runs are provided in Appendix D.1.

The combination $w_\mathbf{h}$**=1000,** $w_\perp$**=750,** $w_\parallel$**=250,** $w_\mathbf{m}$**=0, and** $w_\mathbf{p}$**=1000** is found to be best. The value of 250 for $w_\parallel$ is sufficiently small to prevent an overemphasis on the efficiency, but large enough to reduce the overshoot and improve orbit consistency. The w_m has little effect on the optimisation performance and more often worsens the consistency, therefore the value is set to zero. The explanation for this is that the propellant is (near) the exact amount needed to reach the targeted orbit. The values for w_h, $w_\perp$, $w_\parallel$ are found to work best in this particular combination.
In addition, it is found that the value of $w_\perp$ is highly correlated with realised DeltaV. Especially, in combination with a relative high $w_\parallel$ value. Therefore, a high $w_\perp$ results in a high realised DeltaV.

9.1.4. Fuel-over-Oxidiser Ratio

Even though F/O can be set as a sizing parameter, it is possible to optimise separately. Optimising the F/O ratio separately improves the optimisation performance as both reduces the amount of variables and circumvents codependency. For these reasons the F/O ratios segregated, with the results presented in Table 9.3. The F/O evaluations are found in Appendix G.
Table 9.3 provides the optimal F/O ratios for the highest T and I_{sp}, which mostly have identical F/O values. The Optimisation is accurate to a value of 0.025 (equivalent to the step size) and is performed with $\dot{m}$=650 kg. For the Isobaric powered engine ϵ is set at 34.34, 40, 60, with 40 values presented in Table 9.3.
The PDE F/O ratios have different optimal F/O ratios due to its isochoric combustion process, therefore evaluated separately. The PDE F/O ratios are evaluated at constant p_{in} (20 bar) and at constant $p_{DC,N}$ (600 bar), both with an ϵ of 5.

Propellant Pallets	H2/O2	CH4/O2	C2H2/O2	C2H4/O2
Performance Parameters	Isobaric Combustion			
F/O	0.275	0.350	0.700	0.475
$I_{sp,eff}$	431	335	345	334
	Isochoric Combustion			
$F/O_{p_{31}=const.}$	0.425	0.4	0.775	0.575
$I_{sp,eff_{p_{31}=const.}}$	510	390	368	323
$F/O_{p_{4,N}=const.}$	0.45	0.4	0.8	0.55
$I_{sp,eff_{p_{4,N}=const.}}$	471	322	367	332

Table 9.3: provides the optimal F/O ratios w.r.t. the effective I_{sp}. The ratios are given for an conventional engine and a pulse detonation engine for both a p_{31} and a p_4 limited configuration.

The F/O Optimisation
Table 9.3 provides the F/O ratio's for which thrust is maximised. During the optimisation of the F/O ratios, some odd phenomena are observed, as are illustrated in Appendix G. Further, the I_{sp} of the isobaric process appears. Yet, this is caused by an ϵ of 5, which is an underexpanded nozzle.
Generally, the p_e is continuously decreasing after the stochastic F/O ratio. Contrarily, the acetylenic propellants experience an increase thereafter. The increase is caused by a decreasing γ, which for a constant ϵ increases p_e, see Equation 7.11. The decreased γ is caused by the dissociation of the excess fuel, hence only observed for the hydrocarbons. It is believed that the dissociation occurs after the incomplete combustion limit is surpassed. This explains why the sudden increase happens at the same F/O ratio for both isobaric and isochoric combustion. As expected, the dissociation goes hand in hand with a decreasing T_{cc} as more energy is reserved to the dissociation.
Whether, this dissociation occurs till the levels as illustrated in Appendix G is unlikely, as is evident by the zero thrust points in Appendix G.1. The zero thrust points, are likely caused by the mixture being too rich. Later combustion is achieved due to *advance_to_steady_state*[2] which holds for short dt, however for the richer mixture dt is significantly longer. Fortunately, the model refrains from using highly rich combustion.
The isochoric optimal F/O ratios are higher than the once for the isobaric combustion, which was more evident for the H2 and CH4. Both are best explained by focusing on the balance between H and M, as is discussed in Section 5.1.2. By increasing $\dot{m}_f$, M is decreased. However, as a consequence the enthalpy released per mass unit (H) is reduced. In other words, a balance exists between the total enthalpy per unit mass released and how easily the mixture's heat energy is converted to kinetic energy release, namely through the reduction in specific mass M.
Isochoric combustion can exchange more H for a lower M, as it extracts more H to begin with. Consequently, isochoric combustion requires less complete combustion to reach the same H as isobaric combustion, as a result a relative higher $\dot{m}_f$ is optimal. This effect is enlarged for propellants with a M substantially lower than M_{O2}.
As a final remark, the I_{sp} for the isochoric process at $p_{4,N}$ = const. can be 10 s to 20 s. The deviation is caused by the used T step-size in the golden section method, as described in Section 7.2.4, which overestimates the T_{31}.

[2] *advance_to_steady_state* is used over *advance* due to its shorter computational time.

Influences of ϵ on F/O
During the optimisations a mild but positive correlation between ϵ and F/O is found. Logically, it follows that for a larger ϵ the exhaust is accelerated longer, hence it is more desirable to reduce M to increase the maximum possible acceleration. However, these effects never succeeded above 0.025.

Influence of p_{31} or $p_{4,N}$ Limited Isochoric Combustion
Concerning the isochoric combustion, a limited p_{31} or $p_{4,N}$ combustion are analysed, which had a minor effect on the optimum F/O ratio. However, as expected, the lean and rich limitations were effected substantially. The variation in the I_{sp} is logical as a limited p_{31} allows for higher and lower p_{DC}s, which linearly correlates with p_4, see Section 7.2.4.

Exclusion of Ethylene (C2H4) from the Performance Model for Isobaric Combustion
As the tittle suggest ethylene is excluded from further evaluation, which is a consequence of initial analysis. As is illustrated in Table 9.3 the performance of C2H4 with isobaric combustion is similar to that of methane (CH4), therefore there is no economic justification of developing an ethylene powered engine over a methane powered one. The higher TRL level and the wider availability of methane make it a superior choice. The exclusion Ethylene is limited to the engines operating on the isobaric combustion, namely the aerospike and hybrid engine, as C2H4 still has a performance advantage over CH4 concerning isochroic combustion.

Optimal F/O Ratios Compared to Operated F/O Ratios
As the more familiar propulsion engineer might have realised, the optimal F/O are higher than the ones used by today's engines. The Raptor-D (LCH4/LOX) operates at a 0.275 F/O, The RS-2200 (LH2/LOX) operates at a 0.181 F/O, and the RS-25 operates at a 0.16. The explanation follows the same reason why H2O2 is not evaluated in this thesis. The lower F/O is the result of the aerodynamic compromise that comes with operating at the optimal F/O ratio. The optimal F/O requires a far larger fuel volume, due to the flow fuel density, which increases the A_{ref} and possibly C_D inflicting more drag losses (increasing DeltaV budget). The increased drag losses do not out-way the added performance of operating at the optimal F/O, hence a lower F/O is chosen. This problem is less severe for more dense and less cryogenic propellants like the acetylenes. Therefore, these can be operated closer to the ideal ratio.
To conclude using the optimal F/O ratio's is unrealistic and lower values should be used for H2 and CH4. For C2H2 and C2H4 values closer to the ideal can be used. Furthermore, it is not unrealistic to use higher F/O values than the historical ones, given the improved storage tank technologies[45].

Propellant Pallets	H2/O2	CH4/O2	C2H2/O2	C2H4/O2
F/O for Isobaric Combustion (CC)	0.225	0.300	0.700	0.425
F/O for Isochoric Combustion (DC)	0.350	0.375	0.775	0.55

Table 9.4: Provides the F/O ratios used in the model.

F/O Conclusion
To conclude, It is unlikely that the cryogenic propellants can operate at the ideal F/O ratios, therefore the reduced F/O ratios of 0.225 and 0.300 are chosen for H2/O2 and CH4/O2, respectively.
The acetylene propellants are combusted at the ideal F/O, as their densities are far closer to that of oxygen. Therefore no additional aerodynamic losses are induced, moreover the aerodynamic drag losses of an acteylene/O2 powered vehicle are relatively lower than those of cryogenically powered vehicles. Although, the reduced aerodynamic losses is not accounted for in this thesis, it is worth mentioning.
The isochoric combustion is more energetic hence a higher F/O ratio is expected. This results in that the increased performance changes the optimum between the aerodynamic losses versus the performance loss due to no ideal FO combustion. The higher performance can compensate more for the drag losses, therefore the FO ratios of H2O2 and CH4O2 are increased to 0.350 and 0.375, respectively. The acetylene propellants are combusted at optimal F/O ratios.

9.2. Baseline Performance and General Model Output

To create a better understanding on how the selected engines perform, it is advantageous to evaluate a baseline. The Raptor engine with its currrent specifications serves this purpose. The raptor engine is chosen as it is a good representation of the current technology level of conventional engines. If the current specification are achieved the Raptor engine will be the most powerful T/W engine to date, with a T/W of 200.
The selected engines should offer a substantial improvement over the Raptor engine to justify the economic incentives for their developments. A marginal improvement also introduces with the continuous development arguments raised in Chapter 2 and Section 5.1.3. Were initially a simpler variant (e.g. open-cycle) is developed which is than improved over the years, as was done for the Merlin engines. Such approach does not work for a marginal improvement as it is likely the simpler variant is insufficient to power an SSTO RLV.
Furthermore, this section discusses the general output of the model. Which comes in three forms, namely the performance tables, optimisation output variables, and the output graphs.

General Output Tables
The outputs contains the results for the Raptor engine, were the model is made to optimise he trajectory and configuration of an SSTO RLV powered by the Raptor engine. The expansion ratio (ϵ) is free to optimise as this is dependent on the altitude range the engine operates. The ϵ is constrained for p_e equals 1 atm and 0.225 bar , respectively, as described in Section 7.2.2. The output performance parameters of model are provided in Table 9.5. The model provides :

The fitness :	a measure on how well the vehicle succeeded in minimising the problem function.
The orbit status :	whether the vehicle illustrated orbit capabilities.
The time averaged $I_{sp,eff}$:	a measure of performance relative to time over the trajectory.
The Realised DetlaV :	a measure of the performance relative to the propellant mass.
The $M_{surplus}$ [Mg] :	a measure of margin.

The $M_{surplus}$ [Mg] is a measure of margin as it provides additional mass budget for the system.

Raptor Engine		Constant CC Pressure [300 bar]	
T/W	Performance Parameters	CH4/O2	
200	Fitness [-]	426/375	
	Orbit [-]	F/F	
	$I_{sp,t,eff}$ [s]	348/348	
	DeltaV [m/s]	8548/8557	
	$M_{surplus}$ [Mg]	0/0	
Sizing variables		F/O = 0.275	ϵ = 87.17

Table 9.5: Provides the performance parameters of the simulated the Raptor engine powered scent vehicle.

As expected the performance of the Raptor engine is insufficient to reach orbit, verifying the notion that conventional engines are unsuited for SSTO vehicles. Table 9.5 provides two values for each performance parameter, corresponding to the joint optimisation and the super optimisation. Future tables will only contain the super values as these are more representative, as is discussed in Section 6.2.1.
The time average I_{sp} does not weight the mass rates, which explains the difference in DeltaV for an equal $I_{sp,t,eff}$. However, here the values of 348 is close to the $I_{sp,eff}$, Due to the single burn. From the $I_{sp,t,eff}$ it can be extrapolated if the vehicle is flying a trajectory complementary to the engines performance. A mass average $I_{sp,eff}$ cannot provide this insight as it is skewed toward the performance of the early thrust phase.
The DeltaV in Table 9.5 provides the realised DeltaV[3] and is a measure equivalent to the mass average $I_{sp,eff}$. The realised DeltaV is far below the 9400 m/s generally used as the required budget for LEO.

General Optimisation Variables Outputs
The above values are generated with the burning and steering programs provided below. Note that burnout occurs at 262 s, hence only the first two burning nodes are utilised. Consequently, the Raptor burning pro-

[3] The difference between realised DeltaV and DeltaV is that the former follows from a trajectory simulation whereas the latter is calculated via the Tsiolkovsky Equation 4.1, with a single I_{sp}.

gram lacks the circulation burn, as described in Section 9.1.2. The reason for this is simple, as the vehicle utilises all its propellant to reach the required altitude, which it never does. Therefore, a circulation burn cannot and therefore is not performed.

Burning mass rates ($\vec{\dot{m}}$) : [1905.51, 1972.79, 533.44, 1016.73] [kg/s]
Burning time stamps ($\vec{t_b}$) : [149.85, 184.83, 69.79] [s]
Steering angles ($\vec{\gamma}$) : [43.69, 22.67, 25.91, 42.59, 37.04] [°]
Steering time stamps ($\vec{t_\gamma}$) : [127.13, 36.31, 161.90, 146.30] [s]
Steering angles (super)($\vec{\gamma}$) : [78.97, 5.58, 25.87, 61.71, 32.92] [°]
Steering time stamps (super)($\vec{t_\gamma}$) : [67.2, 152.6, 56.51, 120.48] [s]

A steep initial steering angle is observed for both the joint and super optimisation, which corresponding to an almost tangent vehicle orientation at the end of $t_{b,0}$. The immediate turn is inline with real world observations and appears to represent a gravity turn. Furthermore, the first two mass nodes have a very similar mass rate, indicating that this is likely a single burn. Given that these rates are very close it suggest that model can consistently find the optimum mass rate with a crude precision of 100kg/s.

General Output Plots

The two figures 9.1 and 9.2 contain the optimal trajectory ascent data of the joint optimisation loop (Figure 9.1) and of the super trajectory (Figure 9.2). Each figure provides four plots, each dealing with a a single trajectory aspect.

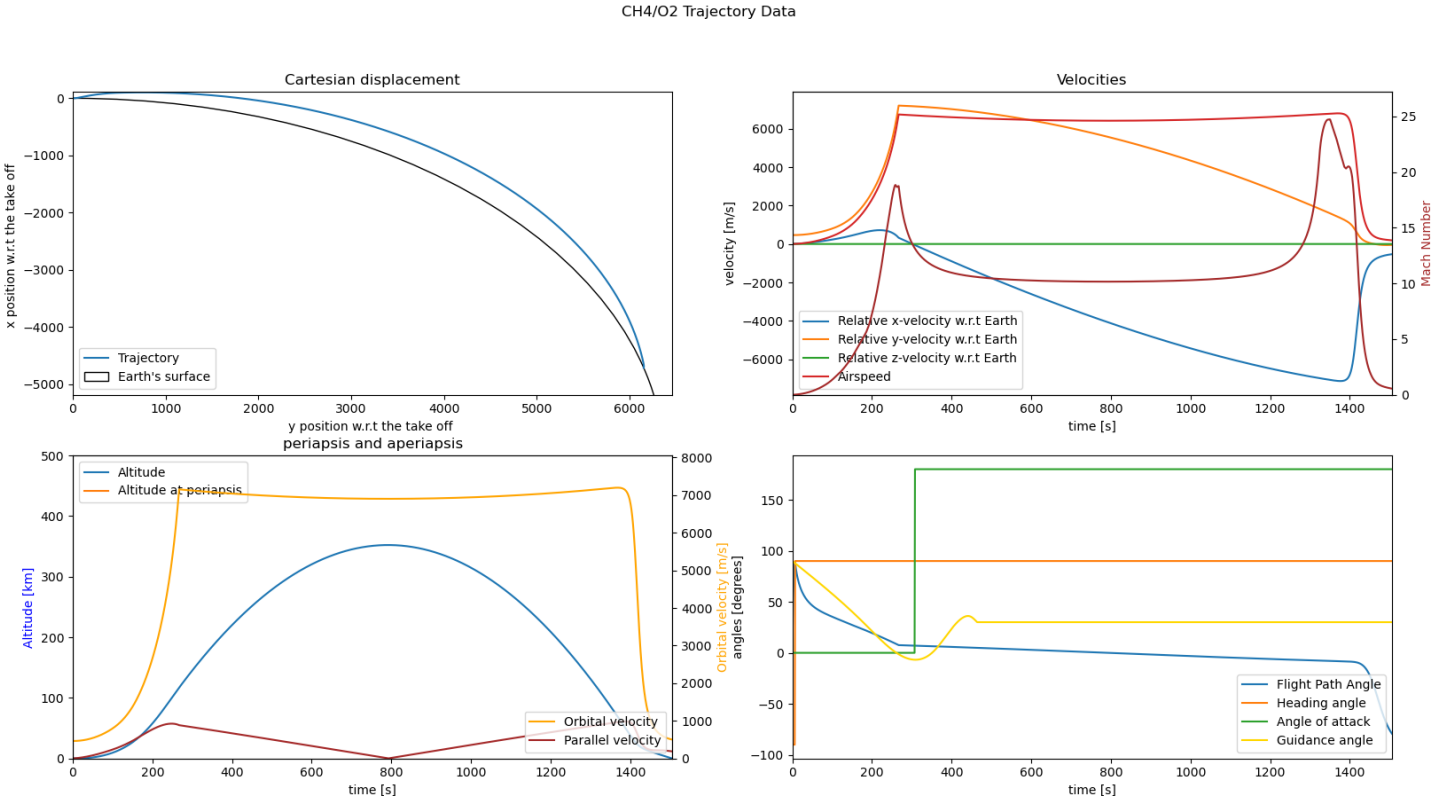

Figure 9.1: Illustrates the ascent trajectory data of the Raptor powered SSTO obtained from the joint optimisation loops

The first plot provides the trajectory in the Cartesian coordinate w.r.t. to a fixed non-rotating Earth, see Appendix A.1. The second plot provides the velocity components in the same Cartesian coordinate system. The velocity in the z-axis is plotted as an verification tool, as Tudatpy is a 3D simulator but used for a 2D model, and is expected to remain zero. Additionally, the Mach number is plotted to eliminate unrealistic ascent trajectories. An oddly high Mach number is observed in Figure 9.2. However, further analysis shows that this is reached at 80-90 km, which is at the same time that falcon-9 reaches burn-out and its max Mach number. The Mach is higher than the ~17 Falcon 9 achieves, even though the exact number is not known. Yet, this is

expected due to the more powerful raptor engines and larger propellant consumption in the first burn phase. The high Mach is largely explained by the low density at 90 km, as the selected engines have substantially lower Mach numbers with similar velocities, as illustrated, for instance, in Figure 9.3.
The third plot provides the mission parameters (the values evaluated in the Problem Function 6.3). The periapsis altitude does not appear in the plot as it never reaches a value above 0 km. Furthermore, it can be seen that both the orbital and altitude never reach the target values, hence orbit is not achieved. Lastly, note that the normal velocity due to how it is calculated is always positive. The trend in the altitude and values of the second plot reveal the true sign.

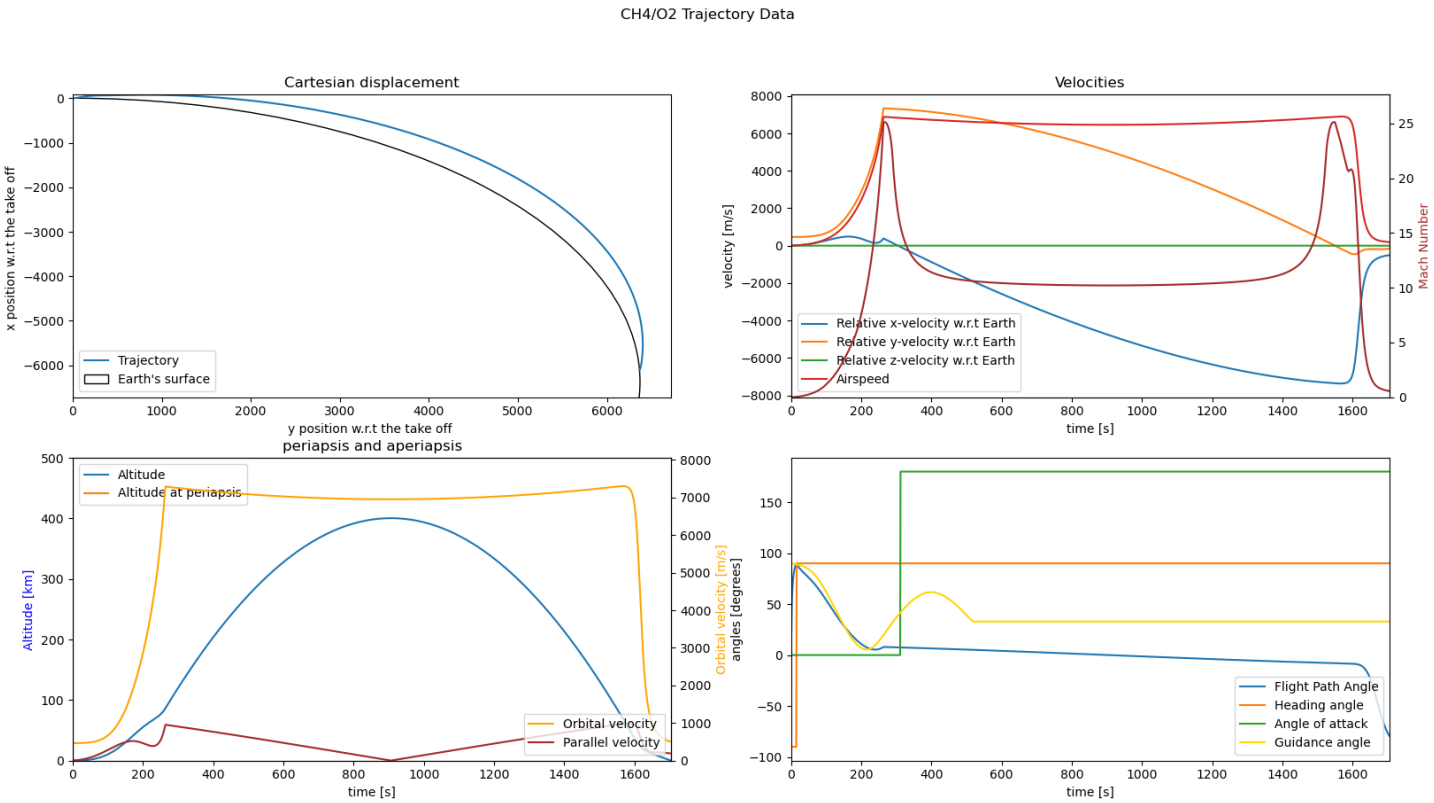

Figure 9.2: Illustrates the ascent trajectory data of the Raptor powered SSTO obtained from the super optimisation loops

The fourth plot provides the aerodynamic angles and relates to the steering module. The flight path angle results from the steering angle until burn out, as the steering is achieved through the thrust which is elaborately discussed in Section 6.2.3. The heading angle and angle of attack require further explanation and are the result of the inner mechanics of Tudatpy. The jumping behaviour originates form operating a 2D model in a 3D simulation, thereby leaving one orientation undefined. The orientation is set to a default setting before its suddenly gets updated. The heading angle is orientation in the direction of the tangent/orbital velocity w.r.t. to an rotating Earth reference frame. Therefore, when the tangent velocity increases the angle flips to the positive value of 90° ($v_{\perp} \geq$ ~400m/s), which is more elaborately illustrated in Appendix J.1. The orientation of the angle of attack is always in the direction of the acceleration with respect to the airspeed, therefore it flips to 180° upon burnout were the drag is in the opposite direction to the airspeed. Because c_L is set at zero the heading angle and angle of attack can only take the values of -90° & 90° and 0° & 180°, respectively. The orientation of the aerodynamic angles has no effect on the inner operations of the model.
Therefore, the aerodynamic angles and z-velocity are best ignored in this thesis and should only be considered when the model is upgraded with an advanced aerodynamic module or is expanded to 3D.
All in all, the model produces representative results which are expected with the given setup, as such the model provides a realistic indication of the potential performance.

9.3. Results of Aerospike Engine Simulations

This section contains the results of the optimised ascent trajectories for the aerospike engines. To reiterate, the mission goal is to deliver a payload of 15 tons to an orbit of a 400 km height. The optimisations are performed with the specification of p_{cc} at 250 and 300 bar, and T/W at 200 and 150. These values are likely achievable by an aerospike engine, due to its close resemblance to conventional engines.
For the aerospike ascent optimisations $\epsilon_{eff,max}$ is set at upper limit of 220, which should be attainable given that the XRS-2200 had an $\epsilon_{eff,max}$ of 173. Predetermining $\epsilon_{eff,max}$ follows from the fact that no weight penalties are given for a larger $\epsilon_{eff,max}$, hence the model would inevitably converge to the upper limit. Therefore, the 220 value is better interpreted as the maximum attainable performance of an aerospike, and does not necessarily represent the final design value. The preset $\epsilon_{eff,max}$ is an sensitivity parameter evaluated in Section 9.3.3. Section 9.3.3 contains other sensitivity analysis too, evaluating the affect of the aforementioned max expansion ratio ($\epsilon_{eff,max}$), the expansion reduction factor $\kappa_{expansion}$, and the directional losses ($\eta_{directional}$).
The section ends with a discussion on the most relevant findings and possible performance improvements.

9.3.1. Performance Analysis of the Aerospike Engine with Varying T/W

Aerospike Engine		Constant CC Pressure [300 bar]		
T/W	Performance Parameters	H2/O2	CH4/O2	C2H2/O2
200	Fitness [-]	66	218	48
	Orbit [-]	T	F	T
	$I_{sp,t,eff}$ [m/s]	480	367	384
	DeltaV [m/s]	11396	8958	9072
	$M_{surplus}$ [Mg]	0	0	0
150	Fitness [-]	42	193	62
	Orbit [-]	T	F	F
	$I_{sp,t,eff}$ [m/s]	477	364	376
	DeltaV [m/s]	11224	8842	9028
	$M_{surplus}$ [Mg]	0	0	0
100	Fitness [-]	27	N/A	N/A
	Orbit [-]	T		
	$I_{sp,t,eff}$ [m/s]	479		
	DeltaV [m/s]	11141		
	$M_{surplus}$ [Mg]	0		

Table 9.6: Provides the performance parameters of the aerospike simulation, generated with LH2/LOX=0.225 [-], LCH4/LOX=0.3 [-], LC2H2/LOX=0.7 [-], LC2H4/LOX=0.475 [-], and $\epsilon_{eff,max}$=220 [-].

Observations in the Performance Parameters
Table 9.6 illustrates that the H2/O2 powered aerospike with p_{cc} at 300 bar possess the required orbit capabilities at all T/W ratios. While, the C2H2/O2 powered aerospike only possess the same orbit capabilities at a T/W of 200.
Besides the orbital capabilities, the table illustrates a decrease in fitness value (improvement) for decrease in T/W (less powerful engine). This observation is a common theme throughout this thesis, for which the explanation is given in previous Section 9.1.1. To summarise, It is expected that the codependency between the time intervals and mass rates induce an imprecision in the performance steps, which makes substantially harder for the optimisation to expel itself from a local optimum. As the powerful engines have more local optima, it is more likely that those get caught in one. Hence, the less powerful engines can only get caught in local optima that are closer to the global optima, which results in a better fit.
The ability to achieve orbit with different DeltaV is closely related to the phenomena described above and a consequence of wasted propellant in terms of overshoots. This is explained in more detail in Section 9.1.1.

Observations in the Ascent Trajectory

An interesting observation is made when studying the optimal trajectory for the H2/O2 powered aerospike in Figure 9.3. As rather unexpected the ascent trajectory deviates significantly from a gravity turn, which is generally understood to be the ideal trajectory for a single stage rocket. Contrarily, there is a suggestion that the observed trajectory is the expected optimal trajectory for the aerospike powered vehicle, which is an steep/vertical ascent followed by a sharp pitch as illustrated in Figure 9.3.

Two explanations for the steep ascent exist. The first and the simplest is that the achieved ascent trajectory

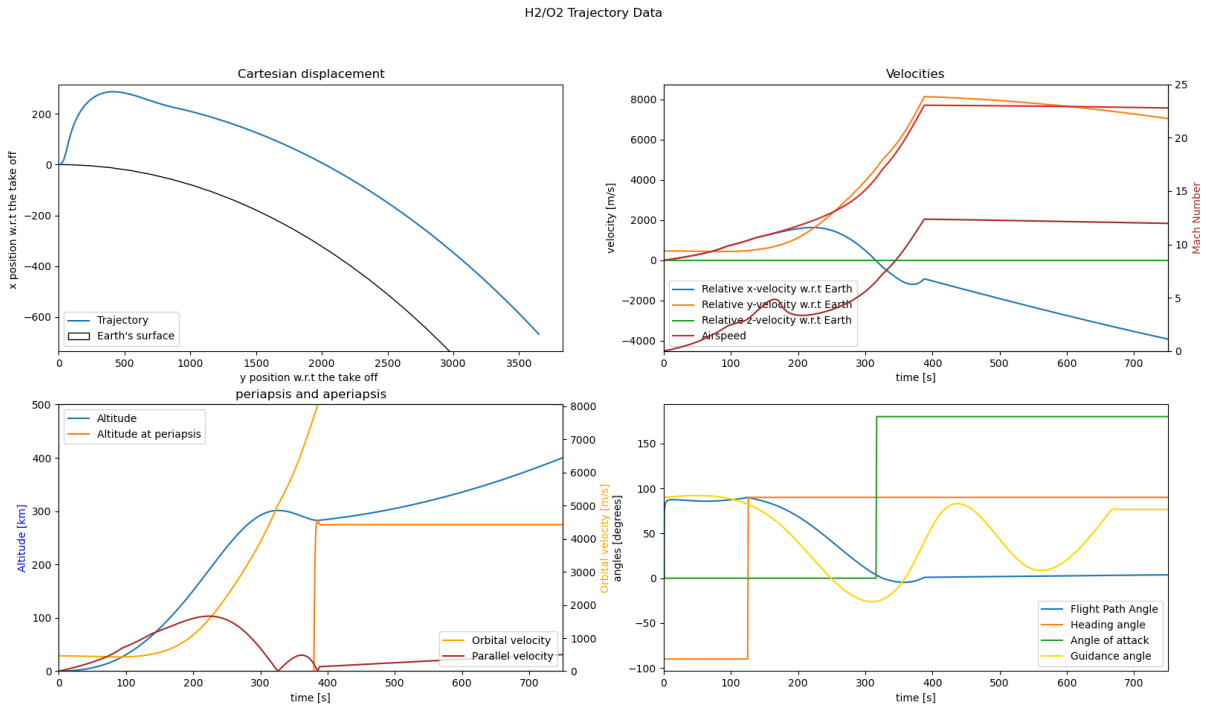

Figure 9.3: Illustrates the trajectory profile of the H2/O2 aerospike powered vehicle, with specifications p_{cc} = 300 [bar] and T/W=150 [-].

is a local optima thus a sub-optimal ascent trajectory. This would be the result of the quasi orbit condition and a surplus of propellant for the H2/O2 engine. While, this is most likely true to some extend, there is some theoretical merit to the steep ascent.

To elaborate, one has to realise that a gravity turn is ideal for constant thrust, which fundamentally differs from an aerospike engine. Studying Equation 4.3 reveals why vertical ascent is more optimal. Remember that T is optimal when $p_e = p_a$, which is exactly what aerospike ensures at every altitude. Thereby, simplifying Equation 4.3 to $T = \dot{m}U_e$, combining this with the implication of equation 5.1 ($U_e \propto 1/p_e$). Hence, T increases with a decreasing p_e, as T increases propellant is spent more effectively. With p_e being equal to p_a it can be concluded that the aerospike is more effective for rapid altitude increase. This is evident by the difference $I_{sp,SL}$ of 431.6 s to the $I_{sp,300km}$ of 489.7 s.

Therefore, there is merit in aerospike powered vehicles prioritising a steep (faster) ascent, which increases the effectiveness of the engine. This in turn makes the vehicle ascent even faster, hence more efficiently (increased I_{sp}). The sharp pitch at the end is required to achieve orbital velocity.

9.3.2. Performance Analysis of the Aerospike Engine with Varying p_{cc}

Aerospike Engine		Constant T/W [200]		
p_{cc} [bar]	Performance Parameters	H2/O2	CH4/O2	C2H2/O2
300	Fitness [-]	66	218	48
	Orbit [-]	T	F	T
	$I_{sp,t,eff}$ [s]	480	367	384
	DeltaV [m/s]	11396	8958	9072
	$M_{surplus}$ [Mg]	0	0	0
250	Fitness [-]	35	255	110
	Orbit [-]	T	F	F
	$I_{sp,t,eff}$ [s]	478	367	379
	DeltaV [m/s]	11209	8910	9112
	$M_{surplus}$ [Mg]	3	0	0
200	Fitness [-]	22	N/A	N/A
	Orbit [-]	T		
	$I_{sp,t,eff}$ [s]	477		
	DeltaV [m/s]	11157		
	$M_{surplus}$ [Mg]	0		

Table 9.7: Provides the performance parameters of the aerospike performance trade-off module, generated with LH2/LOX=0.225 [-], LCH4/LOX=0.3 [-], LC2H2/LOX=0.7 [-], LC2H4/LOX=0.475 [-], and $\epsilon_{eff,max}$=220 [-].

Table 9.7 provides the performance parameters for the trajectory simulations with varying p_{cc} of an aerospike powered ascent vehicle. The The ascent trajectories found illustrate the same pattern as those found for the varying T/W optimisations, provided in Section 9.3.1.
Again, the H2/O2 powered illustrates great resilience to a reduces p_{cc}, as illustrated in Table 9.7. However, the C2H2/O2 powered aerospike losses its orbital capabilities immediately. Therefore, it can be concluded that for an C2H2/O2 powered aerospike to be viable engine forA VT SSTO RLV, a p_{cc} of 300 bar and a T/W of 200 need to be achieved.

9.3.3. Sensitivity Analysis on the Aerospike Engine

As previous described in Section 9.1, the ascent trajectories are ran with the optimised trajectories settings found in Sections 9.3.1 and 9.3.2. The trajectory settings used in sensitivity analyses are those with the specifications p_{cc}=300 and at both T/W values of 150 and 200, hence only the complete sets are evaluated.
originally, the sensitivity of the aerospike is limited to the maximum expansion ratio/design expansion ratio ($\epsilon_{eff,max}$) and the pressure reduction factor ($\kappa_{expansion}$). However, for reason that will be explored later on in this thesis, the sensitivity analysis of the directional losses ($\eta_{direction}$) is added.
The sensitivity analysis explores the robustness of the findings in Sections 9.3.1 and 9.3.2 and identifies possible critical parameters for the aerospike engines.

Sensitivity of the Expansion Reduction Factor $\epsilon_{eff,max}$

The aerospike performance is computed for $\epsilon_{eff,max}$ value of 220, which is higher than the $\epsilon_{eff,max}$ of the RS-2200 ($\epsilon_{eff,max}$=173). The sensitivity of $\epsilon_{eff,max}$ evaluates the significance of this assumptions.
The sensitivity is performed for the $\epsilon_{eff,max}$ values of 200, 180 and 160. The analysis is done for two base with p_{cc} at 300 bar, for both T/W of 150 and 200. The sensitivity table for the T/W=150 is found in Appendix I.1.1 as the same patterns are observed in the table with T/W=200.

Aerospike Engine		p_{cc}=300 [bar] T/W=200					
$\epsilon_{eff,max}$ [-]	Performance Parameters	H2/O2		CH4/O2		C2H2/O2	
200	Fitness [-]	67	(2.2%)	233	(7.0%)	47	(-3.6%)
	Orbit [-]	T		F		T	
	$I_{sp,t,eff}$ [s]	479	(-0.2%)	367	(-0.2%)	384	(-0.1%)
	DeltaV [m/s]	11371	(0.2%)	8902	(-0.6%)	9059	(-0.1%)
	$M_{surplus}$ [Mg]	0		0		0	
180	Fitness [-]	62	(-6.2%)	229	(5.2%)	45	(-6.8%)
	Orbit [-]	T		F		F	
	$I_{sp,t,eff}$ [s]	478	(-0.4%)	366	(-0.3%)	383	(-0.3%)
	DeltaV [m/s]	11299	(-0.4%)	8916	(-0.5%)	9043	(-0.3%)
	$M_{surplus}$ [Mg]	0		-1		0	
160	Fitness [-]	60	(-9.4%)	236	(8.4%)	46	(-4.9%)
	Orbit [-]	T		F		F	
	$I_{sp,t,eff}$ [s]	477	(-0.7%)	365	(-0.6%)	382	(-0.5%)
	DeltaV [m/s]	11268	(-0.7%)	8891	(-0.8%)	9025	(-0.5%)
	$M_{surplus}$ [Mg]	0		0		0	

Table 9.8: Provides the performance parameters and the percentage w.r.t. the base ascent trajectories for the aerospike engine at varying $\epsilon_{eff,max}$.

Table 9.8 illustrates the minor influence of $\epsilon_{eff,max}$, as a reduced $\epsilon_{eff,max}$ values reduce both DetlaV and $I_{sp,t,eff}$ by less than 1%. Moreover, the H2/O2 and C2H2/O2 powered aerospikes both maintains their orbit capabilities. Therefore, a reduction in $\epsilon_{eff,max}$ has negligible consequences for the ascent trajectory.
To conclude, $\epsilon_{eff,max}$ is not a critical parameter. Furthermore, from the T/W evaluation, presented in Table 9.6, the effect of a reduced T/W is more substantial than that of $\epsilon_{eff,max}$. As such, a design should opt for a lower $\epsilon_{eff,max}$ if this reduces the engine mass, to obtain a net performance gain.

In some instances in Tables 9.8 and I.1 the fitness appears to improve when $\epsilon_{eff,max}$ is reduced. This is a consequence of the weaker engines reducing the altitude overshoot in the base trajectory, as is illustrated in Figure 9.4. While, the differences in relative reduction between DeltaV and $I_{sp,t_{avg}}$ is due to $I_{sp,t,avg}$ being the time averaged $I_{sp,eff}$.

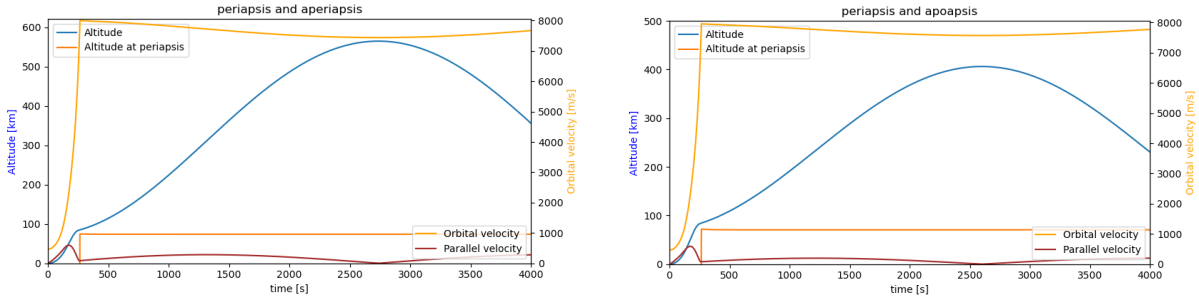

(a) (b)

Figure 9.4: Illustrates the mission profile of the C2H2/O2 powered aerospike with p_{cc}=300 [bar] and T/W=150 [-], and $\epsilon_{eff,max}$=220 [-] (a) and $\epsilon_{eff,max}$=160 [-] (b).

Sensitivity to Expansion Reduction ($\kappa_{expansion}$)
$\kappa_{expansion}$ is the ratio with which p_e deviates from p_a, thereby simulating inefficient expansion. Recall that p_e is computed via $p_e = p_a(1+\kappa_{expansion})$, as described in Section 7.2.3.
The $\kappa_{expansion}$ values 0.1 (10%), 0.2 (20%), and 0.3 (30%) are evaluated. The values are based on the RS-2000 specifications, which would have been the main engine for the X-33 and the VentureStar. The XR-2200 would have had a p_{cc} of 155 bar with an Nozzle Pressure Ratio (NPR) of 150 [73]. This implies that p_e is equal to p_a at SL, hence the $\kappa_{expansion}$ are expected to be small .

The sensitivity is only done for the base ascent with p_{cc} = 300 bar and T/W=200, as the effect of $\kappa_{expansion}$ is negligible.

Aerospike Engine		p_{cc}=300 [bar] T/W=200 [-]					
$\kappa_{expansion}$ [%]	Performance Parameters	H2/O2		CH4/O2		C2H2/O2	
10%	Fitness [-]	69	(0.0%)	217	(0.1%)	49	(0.0%)
	Orbit [-]	T		F		T	
	$I_{sp,t,eff}$ [s]	480	(0.0%)	367	(0.0%)	384	(0.0%)
	DeltaV [m/s]	11396	(0.0%)	8958	(0.0%)	9072	(0.0%)
	$M_{surplus}$ [Mg]	0		0		0	
20%	Fitness [-]	69	(0.0%)	218	(0.0%)	48	(-0.4%)
	Orbit [-]	T		F		T	
	$I_{sp,t,eff}$ [s]	480	(0.0%)	367	(0.0%)	384	(0.0%)
	DeltaV [m/s]	11395	(0.0%)	8957	(0.0%)	9072	(0.0%)
	$M_{surplus}$ [Mg]	0		0		0	
30%	Fitness [-]	69	(0.0%)	218	(0.0%)	49	(0.0%)
	Orbit [-]	T		F		T	
	$I_{sp,t,eff}$ [s]	480	(0.0%)	367	(0.0%)	384	(0.0%)
	DeltaV [m/s]	11395	(0.0%)	8956	(0.0%)	9071	(0.0%)
	$M_{surplus}$ [Mg]	0		0		0	

Table 9.9: Provides the performance parameters and the percentage w.r.t. the base ascent trajectories for the aerospike engine at varying $\kappa_{expansion}$.

Table 9.9 illustrates that the performance of the aerospikes are insensitive with regard to $\kappa_{expansion}$. These findings are inline with the prior $\epsilon_{eff,max}$ sensitivity analysis, as both influence p_e.
Only when $\kappa_{expansion}$ is increased to 0.8 (80%) and 2.5 (250%), that a reduction in the performance is observed. These results are found Appendix I.1.2, yet these $\kappa_{expansion}$ values are unlikely given the XR-2200 specifications.

However, the above findings are in contrast to those presented in [79], which, prior to $\epsilon_{eff} = \epsilon_{max}$, demonstrates a thrust losses of 3%-7% compared to the optimal. Hence, the thrust losses must be due to a different nature. It is believed that these losses are the result of directional losses, as is discussed in Section 7.2.3. Consequently, an additional sensitivity analysis on the directional losses is performed.

Sensitivity of the Directional Losses $\eta_{direction}$
The notion that the directional losses are the prime reason for the performance losses is further evidenced by the I_{sp} of the H2/O2 trajectories. The $I_{sp,sl}$ and $I_{sp,vac}$ levels are significantly higher than the $I_{sp,sl}$=345 s and I_{sp}=455 s for the XR-2200, as illustrated in Table 9.20. Even though the difference of 25-30 s at VAC is explained by the higher p_{cc}, the 70 s at SL cannot. Hence, the latter must be the consequence of the directional losses, as all other factors have been ruled out.
The directional losses are simulated with Equation 9.1, were U_e is the exhaust velocity computed with Equation 5.1. $U_{e,eff}$ replaces U_e in the thrust Equation 4.3. Equation 9.1 reduces $U_{e,eff}$ more, the further ϵ_{eff} is from $\epsilon_{eff,max}$, as is observed in [79].

$$U_{e,eff} = U_e \cdot \left(1 - \eta_{direction}\right)\left(1 - \frac{\epsilon_{eff}}{\epsilon_{max}}\right) \tag{9.1}$$

The $\eta_{direction}$ values are evaluated at 3%, 7%, and 10% which are based on the findings in [79]. The performance parameters and the relative change w.r.t. the base trajectory, namely the specifications p_{cc}= 300 bar and T/W=200, are found in Tab;e 9.3.3. Once again, the sensitivity table based on the trajectories with specifications p_{cc}= 300 bar and T/W=150 is found in Appendix I.1.3, with the only difference that the drop-off points are reached earlier for the T/W=150.
Even thought the equation for the directional losses can equally be interpreted as the friction losses, this is excluded in Section 7.1.2 due to the minor effects.

Aerospike Engine		p_{cc}=300 [bar] T/W=200					
$\eta_{direction}$ [-]	Performance Parameters	H2/O2		CH4/O2		C2H2/O2	
0.03	Fitness [-]	63	(-3.4%)	236	(8.3%)	50	(2.4%)
	Orbit [-]	T		F		T	
	$I_{sp,t,eff}$ [s]	478	(-0.5%)	364	(-1.0%)	382	(-0.4%)
	DeltaV [m/s]	11313	(-0.3%)	8921	(-0.4%)	9041	(-0.3%)
	$M_{surplus}$ [Mg]	0		-1		0	
0.07	Fitness [-]	62	(-5.9%)	777	(256.8%)	58	(19.7%)
	Orbit [-]	T		F		F	
	$I_{sp,t,eff}$ [s]	474	(-1.2%)	358	(-2.5%)	380	(-1.1%)
	DeltaV [m/s]	11260	(-0.8%)	8860	(-1.1%)	8993	(-0.9%)
	$M_{surplus}$ [Mg]	0		-1		0	
0.1	Fitness [-]	61	(-7.8%)	1505	(591.3%)	834	(1615.1%)
	Orbit [-]	T		F		F	
	$I_{sp,t,eff}$ [s]	471	(-1.8%)	353	(-4.0%)	378	(-1.6%)
	DeltaV [m/s]	11217	(-1.2%)	8793	(-1.8%)	8952	(-1.3%)
	$M_{surplus}$ [Mg]	0		0		0	

Table 9.10: Provides the performance parameters and the percentage w.r.t. the base ascent trajectories for the aerospike engine at varying $\eta_{direction}$.

Firstly, it is observed that CH4/O2 reaches its drop-off point for a $\eta_{direction}$ values of 0.07, for both T/W ratios. Incidentally, this is the same value at which the C2H2/O2 powered aerospike engine losses its orbital capabilities[4].
Concerning the H2/O2 powered aerospike, in both analysis the reduction in DeltaV is similar in magnitude ($\sim$ 0.1%). However, the reduction in $I_{sp,t,eff}$ differs with 0.5% to 2.0%. The larger reduction in $I_{sp,t,eff}$ reduction for T/W=150 is expected as the lower T/W engines have higher mass rate in the take-off phase (to achieve the same acceleration). As a result, these vehicles reach burn out faster, therefore have less burn time at $\epsilon_{eff,max}$. As such, while $I_{sp,eff}$ is reduced equally for both configuration, proportionally the reduction is larger for the engines with T/W=150.

To continue, the H2/O2 powered aerospike never reaches a drop-off point in Table 9.3.3, it immediately reaches the drop-off point for the T/W=150 configuration, see Table I.3. However, the drop-off point does not indicate a loss of orbit capabilities, evidenced by the relative low reduction in DeltaV and $I_{sp,t,eff}$. Further analysis show that the reduction in the early launch phase results in the vehicle descending before the circularisation burn can occur, as is illustrated in Figure 9.5. As such, the idle phase period, a low thrust period at between the early high thrust phase and circularisation burn, for this weaker engine is too long.
There is less evidence that the same phenomena causes the loss in orbit capabilities for the C2H2/O2 powered aerospike with T/W=200. Firstly, no drop-off point is observed indicating that optimisation settings are still sufficient close to the ideal orbit. Secondly, prior analysis illustrate that the C2H2/O2 configuration marginally achieves orbit capabilities, as illustrated in Tables 9.6, 9.7, and 9.8.

Therefore, it is reasonable to assume that the H2/O2 aerospike at T/W=150 still maintains orbit capabilities, given the large realised DeltaV. Yet, the model will need to re-optimise both the steering and burning settings. The described phenomena in Figure 9.5 is to a greater extend observed for the $\eta_{direction}$ value of 0.07 and 0.1 too.

[4]The C2H2/O2 powered aerospike with T/W=150 never had orbital capabilities and reaches drop of at a $\eta_{direction}$ values of 0.03, see Appendix I.1.3.

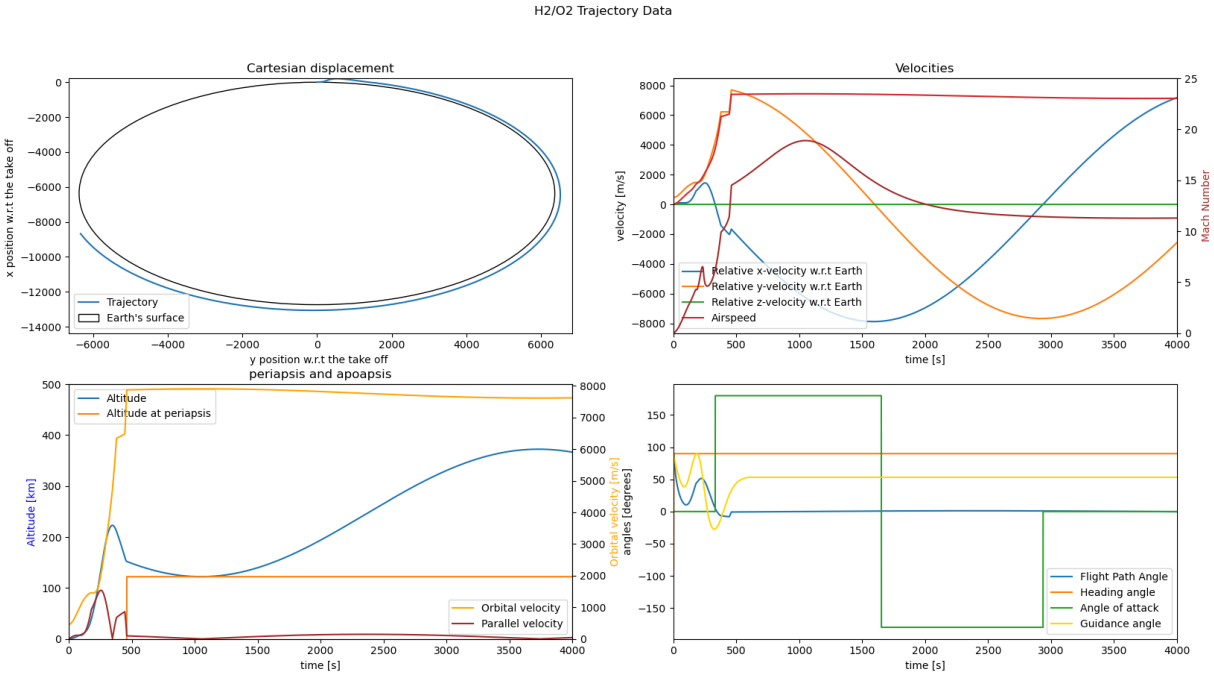

Figure 9.5: Illustrates the trajectory profile of the H2/O2 powered aerospike with p_{cc}=300 [bar], T/W=150 [-], and $\eta_{direction}$=0.03 [-].

Furthermore, when analysing the $I_{sp,eff}$ the same pattern as presented in [79] is observed, as is illustrated in Figure 9.6. Even though the plot taken form [79] uses NPR on the x-axis, t and NPR are closely related through ϵ_{eff} which increases with h, which (generally) increases with t. Because t and NPR are not related one-to-one especially in the early thrust phase, the decreasing percentage observed in Figure 9.6 appears extended for (a). The absolute $I_{sp,eff}$ reduced values are found in Appendix I.1.3.
The hypothesis that the losses are due to $\eta_{direction}$ is strongly evidenced by the close resemblance Figures 9.6 (a) and 9.6 (b). Furthermore, a $\eta_{direction}$ of 0.07 most realistic represents the performance of an aerospike, given the findings of [73] and [79]. As such, $\eta_{direction}$ cannot be neglected for less powerful aerospikes as they significantly affect the ascent settings.

From a theoretical perspective, the directional losses are explained by the Prandtl-Meyer approximation proposed in Section 7.2.3. The Prandtl-Meyer approximation provides a flow direction given the shock expansion fan angle. The fan expands as the ambient pressure drops. However, this flow direction is only parallel with the vehicle's central axis for one specific expansion. Logically, this is at $\epsilon_{max,eff}$, as this would result in the maximum realised DeltaV[5]. At all other expansion the flow direction is off the parallel axis, invoking the directional losses.

Given the merit of Equation 9.1 due to the close resemblance in Figure 9.6, it could provide insights in how to reduce the directional losses. Namely, by reducing the $\epsilon_{eff,max}$ the losses in $I_{sp,eff}$ throughout the ascent are less severe at the cost of a reduced $I_{sp,eff,max}$. The above reasoning combined with the potential mass reduction that comes with a lower $I_{sp,eff}$, as is discussed in the previous $\epsilon_{eff,max}$ sensitivity section, seems to make a strong case that a reduction in $\epsilon_{eff,max}$ is beneficial to the performance of the aerospike. This makes sense, given the Prandtl-Meyer theory, as it would mean that the thrust direction is aligned with the central axis for an extended period of time.

[5]Note that this is only true if thrust is generated at $\epsilon_{max,eff}$ for a prolonged period.

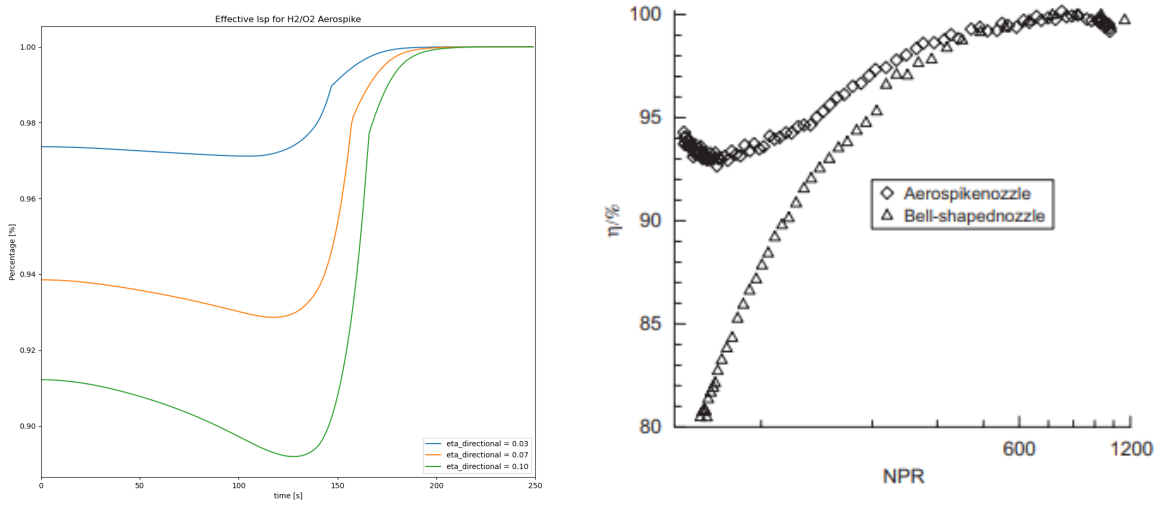

(a) (b)

Figure 9.6: Illustrates the $I_{sp,eff}$ percentage compared to the ideal $I_{sp,eff}$ (a) is the simulated aerospike ascent with p_{cc}=300 [bar] and T/W=150 $I_{sp,eff}$ over time (b) illustrates the performance percentage of $I_{sp,t,eff}$ over ϵ_{eff}, taken from [79].

To conclude, even when considering directional losses the H2/O2 aerospike engine maintains its orbit capabilities. Yet, the same cannot be said for the C2H2/O2 powered aerospike, which likely loses its orbital capabilities. However, directional losses cannot be neglected when computing the performance of an aerospike engine, due to their significant impact on ascent trajectory. The value of $\eta_{direction}$ is most likely 0.07, which inflicts $I_{sp,t,eff}$ and DetltaV performance reductions of ~2% to ~3% and ~2%, respectively. Furthermore, there is strong evidence that a reduced $\epsilon_{eff,max}$ is beneficial to the performance of an aerospike.

9.3.4. Discussion Aerospike Performance

Discussion

Out of all the propellant pallets evaluated for the aerospike engine only the H2/O2 consistently illustrated orbital capabilities (payload of 15 tons to 400 km orbit). This is beneficial for the development of an H2/O2 powered aerospike engine, as it does not require the highest achieved engine specifications (p_{cc}=300 bar, T/W=200). Therefore, a less powerful H2/O2 engine can be developed that still possess the required orbit capabilities, which is economically more desired as it logically has a lower development cost. Complementary, such an engine is well suited for a continuous development philosophy as proposed in Chapter 2. The less powerful engine is the first generation, the specifications are then improved over following development cycles. All while the engine is operated on an SSTO vehicle, generating revenues that can be used to fund the continuous development.

Evaluating the other propellant pallets, it is unlikely that any CH4/O2 powered aerospike will offer any meaningful general orbit capabilities[6]. Unfortunately, CH4 has become the preferred fuel for the private launch industry. On the other hand, the C2H2/O2 powered aerospike illustrated orbital capabilities if the highest engine specification can be reached. However, the orbit capabilities of the C2H2/O2 configuration are often eliminated by the sensitivity parameters, especially concerning is the $\eta_{directional}$. Unlike the H2/O2 configuration, the C2H2/O2 configuration cannot reduce its $\epsilon_{eff,max}$ to partly mitigate the effect of $\eta_{directional}$, as this too would eliminate the orbit capabilities.

The C2H2/O2 likely has lesser orbit capabilities[6], but whether these have the economic incentives to justify its development is left for future research.

The sensitivity analysis does not find any general critical parameters. However, the sensitivity analysis does reveal that the directional losses cannot be neglected, especially for the less capable configurations. Consequently, this effect is best simulated using Equation 9.1. Lastly, there is strong evidence that the directional losses can be partly mitigated by utilising a lower $\epsilon_{eff,max}$.

[6]The ability to deliver any substantial payload to at least LEO (>200 km).

Possible Performance Gains for Aerospike Engines
Even though the directional losses ($\eta_{\text{directional}}$) cannot be neglected for the performance simulation, the effect can be minimised by reducing $\epsilon_{\text{eff,max}}$. A reduction of $\epsilon_{\text{eff,max}}$ reduces the maximum size of the expansion fan, which reduces $I_{\text{sp,eff,max}}$ too. Because The expansion fan reaches max size earlier, the direction of exhaust flow (at $\epsilon_{\text{eff}} = \epsilon_{\text{eff,max}}$) aligns with the central axis for an extended period of time. Thereby, reducing the period of off-axis thrust but also reducing the magnitude of the direction losses for $\epsilon_{\text{eff}} \neq \epsilon_{\text{eff,max}}$.
Lastly, a propellant surplus should be obtainable for the H2/O2 aerospike configuration, given the large realised DeltaV and overshoot in normal velocity. One approach would be to reintroduce the surplus propellant weight (w_{m}) in the Problem Function (Equation 6.3). Alternatively, the model can be ran with increased constraints (e.g. forced idle period) and over a greater number of generations.

9.4. Results of the Pulse Detonation Engine Simulation

This section contains the performance simulations of the Pulse detonation engines. The PDE simulations are done for the T/W ratios of 150 and 200, as it is unlikely that PDEs, due to the absence of turbo-pumps, have lower T/W ratios. In addition, the PDEs are evaluated at DC pressures of 500, 600, and 700 bar. Note that PDEs are only evaluated at 700 bar of a T/W ratio of 150 if this adds information to the evaluation.
As usual, the PDE sensitivity analyses are provided in the second half of this section. The sensitivity evaluates the robustness of performance findings. The sensitivity analyses include the purge and fill time (t_{fill}) and the expansion ratio (ϵ).

9.4.1. Performance Analysis on the Pulse Detonation Engine with Varying $p_{\text{DC,limit}}$

The PDE is evaluated at varying $p_{\text{DC,limit}}$, equal to the Neumann detonation pressure ($p_{4,\text{N}}$ see Equation 7.24). The DC pressure is limited by the material strength of the DC, and thus equal for all propellant pallets. However, each propellant requires a different injector pressure (p_{31}) to achieve this $p_{\text{DC,limit}}$.
The model results are obtained with the optimisation parameters presented in Table 9.1. The optimisation variables include the steering settings ($\vec{\gamma}(t)$), burning settings ($\dot{m}(t)$), and the expansion ratio (ϵ), and are illustrated in Table 9.11.

Pulse Detonation Engine		Constant T/W [200]			
$p_{\text{DC,limit}}$ [bar]	Performance Parameters	H2/O2	CH4/O2	C2H2/O2	C2H4/O2
700	Fitness	N/A	540	N/A	422
	Orbit [-]		F		T
	$I_{\text{sp,t,eff}}$ [s]		344		349
	DeltaV [m/s]		8248		8376
	M_{surplus} [Mg]		0		0
	f_{cyc} [1/s]		123		129
Sizing variables		[-]	$\epsilon = 10.023$	[-]	$\epsilon = 7.412$
600	Fitness	23	626	62	523.38
	Orbit [-]	T	F	T	F
	$I_{\text{sp,t,eff}}$ [s]	496	340	389	352
	DeltaV [m/s]	101312	8186	9190	8388
	M_{surplus} [Mg]	17	0	0	0
	f_{cyc} [1/s]	164	123	145	129
Sizing variables		$\epsilon = 7.693$	$\epsilon = 8.215$	$\epsilon = 7.338$	$\epsilon = 8.453$
500	Fitness	14	551	58	490
	Orbit [-]	T	F	T	F
	$I_{\text{sp,t,eff}}$ [s]	498	339	383	345
	DeltaV [m/s]	10125	8163	9161	8283
	M_{surplus} [Mg]	20	0	0	0
	f_{cyc} [1/s]	164	123	145	129
Sizing variables		$\epsilon = 9.232$	$\epsilon = 9.351$	$\epsilon = 9.200$	$\epsilon = 7.209$

Table 9.11: Provides the performance parameters of the pulse detonation engine simulation at varying $p_{\text{DC,limit}}$, generated with LH2/LOX=0.350 [-], LCH4/LOX=0.375 [-], LC2H2/LOX=0.775 [-], LC2H4/LOX=0.550 [-], and $L_{\text{DC}} = 2$ [m].

General Performance increase
Detonation is ~60% more efficient than deflagration [14]. Therefore, it comes at no surprise that an increase in performance is observed for the H2/O2 and C2H2/O2 configurations, especially, when compared to the baseline, and to a certain extend to the aerospike equivalents. Furthermore, the C2H2/O2 powered PDE even displays more robuts orbit capabilities. Although, the overshoot discussed in Section 9.1.1 explains the difference in realised DeltaV of C2H2 to H2, some caution should be taken in this observation.
Meanwhile, Ethylene (C2H4) provides an improvement over the Raptor engine, but remains insufficient in reaching a DetlaV or fitness that indicates orbit capabilities. Even when $p_{DC,limit}$ is increased to 700 bar, performance only improves marginally. Therefore, a C2H4/O2 powered PDE does not make SSTOs a viability.

Rather unexpected is the lower ϵ-s for the $p_{DC,limit}$ at 600 bar, compared to those with a $p_{DC,limit}$ equal to 500 bar. Contrarily, for a higher pressure limit a larger ϵ is expected, as $p_{4,Dc}$ positively correlates with p_e. With a higher p_{DC} the flow can be expanded more, before pressure thrust becomes to negative or the blowout limit is reached. Note that more expansion leads the a higher U_e, which results in a more efficient thrust production. It is hypothesised that the opposite is observed as a means to reduce the overshoot in normal velocity. The model has difficulties reducing the overshoots, due to the codependency issues, as described in Section 9.1.1. By using a sub-optimal ϵ the model artificially reduces the power of the engine, as less powerful engines have a better performance, as illustrated in Table 9.11. This explain why the ϵ of the C2H4/O2 and CH4/O2 configurations are less/not effected.
The above hypothesis is verified with the ϵ sensitivity analysis. Although, some discrepancies in the ϵs are expected, the ratios in Table 9.11 surpass discrepancy levels.

Performance of Methane (CH4/O2)
The poor performance of methane (CH4/O2) is unexpected and even worse than the Raptor engine. In Table 9.3 CH4 under constant p_{31} illustrated substantial performance gain, yet it worsens under constant $p_{4,N}$. The explanation of this explains the poor performance too. Even though the detonation of methane is more efficient (more heat per unit mass), too few detonations occur to justify the unsteady combustion process. Hence, the low performance lies with the low detonation frequency, which is inversely correlated with D_{CJ}, via Equation 7.33. While, the D_{CJ} of C2H2 is 3199 m/s, The D_{CJ} of CH4 is significantly lower, equal to 2531 m/s. The lower D_{CJ} is a consequence in the difference in detonation temperature, namely 3864 K compared to 4729 K.
To elaborate, C-bonds (LHC fuels) resist detonation, especially at high pressures, which is made worse the further detonation occurs from the stochastic ratio. Therefore, LHC fuels with many C-bonds require high ignition temperature, especially at high pressures, to achieve detonation. In Table 9.3 for p_{31}=20 bar, C2H2 and C2H4 required far higher ignition temperature than CH4 mitigating the higher detonation temperature, as these do not scale equally. As a result, the heat released ($q = \Delta T$) is smaller for C2H2 and C2H4. The high performance of CH4 in Table 9.3, is simply the result that at p_{31}=20 bar, $p_{4,N}$ is ~900 bar.
At constant $p_{4,N}$ the ignition temperatures are far closer, hence the q for C2H2 and C2H4 is far higher. Furthermore, because CH4 is less energetic it requires a larger p_{31} to reach the same $p_{4,N}$, which requires a higher T_{31} reducing q even further.

9.4.2. Performance Analysis on the Pulse Detonation Engine with varying T/W

Pulse Detonation Engine		Pressure Limit DC [600 bar]			
T/W	Performance Parameters	H2/O2	CH4/O2	C2H2/O2	C2H4/O2
200	Fitness	23	626	62	523.38
	Orbit [-]	T	F	T	F
	$I_{sp,t,eff}$ [s]	496	340	389	352
	DeltaV [m/s]	101312	8186	9190	8388
	$M_{surplus}$ [Mg]	17	0	0	0
	f_{cyc} [1/s]	164	123	145	129
Sizing variables		$\epsilon = 7.693$	$\epsilon = 8.215$	$\epsilon = 7.338$	$\epsilon = 8.453$
150	Fitness	49	N/A	58	N/A
	Orbit [-]	T		T	
	$I_{sp,t,eff}$ [s]	499		388	
	DeltaV [m/s]	10429		9080	
	$M_{surplus}$ [Mg]	14		0	
	f_{cyc} [1/s]	164		145	
Sizing variables		$\epsilon = 8.081$	[-]	$\epsilon = 8.191$	[-]

Table 9.12: Provides the performance parameters of the pulse detonation engine simulation at varying T/W, generated with LH2/LOX=0.350 [-], LCH4/LOX=0.375 [-], LC2H2/LOX=0.775 [-], LC2H4/LOX=0.550 [-], and $L_{DC} = 2$ [m].

Table 9.12 provides the performance parameters of the trajectory simulations with varying T/W ratios for the PDE powered vehicles. Table 9.12 illustrates two aspects. Firstly, both the H2/O2 and C2H2/O2 configuration maintain orbit capabilities, which provides larger design margins and thus makes the findings more robust. However, the H2/O2 configuration losses some of its propellant surplus.
Secondly, the same expansion ratio phenomena observed in Table 9.11, is observed in Table 9.12. That larger ϵ are found for less powerful engine further supplements the notion that the optimisation of ϵ is hindered by codependency issues.

9.4.3. Sensitivity Analysis on the Pulse Detonation Engine

The PDEs with specifications of $p_{DC,limit}$ at 600 bar and T/W at 200 serve as the base ascent trajectories. The sensitivity evaluates t_{fill} and ϵ. The former is evaluated to verify the robustness of the performance findings and the criticality of t_{fill}. The latter evaluates the codependency hypothesis, proposed in Section 9.4.1, as ϵ might have converged to a sub-optimal value, which would indicate limitations in the model.

Sensitivity of the Fill and Purge Time (t_{fill})
The purge and fill time is the time the engine needs to reset the detonation cycle and refill the DC with propellant. Consequently, an increase in t_{fill} results in a lower f_{cyc}, as $f_{cyc} = 1/(t_{III} + t_{fill})$. Throughout the fill and purge phase no thrust is produced, hence an increase in t_{fill} results in a reduction in relative thrust per cycle. Therefore, the performance of a PDE is directly related to the achievable t_{fill}. Hence, t_{fill} is evaluated with a sensitivity analysis.
Unfortunately, evaluating t_{fill} directly is not possible, due to the ideal engine configuration assumption. The model will simply increase A_{DC} to compensate for the decreased f_{cyc}, to ensure the specified $\dot{m}(t)$ is achieved. This is interpreted as using larger or additional engines, which is equivalent to reducing T/W. Therefore, the T/W simulations, in Section 9.4.2, are partly related to a reduced f_{cyc} evaluation. However, the T/W simulations uses an unchanged f_{cyc}, hence an alternative approach is presented in this section. The T/W simulations combined with the findings in this section provide the complete impact of an increased t_{fill} (decreased f_{cyc}).
To simulate an increase in t_{fill} without the model increasing A_{cc}, the f_{cyc} is multiplied with $(1 - \eta_{frequency})$. This has the added effect of decreasing the $\dot{m}$ by $\eta_{frequency}$. Consequently, the ascent uses a lower $\dot{m}$ than is optimum. As a result, in some instances insufficient thrust is produced for the take-off phase.

Pulse Detonation Engine		$p_{DC,limit}$=600 [bar] T/W=200							
$\eta_{frequency}$ [-]	Performance Parameters	H2/O2		CH4/O2		C2H2/O2		C2H4/O2	
0.05	Fitness [-]	226	(889.9%)	790	(26.3%)	1993	(3091.7%)	870	(66.2%)
	Orbit [-]	T		F		F		F	
	$I_{sp,t,eff}$ [s]	496	(0.0%	340	(-0.1%)	385	(-0.2%)	351	(-0.1%)
	DeltaV [m/s]	11762	(14.1%)	8162	(-0.3%)	9172	(-0.2%)	8392	(0.1%)
	$M_{surplus}$ [Mg]	0		0		0		0	
	f_{cyc} [1/s]	155	(-5.0%)	117	(-5.0%)	137	(-5.0%)	123	(-5.0%)
	t_{III}/t_{fill} [s]/[s]	0.00411	0.00232	0.0061	0.00243	0.00491	0.00236	0.00573	0.00241
0.1	Fitness [-]	1254	(5383.6%)	1255	(100.6%)	2456	(3834.1%)	2437	(365.8%)
	Orbit [-]	F		F		F		F	
	$I_{sp,t,eff}$ [s]	496	(-0.0%)	339	(-0.3%)	380	(-1.4%)	349	(-0.6
	DeltaV [m/s]	11746	(13.9%)	8220	(0.4%)	6786	(-26.2%)	8348	(-0.5%)
	$M_{surplus}$ [Mg]	0		0		41		0	
	f_{cyc} [1/s]	147	(-10.0%)	111	(-10.0%)	130	(-10.0%)	116	(-10.0%)
	t_{III}/t_{fill} [s]/[s]	0.00411	0.00268	0.0061	0.0029	0.00491	0.00277	0.00573	0.00286
0.2	Fitness [-]	2384	(10323.0	2705	(332.4%)	2705	(4231.8%)	2705	(416.9%)
	Orbit [-]	F		Failed to take-off		Failed to take-off		Failed to take-off	
	$I_{sp,t,eff}$ [s]	493	(-0.6%)	324	(-4.6%)	366	(-5.1%)	332	(-5.4%)
	DeltaV [m/s]	4717	(-54.3%)	9	(-99.9%)	10	(-99.9%)	9	(-99.9%)
	$M_{surplus}$ [Mg]	161		507		507		507	
	f_{cyc} [1/s]	131	(-20.0%)	99	(-20.0%)	116	(-20.0%)	103	(-20.0%)
	t_{III}/t_{fill} [s]/[s]	0.00411	0.00353	0.0061	0.00403	0.00491	0.00373	0.00573	0.00393

Table 9.13: Provides the performance parameters and the percentage w.r.t. the base ascent trajectories for the pulse detonation engine at varying $\eta_{frequency}$.

Note that the I_{sp} is unaffected by a change in f_{cyc} as thrust and mass rate are reduced equally. Table 9.13 provides a reduced $I_{sp,t,eff}$, caused by an engine burnout at lower altitude (lower final $I_{sp,eff}$).
Furthermore, Table 9.13 illustrates that at a $\eta_{frequency}$ of 0.2 the C2H2/O2, CH4/O2, and C2H4/O2 powered PDEs fail to take-off. At these t_{fill} values the mass rate is reduced to such an extend that insufficient thrust is generated to achieve lift-off. Additional engines or larger engines are needed to compensate.

In Table 9.13, the C2H2/O2 configuration immediately reaches the drop-off point, as a result of insufficient mass rate during the take-off phase. To elaborate, the vehicle reaches an insufficient altitude to perform an effective circularisation burn, which also increases the gravity and atmospheric drag losses. In addition, the idle phase, for the reduced thrust, is too long, causing the vehicle to lose altitude. Hence, the poor fit is a consequence of very poor trajectory settings, as is evidenced by the relatively unchanged DeltaV and $I_{sp,eff}$.
For $\eta_{frequency}$=0.1 the limited initial altitude gain combined with a far to long idle phase, causes the vehicle to preemptive termination (crash). While, for $\eta_{frequency}$=0.2 take-off thrust is reduced to such an extend that the vehicle fails to take-off.
Given the small reduction in $I_{sp,eff}$ and DeltaV and the fact that a C2H2/O2 configuration with T/W=150 possess the orbital capabilities, it is safe to assume that a mass penalty can be taken to mitigate the $\eta_{frequency}$ losses. It is only when t_{fill} surpasses 76% of t_{III} ($\eta_{frequency}$=0.3), that t_{fill} becomes a critical parameter. However, commonly t_{fill} is closer to 50% of t_{III} [60].

The H2/O2 powered PDE is less effected by $\eta_{frequency}$, as it can still reach orbit for $\eta_{frequency}$ of 0.05. However, the steering setting are sub-optimal for the effectively changed burning settings. Moreover, orbit is only achieved by utilising the mass surplus, still present in Table 9.11. For $\eta_{frequency}$=0.2 the H2/O2 powered vehicle suffers from the same insufficient thrust issues as described before. All in all, H2/O2 PDE remains a viable option for possible VT SSTO RLV, especially considering that it maintains its orbit capabilities for a reduced T/W, see Table 9.12.

The $I_{sp,t,eff}$ and DeltaV of the CH4/O2 and C2H4/O2 powered PDEs is only limited affected prior to insufficient take-off thrust, at which point both engines fail to take-off. The increase of 0.4% in DeltaV for the CH4/O2

configuration at $\eta_{frequency}$=0.1 is due to the alteration in $\dot{m}$ which allowed the vehicle to consume some of the propellant margin. The actual value is ~8101 m/s.

All in all, a 40% increase in t_{fill} results in a <1% reduction in $I_{p,t,eff}$, which translates to a similar DeltaV reduction, although this cannot be said with certainty. However, a more substantial increase in t_{fill} (~80%) will cause substantial thrust reductions. However, these can be remedied by larger or additional engines, which reduce the T/W but should not effect the orbit capabilities, see Table 9.12.

Sensitivity of the Expansion ratio (ϵ)
Even though ϵ is a sizing parameters its effect is still evaluated, due to possible codependency issues between the burning settings and ϵ. The codependency issues are speculated because of the higher ϵ values for $p_{4,N}$=500 bar than those found for $p_{4,N}$=600 bar, as discussed in Section 9.4.1. Hence, the analysis of ϵ can reveal that the optimisation for ϵ and the burning settings should be segregated.

Pulse Detonation Engine		$p_{DC,limit}$=600 [bar] T/W=200							
ϵ [-]	Performance Parameters	H2/O2		CH4/O2		C2H2/O2		C2H4/O2	
upper limit ϵ		15.864		10.084		8.321		9.241	
7.5	Fitness [-]	23	(-1.5%)	632	(1.1%)	62	(-1.2%)	531	(1.5%)
	Orbit [-]	T		F		F		F	
	$I_{sp,t,eff}$ [s]	496	(-0.1%)	339	(-0.3%)	386	(0.0%)	350	(-0.3%)
	DeltaV [m/s]	10318	(0.1%)	8156	(-0.4%)	9212	(0.2%)	8356	(-0.4%)
	$M_{surplus}$ [Mg]	17		0		0		0	
8.5	Fitness [-]	40	(75.8%)	623	(-0.3%)	64	(2.8%)	523	(-0.1%)
	Orbit [-]	T		F		T		F	
	$I_{sp,t,eff}$ [s]	498	(0.3%)	341	(0.1%)	387	(0.2%)	352	(0.0%)
	DeltaV [m/s]	10314	(0.0%)	8196	(0.1%)	9235	(0.5%)	8389	(0.0%)
	$M_{surplus}$ [Mg]	18		0		0		0	
9.5	Fitness [-]	50	(120.3%)	615	(-1.7%)	N/A		517	(-1.2%)
	Orbit [-]	T		F				F	
	$I_{sp,t,eff}$ [s]	499	(0.6%)	342	(0.4%)			352	(0.2%)
	DeltaV [m/s]	10348	(0.4%)	8228	(0.5%)			8414	(0.3%)
	$M_{surplus}$ [Mg]	18		0				0	
10.5	Fitness [-]	60	(160.4%)	N/A		N/A		N/A	
	Orbit [-]	T							
	$I_{sp,t,eff}$ [s]	500	(0.9%)						
	DeltaV [m/s]	10328	(0.2%)						
	$M_{surplus}$ [Mg]	18							

Table 9.14: Provides the performance parameters and the percentage w.r.t. the base ascent trajectories for the pulse detonation engine at varying $\epsilon_{eff,max}$.

Table 9.14 provides the performance parameters for base trajectories, namely the PDE with specification p_{DC}=600 bar and T/W=200, at varying ϵ. For clarity reasons f_{cyc} is excluded from Table 9.14, as f_{cyc} remains unchanged.
The 3rd top row of Table 9.14 contains the upper ϵ limit for each propellant pallet. The N/A fields in Table 9.14 is were the evaluated ϵ surpasses the limit. A higher ϵ than the limit causes the atmosphere to enter the engine at SL, which results in a blowout.
While, C2H4 only shows negligible improvements for an increased ϵ, other propellant pallets show more substantial increases. Note that the ϵ=9.5 surpasses the the C2H4 limit, hence the gains that can be realised are even smaller.
The CH4/O2 configuration illustrates a slightly larger performance gain, yet these are even insufficient to make CH4/O2 powered PDEs a next generation engine contender, let alone a viable engine forA VT SSTO RLV.

Which leave the C2H2/O2 and H2/O2 configurations. Even though C2H2/O2 shows a minor performance gain, once again the ϵ surpasses the limit, hence gains could be of negligible levels.
Lastly, the H2/O2 configuration illustrates a more substantial gain, with the trend suggesting that larger ϵ-s provide even more performance gains. Moreover, the propellant surplus is increased with ~1,000 kg.
Hence, it can be concluded that the model converges to a sub-optimal ϵ for an H2/O2 powered PDE. Yet, this is not due to codependency as the phenomena would have been observed for all propellants pallets. Rather, the reason for the sub-optimal ϵ is due to the same reason that more powerful engines have worse fits, as elaborated in Section 9.1.1. To summarise, because of the high performance of the H2/O2 powered PDE, it can afford to be caught in a local optima with sub-optimal variables, in this instance the ϵ, where the model weights are insufficient to push it to the global optima. Logically, ϵ has low codependency with $\dot{m}$, as a change in $\dot{m}$ does not effect the benefit of increasing ϵ.

To summarise, the performance is improved the closer ϵ is to its corresponding upper limit. Furthermore, the model finds an ϵ sufficiently close to the optimal value. However, when a PDE engine with substantial orbit capabilities, like the H2/O2 powered PDE, is optimised, ϵ may be sub-optimal and reflect the value of a local optimum. To conclude, for the purpose of this thesis ϵ does not require a segregated optimisation loop.

9.4.4. Discussion Pulse Detonation Engine Performance

Discussion
Like the aerospike engine, the H2/O2 powered PDE possess the required orbit capabilities. Moreover, the C2H2/O2 configuration possess the same orbit capabilities too. However, while the H2/O2 configuration maintained its orbit capabilities for a f_{cyc} reduction of 5%, the C2H2/O2 configuration directly loses its orbit capabilities. Yet, for a 10% f_{cyc} reduction the H2/O2 configuration also loses its orbit capabilities. However, the loss is driven by the complementary poor trajectory settings, which can partly be mitigated by a resizing of the engine. Even so, care must be taken that no excessive snowball effect is initiated rendering the engines unviable, yet this seems unlikely given the results in Table 9.12. Therefore, though the purge and fill time (t_{fill}) cannot be identified as a critical component, it at least should be identified as a sub-critical component. Hence, it has ramifications for the sizing and ascent trajectory of the vehicle.
All in all, the PDEs illustrate a substantial performance increase over both the Raptor engine and the aerospike engines. Even a propellant surplus for the the H2/O2 powered PDE is observed. However, even though the model generally provides a good indication for the ϵ, for the very powerful engines ϵ can have sub-optimal values. Hence, using ϵ-s equal to the upper limits can provide additional performance.

Possible Performance Gains For Pulse Detonation Engines
As a last remark, even more performance can be obtained if the final pressure of the blowdown phase is increased. The current model set the final pressure equal to 1 atm. However, this can be increase to $p_{injector}$, doing so will increase the detonation frequency (f_{cyc}) by cutting short the blowdown phase. Moreover, by removing the low thrust blowdown phase the relative thrust per cycle is increased too. Hence, more thrust cycles and higher thrust level are produced.

9.5. Results of the Precooled Hybrid Airbreathing Rocket Engine Simulations

The T/W evaluations for the hybrid engines are restricted to the values 100 and 150. As mentioned in Sections 6.2.4 and 9.1, it is highly unrealistic that in the foreseeable future breathing engines, let alone the precooled hybrid airbreathing rocket engine, will achieve T/W ratios near 200. It is believed that by the time such feeds are achieved that the literature trade-off in Chapter 4 is outdated. Hence, at that time a different set of engines might be more worth evaluating.
Unlike previous engines, no performance optimisation is done at varying p_{cc}, due to p_{cc} having a minor effect, see Section 9.3.2, which is exemplified for the hybrid engine as it operates at $p_{cc} = p_{29}$ for a significant portion of the thrust phase. Therefore, the p_{cc} evaluations are moved to the sensitivity analysis.
Section 9.3.2 indicated that The latter half of this section contains all the sensitivity analyses, namely Section 9.5.2. Because the hybrid engine has far more design and sizing parameters than previous engines, only pa-

rameters are evaluated that are found to be influential throughout the development or for which the values are uncertain. The motivation is further elaborated in Section 9.5.2. These parameters are the C_D, the E_{cooler}, and the θ, which combined with the p_{cc} complete the set of sensitivity parameters of Section 9.5.2.

9.5.1. Performance Analysis on the Precooled Hybrid Airbreathing Rocket Engine at Varying T/W

The optimisation parameters used are provided in Tables 9.1. The optimisation variables include the steering and burning settings, the F/O for the breathing phase, and the ϵ. The latter is constraint by the exhaust pressures of 1 atm and ~0.225 bar, the lower and upper bounds respectively. The F/O ratios for the non-breathing phase are taken from Table 9.4. The results are provided in Table 9.15.
The model only optimises for T/W=150 if orbit was not achieved at a T/W value of 100, however a T/W value of 150 for a breathing engine is a significant engineering challenge. To reiterate, this thesis considers an unified homogeneous propulsion system. A propulsion system operating both pure rocket engines and hybrid engines might achieve a higher overall T/W ratio. However, this implies that fewer hybrid engine operate on a relative larger intake mass rate, which introduces other engineering challenges.

Precooled Hybrid Airbreathing Rocket Engine		Constant CC Pressure [300 bar]	
T/W	Performance Parameters	H2/O2	CH4/O2
150	fitnes	N/A	105
	Orbit [-]		T*
	$I_{sp,t,eff}$ [s]		406
	DeltaV [m/s]		8967
	$M_{surplus}$ [Mg]		0
Sizing Parameters		[-]	$F/O_{breathing} = 0.467$, $\epsilon = 45.94$
100	Fitness [-]	91	231
	Orbit [-]	T	F
	$I_{sp,t,eff}$ [s]	639	395
	DeltaV [m/s]	12958	8784
	$M_{surplus}$ [Mg]	0	0
Sizing Parameters		$F/O_{breathing} = 0.675$, $\epsilon = 56.72$	$F/O_{breathing} = 0.492$, $\epsilon = 50.85$

Table 9.15: Provides the performance parameters of the precooled hybrid airbreathing rocket engine simulation at varying T/W, generated with LH2/LOX=0.225 [-], LCH4/LOX=0.300 [-], and $\Pi_{HPC} = 85$, $E_{cooler} = 0.8$, $\kappa_{cooler,loss} = 0.03$, $\nu_{HPC} = 0.83$, and θ=20°.

Performance of the T/W ratio at 100

The $I_{sp,t,eff}$ reveals the that Ch4/O2 configuration has a significantly shorter breathing phase, illustrated in Figure 9.7, Hence the large DeltaV difference between the H2/O2 and CH4/O2 configuration in Table 9.15. Furthermore, the fitness for the H2/O2 configuration is substantially higher than previous successful engines. Closer examinations reveals that this is because of the overshoot in both the normal and orbital velocity. While, this is partly contributed to the limited generation number, see Table 9.1, it is fundamentally expected. Unlike the other engines, the hybrid engine produces the majority of its orbital velocity in the earlier phases and the majority of altitude thrust in the latter phases. As a result, the codependency hinders the orbital velocity overshoot primarily, for which the weight is larger, see Section 9.1.3.

The burning program of the CH4/O2 powered engine, closely resembles the hypothesised pattern of Section 9.1.2. Namely, the first node is the take-off node, followed by the breathing node. The next node is the main thrust node, seen in both the aerospike and convectional engines. The last two nodes correspond to the idle phase and circularisation burn, respectively. Yet, the idle phase still utilises a too large a mass rate and lasts too long, to preform an effective circularisation burn. Regardless, the CH4/O2 powered engine fails to illustrate the required orbital capabilities.
Even though, the CH4/O2 powered engine utilises breathing to gain orbital velocity its relative short duration is likely explained by a propellant shortage, as prolonging the breathing phase will deplete the propellant

supply needed to climb to the desired altitude.

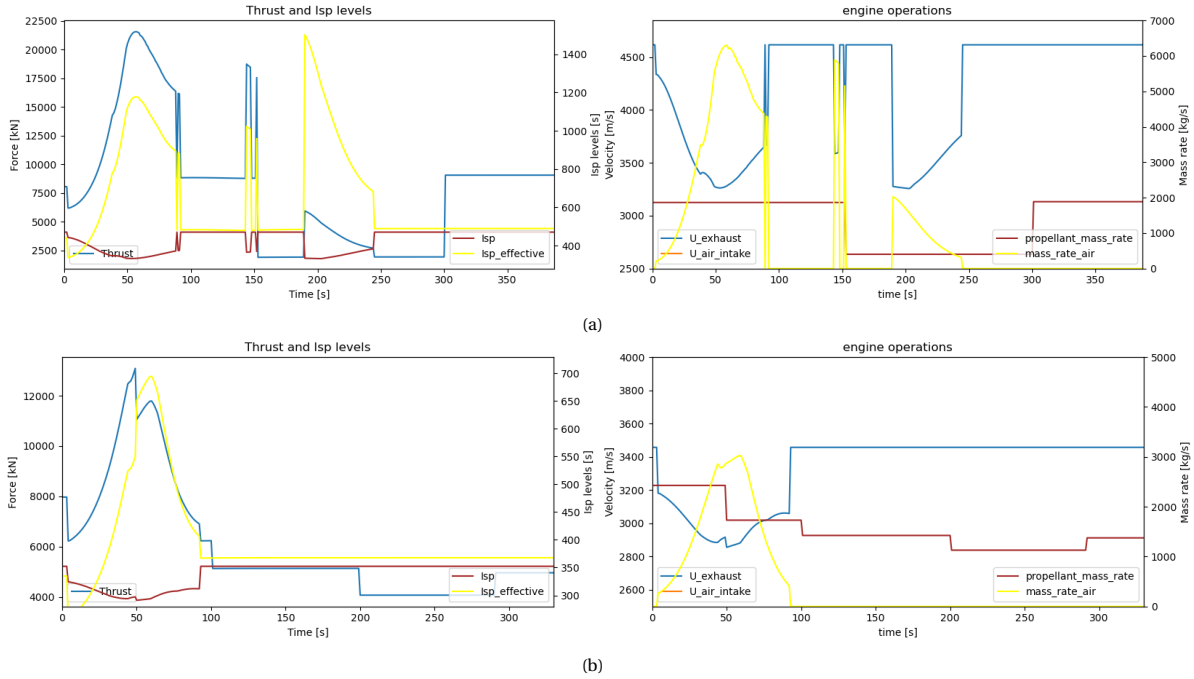

Figure 9.7: Illustrates the precooled hybrid airbreathing rocket engine operational data for (a) a H2/O2 propellant pallet (b) a CH4/O2 propellant pallet.

In Figure 9.7 it appears that the H2/O2 engine operates 3 segregate breathing phases, however the sensitivity analysis on C_D reveals that these are actually two phases and possible a single phase. The reason for the isolated breathing phases is the same as the jumping between phases in the second phase, as illustrated in Figure 9.8. Both are caused by the performance inlet closed conditions of $p_{cc} \geq p_{cc,min}$, as discussed in Section 7.2.5. In these instances, the engine operates closely to $p_{cc,min}$ causing the inlet to open and close again. In reality, this condition does not exist, but is an inelegant efficiency condition preventing the model from exploring many sub-optimal breathing trajectories.

In future research the $p_{cc,min}$ condition can potentially be lifted for the super loop.

Furthermore, the optimisation of the H2/O2 powered engine reduce the burn nodes to three by pushing the other two beyond the burn-out time, illustrated in Figure 9.7. This is the result of to lax constraints in the H2/O2 configuration[7], however the severity is equivalent to local minima issue and fine to ignore for the purpose of this thesis.

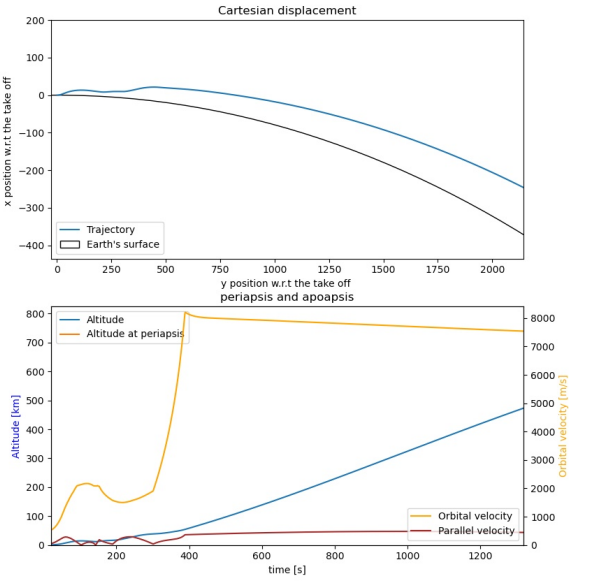

Figure 9.8: Illustrates the ascent trajectory and corresponding mission profile of the H2/O2 powered precooled hybrid airbreathing rocket engine with p_{cc}=300 [bar] and T/W=100.

[7] The model has a tendency to do this as it circumvents codependencies and simplifies the optimisation

Whether the second and third phase merge is not exactly clear, as between these phases the vehicle climbs from an operations range of 10-20 km to one at 25-35 km. A high thrust in the pure rocket phase might be beneficial to quickly ascent to the new operation range. The two operating ranges explain the step-wise ascent observed in Figure 9.8. It is in the second range that the vehicle accelerates to an orbital speed of ~8200 m/s. In total roughly 2500 m/s of acceleration in the early orbital velocity are contributed to the breathing phase.
However, Figure 9.8 reveals that the ascent of the H2/O2 configuration is sub-optimal, evidenced by a slide fall in altitude (negative normal velocity) and a more substantial fall in orbital velocity.

As a last remark, Figure 9.8 illustrates the potential performance that can be gained by utilising a lifting trajectory. This has the potential to fully utilise the performance potential of the hybrid engine, by mitigating the additional atmospheric drag with lift generation. Hence, the reason why Reaction Engines Ltd. insist on using SABRE on a spaceplane like vehicle. Further, when a prolonged breathing phase is used, the addition of a bypass afterburner might be beneficial to reach an $I_{sp,eff}$ of ~2500 s^{-1} [75].

Performance of the T/W ratio at 150
From Table 9.15 it appears the CH4/O2 configuration with a T/W at 150 possess the required orbit capabilities. However, closer evaluation reveals that the ascent trajectory is unachievable, therefore the orbit capabilities of the CH4/O2 configuration only exist on paper. To elaborate, the ascent of the CH4/O2 configuration reaches a Mach number of >25 at an altitude ~ 60 km, as illustrated in Figure 9.9. For reference this would equal the heat loads the Space Shuttle reached upon re-entry. The high Mach number is due to a continues burn of consecutive nodes with $\dot{m} > 1950$ kg/s and no idle phase.

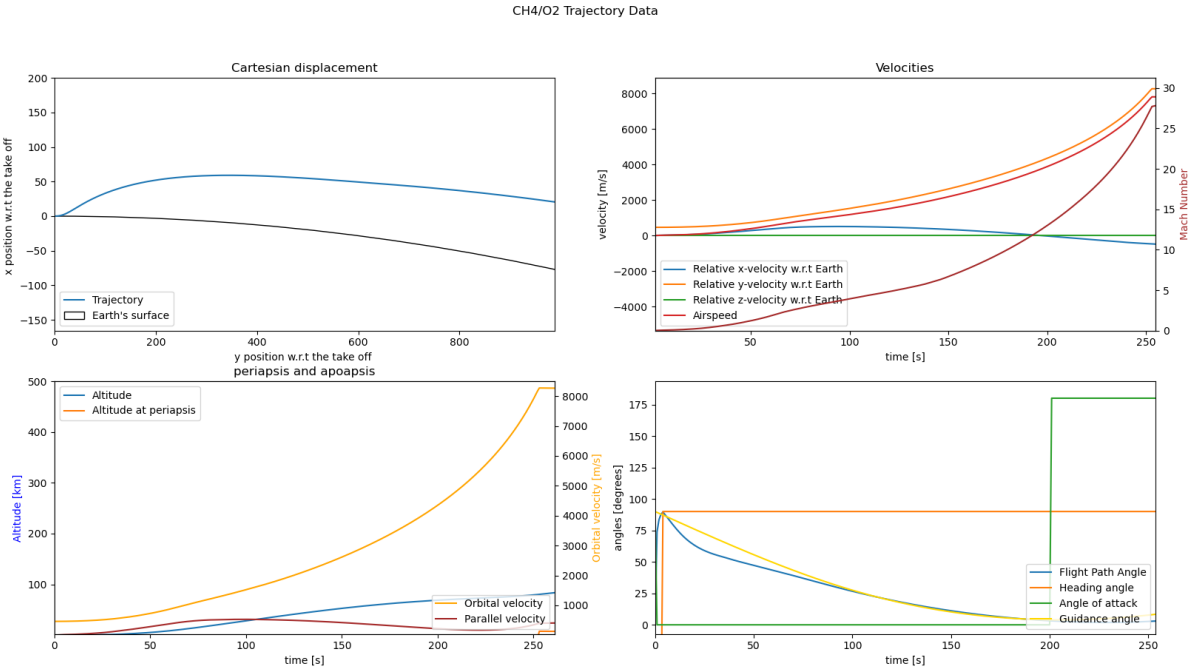

Figure 9.9: Illustrates the trajectory profile of the CH4/O2 powered precooled hybrid airbreathing rocket engine with p_{cc}=300 [bar] and T/W=150 [-] specifications.

This ascent trajectory would almost certainly require an advanced TPS system, as it needs to be intact for the re-entry. This vehicle requires two dedicated development undertakings, which by Chapter 1 should be solemnly reserved for the engine. Hence, the trajectory is not only improbable but also break the economic requirements set in Chapter 2.
Not to mention the T/W ratio of 150, which on itself is already a significant engineering challenge on its own, especially given the weight penalty of the regenerator[8] illustrated by the NEWAC project, as described

[8]The regenerator (2->29) is equivalent to the precooler (1->2), the difference is the location in the engine

in Section 4.1.2.

Although the model illustrates that the CH4/O2 powered engine possess the required orbit capabilities, it cannot be considered a viable engine for a privately developed VT. Furthermore, it is expected that when a more advanced aerodynamic model (varying aerodynamic coefficients) is introduced, that the above trajectory is not found to be optimal.

9.5.2. Sensitivity Analysis on the Precooled Hybrid Airbreathing Rocket Engine

The sensitivity analysis of the hybrid engine accesses the effect of the parameters p_{cc}, θ, C_D, and E_{cooler}. Notable is p_{cc}, which for the other selected engines are optimisation. However, for the hybrid engine a change in p_{cc} is less significant. As for 30% of the burn time, the hybrid engine operates at $p_{cc} = p_{29}$. The long optimisation time is another motivation to limit the performance optimisation runs.
The sensitivity analyses are preformed on the trajectories with the p_{cc} = 300 bar and T/W=100 specification.

Sensitivity of the CC Pressure (p_{cc}) during the Pure Rocket Phase
The p_{cc} sensitivity analyses are done with the pressures as proposed in Section 9.1. As usual, all other operations parameters are kept the same (LH2/LOX=0.225, LCH4/LOX=0.300, Π_{HPC} = 85, E_{cooler} = 0.8, $\kappa_{cooler,loss}$ = 0.03, ν_{HPC} = 0.83, and θ=20°). The results of the p_{cc} are found in Table 9.16

Precooled Hybrid Airbreathing Rocket Engine		T/W=100			
p_{cc} [bar]	Performance Parameters	H2/O2		CH4/O2	
300	Fitness [-]	91	(0.0%)	234	(0.0%)
	Orbit [-]	T		F	
	$I_{sp,t,eff}$ [s]	639	(0.0%)	393	(-0.0%)
	DeltaV [m/s]	12958	(0.0%)	8757	(0.0%)
	$M_{surplus}$ [Mg]	0		0	
250	Fitness [-]	93	(2.9%)	239	(2.3%)
	Orbit [-]	T		F	
	$I_{sp,t,eff}$ [s]	642	(0.4%)	392	(-0.2%)
	DeltaV [m/s]	13061	(0.8%)	8734	(-0.3%)
	$M_{surplus}$ [Mg]	0		0	
200	Fitness [-]	90	(-0.%)8	245	(4.8%)
	Orbit [-]	T		F	
	$I_{sp,t,eff}$ [s]	628	(-1.7%)	392	(-0.3%)
	DeltaV [m/s]	12831	(-1.0%)	8717	(-0.4%)
	$M_{surplus}$ [Mg]	0		0	

Table 9.16: Provides the performance parameters and the percentage w.r.t. the base ascent trajectories for the precooled hybrid airbreathing rocket engine at varying p_{cc} for the pure rocket phase.

The effect of p_{cc} is similar in magnitude to those of the other selected engines. The fitness The fitness improvement in Table 9.16 is due to the codependency between $\dot{m}$ and t_b, as explained before. That this phenomena is observed in the hybrid engine is interesting, as it suggests that the overshoot is caused by a thrust surplus in the later thrust phases, possibly even during the circularisation burn. However, the hybrid engine still produces roughly half of the ascent thrust[9] in the later pure rocket state. Therefore, the notion that a surplus in ascent thrust is the cause for the worse fits for more capable engines cannot be disregard. This is further evidenced when comparing the relative reduction of the aerospike engines, which are many times greater. That the reductions in fitness is due to a reduction in overshoot is evidenced by the worsening fitness of the CH4/O2 configuration.

The reduction in I_{sp,t_eff}, in Table 9.16, is similar to that of the aerospike engine (roughly 0.5%). Comparing to the PDE bears no relevance due to the different combustion process. It can be argued that the I_{sp,t_eff} reduction for the hybrid engine is an overestimation, due to the absence of a dedicated optimisation. Normally, a lower p_{cc} is compensates with a higher $\dot{m}_0$, to maintain the same ascent velocity. Hence, a larger part of the thrust

[9] Thrust which primarily is used to gain altitude/reach the target altitude.

phase occurs in the upper atmosphere, where the $I_{sp,eff}$ is higher.

The DeltaV is only marginally reduced, which is because a significant proportion of the DeltaV is produced in the unaffected breathing phase. Therefore, the DeltaV, especially compared to previous p_{cc} analyses, is minimally affected. Increases in DeltaV are due to an extended breathing phase.

All in all, a reduction in p_{cc} has a insignificant effect on the precooled hybrid airbreathing rocket engine, due to a large portion of the thrust being produced during the unaffected breathing phase. Furthermore, it might even be advantageous to opt for an engine with a lower p_{cc}, if this results in a weight reduction.
Moreover, a reduced p_{cc} does not effect the orbit capabilities, nor causes a drop-off points for the CH4/O2 configuration. Hence, it can be concluded that p_{cc} is not a critical parameter.

Sensitivity of the Drag Coefficient (C_D) due to the Air Intake
A major concern with airbreathing engines is the inlet drag, especially in the high Mach regions. While, pure rocket ascent vehicles are streamlined to reduce drag as much as possible[10], breathing scent vehicles must be designed such that sufficient intake air is collected for the engines too. Therefore, it is unrealistic that both vehicles have the same C_D, which is the case for the current model.
To evaluate the severity of this assumption a C_D sensitivity analysis is performed. The base C_D is 0.25 equivalent to that of the Delta Clipper [37] (at $\alpha = 0°$). How exactly the C_D alters for a breathing rocket, is uncertain as no breathing rocket has been flown before. However, an estimation can be made based on the impact of aero engines. Aero engines typically induce a drag equal to 1.5%-2.0% of the engine thrust, which translates to 10-20 drag counts to the drag coefficients [86] (1 drag count = 0.0001). In addition, the interface of the engine induces a further 0.3%-0.9% thrust loss. While, the issue with the percentages is that the hybrid engine produces significantly more thrust than the typical aero engine, meaning that the percentages cannot directly be translated into the drag. Yet, the drag counts seem like an underestimation.
After consideration the drag count method is chosen, with the increased C_D values of 10%, 20%, 50% and 100%. The last value is more inline with a lifting body. Like the model, the increased C_D is kept constant throughout the ascent. The results are presented in Table 9.17.

Precooled Hybrid Airbreathing Rocket Engine		p_{cc}=300 [bar] T/W=100			
C_D [-]	Performance Parameters	H2/O2		CH4/O2	
+10%	Fitness [-] [-]	91	(-0.1%)	237	(1.1%)
	Orbit [-]	T		F	
	$I_{sp,t,eff}$ [s]	637	(-0.4%)	393	(0.0%)
	DeltaV [m/s]	13148	(1.5%)	8757	(0.0%)
	$M_{surplus}$ [Mg]	0		0	
+20%	Fitness [-] [-]	94	(3.2%)	241	(2.8%)
	Orbit [-]	T		F	
	$I_{sp,t,eff}$ [s]	645	(0.9%)	393	(-0.1%)
	DeltaV [m/s]	13523	(4.4%)	8751	(-0.1%)
	$M_{surplus}$ [Mg]	0		0	
+50%	Fitness [-] [-]	139	(53.0%)	250	(6.7%)
	Orbit [-]	T		F	
	$I_{sp,t,eff}$ [s]	675	(5.6%)	393	(0.0%)
	DeltaV [m/s]	14348	(10.7%)	8757	(0.0%)
	$M_{surplus}$ [Mg]	0		0	
+100%	Fitness [-] [-]	90	(-0.7%)	269	(14.9%)
	Orbit [-]	F		F	
	$I_{sp,t,eff}$	701	(9.6%)	393	(-0.1%)
	DeltaV [m/s]	14772	(14.0%)	8753	(-0.0%)
	$M_{surplus}$ [Mg]	0		0	

Table 9.17: Provides the performance parameters and the percentage w.r.t. the base ascent trajectories for the precooled hybrid airbreathing rocket engine at varying increased C_D.

[10] Note that the aerodynamic design is constrained by the heat levels upon re-entry and lift requirements.

Remarkably, Table 9.17 illustrates a substantial increase in both $I_{sp,t,eff}$ and DeltaV for the H2/O2 powered engine. It is only when drag is increased by 100% that the H2/O2 configuration losses its orbital capabilities. The high DeltaV is the consequence of the vehicle having a period in the lower atmosphere extending the breathing phase. Hence, it never reaches a sufficient velocity to ascent to the target altitude. Letting the model optimise for a C_D of 0.5 could reveal that the orbit capabilities can be obtain, but this is more in line with a lift generating vehicle and thus left for future studies. On the other hand, the CH4/O2 powered engine appears unaffected by any drag increase.

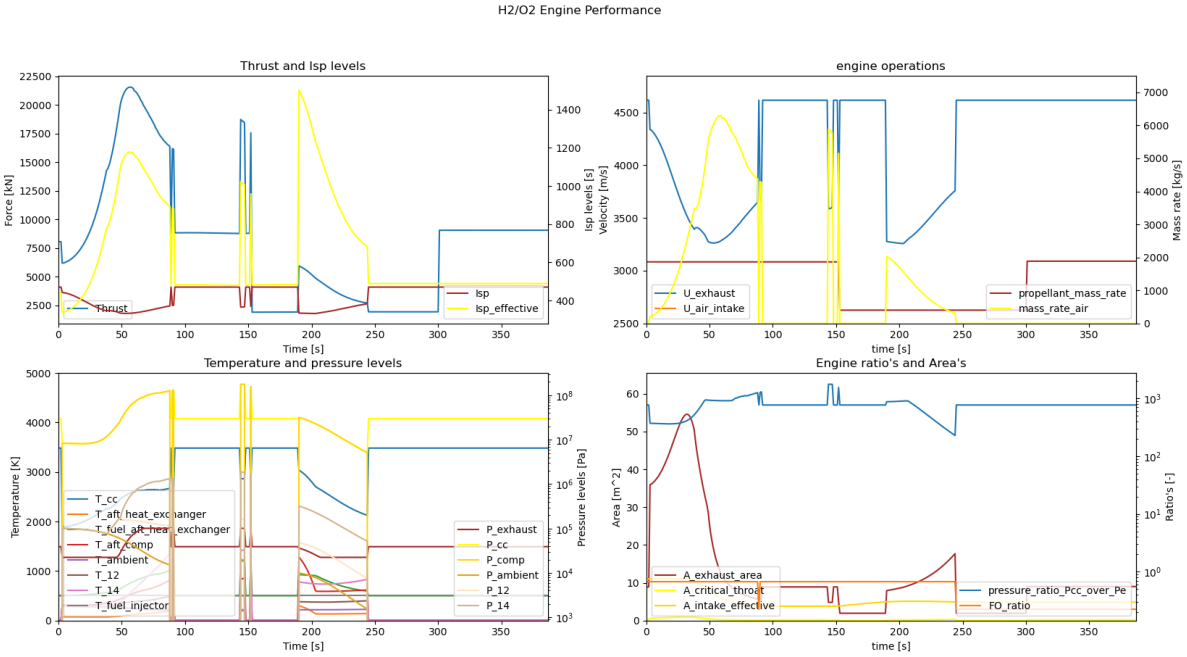

(a)

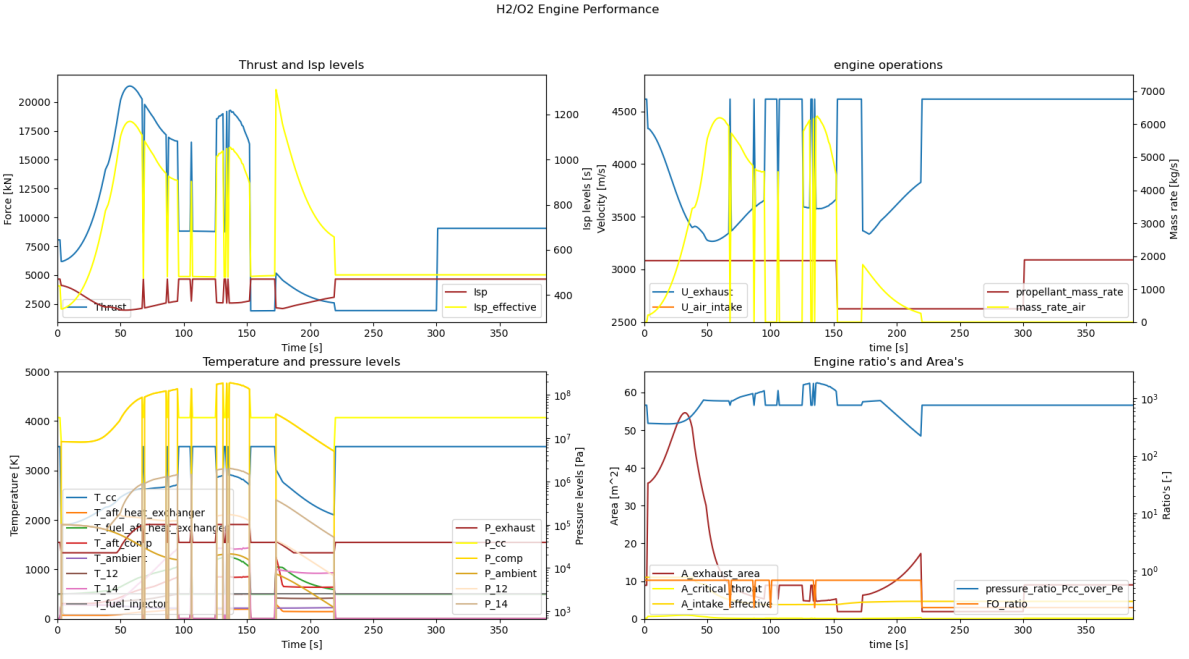

(b)

Figure 9.10: Illustrates the precooled hybrid airbreathing rocket engine operational data, until burnout, with p_{cc}=300 [bar], T/W=150 [-], and C_D=0.25 (a) or C_D=0.30 (+20%) (b).

The performance increase is best understood by analysing Figure 9.10. It is obvious that the 1st breathing phase is significantly prolonged and merges with the 2nd breathing phase. It is the extended breathing phase that is responsible for the performance increase. The increased drag causes the vehicle to gain less altitude, which causes the vehicle operates the breathing phase at a lower altitude (higher ambient pressure). The higher ambient pressure ensures that p_{cc} remains above the 50 bar inlet closed condition, as described Section 7.2.5.
Moreover, the merging of 1st and 2nd breathing phases has two explicit ramifications for the ideal trajectory. Firstly, it indicates that, especially in the early breathing phases, a lot more potential can be gained. Secondly, it suggest that the p_{cc}>50 bar inlet closed condition is to harsh for the ideal trajectory.
The jumping between breathing and non-breathing modes in Figures 9.10 is due to hard coded p_{cc}>50 conditions. In reality, the hard coded condition cannot be directly translated to an operating procedure, thereby eliminating the jumping phenomena.

That the model possibly missed a large gain in performance could be because of either 3 reasons. The simplest is that due to it the computational limitations (too few optimisation generations). Alternatively, the codependency imprecisions, as discussed in Section 9.1.1, the model lacks the required optimisation step precision to achieve these optima. Section 10.2 discusses possible solutions to improve the model precision. Lastly, it could be that the super optimisation termination conditions are too lenient, which require at least an improvement of 0.1% in the fitness every three generations. But, this is also prone to the computational limits too.

The high DeltaV, for C_D, could be the result of the inability to escape the lower atmosphere, therefore not necessarily an indication that the orbit capabilities can be maintained if the model optimises the trajectory again.Therefore, further analysis is required to determine whether orbit can be maintained for a C_D value of 0.5. Note that the C_D value of 0.5 corresponds to a lifting body.

To summarise, the induced inlet drag does not effect the orbit capabilities of the precooled hybrid airbreathing rocket engine, therefore the use of an unchanged C_D does not change performance significantly. Moreover, the C_D sensitivity analysis revealed that more performance can be gained. Furthermore, the increased C_D only had a minor effect on the performance of the CH4/O2 configuration. Whether these finding remains true for a lifting body cannot be said and requires further investigation.

Sensitivity of the Heat Exchanger Effectiveness (E_{cooler})
The most crucial and distinguished component of the hybrid engines is the precooler. Hence, why it is the central point of development within Reaction Engines Ltd., the company behind SABRE. Consequently, the success of the hybrid engines lie with the effectiveness of the heat exchanger.
To reiterate, the heat exchanger is tasked with cooling the flow, such that it can be compressed the flow to a sufficient p_{cc} throughout the breathing phase. As such, it prevents the HPC from reaching the choke limit, as discussed in Section 4.1.3.
The default E_{cooler} is 0.8 based on the NEWAC program and taken from [59], as the effectiveness is not published by Reaction Engines Ltd.. To evaluate the criticality of the heat exchanger, the impact of E_{cooler}) is analysed for the values 0.9, 0.7, 0.6 and 0.5. The results are presented in Table 9.18.

The findings in Table 9.18 are rather remarkable, in the sense that they are unexpected. Even for an E_{cooler} value of 0.5 no drop-off point is reached by either the H2/O2 or the CH4/O2 configuration. An E_{cooler} of 0.5 and lower are already unlikely, given the NEWAC program, [35] and the progress updates by Reaction Engines Ltd.. This implies that effectiveness of the precooler (E_{cooler}) is less critical than originally thought.

The direct effect of E_{cooler} is partly obscured by an initial thrust reduction that prolongs the breathing phase, thereby increasing $I_{sp,eff}$, as described in the C_D sensitivity analysis. A general impact is deduced by analysing the extremes of H2/O2 and observing the general trend in CH4/O2.
The performance gain and loss of the CH4/O2 configuration indicates an inverse exponential relations between the E_{cooler} and the performance parameters, $I_{sp,t,eff}$ and DeltaV. Such a relations implies that initially raising E_{cooler} has diminishing returns on the performance, hence it is worth more to raise a value of 0.6 to 0.7 than it is to raise 0.8 to 0.9.

Precooled Hybrid Airbreathing Rocket Engine		p_{cc}=300 [bar] T/W=100			
E_{cooler} [-]	Performance Parameters	H2/O2		CH4/O2	
0.9	Fitness [-] [-]	86	(-5.8%)	233	(-0.3%)
	Orbit [-]	T		F	
	$I_{sp,t,eff}$	642	(0.4%)	393	(-0.1%)
	DeltaV [m/s]	13004	(0.4%)	8756	(0.0%)
	$M_{surplus}$ [Mg]	0		0	
0.7	Fitness [-] [-]	104	(15.0%)	234	(0.0%)
	Orbit [-]	T		F	
	$I_{sp,t,eff}$	679	(6.2%)	393	(0.0%)
	DeltaV [m/s]	12982	(0.2%)	8757	(0.0%)
	$M_{surplus}$ [Mg]	0		0	
0.6	Fitness [-] [-]	106	(16.4%)	238	(1.8%)
	Orbit [-]	T		F	
	$I_{sp,t,eff}$	666	(4.2%)	390	(-0.9%)
	DeltaV [m/s]	12655	(-2.3%)	8710	(-0.5%)
	$M_{surplus}$ [Mg]	0		0	
0.5	Fitness [-] [-]	107	(17.6%)	249	(6.2%)
	Orbit [-]	T		F	
	$I_{sp,t,eff}$ [s]	676	(5.7%)	385	(-1.9%)
	DeltaV [m/s]	12556	(-3.1%)	8651	(-1.2%)
	$M_{surplus}$ [Mg]	0		0	

Table 9.18: Provides the performance parameters and the percentage w.r.t. the base ascent trajectories for the precooled hybrid airbreathing rocket engine at varying E_{cooler}.

The performance gain and loss of CH4/O2 configurations indicates an inverse exponential relations between the E_{cooler} and the performance parameters, $I_{sp,t,eff}$ and DeltaV. Such a relations implies that initially raising E_{cooler} has diminishing returns on the performance, hence it is more worth raising a value of E_{cooler} 0.6 to 0.7 than it is to raise 0.8 to 0.9.
Translating this relation to the H2/O2 configurations a similar pattern is observe, as E_{cooler} reduces the relative loss in DeltaV becomes larger. Unfortunately, the same pattern cannot be observed in the $I_{sp,t,eff}$, which is increased by the prolonged breathing phase.

To conclude, E_{cooler} does not appear to be a critical parameter for the precooled hybrid airbreathing rocket engine, hence it does not mitigate the orbit capabilities of the H2/O2 configuration. Furthermore, the E_{cooler} illustrates an inverse exponential relation with the performance parameters, $I_{sp,t,eff}$ and DeltaV. Therefore, it is beneficial in the early development to raise the E_{cooler} until the point other components offer better performance return, when this requires a cost-benefit analysis, which is not part of this thesis.

Sensitivity of the ram angle (θ)
The final sensitivity analysis evaluates the impact of the ram angle (θ), which is included as no exact value could be found in the literature. The θ sensitivity analysis is primarily concerned with how long the oblique shock is detached. Detached shocks are poor at compressing the air, which in turn results in a shortened breathing phase (due to $p_{cc,min}$ and $\dot{m}_{intake,min}$). Moreover, they invoke a far larger drag penalty than an attached shock. In addition, from a model perspective detached shocks should be avoided too, as these are approximated as described in Section 7.2.5.
θ is evaluated over a span form 5° to the maximum angle of 43°. While, the angle of 5° is unrealistic due to the heat loads at the tip, the 43° is unrealistic as it would make the intake far too blunt, invoking too large a drag penalty (detached shock). The results are presented in Table 9.19.

Precooled Hybrid Airbreathing Rocket Engine		p_{cc}=300 [bar] T/W=100			
θ [°]	Performance Parameters	H2/O2		CH4/O2	
43	Fitness [-] [-]	444	(388.8%)	251	(7.3%)
	Orbit [-]	F		F	
	$I_{sp,t,eff}$ [s]	651	(1.8%)	384	(-2.2%)
	DeltaV [m/s]	13067	(0.8%)	8636	(-1.4%)
	$M_{surplus}$ [Mg]	0		0	
	$t_{detached}$	97	(870.0%)	45	(200.0%)
35	Fitness [-] [-]	86	(-5.0%)	241	(3.1%)
	Orbit [-]	T		F	
	$I_{sp,t,eff}$ [s]	635	(-0.7%)	389	(-1.1%)
	DeltaV [m/s]	13110	(1.2%)	8698	(-0.7%)
	$M_{surplus}$ [Mg]	0		0	
	$t_{detached}$	24	(140.0%)	44	(193.3%)
30	Fitness [-] [-]	87	(-4.2%)	236	(0.7%)
	Orbit [-]	T		F	
	$I_{sp,t,eff}$ [s]	644	(0.8%)	392	(-0.3%)
	DeltaV [m/s]	13052	(0.7%)	8740	(-0.2%)
	$M_{surplus}$ [Mg]	0		0	
	$t_{detached}$	18	(80.0%)	30	(100.0%)
20	Fitness [-] [-]	91	(-0.0%)	234	(-0.1%)
	Orbit [-]	T		F	
	$I_{sp,t,eff}$ [s]	643	(0.6%)	393	(0.0%)
	DeltaV [m/s]	12897	(-0.5%)	8756	(0.0%)
	$M_{surplus}$ [Mg]	0		0	
	$t_{detached}$	10	(0.0%)	15	(0.0%)
10	Fitness [-] [-]	513	(464.5%)	236	(0.7%)
	Orbit [-]	T		F	
	$I_{sp,t,eff}$ [s]	636	(-0.4%)	392	(-0.2%)
	DeltaV [m/s]	12937	(-0.2%)	8746	(-0.1%)
	$M_{surplus}$ [Mg]	0		0	
	$t_{detached}$	6	(-40.%)0	7	(-53.3%)
5	Fitness [-] [-]	997	(997.5%)	238	(1.4%)
	Orbit [-]	F		F	
	$I_{sp,t,eff}$ [s]	627	(-1.9%)	391	(-0.4%)
	DeltaV [m/s]	12845	(-0.9%)	8735	(-0.2%)
	$M_{surplus}$ [Mg]	0		0	
	$t_{detached}$	3	(-70.0%)	4	(-73.3%)

Table 9.19: Provides the performance parameters and the percentage w.r.t. the base ascent trajectories for the precooled hybrid airbreathing rocket engine at varying θ.

Table 9.19 illustrates that θ mostly has a negligible effect on the performance. It is only when the unrealistic angles of 5° to 43° are used that drop-off points are observed. But, these are attributed to the early thrust difference setting the vehicle off course, effectively invoking a poor trajectory (sub-optimal steering settings). An detached shock mostly slows the flow below or close to the sonic conditions, therefore no or a less powerful normal shock follows, which results in a lower p_{cc}. Hence, a detached shock is a less efficient compression. However, because the detached time ($t_{detached}$) is only a small fraction of the total burn time of ~400 s, it comes at no surprise that the impact is small.

It appears that $t_{detached}$ has a linear relation with θ. Furthermore, from Table 9.19 it is concluded that θ must be as small as possible. Hence, the value of θ is determined by the peak heat limits experienced upon re-entry. Because the detached shock happens for small Mach number (~ 1.2), where only very small θ ensure an attached shock, the non-breathing take-off phase might be extended until a certain M is achieved. However,

the detached shock at these Mach numbers are minor and might not even be as influential as modelled.

Parameters not Accessed by an Sensitivity Analysis
The effect of the parameters Π_{HPC}, $\eta_{ise,comp}$, and $\eta_{cooler,loss}$ are not accessed in this thesis, because both Π_{HPC} and $\eta_{ise,comp}$ have been elaborately researched in [25], While, $\eta_{cooler,loss}$, is an overestimation with preliminary analysis only showing a minor influence compared to the other evaluated parameters. Furthermore, the inlet closed limit conditions, namely $M_{0,limit}$, $T_{29,limit}$, and $p_{cc,limit}$, are not evaluated either, as these would require new optimisation runs. However, their effect can be understood form analysing the ideal ascent trajectories or can be extrapolated from the prior sensitivity analysis.
The influence of $p_{cc,min}$ is discussed in the C_D sensitivity analysis. Preliminary analysis revealed that reducing $\dot{m}_{intake,min}$ will result in premature initiation of the breathing phase. The $T_{29,limit}$ is physically limited by the choke limit [75] and cannot be increased, however this would result in a longer breathing phase or a higher p_{cc}.

9.5.3. Discussion Precooled Hybrid Airbreathing Rocket Engine Performance

Discussion
To conclude, only the H2/O2 powered precooled hybrid airbreathing rocket engine is a viable engine with the required orbital capabilities. Further, analysis demonstrated that the hybrid engine operates for an extended period in the lower atmosphere, utilising its breathing capabilities to generate a significant part of its required orbital velocity. a later pure rocket phase is used to climb to the target altitude.
Although the CH4/O2 powered engine with a T/W of 150 illustrated orbit capabilities, it cannot be considered a viable engine, because the Mach number exceeding 25. The CH4/O2 configuration with a T/W at 100 illustrates the same level of robustness in the sensitivity analyses as the H2/O2 configuration. However, this CH4/O2 configuration was insufficient to obtain the required orbital capabilities.

Furthermore, from the sensitivity analyses, surprisingly, no critical parameter were identified. However, this is invalid for C_D if its value corresponds to that of a lifting body of spaceplane. Further research is required to evaluate whether the generated lift justifies the increased drag, as discussed in Section 3.8. For realistic values all parameters where found to have minor effect. An inverse exponential relation is found between E_{cooler} and the performance, $I_{sp,t,eff}$ and DeltaV. While, θ linearly effected $t_{detached}$, which is of minor effect.

Possible Performance Gains for Precooled Hybrid Airbreathing Rocket Engines
This thesis is limited to unified homogeneous precooled hybrid airbreathing rocket engine, as the development period for more complex architectures is beyond an economically viable time frame (+10 years, see Section 6.2.4). However, a segregated or non-homogeneous system allows different engines to operate in different modes or have some convectional engines to boost the overall T/W. However, such a configuration is dependent on how well the intake flow can be directed to the (operating) hybrid engines.
In addition, the engine operates an extendable ram inlet, like SABRE. Alternatively, a closing flap intake, as is illustrated in Figure 4.4, can be utilised, which operates with a varying ram angle (θ), therefore allowing for better and greater compression control, increasing the p_{cc}.
Potentially, the ascent trajectory can be improved by loosening the performance intake closed conditions, which are the $p_{cc,min}$ and the $\dot{m}_{intake,min}$, as illustrated by the C_D sensitivity analysis. Loosening these constraints can improve the performance parameters by prolonging the breathing phase. However, when loosening these constraints care must be taken that the optimisation efficiency is not diminished too much.
Lastly, the performance could be improved by operating a variable mass rate precooler and a HPC with a varying compression ratios (Π_{HPC}), as was done in [25]. However, in this case the temperature of the stored fuel must be modelled, if mass flow exceeds the engine mass rate. For the HPC the other parameters must be varied according to Π_{HPC}.

9.6. The Performance Trade-Off Between the Selected Engine

This section provides an overview of all the selected engines that make a VT SSTO RLV viable. The viable engines are ordered by their engine type and propellant pallet and discussed in those respective sections. These

sections provide the most important model outputs for all viable engines. Moreover, next to the standard performance parameters the percentage increase w.r.t. the baseline and the introduction of a new performance parameter, namely the Unutilized DeltaV Potential (UPD), are added, increasing direct comparability. The unutilised UDP [m/s]is elaborated next section, but for now understand that it is a proxy measure for unused performance potential.
The section concludes with identifying the most promising engine candidates. These candidates are the main finding of this thesis. The findings serves as a starting point for future research into SSTO powered by the candidate engines.

9.6.1. Unutilized DeltaV Potential (UDP)

Unutilised DeltaV potential, as the name suggest, is a measure of DeltaV that has not been utilised by the vehicle given its current trajectory. Therefore, this is DeltaV that the vehicle theoretically can still utilise in improving its mission profile. To elaborate by an example, take the H2/O2 powered PDE with a final mass surplus of 6 tons. This left over propellant could be used to produce additional thrust, which could be used to improve the mission requirements. The additional thrust increases the realised DeltaV, it is this increase that is the Unutilized DeltaV Potential.
This idea can then be expanded to the overshoots, in both the velocities and altitude. By incorporating mass surplus, velocities, and altitude a more direct comparison measure is constructed, as regardless how the orbit is achieved the measure should be equivalent. To elaborate, an engine that reaches the orbit termination conditions with a large overshoot in the normal velocity, should have the same measure as that same engine reaching the orbit termination conditions with no overshoot but with a mass surplus.

The Unutilized DeltaV Potential is computed by adding the UDP [m/s]of the propellant mass surplus, the overshoot in orbital velocity, the overshoot in normal velocity, and the velocity required to reach the overshoot in altitude.
The DeltaV of the propellant surplus is computed via the Tsiolkovsky rocket equation (Equation 4.1), while the DeltaV from the velocity overshoots is simply the overshoot velocity. However, the DeltaV from the altitude overshoot requires some algebra. Basically, the aim is to translate the altitude into a velocity. The sought after velocity is the difference between the normal velocity at the target altitude minus the normal velocity when the orbit condition is reached. This is the differ between the normal overshoot velocity at the target altitude and the normal velocity when the orbit condition was achieved, which can be computed from the motion equations[11] $ds = v_0 t - 0.5 g_0 t^2$ and $v_t = v_0 - g_0 t$. ds refers the difference between the altitude and target altitude, v_0 is the normal velocity at the target velocity, and v_t is the normal velocity at the orbit condition. As a remark, the above approach is not perfect as it does not consider potential unnecessary gravity or atmospheric losses, however it is a far better direct comparing measure than all previous parameters.

The Unutilized DeltaV Potential (UDP) is further referred to as UDP [m/s]or UDP, indiscriminately. Furthermore, beware that the UDP is not additional DeltaV that can be added to the DeltaV budget, with UDP resulting from propellant surplus bing the exception. The UDP should rather be interpreted as DeltaV that has not contributed to achieving the mission of requirements, delivering 15 tons of payload to a 400 km orbit.

9.6.2. Viable VT SSTO Engine Candidates

All engine configurations that throughout the performance analysis posses the required orbit capabilities are discussed in this section and further referred to as the viable engines. To reiterate, these findings apply to a VT SSTO RLV with a body that resembles that of the Delta Clipper or VentureStar, and thus has no lifting properties. The viable engines are categorised by engine type and propellant pallet, hence engines with different specifications that share the same engine type and propellant pallet are discussed together.
For each viable engine three result outputs are provided, which together provide the complete picture of the ascent trajectory. The first output is the summation of the optimisation variables, These include the steering settings, burning settings and sizing variables. Next follows a detailed performance table, which include similar parameters as the previous performance tables of Sections 9.3, 9.4, and 9.5. In addition, the unutalised DetlaV potential, the maximum and minimum I_{sp}, and the engine mass are provided. Lastly, when applicable

[11] The physics here is the same as the classical physics problem of how fast one needs to throw a ball to reach a certain height.

the percentage relative to the baseline is given.
The last outputs are two plots containing the mission parameters and the performance parameters of the engine throughout the ascent.

H2/O2 Powered Aerospike Engine

Optimisation variables of the H2/O2 powered aerospike engine with T/W=200 [-] and p_{cc}=300 [bar] (a)

Burning mass rates ($\vec{m}$)	:	[1877.4, 1437.01, 1158.92, 826.56] [kg/s]
Burning periods ($\vec{t_b}$)	:	[95.5, 42.52] [s]
Steering angles ($\vec{\gamma}$)	:	[78.34, 19.32, 8.91, 30.66, 62.15] [°]
Steering time intervals ($\vec{t_\gamma}$)	:	[1.08, 155.04, 57.56, 165.54] [s]
Sizing Variables (F/O, $\epsilon_{\text{eff,max}}$)	:	[0.225, 220.0] [-]

Optimisation variables of the H2/O2 powered aerospike engine with T/W=150 [-] and p_{cc}=300 [bar] (b)

Burning mass rates ($\vec{m}$)	:	[1661.1, 950.21, 20.73, 1274.87] [kg/s]
Burning periods ($\vec{t_b}$)	:	[179.94, 198.61] [s]
Steering angles ($\vec{\gamma}$)	:	[41.23, 86.13, 0.41, 20.94, 53.22] [°]
Steering time intervals ($\vec{t_\gamma}$)	:	[0.93, 104.05, 98.15, 69.74] [s]
Sizing Variables (F/O, $\epsilon_{\text{eff,max}}$)	:	[0.225, 220.0] [-]

Optimisation variables of the H2/O2 powered aerospike engine with T/W=200 [-] and p_{cc}=250 [bar] (c)

Burning mass rates ($\vec{m}$)	:	[1905.61, 1715.31, 1133.72, 1558.22] [kg/s]
Burning periods ($\vec{t_b}$)	:	[15.5, 193.29] [s]
Steering angles ($\vec{\gamma}$)	:	[44.39, 18.88, 79.84, 32.84, 54.93] [°]
Steering time intervals ($\vec{t_\gamma}$)	:	[0.96, 193.87, 193.52, 46.11] [s]
Sizing Variables (F/O, $\epsilon_{\text{eff,max}}$)	:	[0.225, 220.0] [-]

The steering program of the aerospike engines contains an immediate rapid turn, which is followed by a gradual turn that mostly maintains the ascent heading. This is observed in the mission profile plots of Figure 9.11 too. The steep ascent is well illustrated in the optimal trajectory of configuration c. in Figure 9.11.
To continue with the burning program, the first mass rate is substantially larger (take-off phase) than the other mass rates and is relatively quickly followed by prolonged but lower mass rate burn (main thrust phase). For configuration a. it can be argued that the main thrust phase is facilitated by the second and third node, but as argued later configuration a. is far from an optimal trajectory. Note that a. b. and c. refer to the engine specifications (p_{cc} and T/W) and are defined with the optimisation variables and corresponds to the sub-figures in Figure 9.11. The third node is the idle node which is characterised as a low or no thrust phase and correspond to a ferry phase. Through the ferry phase the vehicle awaits the conditions to perform the circularisation burn. In addition, the idle phase prevents the vehicle from reaching critical Mach numbers (M»15). Hence, the last node corresponds with the circularisation burn.
As such, the findings of the burning settings are in line with the hypothesis proposed in Section 9.1.2.

Aerospike Engine	p_{cc}=300 [bar] T/W=200 [-]		p_{cc}=300 [bar] T/W=150 [-]		p_{cc}=250 [bar] T/W=200 [-]	
Performance Parameters	values	+% baseline	values	+% baseline	values	+% baseline
UDP [m/s]	649		158		121	
$I_{sp,t,eff}$ [s]	480.15	37.8%	476.9	36.9%	476.5	36.8%
$I_{sp,max}$ / $I_{sp,min}$ [s]/[s]	489.67/431.57	57.9%/18.2%	489.67/431.57	57.9%/18.2%	489.18/427.02	57.7%/17.0%
DeltaV [m/s]	11349	32.6%	11224	31.2%	11281	31.8%
$M_{prop,surplus}$ [Mg]	0		0		0	
M_{engine} [kg]	4597	50.8%	5423	77.9%	4661	52.9%

Table 9.20: Provides the performance parameters of the H2/O2 powered aerospike engines.

Table 9.20 provides the most relevant perforamnce parameters of the H2/O2 aerospike powered ascent vehicles. The highest UDP value for configuration a. confirms the convergence to local optima proposed in Section 9.1.1. To elaborate, this indicates that the most powerful engine, namely a., can improve its trajectory the most, as the high UDP is not a result of a mass surplus. Figure 9.11 illustrates how the ferry phase and circularisation burn are switched for configuration a. The ferry phase maintain sufficient velocity to fulfil

the orbit conditions. Because configuration a. is so powerful it has plenty of propellant and can be wasteful (sub-optimal trajectory).

While, the difference in minimal I_{sp} (SL) compared to Raptor engine is attributed to the use of H2 instead of CH4, as illustrated in Table 9.20. Studying the $I_{sp,eff}$ range, reveals that the advantage of the aerospike begin to excel at the operations at mid/high altitudes. It is at this operation range that the greatest gains in performance are made. While, this is the greatest benefit of aerospikes, it is also their biggest deficit. It is precisely because aerospike require such a large operation range to attain their performance increase, what makes them so unsuited for TSTO operations. TSTO engines have a short operation range due to the two stages and the thrust paused during separation, often combined with idle phase. Therefore, TSTOs are better served with two sets of conventional engines tailored to their specific operation range.

Furthermore, Figure 9.11 illustrates that the UDP of configuration a. and b. provided in Table 9.20 are both underestimated. Configuration a. allows its initial orbital velocity, provided by Earth's rotations, to completely dissipate. While, configuration b. allows its vehicle to lose altitude, which is the result of insufficient thrust ($\dot{m}$) in the ferry phase.
To reiterate, sub-optimal trajectories are not a concern to this thesis as the goal is to illustrate representative orbit capabilities, which clearly is the case for the H2/O2 powered aerospike engines.
The above argumentation indicates that configuration b. is the more powerful configuration compared to configuration c, as c almost flies a perfect ascent. Configuration c. probably has significantly less local optima, therefore it likely operates at the marginal limit of the H2/O2 powered aerospike engines. Hence, it can be concluded that operating at a reduced p_{cc} is significantly worse than operating at a reduced T/W. Therefore, a mass penalty should be taken, if it results in a higher p_{cc}.

As a final remark, the findings here do not include the directional losses, which by the conclusion of Section 9.3.3 cannot be neglected. However, the conclusion also indicated that the losses did not effect the orbital capabilities of the H2/O2 powered aerospike engine. This combined with the fact that the performance losses in Table 9.3.3 are less than the UDP in Table 9.20, made it unnecessary to rerun the model with the directional losses included. Moreover, the losses can partly be mitigated by optimising the $\epsilon_{eff,max}$.

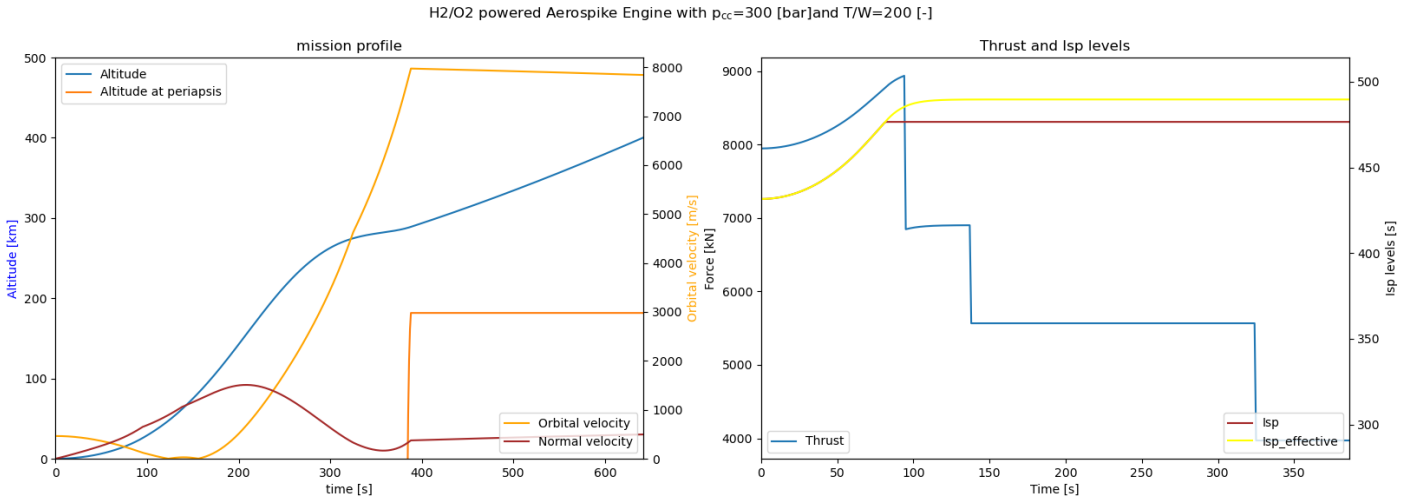

(a)

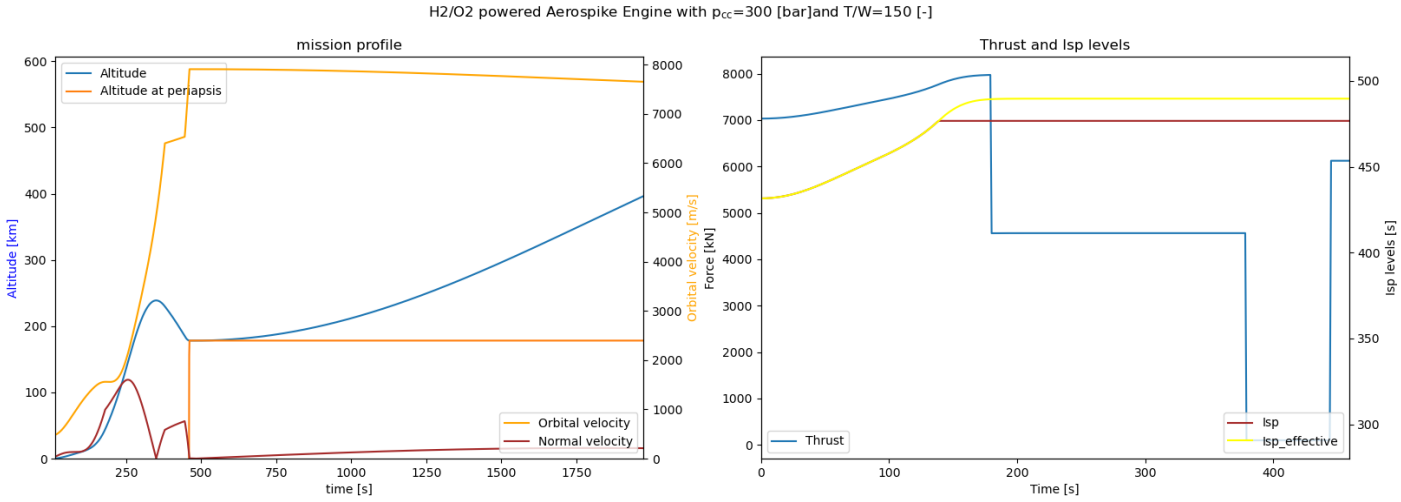

(b)

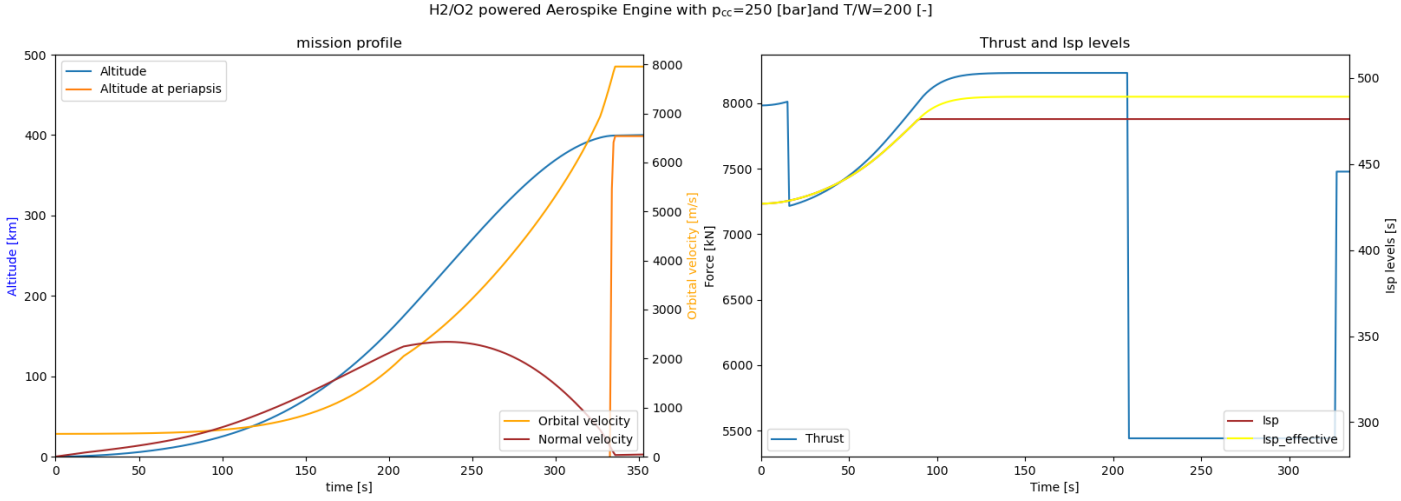

(c)

Figure 9.11: Illustrates the mission profile (left) and the engine operations (right) of an ascent vehicle operating an H2/O2 powered aerospike engines.

C2H2/O2 Powered Aerospike Engine

Optimisation variables of the C2H2/O2 powered aerospike engine with p_{cc}=300 [bar] and T/W=200 [-]

Burning mass rates ($\vec{\dot{m}}$)	:	[2365.49, 27.79, 234.93, 1134.88] [kg/s]
Burning periods ($\vec{t_b}$)	:	[182.65, 107.64, 115.46] [s]
Steering angles ($\vec{\gamma}$)	:	[38.65, 15.53, 18.33, 5.57, 5.1] [°]
Steering time intervals ($\vec{t_\gamma}$)	:	[0.09, 104.86, 30.95, 98.68] [s]
Sizing Variables (F/O, ϵ)	:	[0.7, 220.0] [-]

The Steering settings of the C2H2/O2 powered aerospike contain the exact same pattern as the H2/O2 powered aerospike, that is a steep ascent followed by a circularisation burn. Again this is illustrated by Figure 9.12, where initially the orbital velocity remains unchanged, followed by a sharp increase.
However, the burning settings do lack the main thrust phase, which is replaced by a prolonged take-off phase. This pattern is more similar to the burning settings seen for the PDE engines.

Aerospike Engine	p_{cc}=300 [bar] T/W=200 [-]	
Performance Parameters	values	+% baseline
UDP [m/s]	329	
$I_{sp,t,eff}$ [s]	384.16	10.2%
$I_{sp,max}$ / $I_{sp,min}$ [s]/[s]	389.82/349.1	25.7%/-4.4%
DeltaV [m/s]	9072	6.0%
$M_{prop,surplus}$ [Mg]	0	
M_{engine} [kg]	4129	35.5%

Table 9.21: Provides the performance parameters of the C2H2/O2 powered aerospike engine.

As previously stated, the C2H2/O2 powered engine only marginally illustrates orbit capabilities, given the highest engine specifications are achieved. Even if these specification can be achieved the performance gains w.r.t. the Raptor engine are marginal. In reality, these gains are even smaller as the directional losses are not considered in Table 9.21. Unlike the H2/O2 powered aerospike, the C2H2/O2 powered aerospike cannot reduce its significantly $\epsilon_{eff,max}$ to reduce these losses.

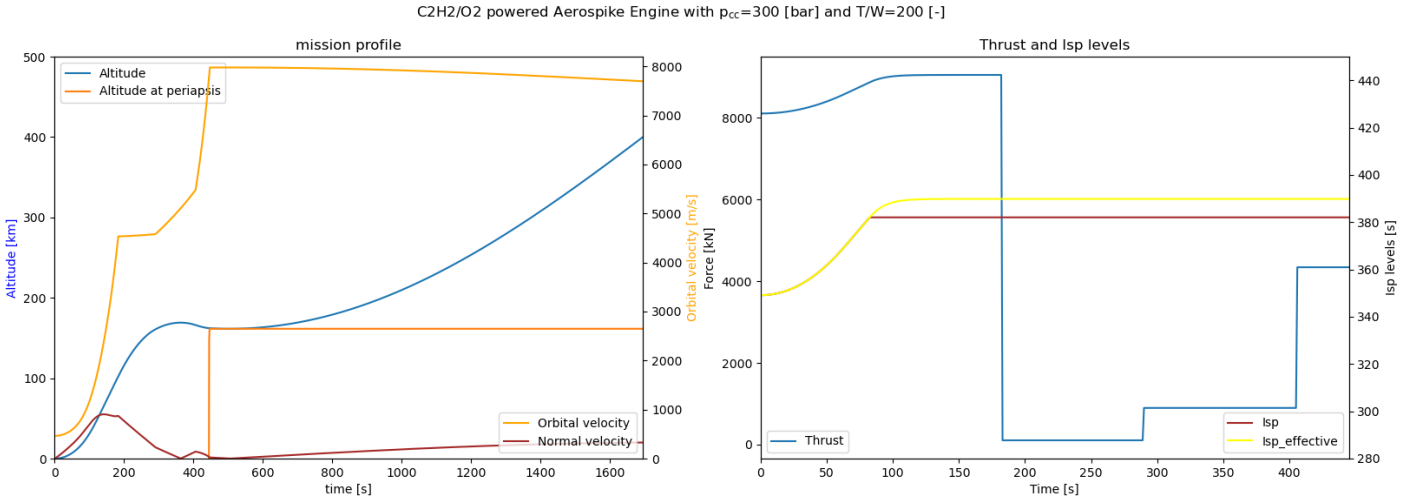

(a)

Figure 9.12: Illustrates the mission profile (left) and the engine operations (right) of an ascent vehicle operating an H2/O2 powered aerospike engines.

On the other hand, some performance gains can still be made. There is the UPD of 329 m/s and also the previously mentioned burning settings. The take-off phase is required to take-off and to quickly gain velocity

to gain altitude, reducing both gravity and atmospheric drag. However, the take-off phase is ideally quickly followed by the main thrust phase, which produces less thrust and consumes less propellant. This reduced thrust phase is required to prevent the vehicle from gaining to much velocity in the lower atmosphere (higher atmospheric drag losses), but also to preserve propellant for later phases. The absence of this phase contributes to a none-ideal circularisation burn (at ~ 150 km). In addition, the idle phase is too long causing the vehicle to descent.

Although the C2H2/O2 powered aerospike has shown great potential, it only possess the required orbital capabilities for highest engine specification. This combined with the fact that aerospikes are only viable for SSTO like vehicles and the presence of better alternatives, make the C2H2/O2 powered aerospike engine unviable from an economical perspective.

H2/O2 Powered Pulse Detonation Engine

Optimisation variables of the H2/O2 powered pulse detonation engine with T/W=200 [-] and p_{DC}=600 [bar] (a)

Burning mass rates ($\vec{\dot{m}}$)	:	[1657.13, 136.27, 597.91, 642.25] [kg/s]
Burning periods ($\vec{t_b}$)	:	[181.24, 61.75] [s]
Steering angles ($\vec{\gamma}$)	:	[69.33, 46.63, 57.75, 0.48] [°]
Steering time intervals ($\vec{t_\gamma}$)	:	[0.01, 123.15, 165.3] [s]
Sizing Variables (F/O, ϵ)	:	[0.35, 7.693] [-]

Optimisation variables of the H2/O2 powered pulse detonation engine with T/W=200 [-] and p_{DC}=500 [bar] (b)

Burning mass rates ($\vec{\dot{m}}$)	:	[1722.36, 143.36, 678.67, 977.88] [kg/s]
Burning periods ($\vec{t_b}$)	:	[183.03, 183.86] [s]
Steering angles ($\vec{\gamma}$)	:	[59.85, 60.11, 1.1, 27.16] [°]
Steering time intervals ($\vec{t_\gamma}$)	:	[0.47, 123.6, 145.57] [s]
Sizing Variables (F/O, ϵ)	:	[0.35, 9.232] [-]

Optimisation variables of the H2/O2 powered pulse detonation engine with T/W=150 [-] and p_{DC}=600 [bar] (c)

Burning mass rates ($\vec{\dot{m}}$)	:	[1791.45, 1288.34, 712.59, 54.92] [kg/s]
Burning periods ($\vec{t_b}$)	:	[115.51, 163.73, 24.83] [s]
Steering angles ($\vec{\gamma}$)	:	[54.41, 4.32, 5.46, 18.28] [°]
Steering time intervals ($\vec{t_\gamma}$)	:	[0.32, 113.63, 179.93, 51.78] [s]
Sizing Variables (F/O, ϵ)	:	[0.35, 8.081] [-]

Like the aerospike engines, the first steering node is an immediate turn away from the vertical launch. Moreover, the first node is roughly 20° steeper than the initial node of the aerospike[12], which is followed by a prolonged steering angle corresponding to the main thrust phase. The last two nodes are dedicated to the circularisation burn.

Oddly enough, the steering nodes for p_{DC}=600 bar (a) and p_{DC}=500 bar (b) are flipped. As a result, the ascent of configuration a. is more straight, which is sub-optimal, while the trajectory for configuration b. resembles more the expected gravity turn. Both are illustrated in Figure 9.13. That configuration a. is sub-optimal is likely the result of the short idle phase (2^{th} burn node) and early circularisation burn. Because configuration a. is very capable, it can afford to be inefficient and convert to a local optimum. The UPD of configuration a. in Table 9.22 supports this statement. This explains why configuration b. has a larger mass surplus as a circularisation burn at a higher altitude is more efficient.

Lastly, the steering settings of configuration c. are far from optimal, as also observed in Figure 9.13. This is the result of very poor burning settings, which only give the vehicle a limited ability to perform a circularisation burn (low final $\dot{m}$). Therefore, the vehicle has to overshoot the altitude, which ensure sufficient burn time, to generate the required DetlaV to complete the circularisation burn.

Generally, the burning program of PDEs lacks the prolonged main thrust node, which shortly follows after

[12]The aerospike follows a steeper ascent trajectory, therefore requires less Sharp initial heading.

the take-off node. Shortly after take-off the vehicle has gained some altitude, thereby quickly increasing the thrust per unit mass[13], and lost mass. At this point the high mass rate at take-off is unnecessary and the main thrust node takes over, as illustrated in Figure 9.11. It is speculated that due to the more limited ϵ of the PDEs, which flattens thrust levels faster, the main thrust node is less severely needed.

The burn programs, with the exception of configuration c., have an incredible level of similarity. This gives great confidence in the model's potential to converge towards a global optima. Furthermore, it suggest that a change in p_{DC} has negligible effect on the ideal ascent. As expected, the initial take-off mass rate is slightly increased, which is to ensure the same level of thrust is achieved. Thus suggesting that the vehicle mass drives the take-off burn node, instead of the engine.
It is hypothesised that PDEs converge to the global optimum due to a relative larger generation number. The PDEs have the least amount of burning and steering nodes, but only have the generation number reduced by 2. Therefore, the PDEs can relatively optimise longer for a smaller set of optimisation variables.

Pulse Detonation Engine	p_{cc}=600 [bar] T/W=200 [-]		p_{cc}=500 [bar] T/W=200 [-]		p_{cc}=600 [bar] T/W=150 [-]	
Performance Parameters	values	+% baseline	values	+% baseline	values	+% baseline
UDP [m/s]	1628		1946		2176	
$I_{sp,t,eff}$ [s]	496.1	42.4%	498.15	43.0%	498.71	43.1%
$I_{sp,max}$ / $I_{sp,min}$ [s]/[s]	498.76/470.59	60.8%/28.9%	501.84/461.31	61.8%/26.4%	499.7/470.11	61.1%/28.8%
DeltaV [m/s]	10312	20.5%	10125	18.3%	10429	21.9%
$M_{prop,surplus}$ [Mg]	17		20		27	
M_{engine} [kg]	4133	35.6%	4322	41.8%	5614	84.2%

Table 9.22: Provides the performance parameters of the H2/O2 powered pulse detonation engines.

Table 9.22 provides an insight in how much DeltaV is lost due to a sub-optimal ascent trajectory. In Table 9.22 it is seen that the UDP of configuration a. is ~320 m/s lower than the less powerful configuration b. Even though the majority of the difference is attributed to the larger propellant surplus, ~ 100 m/s is due to the additional overshoots. This indicates that the sub-optimal trajectory induces an additional 100 m/s of gravity and atmospheric drag losses[14].

In Table 9.22 it appears configuration c. flies the most optimum trajectory. However, the contrary is true, as is illustrated by Figure 9.13 and fitness values in Table 9.12. The reason for the high UPD is because the UPD is computed at the lowest fitness value. Normally, this occurs the moment orbit is reached, however for configuration c. this is prior that moment. The propellant at that point is larger, which raises the UPD. Hence, the UPD is an overestimation as part of the propellant is still required to reach orbit.

Compared to the H2/O2 powered aerospike, the PDEs improve by roughly 10 percentage points. When only adding the UDP as a result of the propellant surplus, it becomes evident that PDEs have a higher DeltaV capability. Furthermore, Table 9.22 illustrates that the PDEs (at T/W=200) are approximately 37% heavier than the Raptor engines. However, the PDEs lack the heavy turbo-pumps, yet this can be explained the longer and thicker DC chamber walls.

Recall that the PDEs simulated in this thesis all have a final blowout pressure equal to 1 atm, which is far from optimal. PDEs designed for ascent vehicles should aim to inject at higher pressures, as an advantage of oxidiser fed PDEs is that the DC does not need to wait for the ambient air to enter the DC again.

[13] As the ambient pressure reduces less rapidly the thrust flattens
[14] Note that by definition the overshoot of a more powerful engine should be more.

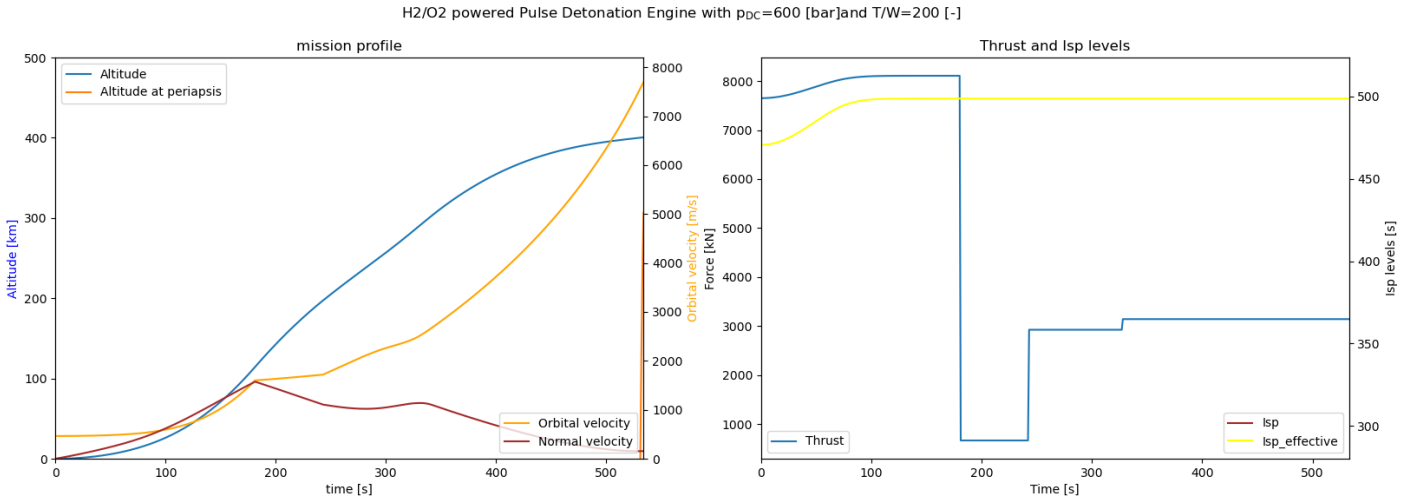

(a)

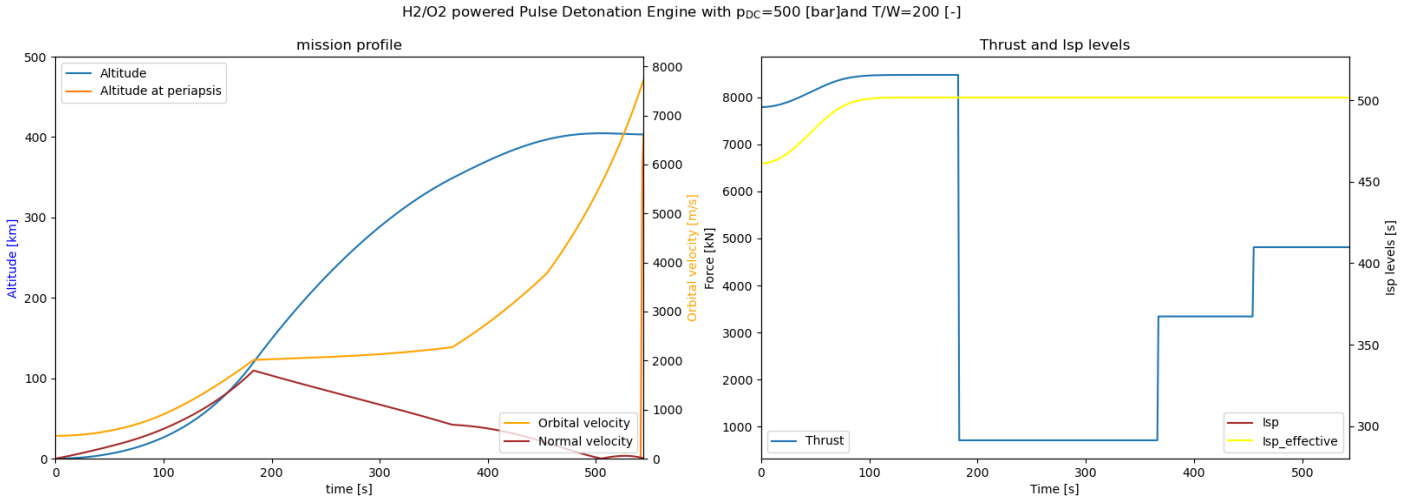

(b)

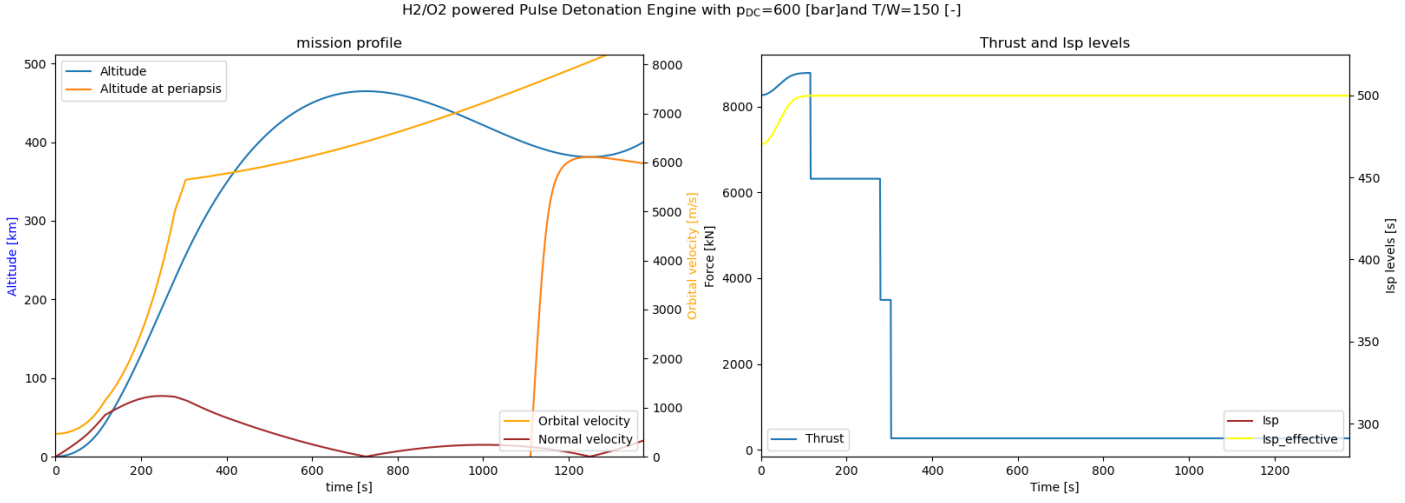

(c)

Figure 9.13: Illustrates the mission profile (left) and the engine operations (right) of an ascent vehicle operating an H2/O2 powered pulse detonation engines.

Therefore, PDEs for ascent vehicles will operate higher final blowdown pressures, which is limited to the injector pressure. Doing so, allows the engine to increase the frequency and produce relatively more thrust per detonation. Furthermore, chocking nozzles can be avoided. That being said, utilising premature injection in a still pressurised DC comes with many more challenges, like, but not limited to, premature detonation/deflagration, blow out of undetonated propellant, and the complementary heat loads. Although, these challenges are impossible to overcome further research is required to make a proper evaluation.

C2H2/O2 Powered Pulse Detonation Engine

Optimisation variables of the C2H2/O2 powered pulse detonation engine with T/W=200 [-] and p_{DC}=600 [bar] (a)

Burning mass rates ($\vec{\dot{m}}$)	:	[1891.0, 1229.17, 1385.55, 1091.08] [kg/s]
Burning periods ($\vec{t_b}$)	:	[155.47, 112.27] [s]
Steering angles ($\vec{\gamma}$)	:	[53.02, 59.32, 39.82, 3.77] [°]
Steering time intervals ($\vec{t_\gamma}$)	:	[0.07, 64.31, 17.26] [s]
Sizing Variables (F/O, ϵ)	:	[0.775, 7.338] [-]

Optimisation variables of the C2H2/O2 powered pulse detonation engine with T/W=200 [-] and p_{DC}=500 [bar] (b)

Burning mass rates ($\vec{\dot{m}}$)	:	[1784.13, 1611.16, 364.39, 1475.36] [kg/s]
Burning periods ($\vec{t_b}$)	:	[150.73, 183.49] [s]
Steering angles ($\vec{\gamma}$)	:	[68.04, 5.38, 0.03, 80.75] [°]
Steering time intervals ($\vec{t_\gamma}$)	:	[1.41, 78.18, 152.47] [s]
Sizing Variables (F/O, ϵ)	:	[0.775, 9.2] [-]

Optimisation variables of the C2H2/O2 powered pulse detonation engine with T/W=150 [-] and p_{DC}=600 [bar] (c)

Burning mass rates ($\vec{\dot{m}}$)	:	[2522.01, 861.16, 2127.23, 2059.53] [kg/s]
Burning periods ($\vec{t_b}$)	:	[172.76, 117.89, 122.88] [s]
Steering angles ($\vec{\gamma}$)	:	[4.15, 2.15, 44.46, 78.48] [°]
Steering time intervals ($\vec{t_\gamma}$)	:	[1.37, 166.15, 139.82, 55.19] [s]
Sizing Variables (F/O, ϵ)	:	[0.775, 8.191] [-]

The steering angles follow a similar pattern to the H2/O2 powered PDE, where even configuration a. and b. resemble the configuration a. and b. of the H2/O2 powered PDE. As such, a similar, although more limited, pattern is observed in the trajectories of configurations a. and b. While a. resembles a more linear climb to the target altitude, b. on the other hand is more parabola shaped, as is illustrated in Figure 9.14.

Concerning the burning program, the take-off mass rate is roughly 100 kg/s larger than its H2/O2 equivalent, which is expected due to the lower $I_{sp,eff}$. Moreover, the take-off node is roughly of the same duration. However, that is were the resemblance stops. Unlike, the previous burning settings all configurations lack the idle phase, which severely limits the effectiveness of the circularisation burn. Figure 9.14 further confirms that the found ascent trajectories are sub-optimal. While, the quasi orbit is satisfied, it is clear that the take-off phase is inadequate to reach the required altitude to perform an effective circularisation burn.

Pulse Detonation Engine	p_{cc}=600 [bar] T/W=200 [-]		p_{cc}=500 [bar] T/W=200 [-]		p_{cc}=600 [bar] T/W=150 [-]	
Performance Parameters	values	+% baseline	values	+% baseline	values	+% baseline
UDP [m/s]	305		79		473	
$I_{sp,t,eff}$ [s]	385.8	10.7%	382.87	9.9%	388.01	11.4%
$I_{sp,max}$ / $I_{sp,min}$ [s]/[s]	391.26/366.19	26.2%/0.3%	391.93/354.3	26.4%/-2.9%	392.5/364.53	26.6%/-0.1%
DeltaV [m/s]	9190	7.4%	9161	7.1%	9080	6.1%
$M_{prop,surplus}$ [Mg]	0		0		0	
M_{engine} [kg]	3699	21.4%	3496	14.7%	6129	101.1%

Table 9.23: Provides the performance parameters of the C2H2/O2 powered pulse detonation engines.

That no trajectory achieved an optimal trajectory could be the result of the C2H2/O2 configuration being insufficient. Alternatively, only a single optimal ascent trajectory exists, hence an insufficient number of op-

timisation generations is used to reach the optimum. Therefore, the orbit capability of the C2H2/O2 powered PDE are taken with caution.

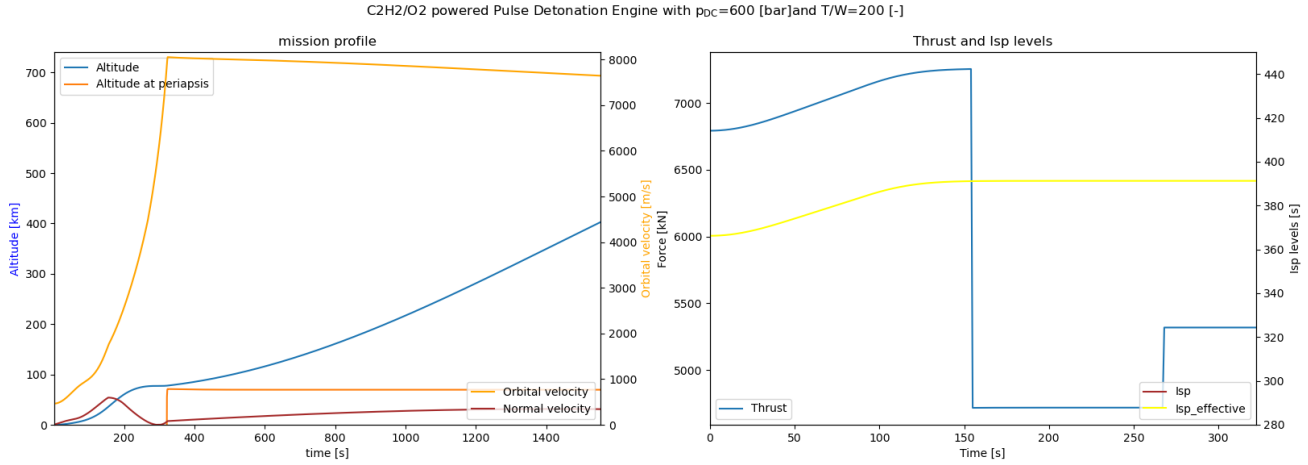

(a)

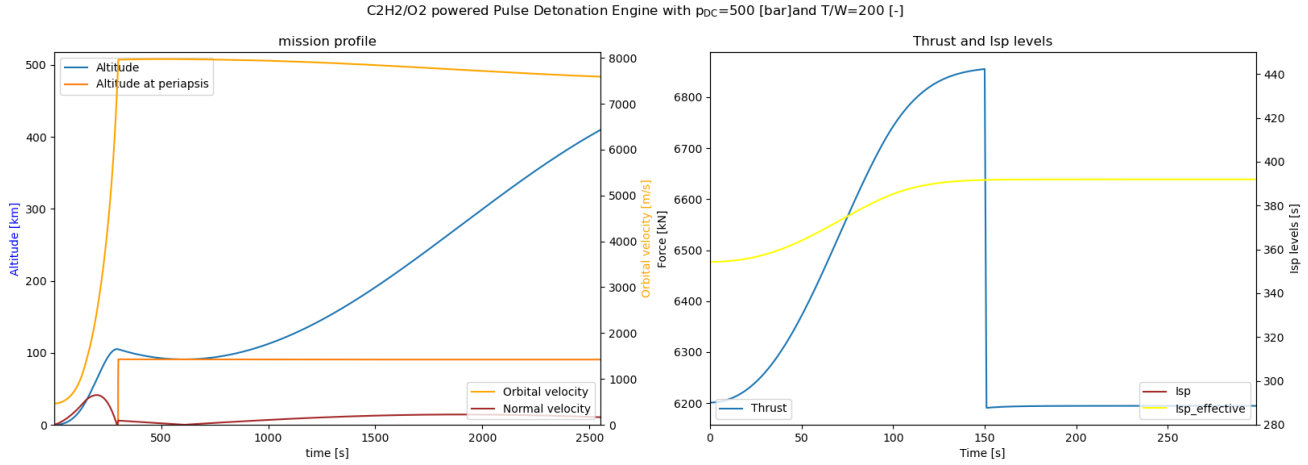

(b)

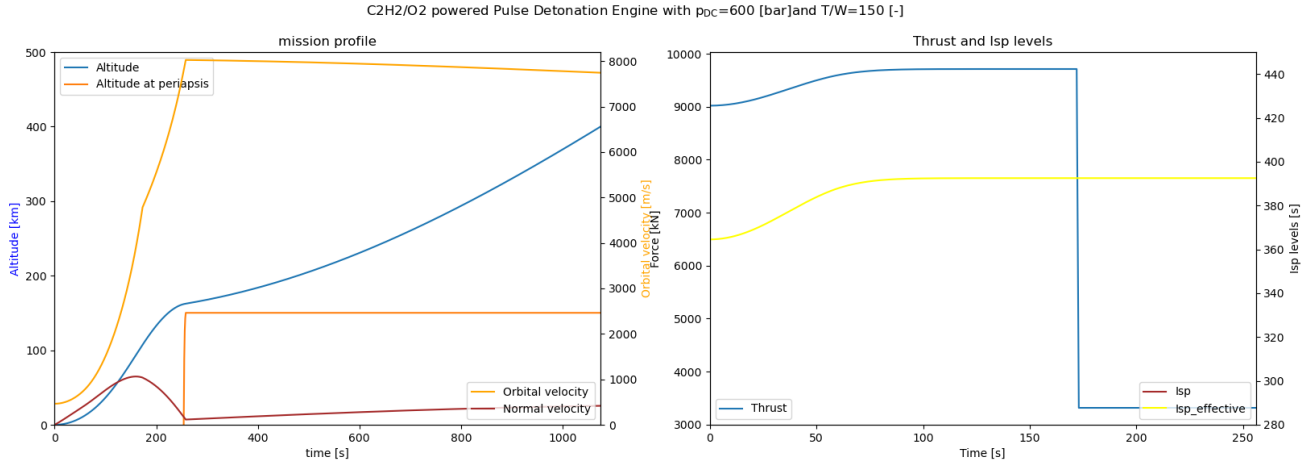

(c)

Figure 9.14: Illustrates the mission profile (left) and the engine operations (right) of an ascent vehicle operating an C2H2/O2 powered pulse detonation engines.

However, the UPD of configurations a. and c. illustrate that an additional 300-400 m/s of velocity can be used to improve the ascent. Furthermore, the poor burning program provides another point of improvement. On top of that some improvement is made by increasing ϵ, see Section 9.4.3. All the above argues that the C2H2/O2 powered engines do posses the required orbit capabilities. Note that the low UPD of configuration b. is the result of increased gravity drag losses, illustrated by the descent in Figure 9.14.

All in all, C2H2/O2 powered PDEs posses lesser orbit capabilities[15] with the evidence suggesting that the required orbital capabilities might very well be possible. However, the latter requires further validation, which could be done through the use of more optimisation generations and more constrains on the burning settings. Hence, when developing an C2H2/O2 powered PDE the specification should aim for those of configuration a., to ensure sufficient margin.

H2/O2 Powered Precooled Hybrid Airbreathing Rocket Engine

Optimisation variables of the H2/O2 powered precooled hybrid airbreathing rocket engine with T/W=100 [-] and p_{cc}=300 [bar]

Burning mass rates ($\vec{\dot{m}}$)	:	[1864.48, 402.7, 1885.83, 1675.09, 1922.36] [kg/s]
Burning periods ($\vec{t_b}$)	:	[152.68, 148.24, 130.09, 141.09] [s]
Steering angles ($\vec{\gamma}$)	:	[11.81, 73.27, 48.19, 4.04, 37.12] [°]
Steering time intervals ($\vec{t_\gamma}$)	:	[121.14, 57.33, 74.54, 129.57, 145.83] [s]
Sizing Variables (F/O, ϵ, $F/O_{breathing}$)	:	[0.225, 56.716, 0.675] [-]

Section 9.5 is mostly dedicated to the H2/O2 powered precooled hybrid airbreathing rocket engine with the specifications p_{cc}=300 [bar] and T/W=100 [-], as it is the only viable engine of that type. Therefore, only additional output findings are discussed, for a detailed discussion the reader is referred to Section 9.5.1 instead.

Studying the steering variables of the H2/O2 powered hybrid engine, the last two steering nodes appear to once again resemble the orientation for circularisation burn. The first steering node forms the biggest difference compared to the other viable engines. While the pure rocket engine required a quick inclination change (large flight path angle), the hybrid engine requires a more gentle flight path angle over an extended period. This initially results in a more vertical ascent which quickly flattens corresponding to the breathing phase. The second node is interpreted as a pull-up node and is the transition between the 1st and 2nd breathing phase, as discussed in Section 9.5.1.
corresponds with the transition between the first and second breathing phase, as discussed in Section 9.5.1 and illustrated in Figure 9.15. Consequently, the third node corresponds with second and third breathing phases. As discussed in Section 9.5.1, even though the burning settings have five nodes, it effectively has three burn nodes, as it pushes the remaining two beyond the burnout time.
Table 9.24 illustrates the sizeable increase in $I_{sp,t,eff}$ and DeltaV, which is the largest increase of all engines.

Precooled Hybrid Airbreathing Rocket Engine	p_{cc}=300 [bar] T/W=100 [-]	
Performance Parameters	values	+% baseline
UDP [m/s]	360	
$I_{sp,t,eff}$ [s]	639.11	83.4%
$I_{sp,max}$ / $I_{sp,min}$ [s]/[s]	1502.24/338.27	384.4%/-7.3%
DeltaV [m/s]	12958	51.4%
$M_{prop,surplus}$ [Mg]	0	
M_{engine} [kg]	8675	184.7%

Table 9.24: Provides the performance parameters of the H2/O2 powered precooled hybrid airbreathing rocket engine.

However, it comes at the cost of a substantially heavier propulsion system. The percentage reduction in $I_{sp,min}$ is due to a lower ϵ, which is the result of the extended operation at lower altitude, where a lower ϵ is more beneficial.
Lastly, the UDP reveals still significant performance gains can be made in the ascent trajectory, especially in the normal velocity overshoot. Moreover, improvements can be made in the overall trajectory settings, as

[15] The ability to deliver any substantial payload to at least LEO (>200 km).

illustrated by the sub-optimal burning program and the loss of orbital velocity in Figure 9.15.

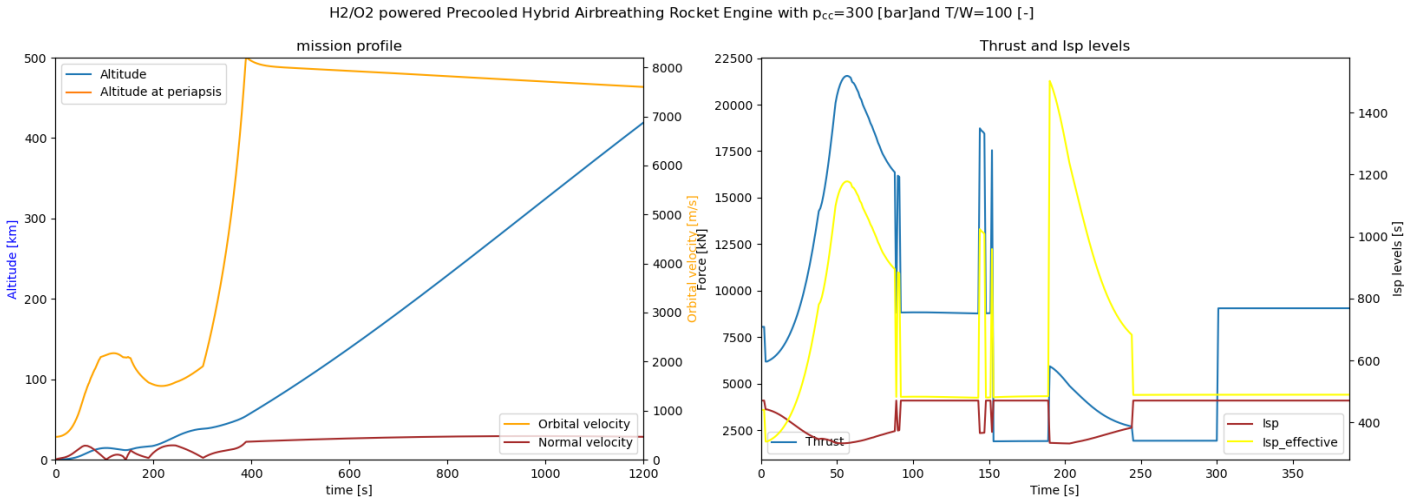

Figure 9.15: Illustrates the mission profile (left) and the engine operations (right) of an ascent vehicle operating an H2/O2 powered precooled hybrid airbreathing rocket engine.

Furthermore, recall that the breathing phase can be significantly extended and merged by removing the $p_{cc,min}$>50 bar inlet closed conditions. Preliminary analysis revealed that an $I_{sp,t,eff}$ of ~800 s^{-1} is achievable with no additional trajectory optimisation.

9.6.3. Selecting the Most Promising VT SSTO RLV Engine

To summarise this section, the performance trade-off started with the aerospike engine, the pulse detonation engine and the precooled hybrid airbreathing rocket engine, each with 2 to 4 propellant types. Out of all these engine configurations nine viable engines configurations are identified. From these nine configurations, one is identified as the most promising candidate for a VT SSTO RLV implementation.

Taking the results from Section 9.6.2 and considering the achievability of each engine, as discussed in Chapters 4 and 5, the most promising candidate is the H2/O2 powered pulse detonation engine.
To elaborate, the pulse detonation engine offers the best performance gain relative to its achievability, and thus offers the best economic incentives to be developed as the main propulsion system for a VT SSTO RLV.
To elaborate, the PDE offers the greatest UDP of all engines, moreover as the majority of the UDP is a consequence of the $M_{prop,surplus}$, a significant mass margin is given to the ascent vehicle. Although part of this can contributed to the optimal trajectory, the other engines never achieved a $M_{prop,surplus}$.

While, the achievability of the aerospike engine is arguably greater, the salvage opportunities are severely limited to non-existent. As described in Section 9.6.2, PDEs are easily implemented on TSTO concepts, due to their similarity with conventional engines. However, aerospike engines only offer an advantage when operating over a large altitude range, which is not the case for a TSTO ascent vehicle.
Salvaging the aerospike development by utilising a lesser capable SSTO, is not plausible either as it is unlikely that the development costs of such an SSTO are justified, as discussed in Chapter 2.

Because PDEs operate so similar to conventional engines, they offer a great advantage over a precooled airbreathing hybrid rocket engine. Namely, PDEs only have a minimal impact on the vehicle shape, unlike the hybrid engine which requires the shape to facilitate the intakes and possible have lifting surfaces. Hence, the ascent vehicle of PDEs requires less development attention, which can then be redirected towards the development of the PDE.
Furthermore, this likely translates to other (sub)system too, hence a PDE powered SSTO can potentially use a larger quantity of off-the-shelf components. While, this is not always more economical than in-house devel-

oped components, it can significantly reduce development time, which ensure an earlier revenue stream.
Yet, most of the individual components of the hybrid engine system are well established technologies. However, integrating these into an SSTO propulsion system, which is exposed to the extreme rocket conditions is were the challenge resides. In addition, the hybrid engine relies on the dedicated development of many support systems, which puts another constraint on the development project, evidenced by the fact that Reaction Engines Ltd. is not developing the ascent vehicle.
Although, the precooled hybrid airbreathing rocket engine shows great performance potential, it is insufficient to outweigh the development risk, especially in the presence of more achievable alternatives.

From all propellant evaluations it can be concluded that the H2/O2 offers the provides the highest margins to achieve the required orbit capabilities, as all H2/O2 powered engines are found viable. Even though, the C2H2/O2 powered engine are occasionally found to be viable, the fact that the utilised ascent trajectories are questionable, gives less confidence (lower margins) in the capabilities. This is further exacerbated when considering the ideal configuration assumption of Section 7.1.2 and ideal launch (equatorial) of Section 6.2.2.
Lastly, it can be concluded that the current industry standard CH4/O2 propellant pallet, is unsuitable for the selected engines in an SSTO configuration.
While, it is true hydrogen (H2) is a challenging propellant, in terms of handability and storability, the alternative Ethyne (C2H2) is just as challenging to handle, as discussed in Section 5.2.1. Fortunately, hydrogen has gotten renewed attention in light of the current energy transition, therefore it is not far-fetched to assume the avilability, handability, and storability will improve in the next 10 years.

Even though the H2/O2 powered PDE is identified as the most promising candidate, it does not render the other viable engines unusable. Depending on future sizing and development cost analyses the preference might switch. This chapter primarily has provided a consistent performance analysis to evaluate the viability of privately developed VT SSTO RLV when utilising the aerospike engine, pulse detonation engine, or precooled hybrid airbreathing rocket engine in various configurations. To this end it can be concluded that a privately developed VT SSTO RLV is a viable vehicle that can be developed given the current technologies.

10

Recommendation and Conclusion

This chapter contains the conclusion of this thesis and recommendations. The conclusion provides the most remarkable finding and provides a brief overview how these are derived. The recommendations are divided into possible model improvements and future study suggestions.

10.1. Conclusion

This thesis set out to determine whether SSTOs are viable ascent vehicles in the foreseeable future. By doing so it aimed to answer the question *to what extend can next generation rocket engines make a VT SSTO RLV viable within a reasonable development time frame?* This thesis evaluates the main research question by optimising the engine configuration and ascent trajectory of an ascent vehicle powered by either an aerospike engine, a pulse detonation engine, or a precooled hybrid airbreathing rocket engine. To that end this thesis can conclude with a reasonable level of certainty that VT SSTOs are viable when considering next generation rocket engines.

Five engine configurations demonstrated the required orbital capability, which is the delivery of an 15,000 kg paylaod to an orbit with a 400 km altitude, for an Delta Clipper like vehicle with the mass budget of the Falcon 9 rocket. All engine configuration and the corresponding specifications that posses this capability are provided in Table 10.1.

All Viable Engine configurations					
Engine Types	Aerospike Engine		Pulse Detonation Engine		Precooled Hyrbid Airbreathing Rocket Engine
Propellant pallets	H2/O2	C2H2/O2	H2/O2	C2H2/O2	H2/O2
p_{cc}=300 bar/p_{DC}=600 bar, T/W=200	X	X	X	X	
p_{cc}=250 bar/p_{DC}=500 bar, T/W=200	X		X	X	
p_{cc}=200 bar, T/W=200	X				
p_{cc}=300 bar/p_{DC}=600 bar, T/W=150	X		X	X	
p_{cc}=300 bar, T/W=100	X				X
p_{cc}=250 bar, T/W=100					X
p_{cc}=200 bar, T/W=100					X

Table 10.1: Provides all engine configurations and the corresponding specifications that fulfil the orbital requirements (15.000 kg payload to 400 km orbit).

To reiterate, the research question was motivated by the stagnation in launch cost of TSTO PRLVs while the general space industry requires further reduction in launch costs. SSTO RLV have the potential of reducing launch cost further, due to a higher reusability level. This determined that the SSTO should be an RLV. By begging the research question it was determine that SSTOs can only be develop by the private launch market.

From this it was determined that the SSTO should operate in the general LEO satellite launch market (payload delivery of 15,00 kg to 20,00 kg to an orbit of 200 km to 400 km) to ensure a sufficient earn-back period. Furthermore, it is established that the initial launch cost should be USD 80-100 million, while the final launch cost should be below USD 60 million.

In the past most SSTO project failed because of overambitious propulsion system, yet these propulsion systems might be achievable with the current technology level. It is this notion that was the primary motivation behind the main research question. As such, great emphasis was put on the achievability of the propulsion system. This is especially true given that a private corporation is the most likely to develop a VT SSTO RLV, which will leverage the use of proven technologies as much as possible to shorten and limit the development time. The majority of the development focus is reserved for the propulsion system. Following this reasoning it is determined that the SSTO utilises an VT ascent and nose re-entry, however the landing procedure is driven by the engine with a slide preference for VL.

After establishing the conditions of the evaluation, this thesis performed two elaborate literature trade-offs, which combines the engine concepts with high performance propellant pallets. This combination is unique in the literature of advanced rocket engine concept, which usually only consider one or the other. The literature trade-off identified the aerospike engine, pulse detonation engine, and precooled hybrid airbreathing rocket engine with the fuels LH2, LCH4, LC2H2, and LC2H4 and oxidisers LO2 and LH2O2 as potential viable concepts.

To evaluate the viability of the selected engine an performance analysis is created for each identified engine type. The developed performance analyses offer an analytical approach to evaluate the performance of these engines, which are faster and more accessible than the alternative CFD models. These performance analyses are the second main outcome of this thesis and are summarised below.
The performance analyses are implemented into the main model, which optimises the engine configuration and ascent trajectory for a given set of orbital requirements and a given vehicle mass budget. The model evaluated each selected engine with its corresponding propellant pallets to identify the orbit capabilities and performance in a VT SSTO set-up for that particular engine. From this data Table 10.1 is created, which marks all specifications for which that particular engine is viable.

Performance Analysis Aerospike Engine
The aerospike is simulated as an ideal convectional nozzle using the frozen equilibrium. While, such approach is common among literature, it is found that an alteration must be made to account for the directional losses. The alteration, illustrated in Equation 10.1, provides a more accurate performance simulation of aerospike engines, which is required due to the significant affect on the trajectory. However, as a benefit the alteration allows for initial sizing of the effective design/maximum expansion ratio.

$$T_{aerospike} = \dot{m}_{prop} U_e \cdot \left(1 - \eta_{direction}\right)\left(1 - \frac{\epsilon_{eff}}{\epsilon_{max}}\right) + A_{e,eff}(p_e - p_a) \tag{10.1}$$

Furthermore, this thesis proposed a more detailed performance analysis with advocates to simulate the convectional nozzle part of the aerospike via the frozen equilibrium, after which the aerospike expansion is simulated via the Prandtl-Meyer approximation. This approach is only required when one wishes to obtain an initial shape of the aerospike, a convectional nozzle expansion ratio, and a more detailed effective aerospike expansion ratio and effective exhaust area. Note that this approach gives greater insight on how the pikes shape influence the directional losses.

Performance Analysis Pulse Detonation Engine
The performance analysis proposed in this thesis is heavily derived from the work of Enda-Fuijware [24]. However, the performance model is altered to be applicable to CD nozzle PDEs. As such, the utilised method segregates the detonation pulse in two phases, to simulate the conditions at the open-end of the DC. These phases are the Chapman-Jouguet detonation wave, followed by an exponential decaying blowdown phase. The expansion in the nozzle is iteratively simulated via a step-wise frozen equilibrium expansion. The outcomes of the iterative method are used to compute the impulse thrust via 10.2.

$$T_{PDE} = \sum_{(t_{\frac{1}{2}}, t_{cyc})}^{i} \left(\dot{m}U_{9,i} + p_{9,i}A_{9,i}\right)(t_i - t_{i-1}) - p_a A_{9,i}(t_{cyc} - t_{\frac{1}{2}}) \tag{10.2}$$

Performance Analysis Precooled Hybrid Airbreathing Rocket Engine
The performance analysis of precooled hybrid airbreathing rocket engine combines the aero engine performance analysis of [59], the precooler analysis of [80], and the frozen equilibrium method as presented in [85]. Although individually all these methodologies are well established, the combination is what allows for a very accessible analysis of engine as complex as the precooled hybrid airbreathing rocket engine. Furthermore, this mythology allows for the evaluation of critical parameters and identification of limit conditions for various components of this particular engine type. To account for the intake air the thrust equation is altered to Equation 10.3.

$$T_{Hybrid} = \dot{m}_{prop}U_e + \dot{m}_{intake}(U_e - U_a) + A_e(p_e - p_a) \tag{10.3}$$

It is because of the consistent derivation of the performance methodologies, as all originate from the continuity equations with the same assumptions, that a direct comparison between the various engines is possible. Hence, it facilitates to a greater extend a more direct comparison between the the evaluated engines, than cannot be obtained from an literature comparisons. In addition, the model provided a greater insights and more detailed understanding by providing a realistic representation of the performance, due to the optimisation of ascent trajectory. The direct comparison of the performance parameters of each engine configuration and its viability in an VT SSTO RLV, is the main contribution of this thesis.

The obtained performance parameters in relation to the economic drivers, reveals that the H2/O2 powered pulse detonation engine is the most viable candidate to facilitate the development of a VT SSTO RLV by the private launch market. This is motivated by the large performance margin the PDE offers, namely a ~20% increase in DeltaV, a ~40% increase in I_{sp}, and a propellant surplus of 17-20 tons, relative to the achievability of the engine (TRL 6-7). While, the precooled hybrid airbreathing rocket engine provided the greatest performance gain, +50% in DeltaV and +83% in I_{sp} when compared to the Raptor engine, but is engineering wise the most complex engine to develop (TRL 5). Whereas, the aerospike is the most achievable engine (TRL 7), it offers no project salvage options, therefore making it economically less attractive than the pulse detonation engine.

The hydrogen oxygen propellant pallet offered the greatest confidence with respect to the orbit capabilities, allowing each evaluated engine to reach orbit. While, the C2H2 possessed orbit capabilities in some instances, the absence of what can be considered a true optimal ascent trajectory and its more limited margin make it less optimal choice.
Unfortunately, this thesis illustrated that the CH4/O2 propellant pallet, the current preferred propellant pallet of the private launch industry, is unsuited for SSTO applications. The same holds true for a C2H4/O2 propellant pallet.

In light of the findings of this thesis it is concluded that the research question has been answered. Hence, next generation engines exist that can be developed by the private launch market which make VT SSTO RLVs viable, given that the vehicle resembles the aerodynamic properties of the DeltaClipper (X-DC) and X-33 and the top level mass budget resembles that of the Falcon 9 rocket. In total five viable engine configuration are identified. Where the H2/O2 powered pulse detonation engine is identified as the most promising configuration and thus is recommended to be develop for a VT SSTO RLV implementation.

10.2. Recommendation

The recommendations are divided by future research proposals and model improvements. While, the former is primarily focused on future research into H2/O2 PDEs powered VT SSTO RLVs, the latter makes suggestions on how the efficiency of the model and the model itself can be improved.

10.2.1. Future Research proposals

Pulse Detonation Engine powered VT SSTO Vehicle Sizing Study

As by the conclusion of this thesis the H2/O2 powered PDEs are the most promising engine make VT SSTO RLV viable. While, the viability is argued with a reasonable level of certainty, the exact vehicle capabilities lack this degree of certainty. To resolve and understand the vehicle's properties to a greater detail a dedicated sizing module, tailored to PDE vehicles is required.

Therefore, future studies should develop a dynamic sizing class for PDE powered vehicles, which can easily be implemented into the model developed in this thesis. The derived mass budgets resulting from the optimisations should be more representative of the actual vehicle and should be evaluated with the Z-parameter, as discussed in Section 3.5. The capabilities can than be better understood by applying either three methods. Firstly, one could run the model with varying payloads and guess or fix the propellant mass. Secondly, an semi-optimisation step can be added that changes the propellant mass based on previous runs. Thirdly, an outer sizing optimisation loop can be added which optimises the propellant mass for a fixed payload.

Transition to 3D Trajectory Optimisation or Mission profile Modelling

The model can be upgraded to optimise a trajectory in 3D space, therefore be even more representative of a mission profile. This would require the creations of a dedicated steering module or a GNC module, to replace the current steering sub-module. In addition, the initial position of the vehicle has to be changed, for which a function is already present in the rocket motion module. Doing the above will allow the model to simulate and optimise the mission profile of the vehicle, therefore provide the actual performance parameters of the engine for that particular mission profile.

Depending on the mission profile alteration to the problem function (Equation 6.3) might be required. For an similar equatorial LEO orbit the function can remain unchanged, with perhaps the addition of an inclination term. More complex profiles will at least require different weights and perhaps an new problem function entirely.

Future Research on the Power Cycle

As indicated the power cycle including the (re)ignition are beyond the scope of this research. Hence, ignition is achieved by setting an ignition temperature in the CC. Future research could expand on the power cycle, especially those of PDEs utilising an CD nozzle. As such, the propulsion modules can be expanded to simulate the entire power cycle, which is beneficial to obtain a better understanding on engine criticality. Furthermore, initial design parameters for the power cycle can be extrapolated, as is the case for ϵ in the current model.

10.2.2. Model Improvements

Increased constraints on the Mass Nodes

The burning programs derived by the model were largely in line with the hypothesised burning programs. Therefore, future research can be more restrictive on the mass rates and burning time. Doing so is equivalent to adding information to the model, therefore the rate of convergence and the change of achieving an optimal trajectory are increased.

Altitude based Steering Nodes

Originally, it was considered to make the steering program a function of the altitude, which could be a more codependency robust method. However, this idea was abandoned as it is redundant to answer the research method. Applying this steering program allows for either two alterations to the joint optimisation loop. The loops can potentially be merged or the the optimisation method for the inner loop can be altered to take

initial guesses. These guesses are than taken form previous loops. Furthermore, such steering model must have a mechanism for dealing with vehicles that have a cruise phase in their ascent trajectory, like the hybrid engine powered vehicles. How much this improves efficiency and robustness is an interesting topic for future studies.

Switching Optimisation
Rather than having the optimisation loops in fixed order a switching optimisation method can be utilised. In this instance, the model switches between the optimisation of the burning settings and the optimisation of the steering settings. Each switch can last for a fixed amount of generations or last until a certain level of convergence is reached. Although it is expected that such an optimisation methodology requires more time and is more prone to initial guess convergence[1], it could increase the convergence robustness.

Fixing Expansion Ratios
In hing sight, the expansion ratio (ϵ) for non-breathing engines with an convectional DC nozzle can be set to the upper limit, thereby reducing the total optimisation variables. The sensitivity analysis of the PDE illustrated that this is optimal for an VT SSTO vehicle.

None Homogeneous expansion Ratios
In this thesis the propulsion system is assumed ideal, homogeneous, and uniform, hence the number of engines is not defined and all engines operate equally with the same ϵ. By lifting these assumptions different expansion ratios and burning programs can be used per engine. However, care must be taken that this does not transition into a two propulsion system configuration, as this is redundant for an SSTO vehicle. Such, adaptation would vastly complicate the model and is only recommended when designing the actual propulsion system or/and mission profile.

[1] The initial values are influential to the final outcome of the optimisation

A

Industry Reference Conventions

A.1. Reference Frames with Respect to the Forces and Guidance.

All relevant reference frames are defined below. The reference frames are defined with the definitions provided in [48].
Vertical body reference frame : Origin : is located at the CoM of the ascent vehicle, Z_V is pointing towards the CoM of the body of origin, X_V, is in the meridian plane pointing to the northern hemisphere and is perpendicular to the Z_V. Y_V follows from the right hand rule.
Vehicle-carried reference frame (F_E): Origin : at centre of mass of the vehicle, Z_E is pointing towards the centre of the earth, X_e is directed towards the north, Y_E follows from right hand rule.
Body-fixed frame (F_b): Origin : at centre of mass of the vehicle, X_b can be chosen arbitrary (mostly parallel to the axis of symmetry), Z_e follows from right hand rule (often parallel to axis of symmetry and gravity) , Y_E follows from right hand rule.
Aerodynamic frame (F_a): Origin : at centre of mass of the vehicle, X_a in the direction of the aerodynamic velocity, Z_a : pointing downwards , Y_a : follows from right hand rule.
Inertial Earth reference frame (F_I): Origin : at Earth centre of mass, X_I follows from the direction of the zero-longitude meridian at time is zero (still), Z_I through the north pole , Y_I follows from right hand rule (still).
Earth-centred, Earth-fixed reference frame (F_C): Origin : at Earth centre of mass, X_I follows from the direction of the zero-longitude meridian at time is t (rotating), Z_I through the north pole , Y_I follows from right hand rule (rotating).
Some forces are better simulated in other reference frames, which reference frame those are has to be determined for each force individually. Whether Earth can be treated as an inertial reference frame should be verified.

A.2. Aeroengine Stage numbering Convention

The fundamental station numbers for the core stream of the gas turbine are listed below, taken from [59].

0 : Ram conditions in free stream
1 : Engine intake front face
2 : First compressor/fan front face
3 : Last compressor exit face
4 : Combust chamber exit plane
5 : Last turbine exit face
6 : Front face of mixer, afterburner, etc.
7 : Propelling nozzle inlet
8 : Propelling nozzle throat
9 : Propelling nozzle or exhaust diffuser exit plane

B

Golden Section Method

The golden section method works for one input parameter at a time. Therefore, the golden section method has to cycle through the input parameters. Cycling can be done through randomisation, or via a set order (co-ordinated descent), or via a smart system. With the latter, once the optimisation of one parameter has been finished, it looks at all the other parameters. Of the others, the one that provided the largest gain is next to be optimised. More complex smart systems which will not be discussed here.
The golden section method requires a span in which the optimum lies. The method takes two points for which it runs the module. The points are determined via the golden section ratio. This, will allow one of the two points to be recycled into the next iteration, thereby eliminating half the run time. A pseudo script is given bellow.

```
X_3 = X_2 - 1/GR * (X_2-X_1) -> f3
X_4 = X_1 + 1/GR * (X_2-X_1) -> f4
if f3 <= f4 :
    X_2 = X_4
    X_4 = X_3, f4 = f3
    X_3 = X_2 - 1/GR * (X_2-X_1) -> f3
if f3 > f4 :
    X_1 = X_3
    X_3 = X_4, f3 = f4
    X_4 = X_1 + 1/GR * (X_2-X_1) -> f4
repeat till |X_4-X_3| < epsilon
```

X_1 and X_2 are the lower- and upperbound, respectively. Whereas X_3 and X_4 are the points investigated in the current iteration. Even though, the golden section method converges linearly [52], it requires a minimum of conditions to be true. The golden section method needs the Weierstrass conditions, which state that the set is nonempty. If the function is monotonic towards the optimum the golden section is guaranteed to find the global optimum.

C

CEA Output Files

```
NOTE. WEIGHT FRACTION OF FUEL IN TOTAL FUELS AND OF OXIDANT IN TOTAL OXIDANTS
              THEORETICAL ROCKET PERFORMANCE ASSUMING EQUILIBRIUM
          COMPOSITION DURING EXPANSION FROM INFINITE AREA COMBUSTOR

 Pin =  4408.8 PSIA
 CASE = _______________

            REACTANT                    WT FRACTION      ENERGY      TEMP
                                         (SEE NOTE)     KJ/KG-MOL      K
 FUEL       CH4(L)                       1.0000000    -89233.000    111.643
 OXIDANT    O2(L)                        1.0000000    -12979.000     90.170

 O/F=    3.65116  %FUEL= 21.500000  R,EQ.RATIO= 1.092601  PHI,EQ.RATIO= 1.092601

                 CHAMBER   THROAT     EXIT     EXIT
 Pinf/P            1.0000   1.7292   310.32   903.13
 P, BAR            303.98   175.79  0.97955  0.33658
 T, K             3766.68  3575.82  2077.81  1760.36
 RHO, KG/CU M    2.2094 1 1.3625 1 1.4089-1 5.7190-2
 H, KJ/KG        -1514.30 -2243.98 -7300.83 -7985.59
 U, KJ/KG        -2890.10 -3534.18 -7996.07 -8574.12
 G, KJ/KG        -44435.8 -42990.7 -30977.6 -28045.0
 S, KJ/(KG)(K)    11.3951  11.3951  11.3951  11.3951

 M, (1/n)          22.763   23.044   24.849   24.870
 (dLV/dLP)t      -1.03582 -1.03219 -1.00050 -1.00005
 (dLV/dLT)p        1.6083   1.5778   1.0156   1.0016
 Cp, KJ/(KG)(K)    6.1125   6.0642   2.2960   2.0876
 GAMMAs            1.1348   1.1311   1.1762   1.1914
 SON VEL,M/SEC     1249.5   1208.0    904.3    837.3
 MACH NUMBER        0.000    1.000    3.762    4.296

 PERFORMANCE PARAMETERS

 Ae/At                       1.0000   34.340   80.000
 CSTAR, M/SEC                1846.8   1846.8   1846.8
 CF                          0.6541   1.8421   1.9480
 Ivac, M/SEC                 2276.0   3606.3   3761.2
 Isp, M/SEC                  1208.0   3401.9   3597.6
```

```
MASS FRACTIONS

*CO              0.18426  0.17229  0.08511  0.07747
*CO2             0.30015  0.31903  0.45608  0.46809
COOH             0.00009  0.00005  0.00000  0.00000
*H               0.00063  0.00053  0.00002  0.00000
HCO              0.00003  0.00002  0.00000  0.00000
HO2              0.00044  0.00028  0.00000  0.00000
*H2              0.00504  0.00466  0.00307  0.00358
HCOOH            0.00002  0.00001  0.00000  0.00000
H2O              0.40370  0.41215  0.45483  0.45079
H2O2             0.00011  0.00006  0.00000  0.00000
*O               0.00668  0.00528  0.00001  0.00000
*OH              0.05340  0.04560  0.00078  0.00006
*O2              0.04545  0.04003  0.00009  0.00000

 * THERMODYNAMIC PROPERTIES FITTED TO 20000.K

 NOTE. WEIGHT FRACTION OF FUEL IN TOTAL FUELS AND OF OXIDANT IN TOTAL OXIDANTS

          THEORETICAL ROCKET PERFORMANCE ASSUMING FROZEN COMPOSITION

Pin =  4408.8 PSIA
CASE = _______________

            REACTANT                    WT FRACTION      ENERGY      TEMP
                                         (SEE NOTE)     KJ/KG-MOL      K
FUEL        CH4(L)                       1.0000000    -89233.000    111.643
OXIDANT     O2(L)                        1.0000000    -12979.000     90.170

O/F=    3.65116  %FUEL= 21.500000  R,EQ.RATIO= 1.092601  PHI,EQ.RATIO= 1.092601

                CHAMBER   THROAT     EXIT     EXIT
Pinf/P            1.0000   1.7667   414.89  1259.66
P, BAR            303.98   172.06  0.73266  0.24132
T, K             3766.68  3438.77  1330.21  1066.84
RHO, KG/CU M    2.2094 1 1.3699 1 1.5079-1 6.1928-2
H, KJ/KG        -1514.30 -2262.74 -6751.76 -7236.48
U, KJ/KG        -2890.10 -3518.77 -7237.62 -7626.15
G, KJ/KG        -44435.8 -41447.8 -21909.6 -19393.2
S, KJ/(KG)(K)    11.3951  11.3951  11.3951  11.3951

M, (1/n)          22.763   22.763   22.763   22.763
Cp, KJ/(KG)(K)    2.2942   2.2702   1.8912   1.7869
GAMMAs            1.1894   1.1917   1.2394   1.2569
SON VEL,M/SEC     1279.2   1223.5    776.0    699.8
MACH NUMBER        0.000    1.000    4.171    4.834

PERFORMANCE PARAMETERS

Ae/At                        1.0000   34.340   80.000
CSTAR, M/SEC                 1813.7   1813.7   1813.7
CF                           0.6746   1.7845   1.8652
Ivac, M/SEC                  2250.1   3386.6   3498.1
Isp, M/SEC                   1223.5   3236.5   3383.0
```

MASS FRACTIONS

*CO	0.18426	*CO2	0.30015	COOH	0.00009
*H	0.00063	HCO	0.00003	HO2	0.00044
*H2	0.00504	HCOOH	0.00002	H2O	0.40370
H2O2	0.00011	*O	0.00668	*OH	0.05340
*O2	0.04545				

* THERMODYNAMIC PROPERTIES FITTED TO 20000.K

NOTE. WEIGHT FRACTION OF FUEL IN TOTAL FUELS AND OF OXIDANT IN TOTAL OXIDANTS

THEORETICAL ROCKET PERFORMANCE ASSUMING EQUILIBRIUM

COMPOSITION DURING EXPANSION FROM INFINITE AREA COMBUSTOR

Pin = 2994.0 PSIA
CASE = _____

	REACTANT	WT FRACTION (SEE NOTE)	ENERGY KJ/KG-MOL	TEMP K
FUEL	H2(L)	1.0000000	-9012.000	20.270
OXIDANT	O2(L)	1.0000000	-12979.000	90.170

O/F= 6.03000 %FUEL= 14.224751 R,EQ.RATIO= 1.316199 PHI,EQ.RATIO= 1.316199

	CHAMBER	THROAT	EXIT	EXIT
Pinf/P	1.0000	1.7400	960.60	1130.75
P, BAR	206.43	118.64	0.21490	0.18256
T, K	3603.91	3387.66	1242.05	1201.63
RHO, KG/CU M	9.4122 0	5.8084 0	2.9490-2	2.5895-2
H, KJ/KG	-983.83	-2156.41	-10538.3	-10655.2
U, KJ/KG	-3177.04	-4198.97	-11267.0	-11360.2
G, KJ/KG	-62720.4	-60188.5	-31815.1	-31239.6
S, KJ/(KG)(K)	17.1304	17.1304	17.1304	17.1304
M, (1/n)	13.663	13.790	14.172	14.172
(dLV/dLP)t	-1.01937	-1.01449	-1.00000	-1.00000
(dLV/dLT)p	1.3357	1.2669	1.0000	1.0000
Cp, KJ/(KG)(K)	7.3582	6.7423	2.9069	2.8770
GAMMAs	1.1470	1.1482	1.2529	1.2562
SON VEL,M/SEC	1586.1	1531.4	955.5	941.1
MACH NUMBER	0.000	1.000	4.575	4.673

PERFORMANCE PARAMETERS

Ae/At	1.0000	69.000	78.100
CSTAR, M/SEC	2320.8	2320.8	2320.8
CF	0.6599	1.8836	1.8951
Ivac, M/SEC	2865.2	4538.1	4558.3
Isp, M/SEC	1531.4	4371.4	4398.0

MASS FRACTIONS

*H	0.00189	0.00150	0.00000	0.00000

```
HO2              0.00009  0.00004  0.00000  0.00000
*H2              0.03604  0.03533  0.03417  0.03417
H2O              0.90749  0.92391  0.96583  0.96583
H2O2             0.00004  0.00002  0.00000  0.00000
*O               0.00247  0.00150  0.00000  0.00000
*OH              0.04665  0.03432  0.00000  0.00000
*O2              0.00533  0.00339  0.00000  0.00000

 * THERMODYNAMIC PROPERTIES FITTED TO 20000.K

NOTE. WEIGHT FRACTION OF FUEL IN TOTAL FUELS AND OF OXIDANT IN TOTAL OXIDANTS

          THEORETICAL ROCKET PERFORMANCE ASSUMING FROZEN COMPOSITION

Pin =  2994.0 PSIA
CASE = _______________

            REACTANT                    WT FRACTION      ENERGY      TEMP
                                         (SEE NOTE)     KJ/KG-MOL      K
FUEL        H2(L)                        1.0000000     -9012.000     20.270
OXIDANT     O2(L)                        1.0000000    -12979.000     90.170

O/F=    6.03000  %FUEL= 14.224751  R,EQ.RATIO= 1.316199  PHI,EQ.RATIO= 1.316199

                CHAMBER   THROAT     EXIT     EXIT
Pinf/P            1.0000   1.7686  1111.47  1312.80
P, BAR            206.43   116.72  0.18573  0.15724
T, K             3603.91  3286.16   985.74   949.81
RHO, KG/CU M    9.4122 0 5.8364 0 3.0960-2 2.7204-2
H, KJ/KG         -983.83 -2178.54 -9901.65 -9999.69
U, KJ/KG        -3177.04 -4178.37 -10501.5 -10577.7
G, KJ/KG        -62720.4 -58471.8 -26787.8 -26270.3
S, KJ/(KG)(K)    17.1304  17.1304  17.1304  17.1304

M, (1/n)          13.663   13.663   13.663   13.663
Cp, KJ/(KG)(K)    3.7857   3.7326   2.7419   2.7157
GAMMAs            1.1915   1.1948   1.2853   1.2888
SON VEL,M/SEC     1616.6   1545.8    878.1    863.1
MACH NUMBER        0.000    1.000    4.810    4.920

PERFORMANCE PARAMETERS

Ae/At                      1.0000   69.000   78.100
CSTAR, M/SEC               2288.1   2288.1   2288.1
CF                         0.6756   1.8457   1.8558
Ivac, M/SEC                2839.5   4365.3   4382.5
Isp, M/SEC                 1545.8   4223.2   4246.4

MASS FRACTIONS

*H              0.00189   HO2             0.00009   *H2             0.03604
H2O             0.90749   H2O2            0.00004   *O              0.00247
*OH             0.04665   *O2             0.00533

 * THERMODYNAMIC PROPERTIES FITTED TO 20000.K
```

D

Optimisation Tables

D.1. Hyper Parameters : the Weights for the Problem Function

Run	w_h	$w_\perp$	$w_\parallel$	w_m	w_p	Fit	%	$M_{prop,final}$	$I_{sp,eff}$	DeltaV	Orbit
I	1000				1000	44	2.2	0	373	8752	T
II	1000	1000	500			25	1.0	0	376	8892	F
III	1000	1000		500		501	20.0	0	370	8934	F
IV	1000		500		1000	61	2.4	0	376	8709	F
V	1000	1000				1	<0.1	0	370	8897	T
VI	1000			500	1000	543	27.1	0	375	8778	F

Table D.1: Provides an overview of performance of varying weight combinations used in Fitness Function 6.3.

Run	w_h	$w_\perp$	$w_\parallel$	w_m	w_p	Fit	%	$M_{prop,final}$	$I_{sp,eff}$	DeltaV	Orbit
I	1000	1000			1000	125	4.2	0	367	8954	F/F
II	1000	1000			500	44	1.8	0	371	8779	T/F
III	1000	1000	250		1000	65	2.0	0	369	8704	T/T
IV	1000	1000	250		500	44	1.6	0	369	8715	T/F
V	1000	1000		250	1000	303	9.3	0	373	8838	T/T
VI	1000	1000		250	500	276	10.0	0	376	8768	F/T
VII	1000	1000	250	250	1000	285	8.1	0	376	8822	T/F
VIII	1000	1000	250	250	500	290	9.7	0	375	8720	F/F
IX	1000	500			1000	130	5.2	0	368	8954	F/F
X	1000	500	250		1000	74	2.7	0	369	8740	T/T
XI	1000	750	250		1000	68	2.3	0	370	8872	T/T
XII	1000	750	500		1000	205	6.8	0	367	8920	T/T
XIII	750	750	500		1000	204	6.8	0	367	8948	F/F
XIV	1000	1000	500		1000	195	5.6	0	370	8896	F/F

Table D.2: Provides all optimisations runs, with corresponding performance parameters and weight combinations used in Fitness Function 6.3, used to determine the final weights used in the model. The performance is obtained with an LCh4/LOX powered aerospike engine, with the operational settings of Table 9.1, ϵ_{max} = 220 [-], and F/O=0.325 [-].

E

Pulse Detonation Engine Model Versus Endo-Fujiwara Paper

This appendix contains the Table E.1, which contains the key state parameters as computed by this research versus the values provided by Endo-Fuijwara at el [24].
The initial state parameters [24] used are; γ = const. = 1.4, D_{CJ} = 2000 m/s, and M_{CJ} = 5. the outcomes are all in terms of the initial states $_1$.

Key Ratios and velocities	PDE Model	Endo-Fuijwara Paper
$p_{DC,N}$ [-]	29.17	29.0
$rho_{DC,N}$ [-]	6	6.0
$p_{DC,2}$ [-]	14.58	15.0
$rho_{DC,2}$ [-]	1.714	1.714
$U_{DC,2}$ [m/s]	833.33	830
$p_{DC,3}$ [-]	4.96	5.0
$rho_{DC,3}$ [-]	0.793	0.788
$p_{DC,ex}$ [-]	1.38	1.4
$rho_{DC,ex}$ [-]	0.319	0.32
$U_{DC,ex}$ [m/s]	833.33	830

Table E.1: The table provides the ratios and velocities generated by the model and those presented in [24], at the indicates stations and time stamps. The ratios are taken w.r.t. to the initial conditions of the [24].

F

Verification and Validation Tables Precooled Hybrid Airbreathing Rocket Engine

F.1. Verification Tables Oblique Shock Inlet (1 -> 12)

The sub appendix contains Figure F.1, which contains the plot of the θ – beta – M equation for various mach numbers. Additionally, the section contains tables with verification values for the oblique shock inlet.

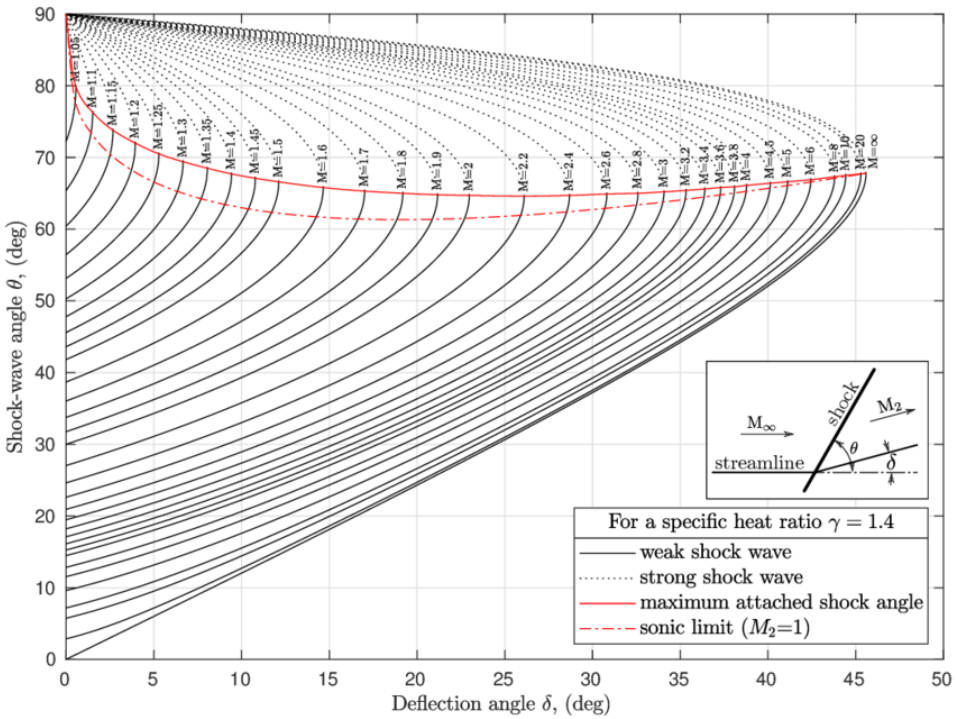

Figure F.1: Illustrates the solutions for $\theta - \beta$ – M equation, taken from [9]

Oblique Shock Wave Inlet with $\theta = 20°$			
	Inlet conditions (1)	Simulated output conditions (12)	Expected output conditions (14)
Mach Number [-]	2	1.209	1.21
Shock Angle [°]	-	53.458	53.4
Pressure [atm]	1	2.846	2.82
Density [kg/m^3]	1.226	2.503	2.49
Temperature [k]	288	401.476	399.7

Table F.1: Provides the results generated by the simulation and those presented in [9] across the oblique shock inlet for a ram angle of 20°.

Oblique Shock Wave Inlet with $\theta = 6.5°$		
	Simulated output conditions (12)	Expected output conditions (14)
Mach Number [-]	2.13	2.11
Shock Angle [°]	29.814	30
Pressure Ratio [-]	1.495	1.513
Temperature Ratio [-]	1.124	1.128

Table F.2: Provides the results generated by the simulation and those presented in [9] across the oblique shock inlet for a ram angle of 6.5° with an initial Mach number of 2.4.

F.2. Verification Table Normal Shock Inlet (13 -> 14)

This sub appendix contains tables with verification test on the normal shock inlet. The numerical examples presented in the tables are taken form [9].

Normal shock inlet			
	input conditions (13)	Simulated output conditions (14)	Expected output conditions (14)
Mach Number [-]	2	0.5776	0.5774
Flow Velocity [m/s]	680	254	255
Pressure [atm]	1	4.501	4.5
Density [kg/m^3]	1.225	3.266	3.269
Temperature [K]	288	487	486

Table F.3: Provides the results generated by the simulation and those presented in [9] across the normal shock.

Limits for Normal Shock Inlet		
	Simulated	Actual
Mach Number [-]	0.382	0.378
Flow Velocity [m/s]	862	bounded
Pressure [atm]	122	inf
Density [kg/m^3]	5.866	6
Temperature [K]	797	inf

Table F.4: Provides the limit conditions generated by the simulation and those presented in [9], simulated with M = 20, T_{13} = 223.3 K, and p_{13} = 2.65E4 Pa.

F.3. Verification Tables of Heat Exchanger

This sub appendix contains the verification table of the Heat exchanger. The numerical example in Table F.5 contains an engine example presented in [59].

Heat Exchanger			
	Input conditions (15)	Simulated output conditions (19)	Expected output conditions (19)
Air Temperature [K]	398.37	306.67	307.74
Air Pressure [kPa]	170	119.00	119.06
Coolant Temperature [K]	284.39	318.13	317.14
Coolant Pressure [kPa]	56.7	39.69	39.69

Table F.5: Provides the results generated by the simulation and those presented in [23] across an air heat exchanger, simulated with $E_{cooler} = 0.8$, $\nu_{p,loss} = 0.3$, $\dot{m}_{air} = 1$ kg/s, and $\dot{m}_{coolant} = 2.733$ kg/s.

F.4. Verification Tables for High Pressure Compressor

This sub appendix contains the verification table of the HPC. The numerical example in Table F.6 contains an engine example presented in [59].

High Pressure Compressor with Π=15.92262			
	Input conditions (15)	Simulated output conditions (19)	Expected output conditions (19)
Pressure Ratio [-]	1	15.92	15.92
Temperature [K]	364.88	838.83	842.85
Pressure [Bar]	1.398	22.26	22.26

Table F.6: Provides the results generated by the simulation and those presented in [59] across the HPC, simulated with $\nu_{ise.eff} = 0.92$.

G

Fuel-over-Oxidiser Ratios

G.1. F/O Ratios Graphs for Convectional Engine

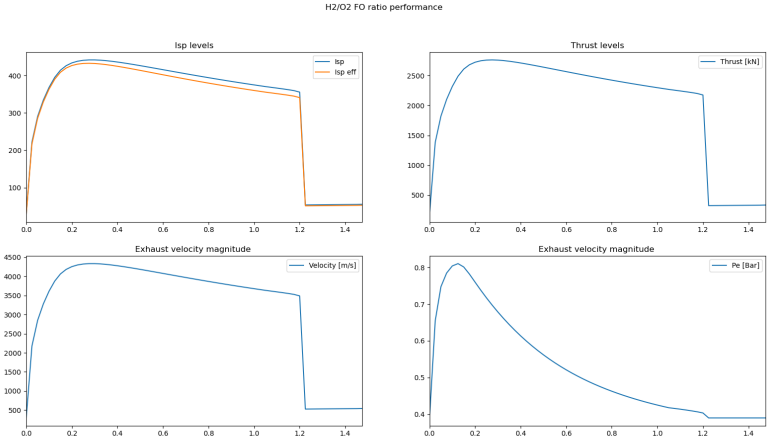

Figure G.1: Illustrates the performance of an H2/O2 at varying F/O ratios for a conventional engine.

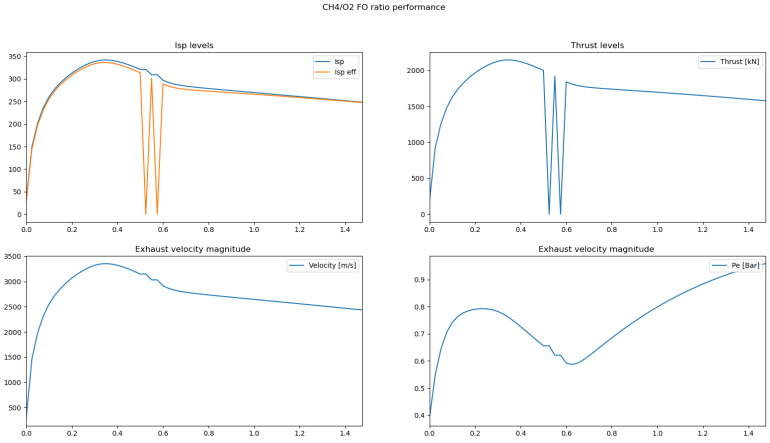

Figure G.2: Illustrates the performance of an CH4/O2 at varying F/O ratios for a conventional engine.

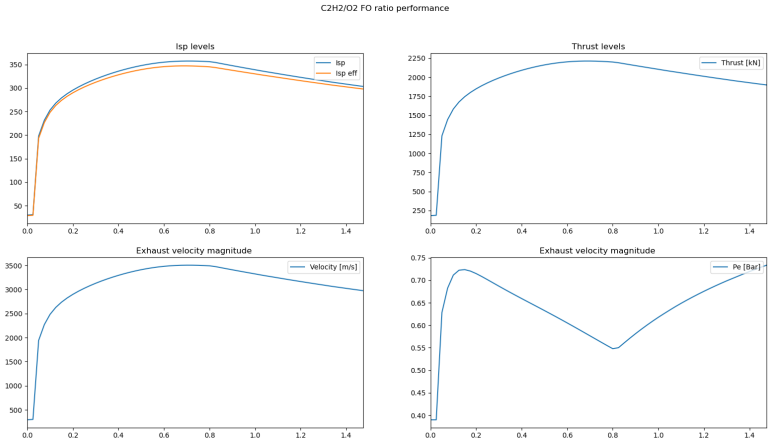

Figure G.3: Illustrates the performance of an C2H2/O2 at varying F/O ratios for a conventional engine.

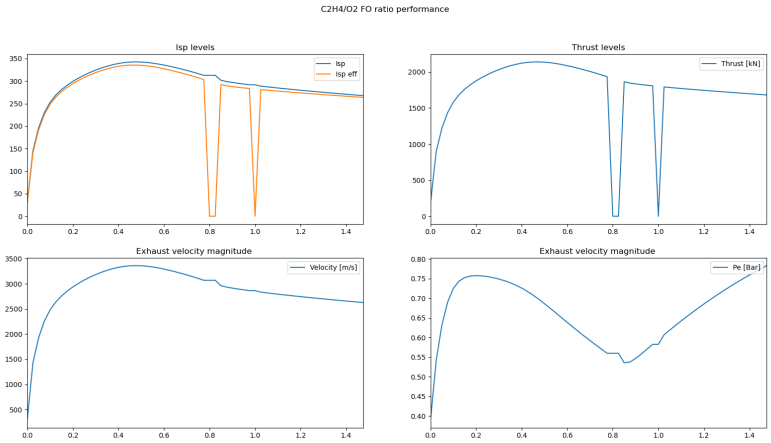

Figure G.4: Illustrates the performance of an C2H4/O2 at varying F/O ratios for a conventional engine.

G.2. F/O Ratios Graphs for Pulse Detonation Engine p_{31} Limited

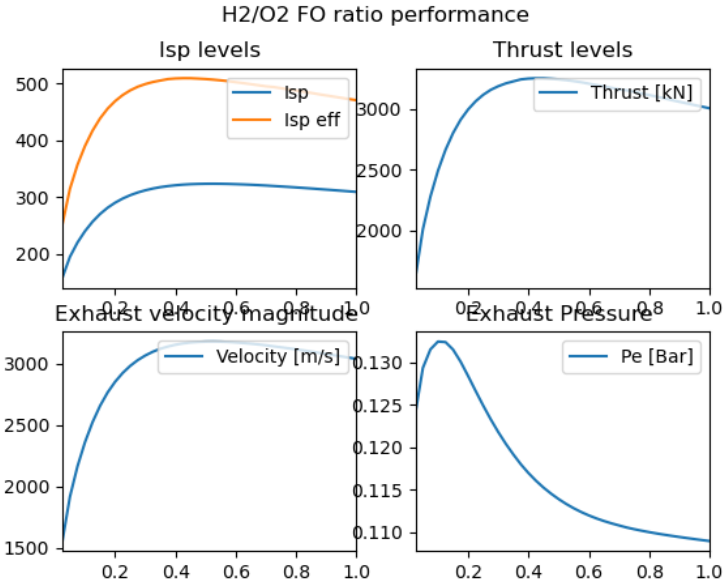

Figure G.5: Illustrates the performance of an H2/O2 at varying F/O ratios for a p_{31} limited PDE.

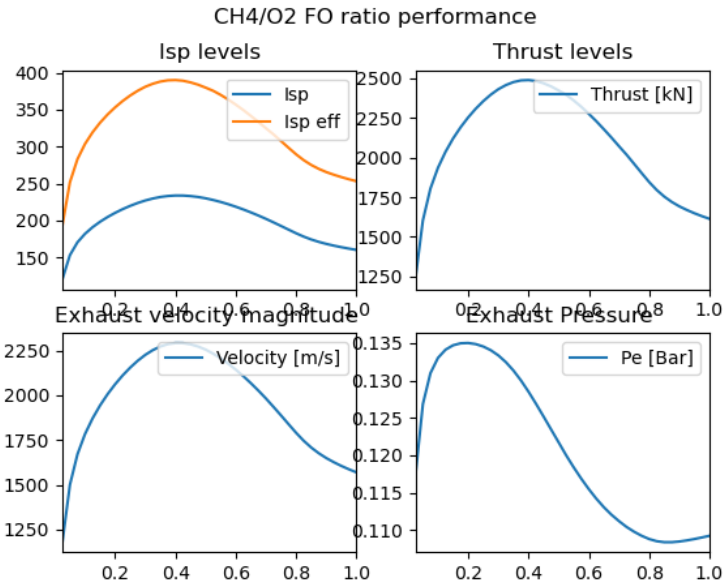

Figure G.6: Illustrates the performance of an CH4/O2 at varying F/O ratios for a p_{31} limited PDE.

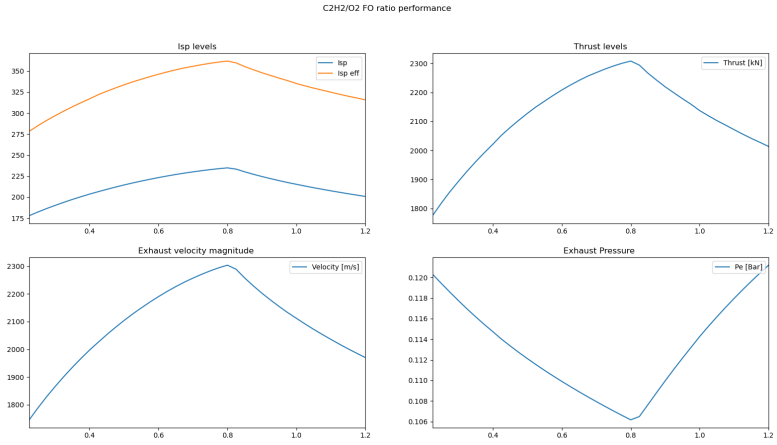

Figure G.7: Illustrates the performance of an C2H2/O2 at varying F/O ratios for a p_{31} limited PDE.

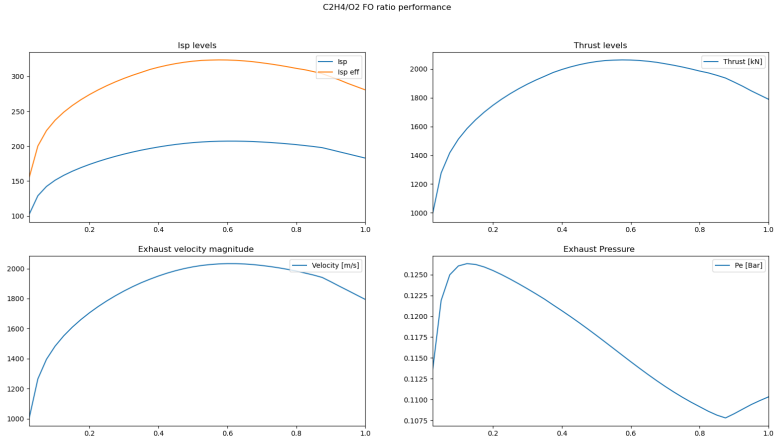

Figure G.8: Illustrates the performance of an C2H4/O2 at varying F/O ratios for a p_{31} limited PDE.

G.3. F/O Ratios Graphs for Pulse Detonation Engine $p_{4,N}$ Limited

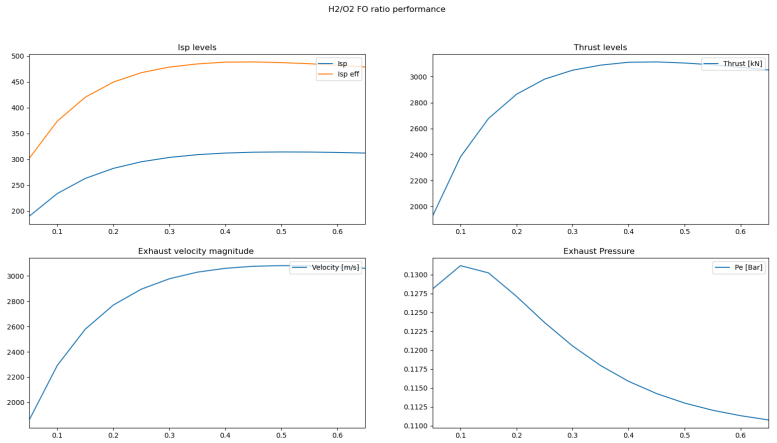

Figure G.9: Illustrates the performance of an H2/O2 at varying F/O ratios for a $p_{4,N}$ limited PDE.

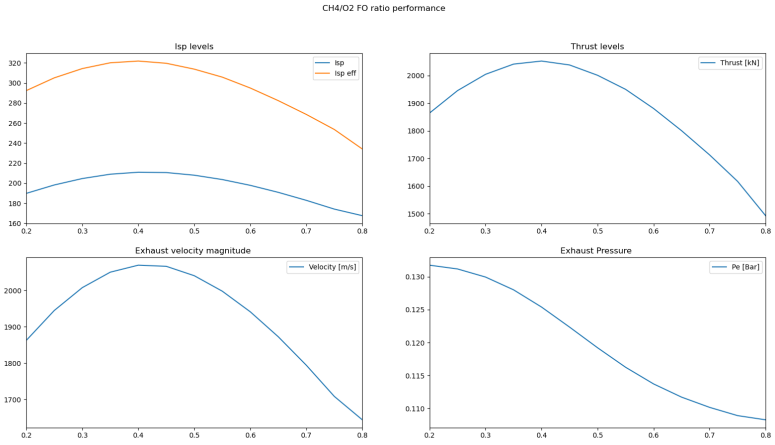

Figure G.10: Illustrates the performance of an CH4/O2 at varying F/O ratios for a $p_{4,N}$ limited PDE.

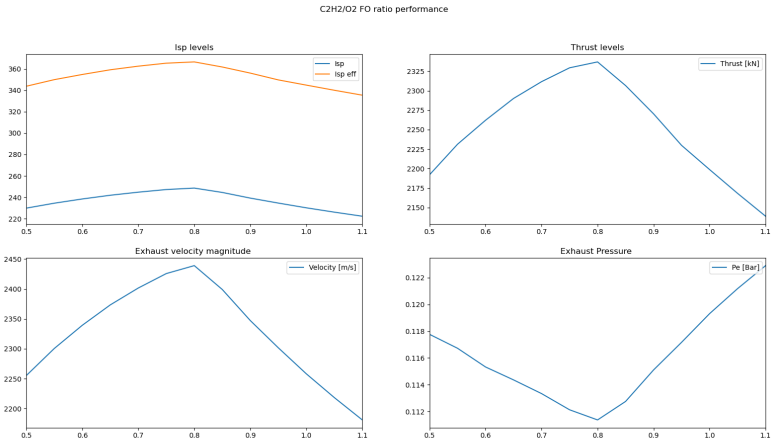

Figure G.11: Illustrates the performance of an C2H2/O2 at varying F/O ratios for a $p_{4,N}$ limited PDE.

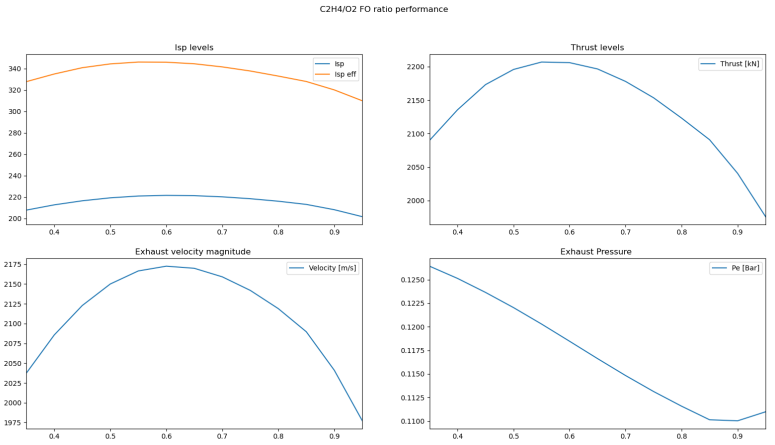

Figure G.12: Illustrates the performance of an C2H4/O2 at varying F/O ratios for a $p_{4,N}$ limited PDE.

H

Settings for Each Optimisation Run

H.0.1. Optimisation Settings of the Aerospike Powered Vehicles

Optimisation variables of the H2/O2 powered aerospike engine with p_{cc}=300 [bar] and T/W=200 [-]

Burning mass rates ($\vec{\dot{m}}$)	:	[1877.4, 1437.01, 1158.92, 826.56] [kg/s]
Burning periods ($\vec{t_b}$)	:	[95.5, 42.52, 187.04] [s]
Steering angles ($\vec{\gamma}$)	:	[78.34, 19.32, 8.91, 30.66, 62.15] [°]
Steering time intervals ($\vec{t_\gamma}$)	:	[1.08, 155.04, 57.56, 165.54, 190.11] [s]
Sizing Variables (F/O, ϵ)	:	[0.225, 220.0] [-]

Optimisation variables of the H2/O2 powered aerospike engine with p_{cc}=300 [bar] and T/W=150 [-]

Burning mass rates ($\vec{\dot{m}}$)	:	[1661.1, 950.21, 20.73, 1274.87] [kg/s]
Burning periods ($\vec{t_b}$)	:	[179.94, 198.61, 66.83] [s]
Steering angles ($\vec{\gamma}$)	:	[41.23, 86.13, 0.41, 20.94, 53.22] [°]
Steering time intervals ($\vec{t_\gamma}$)	:	[0.93, 104.05, 98.15, 69.74, 162.5] [s]
Sizing Variables (F/O, ϵ)	:	[0.225, 220.0] [-]

Optimisation variables of the H2/O2 powered aerospike engine with p_{cc}=250 [bar] and T/W=200 [-]

Burning mass rates ($\vec{\dot{m}}$)	:	[1905.61, 1715.31, 1133.72, 1558.22] [kg/s]
Burning periods ($\vec{t_b}$)	:	[15.5, 193.29, 118.33] [s]
Steering angles ($\vec{\gamma}$)	:	[44.39, 18.88, 79.84, 32.84, 54.93] [°]
Steering time intervals ($\vec{t_\gamma}$)	:	[0.96, 193.87, 193.52, 46.11, 56.22] [s]
Sizing Variables (F/O, ϵ)	:	[0.225, 220.0] [-]

Optimisation variables of the H2/O2 powered aerospike engine with p_{cc}=200 [bar] and T/W=200 [-]

Burning mass rates ($\vec{\dot{m}}$)	:	[2287.87, 928.56, 1571.55, 232.67] [kg/s]
Burning periods ($\vec{t_b}$)	:	[36.57, 127.6, 125.05] [s]
Steering angles ($\vec{\gamma}$)	:	[37.85, 49.92, 36.6, 16.78, 0.78] [°]
Steering time intervals ($\vec{t_\gamma}$)	:	[0.01, 93.26, 189.17, 26.64, 194.82] [s]
Sizing Variables (F/O, ϵ)	:	[0.225, 220.0] [-]

Optimisation variables of the H2/O2 powered aerospike engine with p_{cc}=300 [bar] and T/W=100 [-]

Burning mass rates ($\vec{\dot{m}}$)	:	[1866.64, 907.89, 515.27, 1910.68] [kg/s]
Burning periods ($\vec{t_b}$)	:	[103.09, 27.66, 87.29] [s]
Steering angles ($\vec{\gamma}$)	:	[85.55, 62.2, 25.38, 47.0, 85.58] [°]
Steering time intervals ($\vec{t_\gamma}$)	:	[1.49, 129.77, 109.91, 21.41, 168.63] [s]
Sizing Variables (F/O, ϵ)	:	[0.225, 220.0] [-]

Optimisation variables of the CH4/O2 powered aerospike engine with p_{cc}=300 [bar] and T/W=200 [-]

Burning mass rates ($\vec{\dot{m}}$) : [1999.52, 793.74, 1875.52, 1757.22] [kg/s]
Burning periods ($\vec{t_b}$) : [95.65, 48.37, 150.68] [s]
Steering angles ($\vec{\gamma}$) : [63.48, 42.16, 9.29, 17.52, 56.54] [°]
Steering time intervals ($\vec{t_\gamma}$) : [0.99, 94.58, 39.29, 173.03, 86.3] [s]
Sizing Variables (F/O, ϵ) : [0.3, 220.0] [-]

Optimisation variables of the CH4/O2 powered aerospike engine with p_{cc}=250 [bar] and T/W=200 [-]
Burning mass rates ($\vec{\dot{m}}$) : [1888.4, 1086.2, 1895.24, 61.99] [kg/s]
Burning periods ($\vec{t_b}$) : [176.27, 88.81, 51.72] [s]
Steering angles ($\vec{\gamma}$) : [66.04, 20.77, 15.42, 16.56, 74.43] [°]
Steering time intervals ($\vec{t_\gamma}$) : [1.3, 86.99, 75.92, 103.91, 82.39] [s]
Sizing Variables (F/O, ϵ) : [0.3, 220.0] [-]

Optimisation variables of the CH4/O2 powered aerospike engine with p_{cc}=300 [bar] and T/W=150 [-]
Burning mass rates ($\vec{\dot{m}}$) : [1971.74, 1974.37, 845.61, 858.14] [kg/s]
Burning periods ($\vec{t_b}$) : [182.94, 106.39, 150.92] [s]
Steering angles ($\vec{\gamma}$) : [13.57, 3.48, 59.46, 27.79, 20.73] [°]
Steering time intervals ($\vec{t_\gamma}$) : [0.36, 198.42, 120.13, 195.74, 82.72] [s]
Sizing Variables (F/O, ϵ) : [0.3, 220.0] [-]

Optimisation variables of the C2H2/O2 powered aerospike engine with p_{cc}=300 [bar] and T/W=200 [-]
Burning mass rates ($\vec{\dot{m}}$) : [2365.49, 27.79, 234.93, 1134.88] [kg/s]
Burning periods ($\vec{t_b}$) : [182.65, 107.64, 115.46] [s]
Steering angles ($\vec{\gamma}$) : [38.65, 15.53, 18.33, 5.57, 5.1] [°]
Steering time intervals ($\vec{t_\gamma}$) : [0.09, 104.86, 30.95, 98.68, 189.7] [s]
Sizing Variables (F/O, ϵ) : [0.7, 220.0] [-]

Optimisation variables of the C2H2/O2 powered aerospike engine with p_{cc}=300 [bar] and T/W=150 [-]
Burning mass rates ($\vec{\dot{m}}$) : [1919.85, 1912.61, 917.49, 348.88] [kg/s]
Burning periods ($\vec{t_b}$) : [174.86, 113.17, 183.77] [s]
Steering angles ($\vec{\gamma}$) : [38.94, 0.2, 45.53, 12.72, 31.84] [°]
Steering time intervals ($\vec{t_\gamma}$) : [0.56, 129.45, 132.32, 112.19, 63.24] [s]
Sizing Variables (F/O, ϵ) : [0.7, 220.0] [-]

Optimisation variables of the C2H2/O2 powered aerospike engine with p_{cc}=250 [bar] and T/W=200 [-]
Burning mass rates ($\vec{\dot{m}}$) : [1817.45, 1934.24, 805.26, 566.57] [kg/s]
Burning periods ($\vec{t_b}$) : [143.06, 68.28, 75.85] [s]
Steering angles ($\vec{\gamma}$) : [60.92, 2.37, 23.66, 23.88, 58.22] [°]
Steering time intervals ($\vec{t_\gamma}$) : [1.02, 81.09, 199.45, 149.01, 85.45] [s]
Sizing Variables (F/O, ϵ) : [0.7, 220.0] [-]

H.0.2. Optimisation Settings of the Pulse Detonation Engine Powered Vehicles

Optimisation variables of the H2/O2 powered pulse detonation engine with p_{DC}=600 [bar] and T/W=200 [-]
Burning mass rates ($\vec{\dot{m}}$) : [1657.13, 136.27, 597.91, 642.25] [kg/s]
Burning periods ($\vec{t_b}$) : [181.24, 61.75, 85.25] [s]
Steering angles ($\vec{\gamma}$) : [69.33, 46.63, 57.75, 0.48] [°]
Steering time intervals ($\vec{t_\gamma}$) : [0.01, 123.15, 165.3, 26.86] [s]
Sizing Variables (F/O, ϵ) : [0.35, 7.693] [-]

Optimisation variables of the H2/O2 powered pulse detonation engine with p_{DC}=500 [bar] and T/W=200 [-]

Burning mass rates ($\vec{\dot{m}}$) : [1722.36, 143.36, 678.67, 977.88] [kg/s]
Burning periods ($\vec{t_b}$) : [183.03, 183.86, 87.86] [s]
Steering angles ($\vec{\gamma}$) : [59.85, 60.11, 1.1, 27.16] [°]
Steering time intervals ($\vec{t_\gamma}$) : [0.47, 123.6, 145.57, 176.48] [s]
Sizing Variables (F/O, ϵ) : [0.35, 9.232] [-]

Optimisation variables of the H2/O2 powered pulse detonation engine with p_{DC}=600 [bar] and T/W=150 [-]
Burning mass rates ($\vec{\dot{m}}$) : [1791.45, 1288.34, 712.59, 54.92] [kg/s]
Burning periods ($\vec{t_b}$) : [115.51, 163.73, 24.83] [s]
Steering angles ($\vec{\gamma}$) : [54.41, 4.32, 5.46, 18.28] [°]
Steering time intervals ($\vec{t_\gamma}$) : [0.32, 113.63, 179.93, 51.78] [s]
Sizing Variables (F/O, ϵ) : [0.35, 8.081] [-]

Optimisation variables of the CH4/O2 powered pulse detonation engine with p_{DC}=700 [bar] and T/W=200 [-]
Burning mass rates ($\vec{\dot{m}}$) : [1989.02, 1089.76, 808.83, 1537.95] [kg/s]
Burning periods ($\vec{t_b}$) : [190.24, 67.85, 145.15] [s]
Steering angles ($\vec{\gamma}$) : [26.32, 8.03, 2.69, 75.74] [°]
Steering time intervals ($\vec{t_\gamma}$) : [1.32, 193.07, 124.43, 63.95] [s]
Sizing Variables (F/O, ϵ) : [0.375, 10.023] [-]

Optimisation variables of the CH4/O2 powered pulse detonation engine with p_{DC}=600 [bar] and T/W=200 [-]
Burning mass rates ($\vec{\dot{m}}$) : [1951.67, 1863.82, 598.99, 1920.54] [kg/s]
Burning periods ($\vec{t_b}$) : [112.42, 147.36, 49.38] [s]
Steering angles ($\vec{\gamma}$) : [34.93, 8.01, 47.69, 75.48] [°]
Steering time intervals ($\vec{t_\gamma}$) : [1.32, 174.16, 94.92, 174.18] [s]
Sizing Variables (F/O, ϵ) : [0.375, 8.215] [-]

Optimisation variables of the CH4/O2 powered pulse detonation engine with p_{DC}=500 [bar] and T/W=200 [-]
Burning mass rates ($\vec{\dot{m}}$) : [1945.8, 1727.29, 546.56, 724.14] [kg/s]
Burning periods ($\vec{t_b}$) : [183.43, 78.81, 117.93] [s]
Steering angles ($\vec{\gamma}$) : [40.79, 12.37, 45.79, 72.41] [°]
Steering time intervals ($\vec{t_\gamma}$) : [1.26, 134.2, 137.11, 141.22] [s]
Sizing Variables (F/O, ϵ) : [0.375, 9.351] [-]

Optimisation variables of the C2H2/O2 powered pulse detonation engine with p_{DC}=600 [bar] and T/W=200 [-]
Burning mass rates ($\vec{\dot{m}}$) : [1891.0, 1229.17, 1385.55, 1091.08] [kg/s]
Burning periods ($\vec{t_b}$) : [155.47, 112.27, 190.44] [s]
Steering angles ($\vec{\gamma}$) : [53.02, 59.32, 39.82, 3.77] [°]
Steering time intervals ($\vec{t_\gamma}$) : [0.07, 64.31, 17.26, 59.92] [s]
Sizing Variables (F/O, ϵ) : [0.775, 7.338] [-]

Optimisation variables of the C2H2/O2 powered pulse detonation engine with p_{DC}=500 [bar] and T/W=200 [-]
Burning mass rates ($\vec{\dot{m}}$) : [1784.13, 1611.16, 364.39, 1475.36] [kg/s]
Burning periods ($\vec{t_b}$) : [150.73, 183.49, 133.5] [s]
Steering angles ($\vec{\gamma}$) : [68.04, 5.38, 0.03, 80.75] [°]
Steering time intervals ($\vec{t_\gamma}$) : [1.41, 78.18, 152.47, 103.28] [s]
Sizing Variables (F/O, ϵ) : [0.775, 9.2] [-]

Optimisation variables of the C2H2/O2 powered pulse detonation engine with p_{DC}=600 [bar] and T/W=150 [-]

Burning mass rates ($\vec{\dot{m}}$) : [2522.01, 861.16, 2127.23, 2059.53] [kg/s]
Burning periods ($\vec{t_b}$) : [172.76, 117.89, 122.88] [s]
Steering angles ($\vec{\gamma}$) : [4.15, 2.15, 44.46, 78.48] [°]
Steering time intervals ($\vec{t_\gamma}$) : [1.37, 166.15, 139.82, 55.19] [s]
Sizing Variables (F/O, ϵ) : [0.775, 8.191] [-]

Optimisation variables of the C2H4/O2 powered pulse detonation engine with p_{DC}=700 [bar] and T/W=200 [-]

Burning mass rates ($\vec{\dot{m}}$) : [1998.03, 1591.15, 1738.96, 1564.23] [kg/s]
Burning periods ($\vec{t_b}$) : [170.93, 115.21, 72.25] [s]
Steering angles ($\vec{\gamma}$) : [36.03, 18.84, 67.61, 42.65] [°]
Steering time intervals ($\vec{t_\gamma}$) : [0.74, 133.55, 172.06, 130.04] [s]
Sizing Variables (F/O, ϵ) : [0.55, 7.412] [-]

Optimisation variables of the C2H4/O2 powered pulse detonation engine with p_{DC}=600 [bar] and T/W=200 [-]

Burning mass rates ($\vec{\dot{m}}$) : [1898.75, 1190.02, 1165.49, 1899.5] [kg/s]
Burning periods ($\vec{t_b}$) : [144.47, 156.28, 78.09] [s]
Steering angles ($\vec{\gamma}$) : [51.41, 15.6, 19.7, 11.13] [°]
Steering time intervals ($\vec{t_\gamma}$) : [0.19, 125.88, 126.0, 68.39] [s]
Sizing Variables (F/O, ϵ) : [0.55, 8.453] [-]

Optimisation variables of the C2H4/O2 powered pulse detonation engine with p_{DC}=500 [bar] and T/W=200 [-]

Burning mass rates ($\vec{\dot{m}}$) : [1974.17, 1194.48, 1853.31, 550.87] [kg/s]
Burning periods ($\vec{t_b}$) : [189.51, 177.59, 169.31] [s]
Steering angles ($\vec{\gamma}$) : [29.77, 17.94, 40.61, 21.59] [°]
Steering time intervals ($\vec{t_\gamma}$) : [0.38, 160.1, 135.32, 75.07] [s]
Sizing Variables (F/O, ϵ) : [0.55, 7.207] [-]

H.0.3. Optimisation Settings of the Precooled Hybrid Airbreathing Rocket Engine Powered Vehicles

Optimisation variables of the H2/O2 powered precooled hybrid airbreathing rocket engine with p_{cc}=300 [bar] and T/W=100 [-]

Burning mass rates ($\vec{\dot{m}}$) : [1864.48, 402.7, 1885.83, 1675.09, 1922.36] [kg/s]
Burning periods ($\vec{t_b}$) : [152.68, 148.24, 130.09, 141.09] [s]
Steering angles ($\vec{\gamma}$) : [11.81, 73.27, 48.19, 4.04, 37.12] [°]
Steering time intervals ($\vec{t_\gamma}$) : [121.14, 57.33, 74.54, 129.57, 145.83] [s]
Sizing Variables (F/O, ϵ, $F/O_{breathing}$) : [0.225, 56.716, 0.675] [-]

Optimisation variables of the H2/O2 powered precooled hybrid airbreathing rocket engine with p_{cc}=300 [bar] and T/W=100 [-]

Burning mass rates ($\vec{\dot{m}}$) : [2310.69, 1168.96, 1517.22, 610.56, 937.72] [kg/s]
Burning periods ($\vec{t_b}$) : [6.05, 20.51, 131.46, 29.12] [s]
Steering angles ($\vec{\gamma}$) : [87.34, 26.69, 20.79, 83.09, 83.99] [°]
Steering time intervals ($\vec{t_\gamma}$) : [120.76, 189.52, 199.81, 70.71, 87.69] [s]
Sizing Variables (F/O, ϵ, $F/O_{breathing}$) : [0.225, 80.578, 0.809] [-]

Optimisation variables of the CH4/O2 powered precooled hybrid airbreathing rocket engine with p_{cc}=300 [bar] and T/W=150 [-]

Burning mass rates ($\overrightarrow{\dot{m}}$)	:	[2348.2, 1941.9, 1967.47, 2013.26] [kg/s]
Burning periods ($\overrightarrow{t_b}$)	:	[35.16, 54.55, 196.32] [s]
Steering angles ($\overrightarrow{\gamma}$)	:	[27.8, 18.35, 63.5, 54.41] [°]
Steering time intervals ($\overrightarrow{t_\gamma}$)	:	[99.32, 194.91, 143.44, 92.57] [s]
Sizing Variables (F/O, ϵ, $F/O_{breathing}$)	:	[0.3, 45.942, 0.467] [-]

Optimisation variables of the CH4/O2 powered precooled hybrid airbreathing rocket engine with p_{cc}=250 [bar] and T/W=100 [-]

Burning mass rates ($\overrightarrow{\dot{m}}$)	:	[2426.9, 1730.44, 1424.15, 1129.07, 1375.32] [kg/s]
Burning periods ($\overrightarrow{t_b}$)	:	[49.64, 51.07, 99.73, 91.0] [s]
Steering angles ($\overrightarrow{\gamma}$)	:	[13.85, 14.95, 1.67, 21.81, 18.1] [°]
Steering time intervals ($\overrightarrow{t_\gamma}$)	:	[158.06, 154.16, 25.91, 54.73, 72.45] [s]
Sizing Variables (F/O, ϵ, $F/O_{breathing}$)	:	[0.3, 50.856, 0.492] [-]

Sensitivity Analysis

I.1. Aerospike Sensitivities

I.1.1. Aerospike Sensitivity to $\epsilon_{\text{eff,max}}$

Aerospike Engine		p_{cc}=300 [bar] T/W=150					
$\epsilon_{\text{eff,max}}$ [-]	Performance Parameters	H2/O2		CH4/O2		C2H2/O2	
200	Fitness [-]	43	(1.7%)	198	(1.5%)	62	(-0.2%)
	Orbit [-]	T		F		F	
	$I_{sp,t,eff}$ [s]	476	(-0.2%)	364	(-0.1%)	376	(-0.1%)
	DeltaV [m/s]	11257	(0.3%)	8894	(0.6%)	9015	(-0.1%)
	$M_{surplus}$ [Mg]	0		0		0	
180	Fitness [-]	42	(-0.5%)	204	(5.5%)	62	(-0.6%)
	Orbit [-]	T		F		F	
	$I_{sp,t,eff}$ [s]	475	(-0.4%)	363	(-0.3%)	375	(-0.2%)
	DeltaV [m/s]	11232	(0.1%)	8804	(-0.4%)	9001	(-0.3%)
	$M_{surplus}$ [Mg]	0		0		0	
160	Fitness [-]	42	(1.1%)	210	(8.9%)	60	(-0.9%)
	Orbit [-]	T		F		F	
	$I_{sp,t,eff}$ [s]	474	(-0.6%)	363	(-0.5%)	376	(-0.3%)
	DeltaV [m/s]	11204	(-0.2%)	8780	(-0.7%)	8383	(-0.5%)
	$M_{surplus}$ [Mg]	0		0		0	

Table I.1: Provides the performance parameters and the percentage w.r.t. the base ascent trajectory at varying $\epsilon_{\text{eff,max}}$.

I.1.2. Aerospike Sensitivity to $\kappa_{\text{expansion}}$

Aerospike Engine		p_{cc}=300 [bar] T/W=200					
$\kappa_{\text{expansion}}$	Performance Parameters	H2/O2	%	CH4/O2	%	C2H2/O2	%
80%	Fitness [-]	69	(5.0%)	221	(1.%)4	49	(0.3%)
	Orbit [-]	T		F		T	
	$I_{sp,t,eff}$ [s]	480	(-0.1%)	367	(-0.2%)	384	(-0.1%)
	DeltaV [m/s]	11389	(0.4%)	8949	(-0.1%)	9066	(-0.1%)
	$M_{surplus}$ [Mg]	0		0		0	
250%	Fitness [-]	69	(4.4%)	238	(9.1%)	50	(2.0%)
	Orbit [-]	T		F		T	
	$I_{sp,t,eff}$ [s]	478	(-0.5%)	363	(-1.1%)	383	(-0.4%)
	DeltaV [m/s]	11367	(0.2%)	8918	(-0.4%)	9046	(-0.3%)
	$M_{surplus}$ [Mg]	0		0		0	

Table I.2: Provides the performance parameters and the percentage w.r.t. the base ascent trajectories for the aerospike engine at $\kappa_{expansion}$ equal to 0.8 and 2.5.

I.1.3. Aerospike Sensitivity Table for varying $\eta_{\text{direction}}$

Aerospike Engine		p_{cc}=300 [bar] T/W=150					
$\eta_{\text{direction}}$ [-]	Performance Parameters	H2/O2		CH4/O2		C2H2/O2	
0.03	Fitness [-]	699	(1570.0%)	239	(23.9%)	743	(908.4%)
	Orbit [-]	F		F		F	
	$I_{sp,t,eff}$ [s]	473	(-0.8%)	360	(-1.2%)	372	(-1.2%)
	DeltaV [m/s]	11153	(-0.6%)	8796	(-0.5%)	8934	(-0.6%)
	$M_{surplus}$ [Mg]	0		0		0	
0.07	Fitness [-]	855	(1943.0%)	820	(324.1%)	1021	(1286.7%)
	Orbit [-]	F		F		F	
	$I_{sp,t,eff}$ [s]	467	(-2.1%)	353	(-3.2%)	364	(-3.1%)
	DeltaV [m/s]	11117	(-0.9%)	8717	(-1.4%)	8900	(-1.0%)
	$M_{surplus}$ [Mg]	0		0		0	
0.1	Fitness [-]	1020	(2337.4%)	1271	(557.3%)	1426	(1836.6%)
	Orbit [-]	F		F		F	
	$I_{sp,t,eff}$ [s]	461	(-3.3%)	346	(-5.0%)	358	(-4.9%)
	DeltaV [m/s]	11020	(-1.8%)	8632	(-2.4%)	8819	(-1.9%)
	$M_{surplus}$ [Mg]	0		0		0	

Table I.3: Provides the performance parameters and the percentage w.r.t. the base ascent trajectories for the aerospike engine at varying $\eta_{\text{direction}}$.

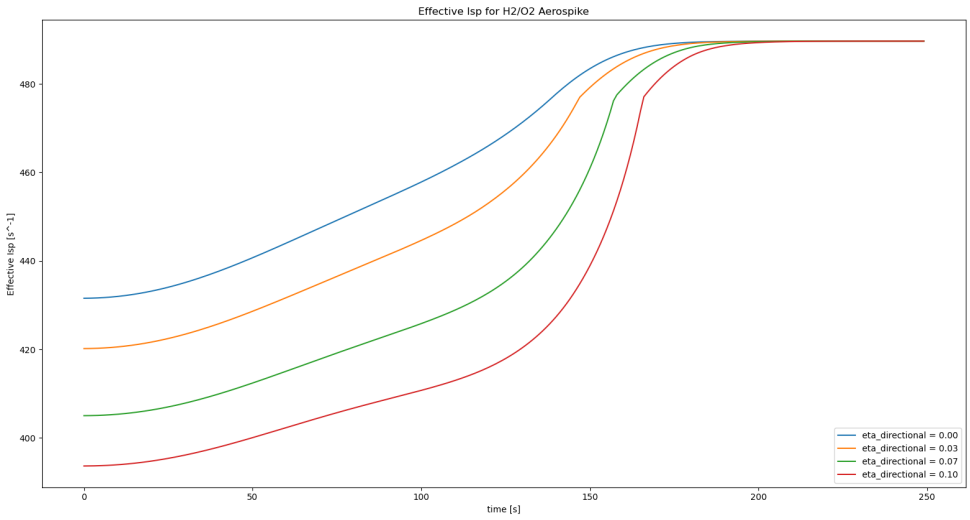

Figure I.1: Illustrates the $I_{sp,eff}$ values of an H2/O2 powered aerospike engine with p_{cc}=300 and T/W=150 at varying $\eta_{\text{directional}}$.

J

Results of the Performance Model

J.1. Results of the H2/O2 Powered Aerospike p_{cc}=250 bar T/W=200

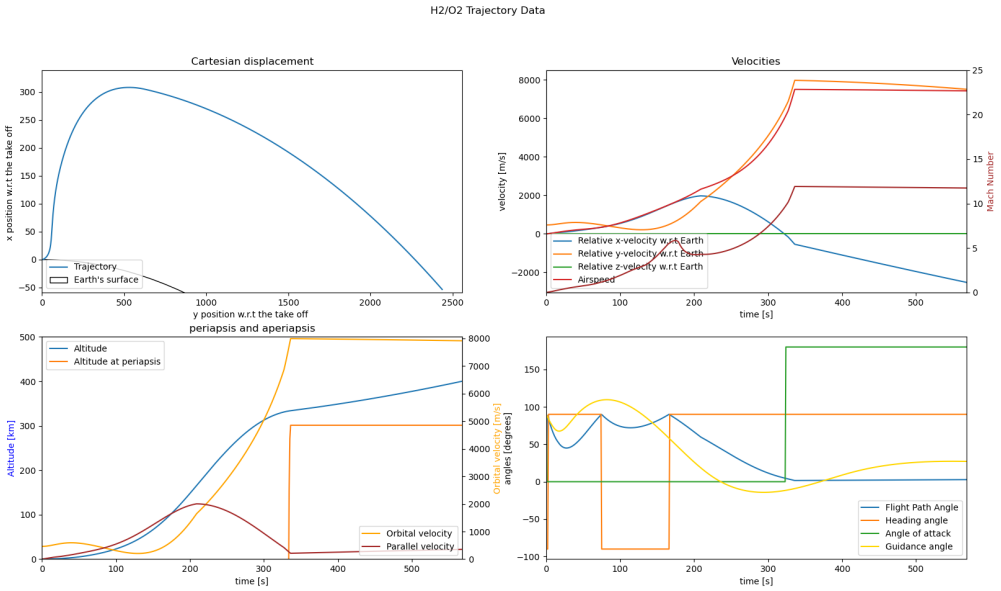

Figure J.1: Illustrates the trajectory data of the aerospike powered ascent vehicle configured with H2/O2, p_{cc} = 250 [bar], and T/W=200 [-].

J.2. Results of the C2H2/O2 Powered Aerospike p_{cc}=300 bar T/W=200

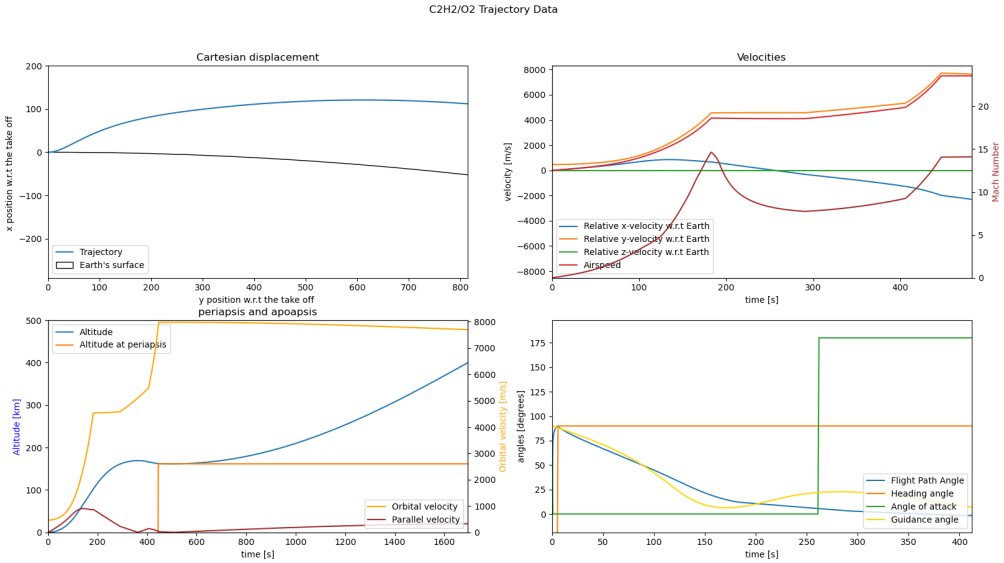

Figure J.2: Illustrates the trajectory data of the aerospike powered ascent vehicle configured with C2H2/O2, p_{cc} = 300 [bar], and T/W=200 [-].

Bibliography

[1] Ucs satellite database, . URL https://cearun.grc.nasa.gov/cgi-bin/CEARUN/donecea3.cgi.

[2] . URL https://engineering.purdue.edu/~propulsi/propulsion/rockets/liquids/xrs2200.html.

[3] The hangar / falcon 9, . URL https://www.spaceflightinsider.com/hangar/falcon-9/.

[4] Ucs satellite database, . URL https://www.UCSSatelliteDatabaseucsusa.org/resources/satellite-database#:~:text=In-depth%20details%20on%20the,purpose%2C%20and%20other%20operational%20details.

[5] Global space industry dynamics, 2017.

[6] Space report 2019, 2019.

[7] Pygmo overview, 2022. URL https://esa.github.io/pygmo2/overview.html#heuristic-global-optimization.

[8] Abdul Ossman Ahmad, Christie Maddock, Thomas Scanlon, and Richard Brown. Prediction of the aerodynamic performance of re-usable single stage to orbit vehicles. *Space Access 2011*, 2011.

[9] John David Anderson Jr. *Fundamentals of aerodynamics*. Tata McGraw-Hill Education, 2010.

[10] Andy. How many satellites orbiting the earth in 2019?, 2019. URL https://www.pixalytics.com/satellites-orbiting-earth-2019/.

[11] GlANFRANCO ANGELINO. Approximate method for plug nozzle design. *AIAA Journal*, 2(10):1834–1835, 1964.

[12] Tarik Barth and José MA Longo. Advanced aerothermodynamic analysis of shefex i. *Aerospace Science and Technology*, 14(8):587–593, 2010.

[13] Francesco Biscani and Dario Izzo. A parallel global multiobjective framework for optimization: pagmo. *Journal of Open Source Software*, 5(53):2338, 2020. doi: 10.21105/joss.02338. URL https://doi.org/10.21105/joss.02338.

[14] Thomas Bussing and George Pappas. Pulse detonation engine theory and concepts. *Developments in high-speed-vehicle propulsion systems(A 97-15029 02-07), Reston, VA, American Institute of Aeronautics and Astronautics, Inc.(Progress in Astronautics and Aeronautics.*, 165:421–472, 1996.

[15] John Butcher. Runge-kutta methods. *Scholarpedia*, 2(9):3147, 2007.

[16] Bill Canis. Commercial space industry launhes a new phase, 2016.

[17] Patrick Carrick. Theoretical performance of high energy density cryogenic solid rocket propellants. In *31st Joint Propulsion Conference and Exhibit*, page 2892, 1995.

[18] Guan-Bang Chen, Yueh-Heng Li, Tsarng-Sheng Cheng, Hung-Wei Hsu, and Yei-Chin Chao. Effects of hydrogen peroxide on combustion enhancement of premixed methane/air flames. *international journal of hydrogen energy*, 36(23):15414–15426, 2011.

[19] Ben Maritz Bill Wiseman Chris Daehnick, Isabelle Klinghoffer. Large leo satellite constellations: Will it be different this time?, 2020.

[20] John Drury Clark. *Ignition!: An informal history of liquid rocket propellants*. Rutgers University Press, 1972.

[21] Jacobus W Cornelisse, HFR Schoyer, and Karel F Wakker. Rocket propulsion and spaceflight dynamics. *London: Pitman*, 1979.

[22] Adam F Dissel, Ajay P Kothari, and Mark J Lewis. Comparison of horizontally and vertically launched airbreathing and rocket vehicles. *Journal of spacecraft and rockets*, 43(1):161–169, 2006.

[23] dr. ir. A. Gangoli Rao. Lecture notes of aero engine technology (ae4238), September 2019.

[24] Takuma Endo and Toshi Fujiwara. A simplified analysis on a pulse detonation engine model. *Transactions of the Japan Society for Aeronautical and space sciences*, 44(146):217–222, 2002.

[25] Víctor Fernández Villacé. *Simulation, design and analysis of air-breathing combined-cycle engines for high speed propulsion*. PhD thesis, Aeronauticos, 2013.

[26] Thong van Nguyen Gennady E. Dumnov Gerald Hagemann, Hans Immich. Advanced rocket nozzles. *Journal of Propuslsion and Power*, 1998.

[27] David G. Goodwin, Harry K. Moffat, Ingmar Schoegl, Raymond L. Speth, and Bryan W. Weber. Cantera: An object-oriented software toolkit for chemical kinetics, thermodynamics, and transport processes. `https://www.cantera.org`, 2022. Version 2.6.0.

[28] B Goracke, Daniel Levack, and Gary Johnson. Tripropellant engine option comparison for ssto. In *Space Programs and Technologies Conference*, page 3609, 1995.

[29] Trevor Hastie, Robert Tibshirani, and Jerome Friedman. The elements of statistical learning: data mining, inference, and prediction. springer series in statistics. *Springer New York*, 2009.

[30] William H Heiser. Single-stage-to-orbit versus two-stage-to-orbit airbreathing systems. *Journal of Spacecraft and Rockets*, 47(1):222–224, 2010.

[31] William H Heiser and David T Pratt. *Hypersonic airbreathing propulsion*. Aiaa, 1994.

[32] J Hinkey, Jr, Thomas Bussing, T Bratkovich, Thomas Bussing, T Bratkovich, and J Hinkey, Jr. Practical implementation of pulse detonations engines. In *33rd Joint Propulsion Conference and Exhibit*, page 2748, .

[33] J Hinkey, Jr, Thomas Bussing, T Bratkovich, Thomas Bussing, T Bratkovich, and J Hinkey, Jr. Practical implementation of pulse detonations engines. In *33rd Joint Propulsion Conference and Exhibit*, page 2748, .

[34] Peggy Hollinger. A space engine that could make flying into orbit common, 2017. URL `https://www.ft.com/content/33f3cfe2-2ecd-11e7-9555-23ef563ecf9a`.

[35] Núria Margarit i Bel and Manuel Martínez Sánchez. Simulation of a liquid rocket engine.

[36] Takashi Ito, Kozo Fujii, and A Hayashi. Computations of the axisymmetric plug nozzle flow fields-flow structures and thrust performance. In *17th Applied Aerodynamics Conference*, page 3211, 1999.

[37] Khlopkov Yuri Ivanovich, Zay Yar Myo Myint, and Khlopkov Anton Yurievich. Aerodynamic investigation for prospective aerospace vehicle in the transitional regime. *International Journal of Aeronautical and Space Sciences*, 14(3):215–221, 2013.

[38] Michaela Brchnelova Giulio Dacome Bardienus Duisterhof Andrea Levoni Louis Lischwe Ericka Matsuda-Martin Jacopo Sem Douwe Sonneveldt Jonas Amend, Bavly Barsom. Hyperion 4 – final report, 2018.

[39] Nicolas Jourdaine, Nobuyuki Tsuboi, Kohei Ozawa, Takayuki Kojima, and A Koichi Hayashi. Three-dimensional numerical thrust performance analysis of hydrogen fuel mixture rotating detonation engine with aerospike nozzle. *Proceedings of the Combustion Institute*, 37(3):3443–3451, 2019.

[40] Thomas A Kaemming and Daniel E Paxson. Determining the pressure gain of pressure gain combustion. In *2018 Joint propulsion conference*, page 4567, 2018.

[41] J Korte. Parametric model of an aerospike rocket engine. In *38th Aerospace Sciences Meeting and Exhibit*, page 1044, 2000.

[42] H Kuczera and C Johnson. The major results of the festip system study. In *9th International Space Planes and Hypersonic Systems and Technologies Conference*, page 6001, 1999.

[43] Matthew Lam, Daniel Tillie, Timothy Leaver, and Brian McFadden. Pulse detonation engine technology: an overview. *The University of British Columbia*, 2004.

[44] W Henry Lambright. Launching commercial space: Nasa, cargo, and policy innovation. *Space Policy*, 34: 23–31, 2015.

[45] Wiley J Larson, Gary N Henry, and Ronald W Humble. *Space propulsion analysis and design*. McGraw-Hill, 1995.

[46] Frank Lu, Jason Meyers, and Donald Wilson. Experimental study of propane-fueled pulsed detonation rocket. In *12th AIAA International Space Planes and Hypersonic Systems and Technologies*, page 6974. 2003.

[47] AGM Maree, E Mooij, and BTC Zandbergen. Space-plane analysis: A trajectory generation and sensitivity analysis. *NASA STI/Recon Technical Report N*, 96:11880, 1993.

[48] E. Mooij. Ae4870b - re-entry systems. University Lecture Notes (2017-2018), 2017.

[49] Heinz E. Mueller. Fluid-dynamic shock ring for controlled flow separation in a rocket engine exhaust nozzle, 11 1973. US Patent 3,925,982.

[50] Arash Naghib-Lahouti and Elhaum Tolouei. Numerical investigation of the effect of base bleed on thrust of a truncated aerospike nozzle in off-design conditions. In *ECCOMAS CFD 2006: Proceedings of the European Conference on Computational Fluid Dynamics, Egmond aan Zee, The Netherlands, September 5-8, 2006*. Citeseer, 2006.

[51] *Space Launch Report: SpaceXFalcon9 Data Sheet*. NASA, 3 2017. Falcon 9 v1.1 Data Sheet (New Apri 29, 2013).

[52] Jorge Nocedal and Stephen Wright. *Numerical optimization*. Springer Science & Business Media, 2006.

[53] Tim Nodd. Are aerospike engines better than traditional rocket engines? URL `https://everydayastronaut.com/aerospikes/`.

[54] Satoshi Nonaka, Hiroyuki Ogawa, and Yoshifumi Inatani. Aerodynamic design considerations in vertical landing rocket vehicle. In *10th AIAA/NAL-NASDA-ISAS International Space Planes and Hypersonic Systems and Technologies Conference*, page 1898, 2001.

[55] John Olds, John Bradford, Ashraf Charania, Laura Ledsinger, David McCormick, and Kirk Sorensen. Hyperion-an ssto vision vehicle concept utilizing rocket-based combined cycle propulsion. In *9th International Space Planes and Hypersonic Systems and Technologies Conference*, page 4944, 1999.

[56] Min Ou, Li Yan, Wei Huang, and Xiao-qian Chen. Thermodynamic performance analysis of scramjet at wide working condition. In *7 th Europian Conference for Aeronautics and Space Science (EUCASS), Milan, Italy*, 2017.

[57] KM Pandey and Pinku Debnath. Review on recent advances in pulse detonation engines. *Journal of Combustion*, 2016, 2016.

[58] Jay P Penn. Ssto vs tsto design considerations—an assessment of the overall performance, design considerations, technologies, costs, and sensitivities of ssto and tsto designs using modern technologies. In *AIP conference proceedings*, volume 361, pages 551–554. American Institute of Physics, 1996.

[59] Dr. Arvind Gangoli Rao Prof. Ir. J.P. van Buijtenen, Dr. Wilfried Visser. Aero engine technology, ae4–238. University course reader, 2018.

[60] Konstantin Ragozin. Thrust performance and heat load modelling of pulse detonation engines, 2020.

[61] DOUGLAS RAPP. High energy-density liquid rocket fuel performance. In *26th Joint Propulsion Conference*, page 1968, 1990.

[62] Grzegorz Rarata and Jaromir Smętek. Explosives based on hydrogen peroxide-a historical review and novel applications. *Materiały Wysokoenergetyczne*, 8, 2016.

[63] J Ruf, P McConaughey, J Ruf, and P McConaughey. The plume physics behind aerospike nozzle altitude compensation and slipstream effect. In *33rd Joint Propulsion Conference and Exhibit*, page 3218, 1997.

[64] ÖZER Salih, Mehmet Akçay, Erdinç Vural, and İlker Turgut YILMAZ. The effects of the use of acetylene gas as an alternative fuel in a gasoline engine. *International Advanced Researches and Engineering Journal*, 4(2):76–86, 2020.

[65] UM Schoettle, H Grallert, and FA Hewitt. Advanced air-breathing propulsion concepts for winged launch vehicles. *Acta Astronautica*, 20:117–129, 1989.

[66] C Segal. Propulsion systems for hypersonic flight. *University of Florida, Gainesville*, 2004.

[67] Hiroki Shirasu, Jephrey South, and James Martin. Analysis of concepts for ssto. In *31st Joint Propulsion Conference and Exhibit*, page 2953, 1995.

[68] NN Smirnov, VF Nikitin, LI Stamov, EV Mikhalchenko, and VV Tyurenkova. Rotating detonation in a ramjet engine three-dimensional modeling. *Aerospace Science and Technology*, 81:213–224, 2018.

[69] Douwe A.W. Sonneveldt. Proposal for adaptable mechanical nozzles for first stage rockets. *Delft repository*, 2020. doi: https://repository.tudelft.nl/islandora/search/?collection=research.

[70] *Capabilities Services*. Space Exploration Technologies Corp. (SpaceX), 2020.

[71] M Dhananiya Lakshmi Sri, L Oblisamy, and G Mari Prabu. Combustion of acetylene and its performance in valveless pulse jet engine.

[72] Caleb Williams Stephanie DelPozzo. Nano/microsatellite market forecast, 10th edition, 2020.

[73] Paul Tartabini, Roger Lepsch, J Korte, and Kathryn Wurster. A multidisciplinary performance analysis of a lifting-body single-stage-to-orbit vehicle. In *38th Aerospace Sciences Meeting and Exhibit*, page 1045, 2000.

[74] Nobuyuki Tomita, Alexander Nebylov, Victor Sokolov, Daisuke Tsurumaru, Tsuyoshi Saotome, and Yoshiaki Ohkami. Feasibility study of a rocket-powered hthl-ssto with an ekranoplane as a takeoff assist. In *Space Plane and Hypersonic Systems and Technology Conference*, page 4517, 1996.

[75] Richard Varvill and Alan Bond. A comparison of propulsion concepts for ssto reusable launchers. *JOURNAL-BRITISH INTERPLANETARY SOCIETY*, 56(3/4):108–117, 2003.

[76] G Venkatasubramanyam and James Martin. Continuing propulsion evaluations for ssto. In *30th Joint Propulsion Conference and Exhibit*, page 3158, 1994.

[77] Thongsay Vongpaseuth, G Venkatasubramanyam, and James Martin. Russian tripropellant engines for ssto. In *31st Joint Propulsion Conference and Exhibit*, page 2952, 1995.

[78] Chang-hui WANG, LIU Yu, and Yun-fei LIAO. Studies on aerodynamic behavior and performance of aerospike nozzles. *Chinese Journal of Aeronautics*, 19(1):1–9, 2006.

[79] Chang-Hui Wang, Yu Liu, and Li-Zi Qin. Aerospike nozzle contour design and its performance validation. *Acta Astronautica*, 64(11-12):1264–1275, 2009.

[80] Helen Webber, Alan Bond, and Mark Hempsell. Sensitivity of pre-cooled air-breathing engine performance to heat exchanger design parameters. In *57th International Astronautical Congress*, pages D2–P, 2006.

[81] E Wintenberger, JM Austin, M Cooper, S Jackson, and JE Shepherd. Impulse of a single-pulse detonation tube. *California Institute of Technology, Pasadena, CA. http://authors. library. caltech. edu/25816*, 2002.

[82] Palmdale Works, NJ Teterboro, Canoga Park Rocketdyne, and Chula Vista Rohr. X-33 advanced technology demonstrator. 1996.

[83] Ayşe Meriç YAZICI and Sefer DARICI. The new opportunities in space economy. *Itobiad: Journal of the Human & Social Science Researches*, 8(4), 2019.

[84] David Young, Timothy Kokan, Christopher Tanner, Ian Clark, Christopher Tanner, and Alan Wilhite. Lazarus: a ssto hypersonic vehicle concept utilizing rbcc and hedm propulsion technologies. In *14th AIAA/AHI Space Planes and Hypersonic Systems and Technologies Conference*, page 8099, 2006.

[85] Barry. T. C. Zandbergen. Thermal rocket propulsion. University course reader, 2016.

[86] Yufei Zhang, Haixin Chen, Song Fu, Miao Zhang, and Meihong Zhang. Drag prediction method of powered-on civil aircraft based on thrust drag bookkeeping. *Chinese Journal of Aeronautics*, 28(4): 1023–1033, 2015. ISSN 1000-9361. doi: https://doi.org/10.1016/j.cja.2015.06.015. URL `https://www.sciencedirect.com/science/article/pii/S1000936115001211`.

[87] Adis Zilic, Darren Hitt, and Alina Alexeenko. Numerical simulations of supersonic flow in a linear aerospike micro nozzle. In *37th AIAA Fluid Dynamics Conference and Exhibit*, page 3984, 2007.